

Aims and Scope: The "Cell Journal (Yakhteh)" is a peer review and quarterly English publication of Royan Institute of Iran. The aim of the journal is to disseminate information through publishing the most recent scientific research studies on exclusively Cellular, Molecular and other related topics. **Cell J**, has been certified by the Ministry of Culture and Islamic Guidance since 1999 and also accredited as a scientific and research journal by HBI (Health and Biomedical Information) Journal Accreditation Commission since 2000 which is an open access journal. **This journal holds the membership of the Committee on Publication Ethics (COPE).**

1. Types of articles

The articles in the field of Cellular and Molecular can be considered for publications in **Cell J**. These articles are as below:

A. Original articles Original articles are scientific reports of the original research studies. The article consists of English Abstract (structured), Introduction, Materials and Methods, Results, Discussion, Conclusion, Acknowledgements, Author's Contributions, and References (**Up to 40**).

B. Review articles Review articles are the articles written by well experienced authors and those who have excellence in the related fields. The corresponding author of the review article must be one of the authors of at least three published articles appearing in the references. The review article consists of English Abstract (unstructured), Introduction, Conclusion, Author's Contributions, and References (**Up to 70**).

C. Systematic Reviews

Systematic reviews are a type of literature review that collect and critically analyzes multiple research studies or papers. The Systematic reviews consist of English Abstract (unstructured), Introduction, Materials and Methods, Results, Discussion, Conclusion, Acknowledgements, Author's Contributions, and References (**Up to 70**).

D. Short communications: Short communications are articles containing new findings. Submissions should be brief reports of ongoing researches. The short communication consists of English Abstract (unstructured), the body of the manuscript (should not hold heading or subheading), Acknowledgements, Author's Contributions, and References (**Up to 30**).

E. Case reports: Case reports are short discussions of a case or case series with unique features not previously described which make an important teaching point or scientific observation. They may describe novel techniques or use equipment, or new information on diseases of importance. It consists of English Abstracts (Unstructured), Introduction, Case Report, Discussion, Acknowledgements, Author's Contributions, and References (**Up to 30**).

F. Editorial: Editorial should be written by either the editor in chief or the editorial board.

G. Imaging in biology: Images in biology should focus on a single case with an interesting illustration such as a photograph, histological specimen or investigation. Color images are welcomed. The text should be brief and informative.

H. Letter to the editors: Letter to editors are welcome in response to previously published **Cell J** articles, and may also include interesting cases that do not meet the requirement of being truly exceptional, as well as other brief technical or clinical notes of general interest.

I. Debate.

2. Submission process

It is recommended to see the guidelines for reporting different kinds of manuscripts here. This guide explains how to prepare the manuscript for submission. Before submitting, we suggest authors to familiarize themselves with **Cell J** format and content by reading the journal via the website (www.celljournal.com). The corresponding author ensures that all authors are included in the author list and agree with its order, and they must be aware of the manuscript submission.

A. Author contributions statements

It is essential for authors to include a statement of responsibility in the manuscript that specifies the contribution of every one of them. This participation must include conception and design of the manuscript, data acquisition or data analysis and interpretation, drafting of the manuscript and/or revising it for critically important intellectual content, revision and final approval of the manuscript and statistical analysis, obtaining funding, administrative, technical, or material support, or supervision. Authors who do not meet the above criteria should be acknowledged in the **Acknowledgments section**.

B. Cover letter and copyright

Each manuscript should be accompanied by a cover letter, signed by all authors specifying the following statement: "The

manuscript has been seen and approved by all authors and is not under active consideration for publication. It has neither been accepted for publication nor published in another journal fully or partially (except in abstract form). Also, no manuscript would be accepted in case it has been pre-printed or submitted to other websites I hereby assign the copyright of the enclosed manuscript to **Cell J**. Corresponding author must confirm the proof of the manuscript before online publishing. Also, it is needed to suggest three peer reviewers in the field of their manuscript.

C. Manuscript preparation

Authors whose first language is not English encouraged to consult a native English speaker in order to confirm his manuscripts to American or British (not a mixture) English usage and grammar. It is necessary to mention that we will check the plagiarism of your manuscript by iThenticate Software. The manuscript should be prepared in accordance with the "International Committee of Medical Journal Editors (ICMJE)". Please send your manuscript in two formats Word and Pdf (including: title, name of all the authors with their degree, abstract, full text, references, tables and figures) and Also send tables and figures separately in the site. The abstract and text pages should have consecutive line numbers in the left margin beginning with the title page and continuing through the last page of the written text. Each abbreviation must be defined in the abstract and text when they are mentioned for the first time. Avoid using abbreviation in the title. Please use the international and standard abbreviations and symbols

It should be added that an essential step toward the integration and linking of scientific information reported in published literature is using standardized nomenclature in all fields of science and medicine. Species names must be italicized (*e.g.*, *Homo sapiens*) and also the full genus and species written out in full, both in the title of the manuscript and at the first mention of an organism in a paper.

It is necessary to mention that genes, mutations, genotypes, and alleles must be indicated in italics. Please use the recommended name by consulting the appropriate genetic nomenclature database, *e.g.*, HUGO for human genes. In another words; if it is a human gene, you must write all the letters in capital and italic (*e.g.*, *OCT4*, *c-MYC*). If not, only write the first letter in capital and italic (*e.g.*, *Oct4*, *c-Myc*). **In addition, protein designations are the same as the gene symbol but are not italicized.**

Of note, Cell J will only consider publishing genetic association study papers that are novel and statistically robust. Authors are advised to adhere to the recommendations outlined in the STREGA statement (<http://www.strega-statement.org>). The following criteria must be met for all submissions:

1. Hardy-Weinberg Equilibrium (HWE) calculations must be carried out and reported along with the P-values if applicable [see Namipashaki et al. 2015 (Cell J, Vol 17, N 2, Pages: 187-192) for a discussion].
2. Linkage disequilibrium (LD) structure between SNPs (if multiple SNPs are reported) must be presented.
3. Appropriate multiple testing correction (if multiple independent SNPs are reported) must be included.

Submissions that fail to meet the above criteria will be rejected before being sent out for review.

Each of the following manuscript components should begin in the following sequence:

Authors' names and order of them must be carefully considered (full name(s), highest awarded academic degree(s), email(s), and institutional affiliation(s) of all the authors in English. Also, you must send mobile number and full postal address of the corresponding author).

Changes to Authorship such as addition, deletion or rearrangement of author names must be made only before the manuscript has been accepted in the case of approving by the journal editor. In this case, the corresponding author must explain the reason of changing and confirm them (which has been signed by all authors of the manuscript). If the manuscript has already been published in an online issue, an erratum is needed.

Title is providing the full title of the research (do not use abbreviations in title).

Running title is providing a maximum of 7 words (no more than 50 characters).

Abstract must include Objective, Materials and Methods, Results, and Conclusion (no more than 300 words).

Keywords, three to five, must be supplied by the authors at the foot of the abstract chosen from the Medical Subject Heading (MeSH). Therefore; they must be specific and relevant to the paper.

The following components should be identified after the abstract:

Introduction: The Introduction should provide a brief background to the subject of the paper, explain the importance of the study, and state a precise study question or purpose.

Materials and Methods: It includes the exact methods or observations of experiments. If an apparatus is used, its manufacturer's name and address should be stipulated in parenthesis. If the method is established, give reference but if the

method is new, give enough information so that another author can perform it. If a drug is used, its generic name, dose, and route of administration must be given. Standard units of measurements and chemical symbols of elements do not need to be defined.

Statistical analysis: Type of study and statistical methods should be mentioned and specified by any general computer program used.

Ethical considerations: Please state that informed consent was obtained from all human adult participants and from the parents or legal guardians of minors and include the name of the appropriate institutional review board that approved the project. It is necessary to indicate in the text that the maintenance and care of experimental animals complies with National Institutes of Health guidelines for the humane use of laboratory animals, or those of your Institute or agency.

Clinical trial registration: All of the Clinical Trials performing in Iran must be registered in Iranian Registry of Clinical Trials (www.ircct.ir). The clinical trials performed abroad, could be considered for publication if they register in a registration site approved by WHO or www.clinicaltrials.gov. If you are reporting phase II or phase III randomized controlled trials, you must refer to the CONSORT Statement for recommendations to facilitate the complete and transparent reporting of trial findings. Reports that do not conform to the CONSORT guidelines may need to be revised before peer-reviewing.

Results: They must be presented in the form of text, tables, and figures. Take care that the text does not repeat data that are presented in tables and/or figures. Only emphasize and summarize the essential features of the main results. Tables and figures must be numbered consecutively as appeared in the text and should be organized in separate pages at the end of the manuscript while their location should be mentioned in the main text.

Tables and figures: If the result of your manuscript is too short, it is better to use the text instead of tables & figures. Tables should have a short descriptive heading above them and also any footnotes. Figure's legend should contain a brief title for the whole figure and continue with a short explanation of each part and also the symbols used (no more than 100 words). All figures must be prepared based on cell journal's guideline in color (no more than 6 Figures and Tables) and also in GIF or JPEG format.

Of Note: Please put the tables & figures of the result in the results section not any other section of the manuscript.

Supplementary materials would be published on the online version of the journal. This material is important to the understanding and interpretation of the report and should not repeat material within the print article. The amount of supplementary material should be limited. Supplementary material should be original and not previously published and will undergo editorial and peer review with the main manuscript. Also, they must be cited in the manuscript text in parentheses, in a similar way as when citing a figure or a table. Provide a legend for each supplementary material submitted.

Discussion: It should emphasize the present findings and the variations or similarities with other researches done by other researchers. The detailed results should not be repeated in the discussion again. It must emphasize the new and important aspects of the study.

Conclusion: It emphasizes the new and important aspects of the study. All conclusions are justified by the results of the study.

Acknowledgements: This part includes a statement thanking those who contributed substantially with work relevant to the study but does not have authorship criteria. It includes those who provided technical help, writing assistance and name of departments that provided only general support. You must mention financial support in the study. Otherwise; write this sentence "There is no financial support in this study".

Conflict of interest: Any conflict of interest (financial or otherwise) and sources of financial support must be listed in the Acknowledgements. It includes providers of supplies and services from a commercial organization. Any commercial affiliation must be disclosed, regardless of providing the funding or not.

References: The references must be written based on the Vancouver style. Thus the references are cited numerically in the text and listed in the bibliography by the order of their appearance. The titles of journals must be abbreviated according to the style used in the list of Journals Indexed in PubMed. Write surname and initials of all authors when there are six or less. In the case of seven or more authors, the names of the first six authors followed by "et al." must be listed. You can download Endnote file for Journal references style: endnote file

The reference of information must be based on the following order:

Article:

Surname(s) and first letter of name & middle name(s) of author(s) .Manuscript title. Journal title (abbr).publication date (year); Volume & Issue: Page number.

Example: Manicardi GC, Bianchi PG, Pantano S, Azzoni P, Bizzaro D, Bianchi U, et al. Presence of endogenous nicks in DNA of ejaculated human spermatozoa and its relationship to chromomycin A3 accessibility. *Biol Reprod.* 1995; 52(4): 864-867.

Book:

Surname(s) and first letter of name & middle name(s) of author(s). Book title. Edition. Publication place: publisher name; publication date (year); Page number.

Example: Edelman CL, Mandle CL. Health promotion throughout the lifespan. 2nd ed. ST Louis: Mosby; 1998; 145-163.

Chapter of book:

Surname(s) and first letter of name & middle name(s) of author(s). Chapter title. In: Surname(s) and first letter of name & middle name(s) of editor(s), editors. Book title. Edition. Publication place: publisher name; publication date (year); Page number.

Example: Phillips SJ, Whisnant JP. Hypertension and stroke. In: Laragh JH, Brenner BM, editors. Hypertension: pathophysiology, diagnosis, and management. 2nd ed. New York: Raven Press; 1995; 465-478.

Abstract book:

Example: Amini rad O. The antioxidant effect of pomegranate juice on sperm parameters and fertility potential in mice. Cell J. 2008;10 Suppl 1:38.

Thesis:

Name of author. Thesis title. Degree. City name. University. Publication date (year).

Example: Eftekhari Yazdi P. Comparison of fragment removal and co-culture with Vero cell monolayers on development of human fragmented embryos. Presented for the Ph.D., Tehran. Tarbiyat Modarres University. 2004.

Internet references**Article:**

Example: Jahanshahi A, Mirnajafi-Zadeh J, Javan M, Mohammad-Zadeh M, Rohani M. Effect of low-frequency stimulation on adenosine A1 and A2A receptors gene expression in dentate gyrus of perforant path kindled rats. Cell J. 2008; 10 (2): 87-92. Available from: <http://www.celljournal.org>. (20 Oct 2008).

Book:

Example: Anderson SC, Poulsen KB. Anderson's electronic atlas of hematology.[CD-ROM]. Philadelphia: Lippincott Williams & Wilkins; 2002.

D. Proofs are sent by email as PDF files and should be checked and returned within 72 hours of receipt. It is the authors' responsibility to check that all the text and data as contained in the page proofs are correct and suitable for publication. **We are requested to pay particular attention to author's names and affiliations as it is essential that these details be accurate when the article is published.**

E. Pay for publication: Publishing an article in Cell J requires Article Processing Charges (APC) that will be billed to the submitting author following the acceptance of an article for publication. For more information please see www.celljournal.org.

F. Ethics of scientific publication: Manuscripts that have been published elsewhere with the same intellectual material will refer to duplicate publication. If authors have used their own previously published work or work that is currently under review, as the basis for a submitted manuscript, they are required to cite the previous work and indicate how their submitted manuscript offers novel contributions beyond those of the previous work. Research and publication misconduct is considered a serious breach of ethics.

The Journal systematically employs iThenticate, plagiarism detection and prevention software designed to ensure the originality of written work before publication. Plagiarism of text from a previously published manuscript by the same or another author is a serious publication offence. Some parts of text may be used, only where the source of the quoted material is clearly acknowledged.

3. General information

A. You can send your manuscript via online submission system which is available on our website. If the manuscript is not prepared according to the format of **Cell J**, it will be returned to authors.

B. The order of article appearance in the Journal is not demonstrating the scientific characters of the authors.

C. **Cell J** has authority to accept or reject the manuscript.

D. The received manuscript will be evaluated by associate editor. **Cell J** uses a single-blind peer review system and if the manuscript suits the journal criteria, we select the reviewers. If three reviewers pass their judgments on the manuscript,

it will be presented to the editorial board of **Cell J**. If the editorial board has a positive judgment about the manuscript, reviewers' comments will be presented to the corresponding author (the identification of the reviewers will not be revealed). The executive member of journal will contact the corresponding author directly within 3-4 weeks by email. If authors do not receive any reply from journal office after the specified time, they can contact journal office. Finally, executive manager will respond promptly to authors' request.

The Final Checklist

The authors must ensure that before submitting the manuscript for publication, they have to consider the following parts:

1. Title page should contain title, name of the author/coauthors, their academic qualifications, designation & institutions they are affiliated with, mailing address for future correspondence, email address, phone, and fax number.
2. Text of manuscript and References prepared as stated in the "guide for authors" section.
3. Tables should be on a separate page. Figures must be sent in color and also in JPEG (Jpg) format.
4. Cover Letter should be uploaded with the signature of all authors.
5. An ethical committee letter should be inserted at the end of the cover letter.

The Editor-in-Chief: Ahmad Hosseini, Ph.D.

Cell Journal (Yakhteh)

P.O. Box: 16635-148, Iran

Tel/Fax: + 98-21-22510895

Emails: Celljournal@royaninstitute.org

info@celljournal.org





IN THE NAME OF GOD

Gone But not Forgotten

In the memory of the late Director of Royan Institute, Founder of Stem Cells Research in Iran and Chairman of *Cell Journal* (Yakhteh). May he rest in peace.

Dr. Saeed Kazemi Ashtiani

OWNED:

Royan Institute, Iranian Academic Center for Education Culture and Research (ACECR)

CHAIRMAN:

Hamid Gourabi, Ph.D., (Professor, Royan Institute, Tehran, Iran)

EDITOR IN CHIEF:

Ahmad Hosseini, Ph.D., (Professor, Shahid Beheshti Medical University, Tehran, Iran)

EDITOR ASSOCIATE:

Saeid Abroun, Ph.D., (Associate Professor, Tarbiat Modares University, Tehran, Iran)

EDITORIAL BOARD:

Saeid Abroun, Ph.D., (Associate Professor, Tarbiat Modares University, Tehran, Iran)
Kamran Alimoghadam, M.D., (Associate Professor, Tehran Medical University, Tehran, Iran)
Alireza Asgari, Ph.D., (Professor, Baghyatallah University, Tehran, Iran)
Mohammad Kazem Aghaee Mazaheri, D.D.S., (Assistant Professor, ACECR, Tehran, Iran)
Gila Behzadi, Ph.D., (Professor, Shahid Beheshti Medical University, Tehran, Iran)
Hossein Baharvand, Ph.D., (Professor, Royan Institute, Tehran, Iran)
Mary Familiari, Ph.D., (Senior Lecturer, University of Melbourne, Melbourne, Australia)
Hamid Gourabi, Ph.D., (Professor, Royan Institute, Tehran, Iran)
Jurgen Hescheler, M.D., (Professor, Institute of Neurophysiology of University Zu Koln, Germany)
Ghasem Hosseini Salekdeh, Ph.D., (Assistant Professor, Agricultural Biotechnology Research Institute, Karaj, Iran)
Esmail Jabbari, Ph.D., (Associate Professor, University of South Carolina, Columbia, USA)
Suresh Jesuthasan, Ph.D., (Associate Professor, National University of Singapore, Singapore)
Bahram Kazemi, Ph.D., (Professor, Shahid Beheshti Medical University, Tehran, Iran)
Saadi Khochbin, Ph.D., (Professor, Inserm/Grenoble University, France)
Ali Khademhosseini, Ph.D., (Associate Professor, Harvard Medical School, USA)
Kun Ping Lu, M.D., Ph.D., (Professor, Harvard Medical School, Boston, USA)
Navid Manuchehrabadi, Ph.D., (Angio Dynamics, Marlborough, USA)
Hosseinali Mehrani, Ph.D., (Professor, Baghyatallah University, Tehran, Iran)
Marcos Meseguer, Ph.D., (Clinical Embryology Laboratory IVI Valencia, Valencia, Spain)
Seyed Javad Mowla, Ph.D., (Professor, Tarbiat Modares University, Tehran, Iran)
Mohammad Hossein Nasr Esfahani, Ph.D., (Professor, Royan Institute, Tehran, Iran)
Toru Nakano, M.D., Ph.D., (Professor, Osaka University, Osaka, Japan)
Donald Newgreen, Ph.D., (Professor, Murdoch Children Research Institute, Melbourne, Australia)
Mojtaba Rezazadeh Valojerdi, Ph.D., (Professor, Tarbiat Modares University, Tehran, Iran)
Mohammad Hossein Sanati, Ph.D., (Associate Professor, National Institute for Genetic Engineering and Biotechnology, Tehran, Iran)
Eimei Sato, Ph.D., (Professor, Tohoku University, Sendai, Japan)
Andreas Serra, M.D., (Professor, University of Zurich, Zurich, Switzerland)
Abdolhossein Shahverdi, Ph.D., (Professor, Royan Institute, Tehran, Iran)
Michele Catherine Studer, Ph.D., (Institute of Biology Valrose, IBV University of Nice Sophia-Antipolis, France)
Peter Timashev, Ph.D., (Sechenov University, Moscow, Russia)
Daniela Toniolo, Ph.D., (Head, Unit of Common Disorders, San Raffaele Research Institute, Milano, Italy)
Christian van den Bos, Ph.D., Managing Director MARES Ltd, Greven, Germany
Catherine Verfaillie, Ph.D., (Professor, Katholie Universiteit Leuven, Leuven, Belgium)
Gianpaolo Zerbin, M.D., Ph.D., (San Raffaele Scientific Institute, Italy)
Shubing Zhang, Ph.D., (Associate Professor, Central South University, China)
Daniele Zink, Ph.D., (Institute of Bioengineering and Nanotechnology, Agency for Science Technology & Science, Singapore)

EXECUTIVE MANAGER:

Farideh Malekzadeh, M.Sc., (Royan Institute, Tehran, Iran)

EXECUTIVE BOARD:

Parvaneh Afsharian, Ph.D., (Royan Institute, Tehran, Iran)
Reza Azimi, B.Sc., (Royan Institute, Tehran, Iran)
Reza Omani-Samani, M.D., (Royan Institute, Tehran, Iran)
Elham Amirchaghmaghi, M.D., Ph.D., (Royan Institute, Tehran, Iran)
Leila Daliri, M.Sc., (Royan Institute, Tehran, Iran)
Mahdi Lotfipannah, M.Sc., (Royan Institute, Tehran, Iran)

ENGLISH EDITOR:

Saman Eghtesad, Ph.D., (Royan Institute, Tehran, Iran)
Vahid Ezzatizadeh, Ph.D., (Royan Institute, Tehran, Iran)
Jane Elizabeth Ferrie, Ph.D., (University College of London, London, UK)
Mojtaba Nemati, M.Sc., (Royan Institute, Tehran, Iran)
Ramin Rezaee, Pharm.D., Ph.D., (Mashhad University of Medical Sciences, Mashhad, Iran)
Kim Vagharfard, M.Sc., (Royan Institute, Tehran, Iran)

GRAPHICS:

Laleh Mirza Ali Shirvani, B.Sc., (Royan Institute, Tehran, Iran)

PUBLISHED & SPONSORED BY:

Publication of Royan Institute (ACECR)

Indexed in:

1. Thomson Reuters (ISI); *Impact Factor: 1.983*
2. PubMed
3. PubMed Central (PMC)
4. National Library Medicine (NLM)
5. Biosis Preview
6. Index Medicus for the Eastern Mediterranean Region (IMEMR)
7. Regional Information Center for Sciences and Technology (RICEST)
8. Index Copernicus International
9. Cambridge Scientific Abstract (CSA)
10. EMBASE
11. Scopus
12. Cinahl Database
13. Google Scholar
14. Chemical Abstract Service (CAS)
15. Proquest
16. Directory of Open Access Journals (DOAJ)
17. Open Academic Journals Index (OAJI)
18. Directory of Research Journals Indexing (DRJI)
19. Scientific Information Database (SID)
20. Iranmedex
21. Islamic World Science Citation Center (ISC)
22. Magiran
23. Science Library Index
24. Biological Abstracts
25. Essential Science Indicators
26. EuroPub

ACECR**Copyright and license information:**

The **Cell Journal** (^{Yakhteh}) is an open access journal which means the articles are freely available online for any individual author to download and use the providing address. The journal is licensed under a Creative Commons Attribution-Non Commercial 3.0 Unported License which allows the author(s) to hold the copyright without restrictions that is permitting unrestricted use, distribution, and reproduction in any medium provided the original work is properly cited.

Editorial Office Address (Dr. Ahmad Hosseini):

Royan Institute, P.O.Box: 16635-148,
Tehran, Iran
Tel & Fax: (+9821)22510895
Website: www.celljournal.org
Emails: info@celljournal.org
celljournal@royaninstitute.org

Printing Company:

Naghsh e Johar Co.
No. 103, Fajr alley, Tehranpars Street,
Tehran, Iran.



CONTENTS

Original Articles

- **Immunomodulatory Activity of Human Bone Marrow and Adipose-Derived Mesenchymal Stem Cells Prolongs Allogenic Skin Graft Survival in Nonhuman Primates**
Fattah Sotoodehjadnematalahi, Reza Moghadasali, Mostafa Hajinasrollah, Ehsan Ehsani, Ensiyeh Hajizadeh-Saffar, Niloofer Sodeifi, Reza F. Saidi, Morteza Zarrabi, Mohammad Farzanehkhah, Bahareh Sadeghi, Hossein Baharvand, Nasser Aghdami 1
- **Correlation of sPD1 with Procalcitonin and C-Reactive Protein Levels in Patients with Sepsis**
Zahra Bakhshiani, Saloomeh Fouladi, Samaneh Mohammadzadeh, Nahid Eskandari 14
- **lncRNA PVT1 Promotes Metastasis of Non-Small Cell Lung Cancer Through EZH2-Mediated Activation of Hippo/NOTCH1 Signaling Pathway**
Shang-Gan Zeng, Jian-Hong Xie, Qun-Ying Zeng, Shao-Hua Dai, Yun Wang, Xue-Mei Wan, Ji-Chun Liu 21
- **Design and Microfabrication of An On-Chip Oocyte Maturation System for Reduction of Apoptosis**
Behnaz Sadeghzadeh Oskouei, Siavash Zargari, Parviz Shahabi, Marefat Ghaffari Novin, Maryam Pashaiasl 32
- **The Contribution of Y Chromosome Genes to Spontaneous Differentiation of Human Embryonic Stem Cells into Embryoid Bodies *In Vitro***
Simin Nafian Dehkordi, Farzaneh Khani, Seyedeh Nafiseh Hassani, Hossein Baharvand, Hamid Reza Soleimanpour-lichai, Ghasem Hosseini Salekdeh 40
- **Inhibition of miR-200b Promotes Angiogenesis in Endothelial Cells by Activating The Notch Pathway**
Tie-Ying Qiu, Jin Huang, Li-Ping Wang, Bi-Song Zhu 51
- **Elevated Secretion of Aldosterone Increases TG/HDL-C Ratio and Potentiates The Ox-LDL-Induced Dysfunction of HUVEC**
Qian Zhang, Yiwen Pan, Xiaochun Ma, Hao Yang, Jun Chang, Ling Hong, Huiwen Yan, Shubing Zhang 61
- **Assessment of Atg7 and LC3II/LC3, as The Markers of Autophagy, in Sperm of Infertile Men with Globozoospermia: A Case-Control Study**
Shaghayegh Foroozan-Boroोजeni, Marziyeh Tavalae, Zahra Zakeri, Richard A. Lockshin, Mohammad Hossein Nasr-Esfahani 70
- **Proteomics Analyses Reveal Functional Differences between Exosomes of Mesenchymal Stem Cells Derived from The Umbilical Cord and Those Derived from The Adipose Tissue**
Bin Liu, Guanglei Qiao, Wen Cao, Chenlu Li, Shaojun Pan, Lirui Wang, Yanlei Liu, Lijun Ma, Daxiang Cui 75
- **Long-Term Effects of Hippocampal Low-Frequency Stimulation on Pro-Inflammatory Factors and Astrocytes Activity in Kindled Rats**
Razieh Rohani, Abbas Ali Alighaei, Mohammad-Amin Abdollahifar, Yousef Sadeghi, Leila Zare, Samaneh Dehghan, Mohammad Hassan Heidari 85
- **Impact of Methyl-β-Cyclodextrin and Apolipoprotein A-I on The Expression of ATP-Binding Cassette Transporter A1 and Cholesterol Depletion in C57BL/6 Mice Astrocytes**
Shirin Azidoost, Hossein Babaahmadi-Rezaei, Zahra Nazeri, Maryam Cheraghzadeh, Alireza Kheirollah 93
- **Ovulation Induction Changes Epigenetic Marks of Imprinting Genes in Mice Fetus Organs**
Anahita Oveisi, Akbar Vahdati, Maryam Shahhoseini, Raha Favaedi, Saman Maroufizadeh, Bahar Movaghar 99
- **Meiosis Resumption of Immature Human Oocytes following Treatment with Calcium Ionophore *In Vitro***
Elham Fazeli, Ahmad Hosseini, Mohammad-Hasan Heidari, Fattaneh Farifteh-Nobijari, Mohammad Salehi, Hojjat-Allah Abbaszadeh, Hamid Nazarian, Zahra Shams Mofarahe, Saman Ayoubi, Sara Hosseini, Mona Shayeghpour, Mojgan Bandehpour, Marefat Ghaffari Novin 109
- **Metformin Protects Myelin from Degeneration in A Mouse Model of Lysophosphatidylcholine-Induced Demyelination in The Optic Chiasm**
Saman Esmailnejad, Saeed Semnanian, Mohammad Javan 119
- **Bioinspired Device Improves The Cardiogenic Potential of Cardiac Progenitor Cells**
Zahra Shams, Babak Akbari, Sarah Rajabi, Nasser Aghdami 129

Corrections

- **Hydrocortisone Promotes Differentiation of Mouse Embryonic Stem Cell-Derived Definitive Endoderm toward Lung Alveolar Epithelial Cells**
Mohammad Reza Mokhber Dezfooli, Siroos Sadeghian Chaleshtori, Azadeh Moradmand, Mohsen Basiri, Hossein Baharvand, Yaser Tahamtani 137
- ***In Vitro* Differentiation of Human Umbilical Cord Blood CD133+ Cells into Insulin Producing Cells in Co-Culture with Rat Pancreatic Mesenchymal Stem Cells**
Fazel Sahraneshin Samani, Marzieh Ebrahimi, Tahereh Zandieh, Reyhaneh Khoshchehreh, Mohamadreza Baghaban Eslaminejad, Nasser Aghdami, Hossein Baharvand 138

Erratum

- **Stem Cells from Human Exfoliated Deciduous Tooth Exhibit Stromal-Derived Inducing Activity and Lead to Generation of Neural Crest Cells from Human Embryonic Stem Cells**
Khadijeh Karbalaie, Somayyeh Tanhaei, Farzaneh Rabiei, Abbas Kiani-Esfahani, Najmeh Sadat Masoudi, Mohammad Hossein Nasr-Esfahani, Hossein Baharvand 140
- **Conditioned Media Derived from Human Adipose Tissue Mesenchymal Stromal Cells Improves Primary Hepatocyte Maintenance**
Zahra Azhdari Tafti, Mehdi Mahmoodi, Mohamad Reza Hajizadeh, Vahid Ezzatizadeh, Hossein Baharvand, Massoud Vosough, Abbas Piryaeei 143

Immunomodulatory Activity of Human Bone Marrow and Adipose-Derived Mesenchymal Stem Cells Prolongs Allogenic Skin Graft Survival in Nonhuman Primates

Fattah Sotoodehnejadnematlahi, Ph.D.^{1#}, Reza Moghadasali, Ph.D.^{2,3,4##}, Mostafa Hajinasrollah, D.V.M.², Ehsan Ehsani, Ph.D.^{2,5}, Ensiyeh Hajizadeh-Saffar, M.D., Ph.D.³, Niloofar Sodeifi, M.D.⁶, Reza F. Saidi, M.D.⁷, Morteza Zarrabi, Ph.D.⁸, Mohammad Farzanehkah, M.Sc.⁸, Bahareh Sadeghi, M.Sc.⁸, Hossein Baharvand, Ph.D.^{1,4}, Nasser Aghdami, M.D., Ph.D.⁴

1. Department of Biology, School of Basic Science, Science and Research Branch, Islamic Azad University, Tehran, Iran
2. Department of Stem Cells and Developmental Biology, Cell Sciences Research Center, Royan Institute for Stem Cell Biology and Technology, ACECR, Tehran, Iran
3. Department of Regenerative Medicine, Cell Sciences Research Center, Royan Institute for Stem Cell Biology and Technology, ACECR, Tehran, Iran
4. Department of Developmental Biology, University of Science and Culture, Tehran, Iran
5. Department of Biology, Roudehen Branch, Islamic Azad University, Roudehen, Iran
6. Department of Andrology, Reproductive Biomedicine Research Center, Royan Institute for Reproductive Biomedicine, ACECR, Tehran, Iran
7. Department of Surgery, Shariati Hospital, Tehran University of Medical Sciences, Tehran, Iran
8. Royan Stem Cell Technology Company, Cord Blood Bank, Tehran, Iran

#The first two authors equally contributed to this work.

*Corresponding Address: P.O.Box: 16635-148, Department of Stem Cells and Developmental Biology, Cell Sciences Research Center, Royan Institute for Stem Cell Biology and Technology, ACECR, Tehran, Iran
Email: rezamoghadassali@royaninstitute.org

Received: 16/April/2019, Accepted: 9/November/2019

Abstract

Objective: In the present study, we examined the tolerance-inducing effects of human adipose-derived mesenchymal stem cells (hAD-MSCs) and bone marrow-derived MSCs (hBM-MSCs) on a nonhuman primate model of skin transplantation.

Materials and Methods: In this experimental study, allogenic and xenogeneic immunomodulatory properties of human AD-MSCs and BM-MSCs were evaluated by mixed lymphocyte reaction (MLR) assays. Human MSCs were obtained from BM or AD tissues (from individuals of either sex with an age range of 35 to 65 years) and intravenously injected (2×10^6 MSCs/kg) after allogeneic skin grafting in a nonhuman primate model. The skin sections were evaluated by H&E staining for histopathological evaluations, particularly inflammation and rejection reaction of grafts after 96 hours of cell injection. At the mRNA and protein levels, cellular mediators of inflammation, such as CD4+IL-17+ (T helper 17; Th17) and CD4+INF- γ + (T helper 1, Th1) cells, along with CD4+FoxP3+ cells (Treg), as the mediators of immunomodulation, were measured by RT-PCR and flow cytometry analyses.

Results: A significant Treg cells expansion was observed in MSCs-treated animals which reached the zenith at 24 hours and remained at a high concentration for 96 hours; however, Th1 and Th17 cells were significantly decreased. Our results showed that human MSCs significantly decrease Th1 and Th17 cell proliferation by decreasing interleukin-17 (IL-17) and interferon- γ (INF- γ) production and significantly increase Treg cell proliferation by increasing FoxP3 production. They also extend the allogenic skin graft survival in nonhuman primates. Histological evaluations showed no obvious presence of inflammatory cells or skin redness or even bulging after MSCs injection up to 96 hours, compared to the group without MSCs. There were no significant differences between hBM-MSCs and hAD-MSCs in terms of histopathological scores and inflammatory responses ($P < 0.05$).

Conclusion: It seems that MSCs could be regarded as a valuable immunomodulatory tool to reduce the use of immunosuppressive agents.

Keywords: Adipose, Allogenic, Bone Marrow, Immunomodulation, Mesenchymal Stem Cells

Cell Journal (Yakhteh), Vol 23, No 1, April-June (Spring) 2021, Pages: 1-13

Citation: Sotoodehnejadnematlahi F, Moghadasali R, Hajinasrollah M, Ehsani E, Hajizadeh-Saffar E, Sodeifi N, Saidi R, Zarrabi M, Farzanehkah M, Sadeghi B, Baharvand H, Aghdami N. Immunomodulatory activity of human bone marrow and adipose-derived mesenchymal stem cells prolongs allogenic skin graft survival in nonhuman primates. Cell J. 2021; 23(1): 1-13. doi: 10.22074/cellj.2021.6895.

This open-access article has been published under the terms of the Creative Commons Attribution Non-Commercial 3.0 (CC BY-NC 3.0).

Introduction

Mesenchymal stem cells (MSCs), as a diverse population of plastic-adherent cells, exhibit fibroblast-like morphology under the *ex vivo* culture conditions. MSCs do not express hematopoietic stem cell markers, and they are originally isolated from the bone marrow

(BM), as well as other adult tissues, such as adipose tissue (1). In particular, adipose-derived MSCs (AD-MSCs) are regarded as an interesting source of MSCs, as the collection of adipose tissue is a less invasive procedure, and it is easily obtained, providing a considerable number of cells compared to BM-MSCs (2). AD-MSCs are well-

known due to their immunomodulatory properties.

Because of their immunosuppressive potential, even in the absence of immunosuppressive agents, allogeneic or even xenogeneic administration of these cells into immunocompetent recipients would be feasible. AD-MSCs have been used for the treatment of a wide range of diseases, since these cells do not express major histocompatibility complex-II markers and exert immunosuppressive properties mediated by prostaglandin E2 (3, 4). In addition, preclinical and clinical investigations have shown that AD-MSCs transplantation, as allogenic agents, are able to control graft-versus-host disease (GVHD). Considering the immunosuppressive and anti-inflammatory properties of human MSCs (hMSCs), several studies suggested MSCs as an appropriate modality for cell therapy compared to other cell types (5, 6). Different *in vitro* studies showed the suppression of lymphocytes alloreactivity in mixed lymphocytes cultures mediated by a human leukocytes antigen (HLA)-independent mechanism (7, 8).

Besides, some investigations demonstrated that the intravenous administration of MSCs improves the lung, renal and neural tissue features in animal models of injury, suggesting marked paracrine effects for MSCs. Moreover MSCs can tilt the balance of pro-inflammatory and anti-inflammatory cytokines in favor of anti-inflammatory cytokine production at the site of injury (9). Different studies indicated that several immune cells involved in T lymphocytes proliferation and dendritic cells maturation are suppressed by MSCs; conversely, some indicated that MSCs are able to increase the production of anti-inflammatory cytokines or induce regulatory T cell (T_{regs}) activity (10-12).

It has been shown that the auto-reactive T cells play crucial roles in the secretion of cytotoxic compounds, leading to early graft rejection during the post-transplant period (13). In contrast, T_{regs} are critical cells with immunomodulatory functions (14, 15). As a subpopulation of peripheral CD4+ T cells, T_{regs} have distinct surface (e.g. CD4+CD25+) and intracellular (e.g. FoxP3+) markers and can confront T cell autoreactivity through the secretion of immunosuppressive cytokines and their surface receptors. Furthermore, they suppress antigen presentation via their inhibitory surface receptors, cytolytic function, and secretion of soluble factors (16). In view of these facts, approaches developed based on the increment of the number of Tregs, could effectively contribute to immunomodulation following skin grafting (17, 18).

In this study, we compared the immunomodulatory properties of MSCs derived from different sources (i.e. BM and AD) in a nonhuman primate model of skin allograft.

Materials and Methods

Cell culture and isolation of mesenchymal stem cells from human bone marrow

In this experimental study, 100-150 ml of BM was aspirated from iliac crest of chosen patients (of either

sex with an age range of 35 to 65 years) with radiologic evidence and 1.5 Tesla magnetic resonance imaging (MRI) (VB33DVision Plus; Siemens, Erlangen, Germany) of knee osteoarthritis (OA) who were selected for cell therapy under local anesthesia. Anesthesia was performed using a lidocaine solution (2%) and sedation by an intravenous injection of midazolam (0.1 mg/kg, Tehran Chemie pharmaceutical Co., Iran) and fentanyl (25-50 mg/100 mm, Aburaihan pharmaceutical Co., Iran). BM was collected in a centrifuge tube (50 ml, TPP, Switzerland), containing anti-coagulant (Heparin, Rotexmedica, Germany; 300 μ l Rotexmedica for 50 ml of BM). The aspirated BM was diluted at a ratio of 1:1 with α -MEM medium (Gibco, USA); then, layered very gently onto Lymphodex solution (gravity: 1.077-1.080; Inno-Train Diagnostik, Germany) and centrifuged (Hettich Universal 320, Germany) at 1400 rpm for 30 minutes to collect mononuclear cells (MNCs). MNCs were then re-suspended in 5ml of α -MEM (Gibco, USA) supplemented with 10% fetal bovine serum (FBS, Hyclone, USA), 1% L-glutamine (L-glu, Gibco, USA), and 1% penicillin/streptomycin (pen/strep, Gibco, USA). The culture was maintained at 37°C in a humidified atmosphere (Labotect CO₂-incubator, Germany), containing 95% air and 5% CO₂ and passaged every 3 days. Fibroblast-like MSCs became ready for the characterization after the third passage.

All animal care, experimental, and transplantation processes and postoperative euthanasia were performed in strict accordance with the ethical principles of the NIH Guide for the Care and Use of Laboratory Animals (NIH Publication No. 85-23, revised 2010) following the approval of the Institutional Review Board and Institutional Ethics Committee of Royan Institute (approval No. EC.92.1005).

Cell culture and isolation of mesenchymal stem cells from human adipose tissue

Adipose tissue was first isolated by liposuction from abdominal subcutaneous fat of individuals (of either sex with an age range of 35 to 65 years) and then, transferred into a sterile tube (50 ml, TPP, Switzerland), containing phosphate-buffered saline (PBS, Gibco, USA) and 1% pen/strep (Gibco, USA). The tube was kept on the ice. The adipose tissue was washed several times with sterile water to remove red blood cells. Then, the tissue (which is normally between 150-250 ml) was sectioned into smaller pieces and 0.075% collagens I (Sigma, USA) was added for digestion. The tissues were placed in an incubator (with 5% CO₂ at 37°C) for 2 hours, while spinning every 15 minutes. After 2 hours, α -MEM (Gibco, USA, at twice concentration of the enzyme) was added to the tube to neutralize the enzyme by pipetting up and down to release the cells from adipose tissue. Then, the sample was centrifuged at 1500 rpm for 5 minutes, and the pellet (stromal vascular fraction) was diluted in 4-5 ml of α -MEM (Gibco, USA). Afterward, the suspension was passed through a Mesh filter (Falcon, UK). The cells were transferred to a 25T flask (TPP, Switzerland), containing

α -MEM supplemented with 10% FBS (Hyclone, USA), 1% pen/strep (Gibco, USA), and 1% L-glu (Gibco, USA) and kept in an incubator (with 5% CO₂ at 37°C). The medium was replaced with a fresh medium every four days until reached 90% confluency. The cell culture was continued until the third passage.

Analysis of the cell surface markers of human bone marrow-derived mesenchymal stem cells and adipose-derived mesenchymal stem cells

Surface markers of human bone marrow-derived mesenchymal stem cells (hBM-MSCs) and adipose-derived mesenchymal stem cells (hAD-MSCs) were analyzed using fluorescence-activated cell sorting (FACS, BD Pharmingen, USA). For immunophenotyping, hBM-MSCs and hAD-MSCs were dissociated in 0.05% trypsin-EDTA (Gibco, USA) and washed in PBS (Gibco, USA) supplemented with 1% heat-inactivated FBS (Hyclone, USA) and 2 mM EDTA (Merck, Darmstadt, Germany). Next, 4-5×10⁵ cells were incubated with primary antibodies for surface markers for two hours and with the secondary antibodies for 30 minutes, both done at 4°C. Surface markers that were analyzed included CD44, CD73 (BD Pharmingen, USA), CD105 (R&D Systems Inc, Minneapolis, MN, USA) conjugated with phycoerythrin (PE)-Mouse IgG1k (BD Pharmingen™, Cat NO: 551436) and CD90 (Dako, Glostrup, Denmark) conjugated with fluorescein isothiocyanate (FITC)-Mouse IgG2b (Millipore, Cat NO: MABC006F), which were supposed to be expressed by fully differentiated MSCs, as well as CD34 and CD45 (BD Pharmingen) conjugated with FITC, which are markers of hematopoietic stem cells (HSCs), and they are not expressed on MSCs. In all experiments, controls were stained with appropriate isotype-matched antibodies. The flow cytometry analysis was performed triplicate using a BD FACS Calibur Flow Cytometer (BD Biosciences, Franklin Lakes, NJ, USA). Data were analyzed by WinMDI 12.9 software (freeware from Joe Trotter, The Scripps Research Institute, La Jolla, CA, USA).

Lineage differentiation for characterization of human bone marrow-derived mesenchymal stem cells and adipose-derived mesenchymal stem cells

For further characterizations, osteogenic and adipogenic differentiations of hBM- and hAD-MSCs were induced using the following protocol. In this stage, 1×10⁴ cells per well (TPP, Switzerland) were seeded in 6-well plates and treated with conductive medium for 21 days. The media of wells were changed every three days. At 50% confluency, the medium was supplemented with 0.5 μ M ascorbic acid-2-phosphate (Sigma-Aldrich, USA), 1 μ M dexamethasone (Stem Cell Technologies, Canada), and 10 mM β -glycerophosphate (Sigma-Aldrich, USA) for osteogenic induction. The cells were analyzed for mineralization using alizarin red (Sigma-Aldrich, USA) staining. To induce adipogenic differentiation, cells were incubated with complete medium including 50 μ g/ml indomethacin (Sigma-Aldrich, USA), 100 nM

dexamethasone (Sigma-Aldrich, USA), insulin (Sigma-Aldrich, USA), and 3-isobutyl-1-methylxanthine (Sigma-Aldrich, USA). Finally, the cells were analyzed for lipid content by oil-red (Sigma-Aldrich, USA) staining.

Non-proliferating lymphocytes analysis using cell proliferation assay

Responder T cells were first labeled with carboxyfluorescein diacetate succinimidyl ester (CFSE) (Invitrogen, USA). For this purpose, responder T cells were labeled with 1 μ M of CFSE for 15 minutes at 37°C in PBS (Gibco, USA) supplemented with 0.1% bovine serum albumin (BSA, Sigma-Aldrich, USA). Cells were washed twice with PBS (Gibco, USA) + 1% FBS (Hyclone, USA), re-suspended in media+10% FBS (Hyclone, USA), and incubated at room temperature for further 10 minutes. Then, the cells were collected and analyzed by flow cytometry. Immunomodulatory properties of hAD-MSCs and hBM-MSCs were assessed in the MLR medium, including responder (R) and stimulator (S) human T cells (R+S+AD-MSCs), and CFSE-labeled responder T cells were added to cultured MSCs at different ratios of 1:10, 1:5, 1:1 and 2:1 co-culture ratio of MSCs to responder T cells for 24, 48, 72, and 96 hours (Fig.1A-C).

Immunosuppressive activity of mesenchymal stem cells in mixed lymphocyte reaction

For the assessment of immunomodulatory properties of allogenic hAD-MSCs and hBM-MSCs, MNCs were isolated from the peripheral blood of humans. For the evaluation of immunomodulatory properties of xenogeneic hAD-MSCs and hBM-MSCs, MNCs were isolated from the peripheral blood of monkeys by the Lymphodex solution (gravity: 1.077-1.080; Inno-Train Diagnostik, Germany) and used as stimulators and responders. For peripheral blood sampling from primates, the tibial vein was used. Then, the skin over the venipuncture site was sterilized using alcohol (70%). For blood sampling, a needle (1.2-2.0 mm) and a syringe (2.5-10 mL) were used. Then, the needle was withdrawn, and the area over the vein was put under pressure for at least one minute, to avoid hematoma formation. Then, peripheral blood (5 ml) was collected under heparin (Heparin, Rotexmedica, Germany) and MNCs were isolated from heparinized blood by gradient centrifugation as stimulators and responders. The stimulators, but not the responders, were treated with mitomycin C (MMC, M0503, Sigma-Aldrich, USA) (50 μ g/ml at 37°C for 1 hour). The stimulators (5×10⁵/well) and responders (2.5×10⁵/well) as the experimental groups were loaded into a 96-well plate and MMC-treated MSCs (2.5×10⁵/well) were added. After 5-day routine culture, the MTT solution (5 mg/ml PBS) (Sigma-Aldrich, USA) was added, and the cells were incubated for 4 hours at 37°C. Afterwards, the MTT solution was removed, and 200 μ l DMSO (WAK-Chemie Medical, Germany) was added. The extinction of the solution was measured at 570 nm using a Multiskan Bichromatic microplate reader (Labsystems, Helsinki, Finland) to assay immunosuppressive activity (Figs.1D-F, 2A-C).

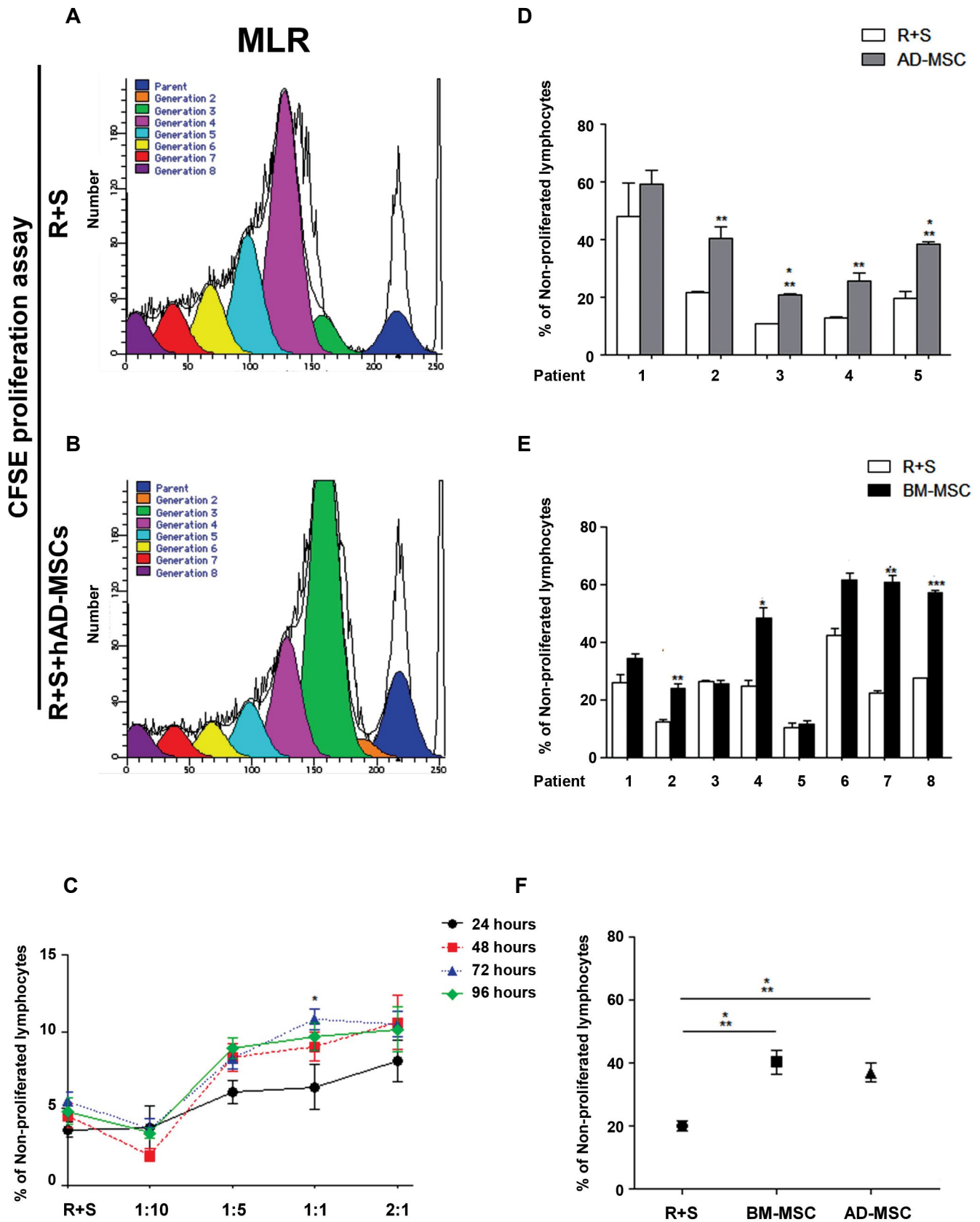


Fig.1: Allogenic immunomodulatory properties of *in vitro* expanded hAD-MSCs obtained from the aspirate of adipose tissue. **A-C.** Immunomodulatory properties of hAD-MSCs were assessed in the MLR medium following co-culture of hAD-MSCs and responder (R) and stimulator (S) human T cells (R+S+hAD-MSCs) at different ratios (1:10, 1:5, 1:1, and 2:1) and different time periods (24, 48, 72, and 96 hours). The cell ratio of 1:1 and culture period of 72 hours were selected as the optimal conditions. The comparison of the immunomodulatory properties of **D.** hAD-MSCs (n=5 patients) and **E.** hBM-MSCs (n=8 patients), was made under the optimal conditions in the MLR medium. No significant difference was observed among R+S and R+S+hBM-MSCs (patients 1, 3, and 5), and R+S+hAD-MSCs (patient 1). **F.** Also, no significant difference was found between hAD-MSCs and hBM-MSCs. Data are presented as the mean \pm standard deviation. *, P<0.05, **, P<0.01, ***, P<0.001, hAD-MSCs; Human adipose-derived mesenchymal stem cells, hBM-MSCs; Human bone marrow-derived mesenchymal stem cells. MLR; Mixed lymphocyte reaction, BM-MSCs; Bone marrow-derived mesenchymal stem cells, and AD-MSCs; Adipose-derived mesenchymal stem cells.

Human mesenchymal stem cells transplantation into healthy monkeys

After washing hAD-MSCs and BM-MSCs twice with PBS (Gibco, USA)+1% FBS (Hyclone, USA), the cells were re-suspended in media supplemented with 10% FBS (Hyclone, USA) and incubated at room temperature for further 10 minutes. Then, rhesus monkeys were intravenously injected with approximately 2×10^6 MSCs/kg. The blood specimens as heparinized were collected at certain time points (i.e. 6, 12, 24, 48, 72, and 96 hours) and assessed by real-time polymerase chain reaction (RT-PCR) and flow cytometry.

Real-time polymerase chain reaction

cDNA was synthesized using 100 ng total RNA by SuperScript™ III Reverse Transcriptase (Life Technologies, USA) and amplified by ExTaq (Takara, Japan). RT-PCR was performed using Platinum SYBR Green qPCR SuperMix-UDG plus ROX (Invitrogen, USA), according to the manufacturer's instructions in an ABI7300 RT-PCR System (Applied Biosystems, USA). Primer sequences were as follows:

GAPDH-

F: 5'-CTCATTTCCTGGTATGACAACGA-3'

R: 5'-CTTCCTCTTGTGCTCTTGCT-3'

FoxP3-

F: 5'-CCAGCCATGATCAGCCTCAC-3'

R: 5'-CCGAAAGGGTGCTGTCCTTC-3'

INF- γ -

F: 5'-GGTTCTCTTGGCTGTTACTG-3'

R: 5'-TCTTTTGGATGCTCTGGTCA-3'

IL-17-

F: 5'-AACCGATCCACCTCACCTTG-3'

R: 5'-CCCACGGACACCAGTATCTT-3'.

Real-time PCR data were analyzed by an ABI PRISM 7500 RT-PCR program. RT-PCR program included polymerase activation and initial denaturation (95°C, 10 minutes), denaturation (95°C, 10 minutes), annealing and extension (60°C, 60 seconds) for 40 cycles. All of the absolute data were normalized against a housekeeping gene (*GAPDH*) and control group, including embryonic stem cells (ESCs) and mouse embryonic fibroblast (MEF) using the $\Delta\Delta C_t$ method. The assay was run in triplicate to obtain gene expression data.

Intracellular staining for flow cytometry

Single T cell suspensions (0.1×10^6 cells) were washed with BD Perm/Wash Buffer (BD, London, UK). After washing, 200 μ l BD Cytfix/Cytoperm solution (BD, USA) was added to each cell pellet, and the cells were incubated for 20–30 minutes at 4°C. The cells were then washed twice with BD Perm/Wash Buffer and incubated in PBS (pH=7.4) (Gibco, USA), containing 5% BSA (Sigma-Aldrich, USA) for 10-15 minutes at room temperature. After washing with BD Perm/Wash Buffer,

the cells were aliquoted into tubes and then treated with a conjugated antibody based on the manufacturer's protocol (i.e., incubated for 30-45 minutes at 4°C in dark). Th-1 and Th-17 cells were examined for the expression of intracellular cytokines IL-17 (eBioscience, USA), IFN- γ (BD Bioscience, USA), Foxp3 (Biolegend, San Diego, CA, USA), and CD25 (BD Bioscience) conjugated with PE-labelled mouse anti-human antibodies and CD4 conjugated with FITC-labelled mouse anti-human antibodies, as well as PE-conjugated mouse IgG1 isotype control (BD Bioscience) by cell staining. All samples were analyzed by a flow cytometer (BD FACSCalibur™, USA) and FlowJo software.

ELISA assay for cytokine production

As the control and responder T cells to immunosuppressive factors, at the protein level, T cells isolated from rhesus after allogenic skin grafting and before hAD-MSCs transplantation, were exposed to TGF- β (10 and 20 ng/ml) (Sigma-Aldrich, USA) as an immunosuppressive factor, and the percentage of IL17 and IFN- γ were decreased. The supernatant of wells, containing T cells treated with TGF- β (10 and 20 ng/ml) was evaluated for IL-17 and IFN- γ , as immunomodulatory cytokines, using a commercially available enzyme-linked immunosorbent assay (ELISA; eBioscience, USA), according to the manufacturer's protocol.

Rhesus model of skin allograft

Eight healthy male rhesus monkeys (weighing 3-5 kg) were used for the induction of a model of skin allograft. Monkeys were gifted from the Royan Institute Primate Research Center. In this study, we used the minimum possible number of animals. Animals were housed individually in latticed cages ($2 \times 2 \times 2$ m³), and they had free access to food and water throughout the study. The cages were equipped by door handles for animal visit, sampling, and injection. The cage floor was made of PVC (Polyvinyl chloride) pipes for the prevention of bedsores. Also, these pipes allow the drainage of urine and stool. Also, they were assessed for tuberculosis, simian immunodeficiency virus, herpes viruses A and B, and hepatitis viruses A and B. To ensure that monkeys receiving transplanted skin are not genetically identical by a chance, ABO grouping, HLA typing (HLA-ABC-FITC and HLA-DR-PE, eBioscience, USA), RBC cross-match (Table 1), and mixed-lymphocyte reaction test were performed before transplantation on donor and recipient lymphocytes for tissue typing before transplantation. Then, eight monkeys were divided into two groups. In each group, four monkeys underwent heterotopic cross skin grafts transplantation (4×4 cm skin patch) pairwise under inhaled anesthesia. Generally, donor skin grafts are typically taken from the back wall and implanted on the back of the recipient site to reduce the probability of animal picking at the graft site. It is essential to remove cutaneous fat tissue from the skin graft before transplantation; however subcutaneous

tissue and microvasculature are not removed from the recipient site. For one pair, one monkey received a total of 2×10^6 hBM-MSCs/kg (test), while another received no treatment (control). For another pair, one monkey received a total of 2×10^6 hAD-MSCs/kg (test), whereas another received no treatment (control). The cells were intravenously transplanted into rhesus monkeys on day 0. Allograft rejection was monitored macroscopically by graft peripheral redness and bulging, and histological evaluations of rejection were carried out microscopically on the skin biopsy at appropriate time points.

Histopathological analyses and qualitative evaluations of inflammation and rejection

Histopathological analyses were performed 96 hours after allogenic skin grafting. Tissues were washed twice with PBS (Gibco, USA) and then fixed with 4% paraformaldehyde (Sigma-Aldrich, USA) for 24 hours at 4°C. Afterwards, the tissues were dehydrated through a series of graded alcohol solutions and xylol and then embedded in paraffin. The paraffin-embedded tissues were sectioned into 5-µm thick sections, mounted on poly-l lysine (Sigma-Aldrich, P1524, USA)-coated glass slides and placed in an oven at 60°C for 12 hours. Next, they were deparaffinized and dewaxed in xylene, stained with hematoxylin and eosin (H&E) and observed under a light microscope. To assess the presence of rejection, H&E-stained sections were examined and scored for inflammation, as previously described. Briefly, inflammatory cells, including polymorphonuclear leukocytes (PMNs), non-phagocytic cells, and phagocytic cells were scored based on the following scales: 0: No cell, 1: 1 to 5 cells per high-power field (hpf=400x), 2: 6 to 25 cells per high-power field (hpf=400x), 3: 26 to 50 cells per high-power field, 4: 51 to 75 cells per high-power field, 5: 76 to 100 cells per high power-field and 6: Over 100 cells per high-power field. Also, epidermis was scored as follows: 0: Normal, 1: Completely healed, 2: Healed but thin, 3: Ulcerative but healing and 4: Completely ulcerative or destroyed. Since we did not

have more than two animals, histopathological scores were not statistically analyzed, and the evaluations of inflammation and rejection were only presented as a situational report on MNCs infiltration, presence and absence of phagocytic and non-phagocytic cells, and epidermis destruction or healing.

In vivo analysis of Th1, Th17 and T reg populations

To test the immunomodulatory effect of hMSCs on Th1, Th17 and Treg population and related cytokines production, *in vivo* assays were carried out as follows; a total of 2×10^6 of hBM-MSCs/kg or hAD-MSCs/kg were intravenously injected to rhesus monkeys on day of skin grafting. Peripheral blood MNCs (PBMNCs) were isolated from heparinized blood by gradient centrifugation at appropriate time points (24, 48, 72, and 96 hours) following transplantation and then, Th1 markers (anti-CD4 and anti-IFN-γ), Th17 markers (anti-CD4 and anti-IL-17) and Treg markers (anti-CD4 and anti-FoxP3) were analyzed using flow cytometry.

In vivo cytokine assessments

To determine the mRNA levels of cytokines released by T cells, some MNCs isolated in the above-noted experiment, were analyzed for mRNA level of cytokines, such as IFN-γ, IL-17, and FoxP3, which are released by Th1, Th17 and Treg, respectively.

Statistical analysis

Because of having a small sample size, histopathological evaluations were reported as descriptive and each report was confirmed or rejected with additional experiments. Cellular data were measurable as statistical comparisons, and the analysis was conducted by the GraphPad Prism version 7.03 (GraphPad Software, Inc., USA). Data are presented as mean ± standard deviation (SD) of the mean for a minimum of three measurements at each time point. Statistical analysis was performed using one-way ANOVA to evaluate significant differences between groups at P<0.05.

Table 1: ABO grouping, RBC cross-matching, and HLA typing of monkeys

Blood typing	Monkey code	ABO/Rh	RBC cross-match scores	HLA																				
				A						B						DR								
				14	5	7	18	19	23	24	34	39	43	44	45	46	47	48	10	14	16	17	18	
No cell	2005	B-	+2	*	-	*	-	-	*	*	*	*	*	-	-	-	*	*	-	-	-	-	-	
BM-MSCs	2010	B-	+2	*	*	*	*	-	*	*	-	*	*	*	-	-	*	*	-	*	*	*	-	
No cell	2017	B-	+2	*	*	*	-	-	-	*	-	*	-	-	*	-	*	*	-	-	-	-	-	
AD-MSCs	2011	B-	+2	*	*	*	-	*	*	*	-	*	-	*	-	*	*	*	*	*	-	-	-	*

47: HLA-B and 48: HLA-B were considered controls., ABO blood group, RBC; Red blood cells, HLA; Human leukocyte antigen, BM-MSCs; Bone marrow-derived mesenchymal stem cells, and AD-MSCs; Adipose-derived mesenchymal stem cells.

Results

Characterization of human adipose-derived mesenchymal stem cells and bone marrow-derived mesenchymal stem cells

hAD-MSCs and BM-MSCs obtained from Royan Stem Cell Bank (RSCB) showed a fibroblastic spindle-shaped morphology after two weeks of culture. To verify differentiation capacity, hAD-MSCs and BM-MSCs were differentiated into adipocyte and osteocyte lineages in specific induction media. Oil red and alizarin red dye were used to examine adipogenic and osteogenic differentiation capacity, respectively. Immunophenotypic characterization of MSCs was performed by a Flow cytometer (BD FACSCalibur™) and FlowJo software. MSCs (hAD vs. hBM) were positive for CD44 (83 vs. 99.54%, respectively), CD73 (89 vs. 94.06%, respectively), CD90 (94 vs. 88.91%, respectively) and CD105 (77 vs. 96.74%, respectively), as mesenchymal stem cell markers. The results showed that hAD-MSCs and hBM-MSCs were not contaminated by hematopoietic cell lineages [i.e. cells were CD34 and CD45 negative] (Fig.S1, See Supplementary Online Information at www.celljournal.org).

In vitro immunosuppressive capacity of human adipose-derived mesenchymal stem cells and bone marrow-derived mesenchymal stem cells

Allogenic immunomodulatory properties of hAD-MSCs were assessed in the MLR medium, containing responder (R) and stimulator (S) human T cells (R+S+AD-MSCs) at different

ratios of 1:10, 1:5, 1:1, and 2:1 at various time periods (24, 48, 72, and 96 hours). The cell ratio of 1:1 and culture period of 72 hours, showed optimal results (Fig.1A-C). Immunomodulatory properties of hAD-MSCs (n=5 patients) (Fig.1D) and hBM-MSCs (n=8 patients) (Fig.1E) were assessed at optimal ratios in the MLR medium. There were no significant differences among R+S and R+S+BM-MSCs (patients 1, 3, and 5), and R+S+AD-MSCs (patient 1). So, these patients were excluded at later stages. There were no significant differences between hAD-MSCs and hBM-MSCs (Fig.1F).

Xenogeneic immunomodulatory properties of human AD-MSCs (Fig.2A) and BM-MSCs (Fig.2B) were evaluated in the MLR medium by co-culturing hAD-MSCs, responder (R) and stimulator (S) monkey T cells (R+S+AD-MSCs) under optimal conditions (i.e., at the ratio of 1:1 for 72 hours). Immunomodulatory properties of hAD-MSCs (from patients 2, 3, 4, and 5) and hBM-MSCs (from patients 2, 4, 6, 7 and 8) were evaluated under optimal conditions in the MLR medium. There were significant differences among R+S, R+S+BM-MSCs, and R+S+AD-MSCs in all groups. However, there was no significant difference in xenogeneic immunomodulatory properties when comparing hBM-MSCs and hAD-MSCs (Fig.2C). *In vitro* immunomodulatory effects of hAD-MSCs and hBM-MSCs on rhesus T cells subset were assessed. Significant differences were observed in the mRNA level of *IL-17* (Th17), *IFN-γ* (Th1) and *Treg* (FoxP3) between hBM-MSCs and hAD-MSCs, as compared to R+S alone (Fig.2D).

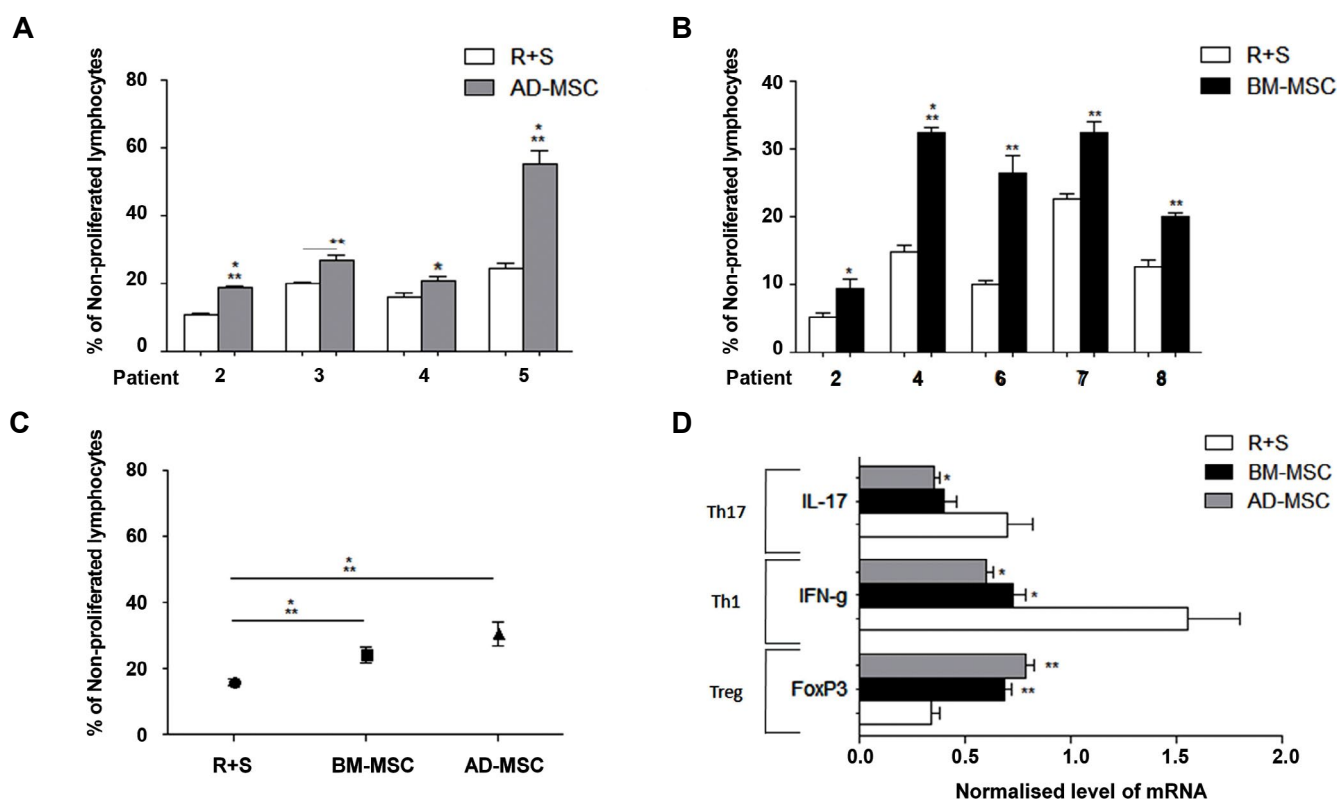


Fig. 2: Xenogeneic immunomodulatory properties of hAD-MSCs and hBM-MSCs. **A.** Xenogeneic immunomodulatory properties of human AD-MSCs and **B.** BM-MSCs were evaluated in the MLR medium following co-culture of hAD-MSCs and responder (R) and stimulator (S) monkey T cell (R+S+AD-MSCs) under the optimal conditions (i.e., at the ratio of 1:1 for 72 hours). The comparison of the immunomodulatory properties of hAD-MSCs (patients 2, 3, 4, and 5) and hBM-MSCs (patients 2, 4, 6, 7 and 8) was made under the optimal conditions in the MLR medium. **C.** Significant differences were found among R+S and R+S+BM-MSCs, and R+S+AD-MSCs in all groups. Also, no significant difference was observed in xenogeneic immunomodulatory properties between hBM-MSCs and hAD-MSCs. **D.** *In vitro* immunomodulatory effects of hAD-MSCs and hBM-MSCs on rhesus T cells subset were assessed. There were significant differences in the mRNA level of *IL-17* (Th17), *IFN-γ* (Th1) and *Treg* (FoxP3) among hBM-MSCs and hAD-MSCs, and R+S. Data are presented as the mean \pm standard deviation. *, $P < 0.05$; **, $P < 0.01$; ***, $P < 0.001$, hAD-MSCs; Human adipose-derived mesenchymal stem cells, and hBM-MSCs; Human bone marrow-derived mesenchymal stem cells.

***In vivo* immunomodulatory effect of hMSCs on T cells of healthy recipient monkeys**

hAD-MSCs and hBM-MSCs (approximately 2×10^6 MSCs/animal) were intravenously injected to healthy rhesus monkeys (Fig.3A). The blood samples were assessed for FoxP3⁺ T cells (by RT-PCR, Fig.3B) and CD4⁺CD25⁺ T cells (by flow cytometry) (Fig.3C) at appropriate time points (6, 12, 24, 48, 72, and 96 hours). No significant difference was found in xenogeneic immunomodulatory properties between hBM-MSCs and hAD-MSCs in a healthy recipient monkey, 6-96 hours after MSC transplantation. However, there was a significant difference in xenogeneic immunomodulatory properties between hBM-MSCs and hAD-MSCs in Foxp3⁺ T cells and CD4⁺CD25⁺ T cells ($P < 0.05$), 24-96 hours after MSC transplantation. Also, there was a significant difference in xenogeneic immunomodulatory properties between hBM-MSCs and hAD-MSCs in Foxp3⁺ T cells ($P < 0.05$) and CD4⁺CD25⁺ T cells ($P < 0.001$), before 24 hours of MSC transplantation (Fig.3B, C).

Skin grafting and immunomodulatory effects of human adipose-derived mesenchymal stem cells

Immunomodulatory effects of hAD-MSCs were evaluated on T cell subsets after skin grafting at different time points (6, 12, 24, and 48 hours, Fig.3D). Foxp3, IL-17 and INF- γ expression levels were compared after grafting hAD-MSCs (48 hours) and the skin (Fig.3E). At the protein level, as a control, T cells of rhesus after allogenic skin grafting and before hAD-MSCs transplantation were treated with TGF- β (10 and 20 ng/ml) as an immunosuppressive factor, and the percentages of IL17 and INF- γ were decreased (Fig.3F). Results showed that after hAD-MSCs injection, CD4⁺IL-17⁺ (Th17) and CD4⁺INF- γ ⁺ (Th1) cells were decreased, while CD4⁺FoxP3⁺ cells (Treg) were increased (Fig.3G-I).

Comparative immunomodulatory effect of human adipose-derived mesenchymal stem cells and bone marrow-derived mesenchymal stem cells after skin grafting

HAD-MSCs and hBM-MSCs (2×10^6 MSCs/kg) were intravenously transplanted into rhesus monkey on the day of skin grafting (Fig.4A). The skin sections were analyzed by H&E staining for inflammation and rejection, 96 hours after transplantation. Histological assessments showed no trace of inflammation and exhibited redness or bulging in the internal part of skin biopsies after MSCs transplantation up to 96 hours, compared to the group without MSCs (Fig.4B). However, there were no significant differences between hAD-MSCs and hBM-MSCs in histopathological scores in terms of PMNs, non-phagocytic cells, and phagocytic cells counts and destroyed epidermis (Table.2). Also, RT-PCR and flow cytometry were used to detect Th1 (anti-CD4 and anti-IFN- γ), Th17 (anti-CD4 and anti-IL-17) and T regulatory markers (anti-CD4 and anti-FoxP3). At the mRNA level, after the intravenous transplantation of MSCs, the percentages of Th1 and Th17 cells were reduced, while the percentage of Treg cells was increased (Fig.4C). Also, at the protein level, after intravenous transplantation of MSCs, the percentages of Th1 and Th17 cells were decreased, while Treg cells were increased (Fig.4D). These results showed that MSCs have immunomodulatory properties. However, there was a pilot *in vivo* evaluation with a small sample size of monkeys because of some limitations in time and cost for the proof-of-concept of immunomodulatory properties of MSCs. So, we could not draw any significant conclusion on the efficacy due to the experiment design, including limited sample size, lack of control group, and single-dose infusion. It seems that we need more animal samples, skin biopsies and other tissue samples to perform the statistical analysis of immunomodulatory properties of MSCs after transplantation in future studies.

Table 2: Inflammatory cells and epidermal healing scoring after skin transplantation with and without MSCs up to 96 hours

Groups	Site	Inflammatory cells			Epidermis Destroyed (0 to 4)
		PMNs (0 to 6)	Non-Phagocytic cells (0 to 6)	Phagocytic cells (0 to 6)	
No cell	Ext	0	1	1	0
	Int	5	N/A	N/A	3
BM-MSCs	Ext	0	2	1	0
	Int	6	N/A	N/A	4
No cell	Ext	6	1	1	1
	Int	3	1	0	2
AD-MSCs	Ext	0	2	2	1
	Int	4	N/A	N/A	3

Ext; External biopsy, Int; Internal biopsy, N/A; Not applicable (because of the presence of acute inflammation), PMN; Polymorphonuclear cells, Non-phagocytic cells; Lymphocytes and plasma cells, BM-MSCs; Bone marrow-derived mesenchymal stem cells, and AD-MSCs; Adipose-derived mesenchymal stem cells.

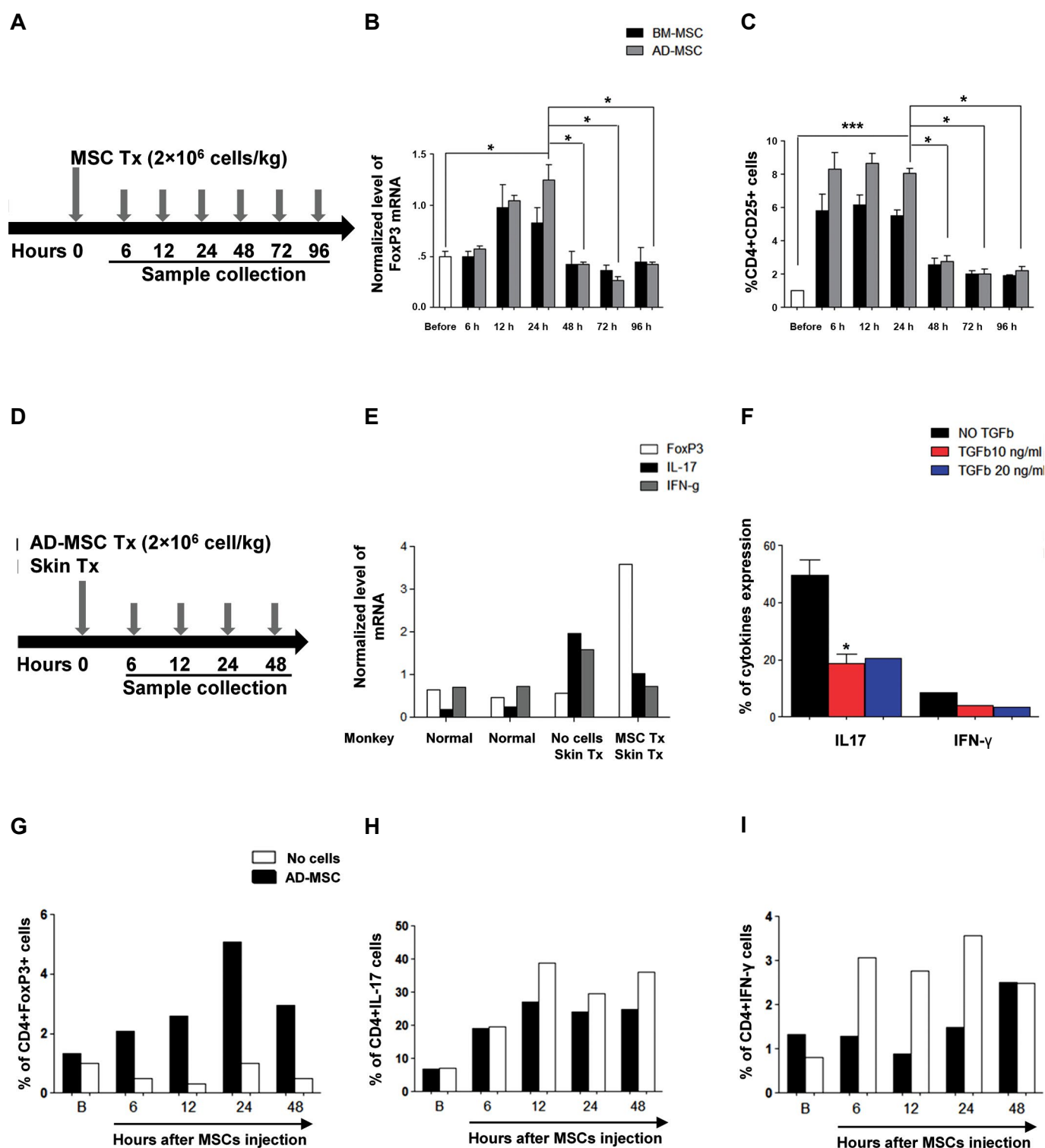


Fig.3: Immunomodulatory effects of hAD-MSCs and hBM-MSCs transplantation on T cell subsets in a healthy monkey recipient and immunomodulatory effects of hAD-MSCs transplantation on rhesus T cell subsets after skin grafting. **A.** A schematic overview of *in vivo* cell transplantation in a healthy monkey recipient. **B, C.** No significant differences in xenogeneic immunomodulatory properties were found between hBM-MSCs and hAD-MSCs in a healthy monkey recipient, 6-96 hours after cell transplantation. However, a significant difference was found in xenogeneic immunomodulatory properties when comparing hBM-MSCs and hAD-MSCs in terms of Foxp3+ T cells and CD4+CD25+ T cells (* $P < 0.05$), 24-96 hours after cell transplantation. Also, a significant difference was observed in xenogeneic immunomodulatory properties between hBM-MSCs and hAD-MSCs in terms of Foxp3+ T cells (* $P < 0.05$) and CD4+CD25+ T cells (** $P < 0.001$), before 24 hours of cell transplantation. **D.** Schematic overview of *in vivo* hAD-MSCs transplantation with skin graft. **E.** Immunomodulatory effect of hAD-MSCs transplantation on monkey T cells subsets 48 hours after skin grafting in a monkey model. **F.** As a control, at the protein level, T cells of rhesus after skin graft and before hAD-MSCs transplantation were exposed to TGF- β (10 and 20 ng/ml) as an immunosuppressive factor, and the percentage of IL17 and IFN- γ were decreased. **G-I.** At the protein level, after hAD-MSCs IV transplantation, 6-48 hours after cell transplantation, the percentage of CD4+IL-17+ and CD4+IFN- γ + cells, as the cellular mediators of inflammation, was decreased, while the number of CD4+FoxP3+ cells, as the mediators of immunomodulation, was increased. Data are presented as the mean \pm standard deviation. *, $P < 0.05$, ***, $P < 0.001$, hAD-MSCs; Human adipose-derived mesenchymal stem cells, and hBM-MSCs; Human bone marrow-derived mesenchymal stem cells. h; Hour; IL; Interleukin, and IFN; Interferon.

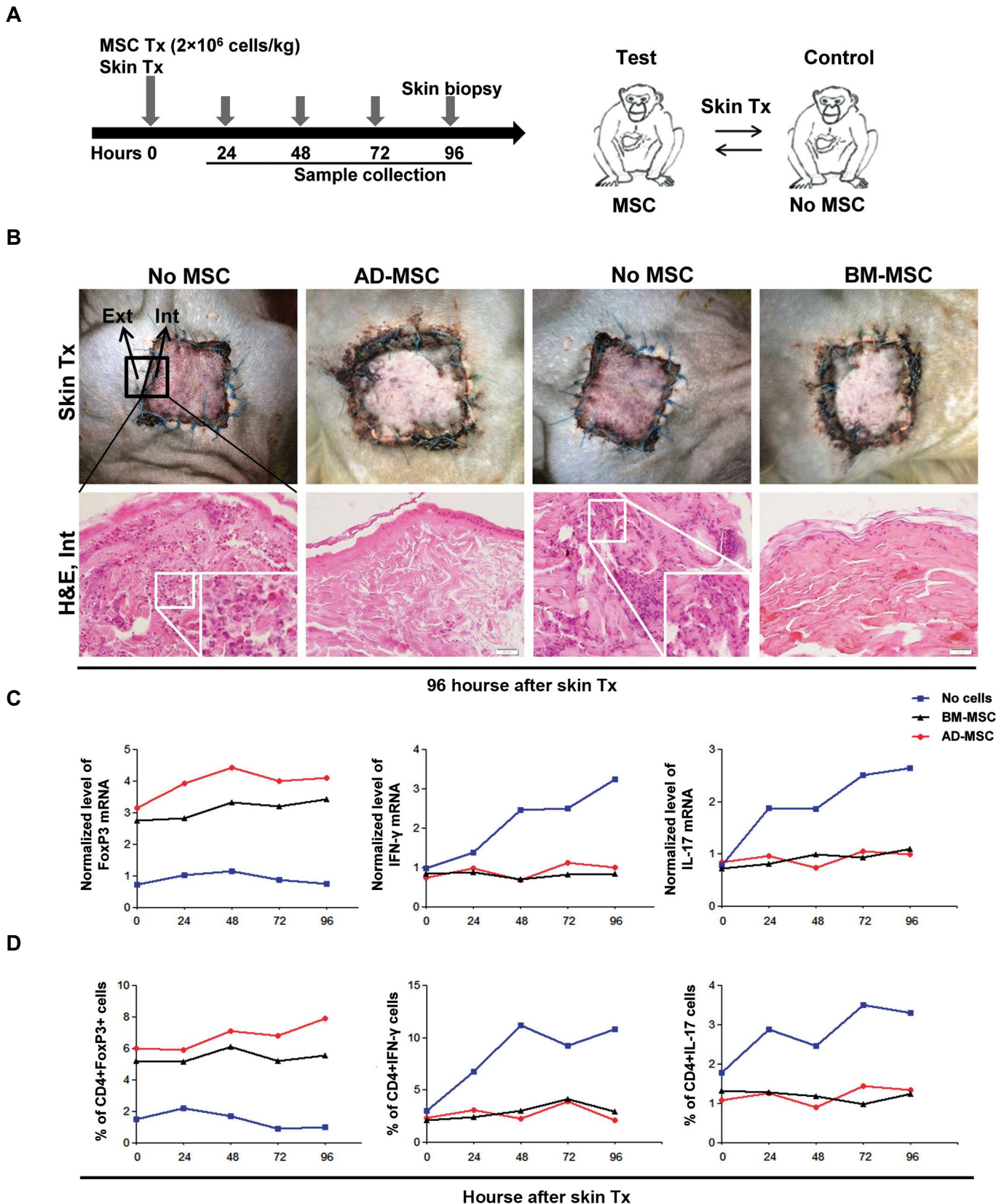


Fig.4: Immunomodulatory effect of human adipose-derived mesenchymal stem cells (hAD-MSCs) and human bone marrow-derived mesenchymal stem cells (hBM-MSCs) transplantation on rhesus T cell subsets after allogenic skin grafting. **A.** A schematic overview of *in vivo* cell transplantation with skin grafting. Immunomodulatory effects of hAD-MSCs and hBM-MSCs transplantation on monkey T cells subsets 24, 48, 72, and 96 hours after skin grafting in a monkey model. **B.** Inflammatory features, such as redness and bulging can be detected around skin graft area without cell transplantation. Visual inspection and histopathological analysis of transplanted tissues showed mild inflammation around allogenic skin graft after cell transplantation compared with monkeys receiving no cell transplantation and showed severe inflammation. **C.** At the mRNA level, after IV transplantation of hBM-MSCs and hAD-MSCs, the percentages of Th1 and Th17, as the cellular mediators of inflammation, were decreased, while the percentage of Treg, as mediators of immunomodulation, was increased. **D.** Also, at the protein level, after IV transplantation of hBM-MSCs and hAD-MSCs, the percentages of Th1 and Th17 were decreased, while the number of Tregs was increased.

Discussion

Several experiments showed that the beneficial paracrine effects of MSCs transplantation are stronger than their differentiation ability (19). MSCs are now known to have potent anti-inflammatory and immunomodulatory properties besides their regenerative capacities (20, 21). The immunomodulatory potential of hBM-MSCs and hAD-MSCs has led to their application against various inflammatory and auto-immune disorders as well as organ transplantation (22). In this regard, studies showed that autologous or allogenic MSCs could suppress the proliferation of both CD4+ and CD8+ T lymphocytes, which were stimulated by mitogens or specific antigens (23) via mechanisms, which are not limited to major histocompatibility complex [MHC, (7)]. In addition, MSCs affect other T cells functions, including a decrement in pro-inflammatory factors, such as IFN- γ , IL-2, and TNF α , along with an increment in the secretion of IL-4 and IL-10, which are well-known for their anti-inflammatory effects (24). Although several studies have reported the immunosuppressive effects of MSCs on other immune cells, such as B cells (25), neutrophil cells (26), natural killer (NK) cells (27) and dendritic cells [DC, (28)]. *in vitro* and *in vivo* studies highlighted the increased generation of CD4+CD25+ T regulatory cells as a critical part of MSCs immunosuppressive effects (21, 29).

MSCs act via cell-cell contact and releasing soluble factors, such as transforming growth factor (TGF)- β , hepatocyte growth factor (HGF) (30), prostaglandin E₂ [PGE₂, (31)], indoleamine-2,3-dioxygenase, inducible nitric-oxide synthase [iNOS, (32)], and IL-10 (33), which promote lymphocytes suppression, and they were reported to be potentially responsible for immunomodulatory effects of MSCs. In general, MSCs isolated from various sources, such as the bone marrow, adipose tissue, and Wharton's jelly have shown somehow similar suppressive effects on the proliferation of CD4+ and CD8+ T-cell populations (34). In this study, allogenic and xenogeneic immunomodulatory properties of hAD-MSCs and hBM-MSCs were confirmed *in vitro* on human and monkey T cell subsets before transplantation. Also, a 1:1 cell ratio and a culture period of 72 hours showed the optimal results for immunomodulatory properties and selected for next analyses.

T helper cells (Th) are CD4+ subset of T cells that recognize cell surface proteins presented by MHC. Their differentiation into Th1, Th2, and Th17 cells depends on cytokine environment around the site of the antigen presentation (35). When CD4+ T cells are induced in the presence of IL-12 and IFN- γ , they shift toward Th1 phenotype. IFN- γ is a pivotal cytokine produced by Th1 cells. Th1 cells promote the activation and recruitment of macrophages to the inflammation site and induce the removal of intracellular pathogens

and delayed-type hypersensitivity (DTH) reactions by activating cellular immunity responses (36). Another pro-inflammatory subset of Th cells is Th17 cell, an effector phenotype characterized by preferential secretion of IL-17A (IL-17), while expressing other cytokines, including IL-17 F, IL-21, and IL-22. Although most of recent studies indicated that MSCs are able to suppress Th17 cell-mediated immune responses via different mechanisms, some experiments showed Th17 cell-promoting effects on MSCs (37).

Treg is a subset of CD4+ T cells with potent suppressive functions necessary for the prevention of autoimmune conditions and reduction of inflammatory reactions via cell-cell contact and secretion of soluble factors. These cells are generally characterized by the expression of a surface marker CD25 (IL-2 receptor alpha chain) and the intracellular marker FOXP3. Treg could downregulate the activation of inflammatory Th cells subtypes (i.e. Th1 and Th17), just like other inflammatory cells. As indicated in several *in vitro* and *in vivo* studies, MSCs could increase the number and functionality of Treg cells (17, 21, 38-40).

In our study, immune modulatory effect of hAD-MSCs and hBM-MSCs transplantation on monkey T cell subsets, 96 hours after allogenic skin grafting, was assessed in a monkey model. Inflammatory features, such as redness and bulging were observed around allogenic skin graft area in the absence of hAD-MSCs and hBM-MSCs transplantation. Also, visual inspection and histopathological analysis showed mild inflammation around allogenic skin graft after cell transplantation, compared with monkeys receiving no cell transplantation and showed high inflammation. At the mRNA and protein levels, after the intravenous transplantation of hBM-MSCs and hAD-MSCs, the percentages of CD4+IL-17+ (Th17) and CD4+INF- γ + (Th1) cells, as the cellular mediators of inflammation were significantly decreased, while CD4+FoxP3+ cells (Treg) as the mediators of immunomodulation were significantly increased. These findings are consistent with previous studies, which reported a decrement in Th1/Th17, but an increment in Treg response following MSCs transplantation. The above-mentioned changes could extend the skin graft survival by inhibiting different graft rejection mechanisms. So, histopathological reports in a short time was (acute phase) confirmed the immunomodulatory properties of MSCs after skin transplantation *in vivo* that already we had shown *in vitro*. However, further research with more examples in a long time (chronic phase) is needed in future studies.

Conclusion

Our study describes immunomodulatory effect of hAD-MSCs and hBM-MSCs transplantation on monkey T cells subsets, 96 hours after allogenic skin graft, in a monkey model; nevertheless, due to research limitations, as our

findings are limited to a small sample size and the acute phase of immune response following skin graft, longer *in vivo* experiments are required to get more detailed information on the chronic phase of immune response.

Acknowledgments

We express our gratitude to Mehrnaz Tayebi Kamardi for her technical assistance and critical comments. Also, we would like to particularly thank Dr. Ehsan Mirsadeghi, Mr. Mojtaba Karimpour and Mr. Ali Inanloo for their help in animal handling. There is no conflict of interest. This study was supported by a grant from Royan Institute and the Royan Charity Association for Health Research (Tehran, Iran).

Authors' Contributions

R.M., F.S., E.H.S., N.A.; Conception and design of the study, collection and assembly of data, data analysis and interpretation, and manuscript writing. R.M., E.E., N.S., R.F.S., M.Z., M.F., B.S., M.H., H.B.; Collection, evaluation and assembly of data. M.Z., M.F., B.S.; ABO grouping, RBC cross-matching, and HLA typing. R.M., H.B., N.A.; Final approval of the manuscript. All authors read and approved the final manuscript.

References

- Ullah I, Subbarao RB, Rho GJ. Human mesenchymal stem cells-current trends and future prospective. *Biosci Rep*. 2015; 35(2). pii: e00191.
- Bajek A, Gurtowska N, Olkowska J, Kazmierski L, Maj M, Drewa T. Adipose-derived stem cells as a tool in cell-based therapies. *Arch Immunol Ther Exp (Warsz)*. 2016; 64(6): 443-454.
- Yañez R, Oviedo A, Aldea M, Bueren JA, Lamana ML. Prostaglandin E2 plays a key role in the immunosuppressive properties of adipose and bone marrow tissue-derived mesenchymal stromal cells. *Exp Cell Res*. 2010; 316(19): 3109-3123.
- Li N, Hua J. Interactions between mesenchymal stem cells and the immune system. *Cell Mol Life Sci*. 2017; 74(13): 2345-2360.
- Wang M, Yuan Q, Xie L. Mesenchymal stem cell-based immunomodulation: properties and clinical application. *Stem Cells Int*. 2018; 2018: 3057624.
- Gao F, Chiu SM, Motan DA, Zhang Z, Chen L, Ji HL, et al. Mesenchymal stem cells and immunomodulation: current status and future prospects. *Cell Death Dis*. 2016; 7: e2062.
- Le Blanc K, Tammik L, Sundberg B, Haynesworth SE, Ringden O. Mesenchymal stem cells inhibit and stimulate mixed lymphocyte cultures and mitogenic responses independently of the major histocompatibility complex. *Scand J Immunol*. 2003; 57(1): 11-20.
- Lin L, Du L. The role of secreted factors in stem cells-mediated immune regulation. *Cell Immunol*. 2018; 326: 24-32.
- Rasmuson I, Ringdén O, Sundberg B, Le Blanc K. Mesenchymal stem cells inhibit the formation of cytotoxic T lymphocytes, but not activated cytotoxic T lymphocytes or natural killer cells. *Transplantation*. 2003; 76(8): 1208-1213.
- Roux C, Saviane G, Pini J, Belaid N, Dhib G, Voha C, et al. Immunosuppressive mesenchymal stromal cells derived from human-induced pluripotent stem cells induce human regulatory T cells *in vitro* and *in vivo*. *Front Immunol*. 2018; 8: 1991.
- Khosravi M, Bidmeshkipour A, Cohen JL, Moravej A, Hojjat-Assari S, Naserian S, et al. Induction of CD4+ CD25+ FOXP3+ regulatory T cells by mesenchymal stem cells is associated with modulation of ubiquitination factors and TSDR demethylation. *Stem Cell Res Ther*. 2018; 9(1): 273.
- Guillén MI, Platas J, Pérez Del Caz MD, Mirabet V, Alcaraz MJ. Paracrine anti-inflammatory effects of adipose tissue-derived mesenchymal stem cells in human monocytes. *Front Physiol*. 2018; 9: 661.
- Grant CR, Liberal R, Mieli-Vergani G, Vergani D, Longhi MS. Regulatory T-cells in autoimmune diseases: challenges, controversies and--yet--unanswered questions. *Autoimmun Rev*. 2015; 14(2): 105-116.
- Facciabene A, Motz GT, Coukos G. T-regulatory cells: key players in tumor immune escape and angiogenesis. *Cancer Res*. 2012; 72(9): 2162-2171.
- Duggleby R, Danby RD, Madrigal JA, Saudemont A. Clinical grade regulatory CD4+ T cells (Tregs): moving toward cellular-based immunomodulatory therapies. *Front Immunol*. 2018; 9: 252.
- Roncarolo MG, Gregori S, Bacchetta R, Battaglia M. Tr1 cells and the counter-regulation of immunity: natural mechanisms and therapeutic applications. *Curr Top Microbiol Immunol*. 2014; 380: 39-68.
- Liu Q, Zheng H, Chen X, Peng Y, Huang W, Li X, et al. Human mesenchymal stromal cells enhance the immunomodulatory function of CD8(+) CD28(-) regulatory T cells. *Cell Mol Immunol*. 2015; 12(6): 708-718.
- Li H, Shen S, Fu H, Wang Z, Li X, Sui X, et al. Immunomodulatory functions of mesenchymal stem cells in tissue engineering. *Stem Cells Int*. 2019; 2019: 9671206.
- Galipeau J, Sensébé L. Mesenchymal stromal cells: clinical challenges and therapeutic opportunities. *Cell Stem Cell*. 2018; 22(6): 824-833.
- Hu MS, Borrelli MR, Lorenz HP, Longaker MT, Wan DC. Mesenchymal stromal cells and cutaneous wound healing: a comprehensive review of the background, role, and therapeutic potential. *Stem Cells Int*. 2018; 2018: 6901983.
- Lee DK, Song SU. Immunomodulatory mechanisms of mesenchymal stem cells and their therapeutic applications. *Cell Immunol*. 2018; 326: 68-76.
- Waldner M, Zhang W, James IB, Allbright K, Havis E, Bliley JM, et al. Characteristics and immunomodulating functions of adipose-derived and bone marrow-derived mesenchymal stem cells across defined human leukocyte antigen barriers. *Front Immunol*. 2018; 9: 1642.
- Reis M, Mavin E, Nicholson L, Green K, Dickinson AM, Wang XN. Mesenchymal stromal cell-derived extracellular vesicles attenuate dendritic cell maturation and function. *Front Immunol*. 2018; 9: 2538.
- Kaundal U, Bagai U, Rakha A. Immunomodulatory plasticity of mesenchymal stem cells: a potential key to successful solid organ transplantation. *J Transl Med*. 2018; 16(1): 31.
- Corcione A, Benvenuto F, Ferretti E, Giunti D, Cappiello V, Cazzanti F, et al. Human mesenchymal stem cells modulate B-cell functions. *Blood*. 2006; 107(1): 367-372.
- Raffaghello L, Bianchi G, Bertolotto M, Montecucco F, Busca A, Dallegri F, et al. Human mesenchymal stem cells inhibit neutrophil apoptosis: a model for neutrophil preservation in the bone marrow niche. *Stem Cells*. 2008; 26(1): 151-162.
- Sotiropoulou PA, Perez SA, Gritzapis AD, Baxevas CN, Papatheofanis M. Interactions between human mesenchymal stem cells and natural killer cells. *Stem Cells*. 2006; 24(1): 74-85.
- Jiang XX, Zhang Y, Liu B, Zhang SX, Wu Y, Yu XD, et al. Human mesenchymal stem cells inhibit differentiation and function of monocyte-derived dendritic cells. *Blood*. 2005; 105(10): 4120-4126.
- Prevosto C, Zancolli M, Canevali P, Zocchi MR, Poggi A. Generation of CD4+ or CD8+ regulatory T cells upon mesenchymal stem cell-lymphocyte interaction. *Haematologica*. 2007; 92(7): 881-888.
- Nasef A, Mazuric C, Bouchet S, François S, Chapel A, Thierry D, et al. Leukemia inhibitory factor: Role in human mesenchymal stem cells mediated immunosuppression. *Cell Immunol*. 2008; 253(1-2): 16-22.
- Németh K, Leelahavanichkul A, Yuen PS, Mayer B, Parmelee A, Doi K, et al. Bone marrow stromal cells attenuate sepsis via prostaglandin E(2)-dependent reprogramming of host macrophages to increase their interleukin-10 production. *Nat Med*. 2009; 15(1): 42-49.
- Sato K, Ozaki K, Oh I, Meguro A, Hatanaka K, Nagai T, et al.

- Nitric oxide plays a critical role in suppression of T-cell proliferation by mesenchymal stem cells. *Blood*. 2007; 109(1): 228-234.
33. Semedo P, Correa-Costa M, Antonio Cenedeze M, Maria Avancini Costa Malheiros D, Antonia dos Reis M, Shimizu MH, et al. Mesenchymal stem cells attenuate renal fibrosis through immune modulation and remodeling properties in a rat remnant kidney model. *Stem Cells*. 2009; 27(12): 3063-3073.
 34. Najar M, Raicevic G, Boufker HI, Fayyad Kazan H, De Bruyn C, Meuleman N, et al. Mesenchymal stromal cells use PGE2 to modulate activation and proliferation of lymphocyte subsets: Combined comparison of adipose tissue, Wharton's Jelly and bone marrow sources. *Cell Immunol*. 2010; 264(2): 171-179.
 35. Wan YY, Flavell RA. How diverse--CD4 effector T cells and their functions. *J Mol Cell Biol*. 2009; 1(1): 20-36.
 36. Hermann-Kleiter N, Baier G. NFAT pulls the strings during CD4+ T helper cell effector functions. *Blood*. 2010; 115(15): 2989-2997.
 37. Carrión F, Nova E, Luz P, Apablaza F, Figueroa F. Opposing effect of mesenchymal stem cells on Th1 and Th17 cell polarization according to the state of CD4+ T cell activation. *Immunol Lett*. 2011; 135(1-2): 10-16.
 38. English K, French A, Wood KJ. Mesenchymal stromal cells: facilitators of successful transplantation? *Cell Stem Cell*. 2010; 7(4): 431-442.
 39. Griffin MD, Ritter T, Mahon BP. Immunological aspects of allogeneic mesenchymal stem cell therapies. *Hum Gene Ther*. 2010; 21(12): 1641-1655.
 40. Lei H, Schmidt-Bleek K, Dienelt A, Reinke P, Volk H-D. Regulatory T cell-mediated anti-inflammatory effects promote successful tissue repair in both indirect and direct manners. *Front Pharmacol*. 2015; 6: 184.
-

Correlation of sPD1 with Procalcitonin and C-Reactive Protein Levels in Patients with Sepsis

Zahra Bakhshiani, M.Sc.¹, Salomeh Fouladi, Ph.D.¹, Samaneh Mohammadzadeh, Ph.D.², Nahid Eskandari, M.D., Ph.D.^{1,3*}

1. Department of Immunology, Faculty of Medicine, Isfahan University of Medical Sciences, Isfahan, Iran
2. Poursina Hakim Digestive Diseases Research Center, Isfahan University of Medical Sciences, Isfahan, Iran
3. Applied Physiology Research Center, Isfahan University of Medical Sciences, Isfahan, Iran

*Corresponding Address: P.O.Box: 8174673461, Department of Immunology, Faculty of Medicine, Isfahan University of Medical Sciences, Isfahan, Iran
Email: neskandari@med.mui.ac.ir

Received: 14/May/2019, Accepted: 04/November/2019

Abstract

Objective: Sepsis results from dysregulated host responses to infection, and it is a major cause of mortality in the world. Co-inhibitory molecules, such as PD-1, play a critical role in this process. Considering the lack of information on the relation between sPD1 and sepsis, the present study aimed to examine the sPD1 level in septic patients and evaluate its correlation with procalcitonin (PCT) and C-reactive protein (CRP) levels.

Materials and Methods: This descriptive cross-sectional study consisted of three groups, including septic patients (n=15), suspected of sepsis (n=15), and healthy subjects (n=15). White blood cells (WBCs) and platelet (PLT) counts are evaluated. The serum levels of CRP, PCT, and sPD1 were measured by immunoturbidimetric assay, electrochemiluminescence technology, and the enzyme-linked immunosorbent assay (ELISA), respectively.

Results: Our study indicated that there was a significant difference in WBC and PLT counts between the septic group compared to suspected and control groups ($P < 0.001$, $P < 0.01$, respectively). The CRP level was significantly higher in septic compared to suspected and control groups ($P < 0.001$). There was also a significant difference between the PCT level in septic and suspected groups in comparison with the controls ($P < 0.001$, $P < 0.01$). The sPD1 level was significantly higher in septic patients compared to suspected and control groups ($P < 0.001$). In septic patients, sPD1 levels were correlated positively with the CRP and PCT levels.

Conclusion: Overall, sPD1 correlation with inflammatory markers, might propose it as a potential biomarker to sepsis diagnosis. However, the clinical application of serum sPD-1 testing in patients with sepsis requires further investigation.

Keywords: C-Reactive Protein, Procalcitonin, Sepsis, sPD1

Cell Journal (Yakhteh), Vol 23, No 1, April-June (Spring) 2021, Pages: 14-20

Citation: Bakhshiani Z, Fouladi S, Mohammadzadeh S, Eskandari N. Correlation of sPD1 with procalcitonin and c-reactive protein levels in patients with sepsis. Cell J. 2021; 23(1): 14-20. doi: 10.22074/cellj.2021.6941.

This open-access article has been published under the terms of the Creative Commons Attribution Non-Commercial 3.0 (CC BY-NC 3.0).

Introduction

Sepsis refers to a life-threatening dysfunction of the organ that is caused by a dysregulated response of the host to the infection and, if not controlled, may become the severe form, septic shock. Sepsis is one of the most important causes of morbidity and mortality all over the world and often requires urgent and supportive treatment in the intensive care unit (ICU) due to the involvement of several organs. About 18 million new cases of sepsis are reported each year, with a mortality rate of 30-50% (1).

Clinical symptoms of sepsis include tachycardia, tachypnea, fever, leukocytosis, etc. Severe Sepsis is associated with hypoperfusion, organ dysfunction, or hypotension (2).

In sepsis, invasion of the microorganisms to the bloodstream occurs, so that they localize and proliferate and release their pathogenic factors into the bloodstream. These products can stimulate the release of endogenous sepsis mediators from endothelial cells, neutrophils, monocytes, macrophages, and plasma cell

precursors (3, 4).

Traditionally, sepsis was considered as an excessive systemic proinflammatory reaction to invasive microbial pathogens. More recently, it has been suggested that the early phase of hyperinflammation is followed or overlapped by long-term immunosuppression, considered as sepsis-induced immunoparalysis. The immunoparalytic status is determined by impaired innate and adaptive immune responses and may play an important role in the pathogenesis of multiple organ failure, tissue damage, and death caused by sepsis (5, 6).

Early diagnosis and immediate anti-microbial therapy in the treatment of sepsis is essential in order to save the patient's life. In addition to clinical evaluations, laboratory hematologic, microbiological, and immunological tests are needed to diagnose sepsis (7, 8).

Many cytokines or other proteins have been studied as potential biomarkers to determine a hyperinflammatory status in patients with sepsis. From these, C-reactive

protein (CRP) and procalcitonin (PCT), white blood cells (WBC), interleukin-1 (IL-1) and IL-6 can be referred. Compared with CRP, the PCT test has a higher diagnostic and prognostic value and can differentiate bacterial and viral meningitis (9, 10).

Immune system suppression is one of the major causes of mortality in patients with severe sepsis (11, 12). Negative co-stimulatory molecules play an important role in the immune system function and regulate cell proliferation, differentiation, and apoptosis negatively.

With knowledge of the mechanism of the immune response in sepsis, several immunosuppression markers are proposed, such as the superfamily B7-CD28 called programmed cell death 1 (PD-1) so that PD1 and programmed death ligand-1 (PD-L1) inhibit the function of B and T cells (13, 14).

PD1 has two forms, a form bind to the membrane, and another soluble form, called soluble PD-1 (sPD-1). sPD-1 is encoded by PD-1Dex3. It has no transmembrane region, and it has a biological function. sPD-1 could enter the bloodstream so that it can perform its function in the immune response (15).

Considering the limited information available concerning the relation between sPD-1 and sepsis, this study aimed to investigate the serum sPD-1 value as an immunosuppressive phase marker compared to CRP and PCT levels in recognized sepsis, suspected sepsis, and healthy subjects. Moreover, the relation between the sPD1 level and these two inflammatory markers was studied.

Materials and Methods

Study subjects

In a descriptive cross-sectional study, patients (n=30) who admitted to medical or surgical ICUs Fatema-Zahra hospital in Najafabad-Isfahan (from October to December 2019), who were older than 18 year of age, and fulfilled a consensus panel definition of sepsis were included in the study. Sepsis was defined as the presence of systemic inflammatory response syndrome and a known or suspected source of infection. The exclusion criteria were including bone marrow irradiation, chemotherapy, or radiation therapy within the past six months, human immunodeficiency virus (HIV) infection or viral hepatitis, and consumption of immunosuppressive medications.

Before initiation of antibiotic therapy in suspected of sepsis patients, whole blood was taken from the subjects for blood culture (3-4 ml), complete blood count (CBC) (1-2 ml), PCT, CRP, and sPD1 measurements (2-3 ml). Serum was separated from blood cells by centrifugation and stored in 3 plastic

tubes at -20°C for measurements of PCT, CRP, and sPD1 levels.

Finally, according to clinical symptoms of sepsis, microbiologic and laboratory results,

patients categorized into two groups: 1. Proven sepsis (n=15) with clinical symptoms of sepsis and positive blood culture test and 2. Suspected sepsis (n=5) with clinical symptoms but negative blood culture result.

Healthy volunteers (n=15) were recruited as healthy controls. All the control subjects were age- and sex-matched. The study protocol was confirmed by the Ethics Committee of Isfahan University of Medical Sciences (Code of Ethics: IR.MUI.REC.1384012). Written consent was obtained from all subjects or their families.

Hematological examination

A CBC is performed on the automated hematology analyzer KX-21 (Japan) using the study participants' ethylenediaminetetraacetic acid (EDTA, VACUTEST KIMA, Italy) blood tubes, which are obtained via the phlebotomy component. WBCs and PLT counts are the most important parameters in the sepsis.

Microbiological examination

Four ml of blood was added to blood culture media (Biphasic) and incubated at 37°C for 5-7 days. The positive blood cultures media were sub-cultured on blood agar (Himedia, India) and EMB media. The isolated microbes were identified by standard bacteriological methods.

Measurements of C-reactive protein, Procalcitonin, and sPD-1 levels

For the quantitative determination of CRP in serum, latex particle enhanced immunoturbidimetric assay was performed using the Mindray BS- 400 analyzer (China).

Latex particles coated with an antibody specific to human CRP clumps in the presence of CRP in the serum sample forming immune complexes. The intensity of the scattered light is proportional to the CRP level in the serum. The light scattering is measured by reading turbidity (absorbance) at 570 nm. The CRP concentration is determined via a calibration curve.

The lower limit of detection was 0.1 mg/L, and the expected value for CRP in healthy individuals was below 6.2 mg/L.

The serum level of PCT was measured using the electro-chemiluminescence (ECL) technology (Roche Diagnostics, Germany). Related concentrations were measured according to protocols using an immunoassay analyzer. The lower detection limit was 0.02 ng/mL.

Through the first incubation, antigen in the sample, a biotinylated monoclonal PCT-specific antibody, and a monoclonal PCT-specific antibody labeled with a ruthenium complex react to form a sandwich complex. During the second incubation, by the addition of streptavidin-coated microparticles, the complex becomes bound to the solid phase by the interaction of biotin and streptavidin. Then the reaction mixture is aspirated into the measuring cell where the microparticles are magnetically captured onto the surface of the electrode. Unbound substances are then removed with ProCell/ProCell M. Then, the application of a voltage to the electrode induces chemiluminescent emission, which is measured by a photomultiplier.

Finally, for determining the results, a calibration curve which is specific to the instrument generated by 2-point calibration and a master curve provided via the reagent barcode.

The concentration of sPD1 was measured by the ELISA according to the kit protocol (DuoSet Human PD-1, R&D systems, Minneapolis, MN, USA) on an automatic microplate reader (Stat Fax 2100, USA). The detection range of the kit was 156-10000 pg/ml.

In brief, high bind microtiter plates were incubated with the capture antibody, sealed, and incubated overnight. On the next day, plates were washed (3 x with phosphate buffered saline (PBS) containing 0.05% Tween). Then, 300 μ L /well bovine serum albumin (BSA) (1% in PBS) was added as a blocking agent. The plates were incubated at room temperature for 1 h. After a washing step, calibrators or patient samples were added, sealed, and incubated at RT for 2 hours. For the preparation of the calibration curve, 1:2 dilutions of the standard ranging from 10 ng/mL to 156 pg/mL, was used. After the washing step, the detection antibody was added, sealed, and incubated for 2 hours. Once again, plates were washed, and Streptavidin-HRP was added and incubated for 20 minutes. After the last washing step, the substrate solution was added to each

well and incubated for 20 minutes at RT. Then stop solution was added to each well. Finally, absorbance was read at 450 nm with wavelength correction set at 540 nm.

Statistical analysis

Data analysis was conducted using IBM SPSS 21 statistics (IBM, USA). Values are represented as mean \pm standard deviation (SD). Shapiro-Wilk Normality test was performed to confirm the normality of data distribution. The difference between the groups was examined through the one-way analysis of variance (ANOVA) test along with the Tukey HSD post hoc. The Chi-square test was used to compare the qualitative variables. Pearson's correlation coefficient test was used to assess the strength of the correlation between the sPD1 and other variables. The level of statistical significance was set at $P < 0.05$.

Results

Characteristics of the patients

In this study, Blood cultures were positive for all patients. The identified bacteria included *Staphylococcus aureus* (n=3) *Streptococcus beta-hemolytic group A* (n=3), *Escherichia coli* (n=2), *Klebsiella pneumoniae* (n=5), and *Enterobacter* (n=2). The age and sex distribution in the proven, suspected sepsis, and control groups are shown in Table 1.

Hematological examination

This study evaluated WBC and platelet counts in different groups. Results showed that there was a significant difference in WBC counts between the septic and suspected groups compared to healthy controls ($P < 0.001$). There is also a significant difference between septic and suspected groups ($P < 0.01$).

There was a significant difference in PLT counts between septic group compared to suspected and control groups ($P < 0.01$). The results are summarized in Table 2.

Table 1: Characteristics of the study groups

Parameter	Septic patients	Suspected group	Control group	P value
Number	15	15	15	
Age (Y)	48.46 \pm 17.6	41.66 \pm 19.38	44.4 \pm 14.8	>0.05
Gender (M/F)	8/7	9/6	10/5	>0.05

$P > 0.05$ compared to the controls. Data indicated as mean \pm standard deviation (SD) (n=15 per group).

Table 2: Variable values of the study groups

Parameter	Septic patients	Suspected group	Control group
WBC ($\times 10^3/\mu\text{l}$)	14.7 \pm 6.53	9 \pm 2.3	5.4 \pm 0.86
PLT ($\times 10^3/\mu\text{l}$)	178.66 \pm 74.97	263.67 \pm 65.171	267 \pm 76.075
CRP (mg/L)	50.97 \pm 11.4	29.54 \pm 16.9	4.38 \pm 2.04
PCT (ng/ml)	4.55 \pm 2.2	2.2 \pm 1.4	0.19 \pm 0.1
sPD1 (pg/ml)	195.1 \pm 151.7	23.9 \pm 12.3	13.1 \pm 7.8

Data indicated as mean \pm standard deviation (SD, n=15 per group). WBC; White blood cells, PLT; Platelet, CRP; C-reactive protein and PCT; procalcitonin.

Serum levels of C-reactive protein, Procalcitonin, and sPD1

This study evaluated the CRP, PCT, and sPD1 serum levels in different groups. There was a significant difference between the mean of CRP level in septic patients and the suspected group compared to healthy controls ($P < 0.001$). In addition, it was observed a significant difference between septic and suspected groups ($P < 0.001$).

Results showed that the PCT level was significantly higher in septic and suspected groups in comparison with the controls ($P < 0.001$, $P < 0.01$, respectively). There was also a significant difference between the mean of PCT level in septic compared to the suspected group ($P < 0.01$).

The results showed that there was a significant difference between the sPD1 levels in septic patients compared to suspected and control groups ($P < 0.001$). But there was not a significant difference between the mean of sPD1 level in suspected compared to the control group ($P > 0.05$). The results are shown in Table 2 and Figure 1.

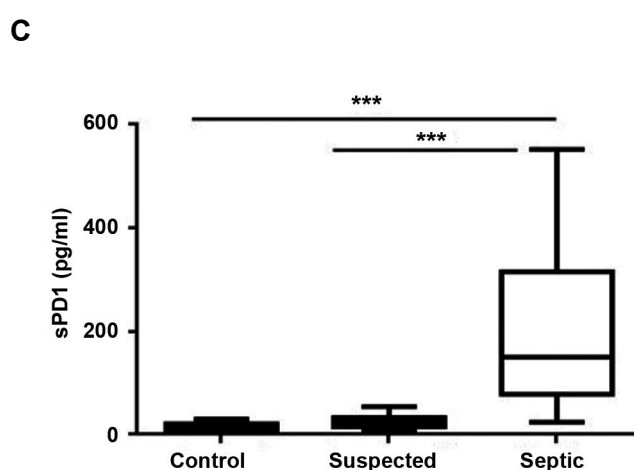
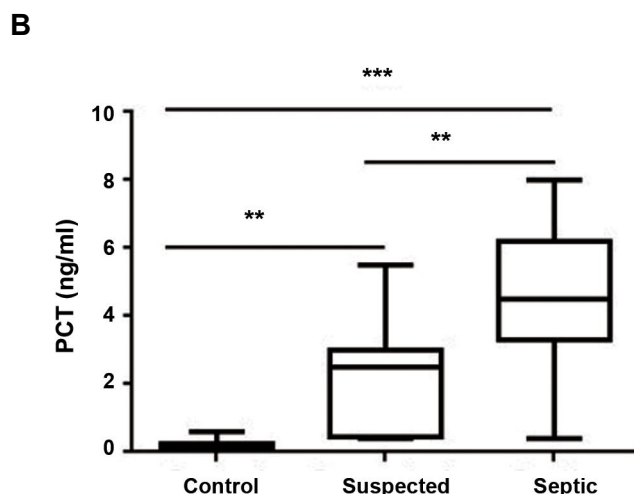
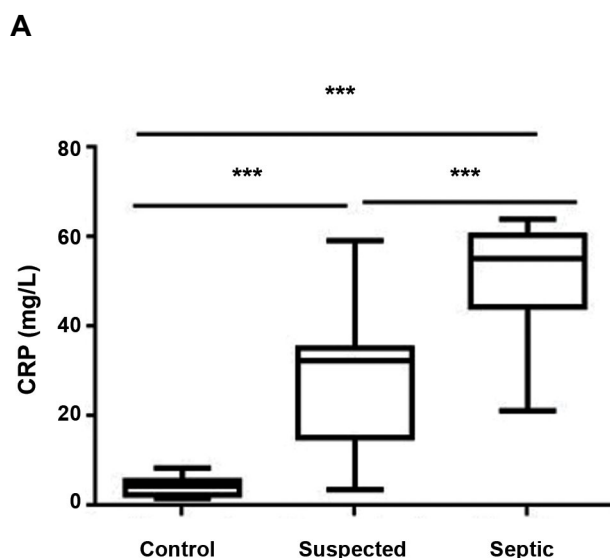


Fig.1: Comparison of serum levels of CRP, PCT, and sPD1 in the different groups. **A.** There was a significant difference between the mean of CRP level in septic patients and the suspected group compared to healthy controls. **B.** PCT level was significantly higher in septic and suspected groups in comparison with the controls. **C.** There was a significant difference between the sPD1 levels in septic patients compared to suspected and control groups. Procalcitonin. Data indicated as mean \pm standard deviation (SD, n=15). CRP; C-reactive protein, PCT; **, $P < 0.01$, and ***, $P < 0.001$.

Sensitivity, specificity, positive predictive value, and negative predictive values

The optimum cut-off value was found to be 6.2 mg/l for CRP, 0.5 ng/ml for PCT, and 42 pg/ml for sPD1. At cut-off values, sensitivity, specificity, PPV, and NPV values of these parameters were calculated for the diagnosis of sepsis, and the results are shown in Table 3.

Table 3: Sensitivity, specificity, PPV, and NPV values of serum variables

Variable	Sensitivity (%)	Specificity (%)	PPV (%)	NPV (%)
CRP (mg/L)	80	86.6	85.7	81.2
PCT (ng/ml)	66.7	86.7	83.3	72.2
sPD1 (pg/ml)	60	93.3	90	70

PPV; Positive prediction value, NPV; Negative prediction value, CRP; C reactive protein, and PCT; Procalcitonin.

Correlation among serum sPD-1 and other parameters

The result showed that there was a significant positive correlation between the serum sPD1 level and values of serum PCT and CRP in the septic patients ($r=0.668$, $P=0.007$; $r=0.515$, $P=0.049$, respectively), Figure 2. However, no correlation detected between sPD-1 levels and age, WBC or PLT counts in all three groups ($P>0.05$).

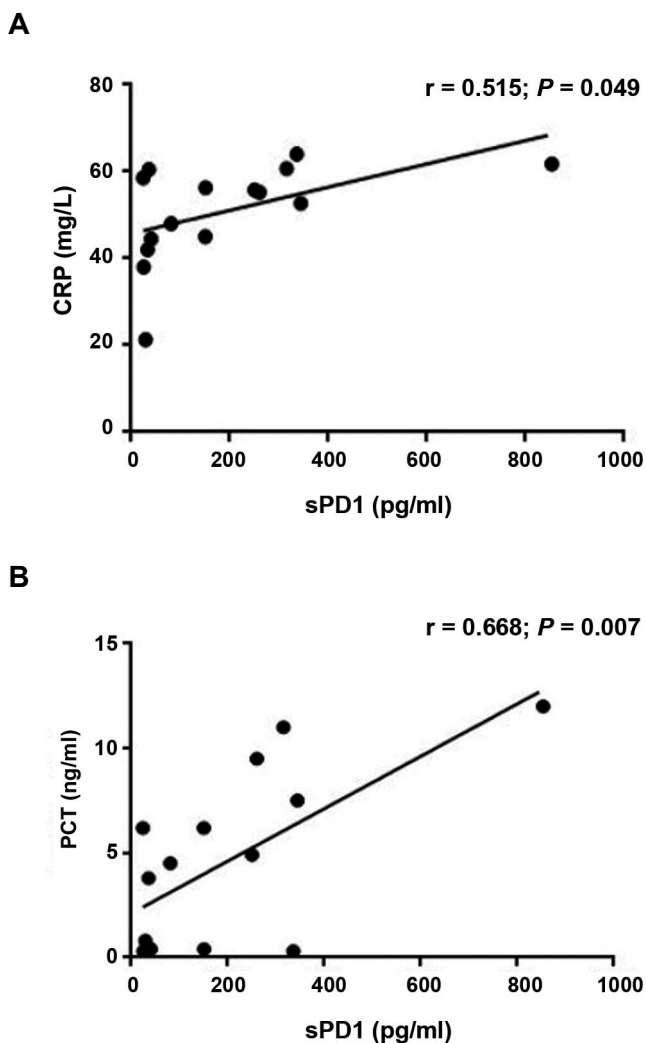


Fig.2: The correlations among sPD1, CRP, PD1, and PCT levels in septic patients. There was a significant positive correlation between the serum level of **A.** CRP and **B.** PCT with sPD1 in patients with sepsis ($n=15$). CRP; C-reactive protein and PCT; Procalcitonin.

Discussion

In the present study, we found that sPD-1 levels in patients with sepsis were higher than those who were suspected of sepsis and healthy controls. Also, sPD-1 levels were positively correlated with PCT and CRP levels. These findings suggest that this increased level might propose sPD-1 as a potential bio-marker to sepsis diagnosis.

Immune dysfunction is regularly attendant with an increased risk of death from sepsis. The latest studies indicated that pro- and anti-inflammatory reactions

occurred in sepsis concurrently, even in the early stage. With knowledge of the mechanism of immunologic response at a different stage of sepsis, it seems immunosuppression is thought-out to be the main factor affecting the outcome of septic patients (16, 17).

PD-1 is one of the best known co-inhibitory molecules. It has been observed in studies that the expression of this molecule on macrophages and peripheral blood monocytes was increased in a mouse model of sepsis, and the administration of PD1 antagonist has improved the survival of the infected animal (18, 19). According to the results of a clinical study in recent years, PD-1 expression on the surface of T lymphocytes in patients with sepsis was significantly increased (20). The inhibition of the PD-1/PD-L1 pathway with anti-PD-1 and anti-PD-L1 antibodies reduces sepsis-induced apoptosis in lymphocytes and returns the ability of immune cells to produce proinflammatory cytokines (20, 21).

The overexpression of PD-1 on the T lymphocytes or changed sPD-1 levels has been observed in patients with aplastic anemia (22), immune thrombocytopenia (ITP) (23), rheumatoid arthritis (RA) (24), or cancer (25, 26).

There are only a few studies demonstrating sPD1 levels in sepsis.

Zhao et al. (27) described that sPD-1 levels were increased in sepsis patients, and its value has also increased with increased severity of the disease. Their study showed that sPD-1 was an independent risk factor for the 28-day mortality of septic patients. Thus, sPD-1 may be used as an immunological biomarker for early assessment of the severity and prognosis of sepsis.

Yongzhen Zhao et al. (28) in another study found that peripheral blood levels of sPD-1 and sPD-L1, PD-1 expression on CD4⁺ T cells and CD8⁺ T cells and PD-L1 expression on monocytes are higher in non-survivors than in survivors sepsis, and the levels of sPD-1 and sPD-L1 have a correlation with the severity of the disease. They conclude that monitoring the concentrations of sPD-1 may improve the prognostic assessment in septic patients during the first week of treatment.

We also found that sPD-1 levels in patients with sepsis were higher than suspected and control groups. Despite the similarity of our result in this regard with other studies, the results of Lange et al. (29) study showed that sPD-1 values in patients with sepsis and septic shock were lower than control people and not related to the severity of the disease. This difference may be due to the level of sPD-1 in healthy control is higher than healthy subjects in our study, which should be further investigated in different populations. Another cause of this discrepancy may be related to differences in patient characteristics, such as age, sex, race, or even sampling time and disease status.

However, the exact function of the sPD-1 is not well known in sepsis. The increase in membrane-bound PD-1 may lead to a secondary increase in sPD-1 levels. It seems that similar to rheumatoid arthritis patients,

PD-1 and PD-L1 overexpressed, and the sPD-1/sPD-L1 concentrations also increased to prevent the regulatory effect of membrane-bound PD-1 and PDL1 (28).

It should be noted that the detection of serum sPD-1 is easier than the detection of membrane-bound PD-1 by flow cytometry and accelerates the diagnosis of disease in clinical applications.

CRP is a conventional marker used for diagnosis of sepsis and inflammation, In this study, as well as similar studies, the concentration of CRP was higher in septic and suspected compared to healthy controls (30, 31). Although some studies have shown that inflammatory factors such as CRP increase with age, in this study, the average age of participants is less than 50 years, and thus, the effect of age disappears (32).

In this study, like most similar studies, PCT levels also were significantly increased in septic and suspected patients compared to control subjects (33, 34). PCT concentrations slightly increased in bacterial infections without a systemic inflammatory response, like localized infections (35). Maybe that's why in our study, PCT levels were significantly higher in septic compared to suspected of sepsis patients.

In the study conducted by Zhao et al. (27), they found that as the disease progressed, the levels of sPD-1, CRP, and PCT gradually increased. But in another study performed by them, CRP and PCT as the inflammatory markers showed no significant correlation with sPD-1/sPD-L1 (28).

Contrary to this study, our results showed that the sPD-1 level is positively correlated with the level of CRP and PCT in patients with sepsis. Differences in the severity of disease in the patient sample could also have contributed to the differences. Our study selected patients with general sepsis, while Zhao et al. (28) selected severe sepsis and septic shock patients. Different methods of assessment also should be considered.

The sPD-1 had a higher PPV and NPV values in patients with sepsis, the specificity was higher, but the sensitivity was low. These findings are consistent with the results of a similar study and could indicate the role of sPD-1 in the diagnosis of sepsis (28).

This study had a few limitations. We measured only the sPD-1 level, and the expression of PD-1 / PD-L1 and sPDL1 was not measured. Patient follow-up was not carried out, and the sPD-1 level changes were not evaluated during the disease. The severity of the disease was not graded accurately, and we could not evaluate the correlation of other variables with the severity of the disease. Finally, this study was conducted at a center only, and further studies are needed larger sample size to confirm the results of the study.

Conclusion

Overall, the serum levels of sPD-1 were significantly

increased in patients with sepsis. The serum sPD-1 levels were positively correlated with the CRP and PCT levels in septic patients. This test was more specific than these two markers. The sPD1 correlation with inflammatory markers might propose it as a potential biomarker for the sepsis diagnosis. However, the clinical application of serum sPD-1 testing in patients with sepsis requires further investigation.

Acknowledgments

The authors wish to thank the authorities in the research council of Isfahan University of Medical Sciences. There is no financial support and conflict of interest in this study.

Author's Contributions

S.F., Z.B.; Participated in the study design. S.M., Z.B.; Contributed to all experimental. S.F.; contributed to data and statistical analysis, and interpretation of data. N.E.; Supervised the study and drafted the manuscript. Z.B.; Drafted the manuscript. All authors participated in the finalization of the manuscript and approved the final draft.

References

- Reinhart K, Daniels R, Kissoon N, Machado FR, Schachter RD, Finfer S. Recognizing sepsis as a global health priority—a WHO resolution. *N Engl J Med*. 2017; 377(5): 414-417.
- Lever A, Mackenzie I. Sepsis: definition, epidemiology, and diagnosis. *BMJ*. 2007; 335(7625): 879-883.
- Rimmelé T, Payen D, Cantaluppi V, Marshall J, Gomez H, Gomez A, et al. Immune cell phenotype and function in sepsis. *Shock*. 2016; 45(3): 282-291.
- Stearns-Kurosawa DJ, Osuchowski MF, Valentine C, Kurosawa S, Remick DG. The pathogenesis of sepsis. *Annu Rev Pathol*. 2011; 6: 19-48.
- Volk HD, Reinke P, Döcke WD. Clinical aspects: from systemic inflammation to immunoparalysis. *Chem Immunol*. 2000; 74: 162-177.
- Germain RN. Maintaining system homeostasis: the third law of Newtonian immunology. *Nat Immunol*. 2012; 13(10): 902-906.
- Evans T. Diagnosis and management of sepsis. *Clin Med (Lond)*. 2018; 18(2): 146-149.
- Sheldon IM. Detection of pathogens in blood for diagnosis of sepsis and beyond. *EBioMedicine*. 2016; 9: 13-14.
- Marshall JC, Reinhart K; International Sepsis Forum. Biomarkers of sepsis. *Crit Care Med*. 2009; 37(7): 2290-2298.
- Alkholi UM, Abd Al-Monem N, Abd El-Azim AA, Sultan MH. Serum procalcitonin in viral and bacterial meningitis. *J Glob Infect Dis*. 2011; 3(1): 14-18.
- Boomer JS, To K, Chang KC, Takasu O, Osborne DF, Walton AH, et al. Immunosuppression in patients who die of sepsis and multiple organ failure. *JAMA*. 2011; 306(23): 2594-2605
- Venet F, Monneret G. Advances in the understanding and treatment of sepsis-induced immunosuppression. *Nat Rev Nephrol*. 2018; 14(2): 121-137.
- Brown KE, Freeman GJ, Wherry EJ, Sharpe AH. Role of PD-1 in regulating acute infections. *Curr Opin Immunol*. 2010; 22(3): 397-401.
- Okazaki T, Honjo T. PD-1 and PD-1 ligands: from discovery to clinical application. *Int Immunol*. 2007; 19(7): 813-824.
- Dai S, Jia R, Zhang X, Fang Q, Huang L. The PD-1/PD-Ls pathway and autoimmune diseases. *Cell Immunol*. 2014; 290(1): 72-79.
- Xie JF, Qiu HB, Yang Y. T-cell co-inhibitory molecules in sepsis-induced immunosuppression: from bench to bedside. *Chin Med J (Engl)*. 2017; 130(10): 1249-1252.
- Hotchkiss RS, Monneret G, Payen D. Sepsis-induced immunosuppression: from cellular dysfunctions to immunotherapy. *Nat Rev Immunol*. 2013; 13(12): 862-874.
- Huang X, Venet F, Wang YL, Lepape A, Yuan Z, Chen Y, et al. PD-1 expression by macrophages plays a pathologic role in altering mi-

- icrobial clearance and the innate inflammatory response to sepsis. *Proc Natl Acad Sci USA*. 2009; 106(15): 6303-6308.
19. Brahmamdam P, Inoue S, Unsinger J, Chang KC, McDunn JE, Hotchkiss RS. Delayed administration of anti-PD-1 antibody reverses immune dysfunction and improves survival during sepsis. *J Leukoc Biol*. 2010; 88(2): 233-240
 20. Chang K, Svabek C, Vazquez-Guillamet C, Sato B, Rasche D, Wilson S, et al. Targeting the programmed cell death 1: programmed cell death ligand 1 pathway reverses T cell exhaustion in patients with sepsis. *Crit Care*. 2014; 18(1): R3.
 21. Zhang Y, Li J, Lou J, Zhou Y, Bo L, Zhu J, et al. Upregulation of programmed death-1 on T cells and programmed death ligand-1 on monocytes in septic shock patients. *Crit Care*. 2011; 15(1): R70.
 22. Wu H, Miao M, Zhang G, Hu Y, Ming Z, Zhang X. Soluble PD-1 is associated with aberrant regulation of T cells activation in aplastic anemia. *Immunol Invest*. 2009; 38(5): 408-421
 23. Birtas Atesoglu E, Tarkun P, Demirsoy ET, Geduk A, Mehtap O, Batman A, et al. Soluble Programmed death 1 (PD-1) is decreased in patients with immune thrombocytopenia (ITP): potential involvement of PD-1 pathway in ITP immunopathogenesis. *Clin Appl Thromb Hemost*. 2016; 22(3): 248-251.
 24. Greisen SR, Rasmussen TK, Stengaard-Pedersen K, Hetland ML, Hørslev-Petersen K, Hvid M, et al. Increased soluble programmed death-1 (sPD-1) is associated with disease activity and radiographic progression in early rheumatoid arthritis. *Scand J Rheumatol*. 2014; 43(2): 101-108
 25. Xiao H, Huang B, Yuan Y, Li D, Han LF, Liu Y, et al. Soluble PD-1 facilitates 4-1BBL-triggered antitumor immunity against murine H22 hepatocarcinoma in vivo. *Clin Cancer Res*. 2007; 13(6): 1823-1830.
 26. Cheng H-Y, Kang P-J, Chuang Y-H, Wang Y-H, Jan M-C, Wu C-F, et al. Circulating programmed death-1 as a marker for sustained high hepatitis B viral load and risk of hepatocellular carcinoma. *PLoS One*. 2014; 9(11): e95870.
 27. Zhao Y, Jia Y, Li C, Fang Y, Shao R. The risk stratification and prognostic evaluation of soluble programmed death-1 on patients with sepsis in emergency department. *Am J Emerg Med*. 2018; 36(1): 43-48.
 28. Zhao Y, Jia Y, Li C, Shao R, Fang Y. Predictive value of soluble programmed death-1 for severe sepsis and septic shock during the first week in an intensive care unit. *Shock*. 2019; 51(3): 289-297.
 29. Lange A, Sunden-Cullberg J, Magnuson A, Hultgren O. Soluble B and T lymphocyte attenuator correlates to disease severity in sepsis and high levels are associated with an increased risk of mortality. *PLoS One*. 2017; 12(1): e0169176
 30. Henriquez-Camacho C, Losa J. Biomarkers for sepsis. *Biomed Res Int*. 2014; 2014: 547818.
 31. Kibe S, Adams K, Barlow G. Diagnostic and prognostic biomarkers of sepsis in critical care. *J Antimicrob Chemother*. 2011; 66 Suppl 2: ii33-ii40.
 32. Wyczalkowska-Tomasik A, Czarkowska-Paczek B, Zielenkiewicz M, Paczek L. Inflammatory markers change with age, but do not fall beyond reported normal ranges. *Arch Immunol Ther Exp (Warsz)*. 2016; 64(3): 249-254.
 33. Vijayan AL, Vanimaya, Ravindran S, Saikant R, Lakshmi S, Kartik R, et al. Procalcitonin: a promising diagnostic marker for sepsis and antibiotic therapy. *J Intensive Care*. 2017; 5: 51.
 34. Adib M, Bakhshiani Z, Navaei F, Saheb Fosoul F, Fouladi S, Kazemzadeh H. Procalcitonin: a reliable marker for the diagnosis of neonatal sepsis. *Iran J Basic Med Sci*. 2012; 15(2): 777-782.
 35. Morgenthaler NG, Struck J, Fischer-Schulz C, Seidel-Mueller E, Beier W, Bergmann A. Detection of procalcitonin (PCT) in healthy controls and patients with local infection by a sensitive ILMA. *Clin Lab*. 2002; 48(5-6): 263-270.

lncRNA *PVT1* Promotes Metastasis of Non-Small Cell Lung Cancer Through EZH2-Mediated Activation of Hippo/NOTCH1 Signaling Pathways

Shang-Gan Zeng, M.D.¹, Jian-Hong Xie, B.Sc.², Qun-Ying Zeng, B.Sc.², Shao-Hua Dai, M.D.¹, Yun Wang, B.Sc.¹,
Xue-Mei Wan, B.Sc.³, Ji-Chun Liu, M.D.^{3*}

1. Department of Thoracic Surgery, The First Affiliated Hospital of Nanchang University, Nanchang 330006, P.R China

2. Department of Surgery, Suichuan People's Hospital, Ji'an 343900, P.R China

3. Department of Cardiovascular Surgery, The First Affiliated Hospital of Nanchang University, Nanchang, 330006, P.R China

*Corresponding Address: P.O.Box: 330006, Department of Cardiovascular Surgery, The First Affiliated Hospital of Nanchang University, No. 17, Yongwaizheng Street, Nanchang, 330006, Jiangxi Province, P.R China
Email: liujichun999@163.com

Received: 14/June/2019, Accepted: 3/November/2019

Abstract

Objective: Although growing evidences have showed that long non-coding RNA (lncRNAs) plasmacytoma variant translocation 1 (*PVT1*) plays a critical role in the progression of non-small cell lung cancer (NSCLC), there are still many unsolved mysteries remains to be deeply elucidated. This study aimed to find a new underlying mechanism of *PVT1* in regulating the tumorigenesis and development of NSCLC.

Materials and Methods: In this experimental study, Quantitative reverse transcription polymerase chain reaction (qRT-PCR) was used to profile the expression of *PVT1* in NSCLC tissues and cells. The effects of *PVT1* on cell growth, migration and invasion were detected by colony formation assay, Matrigel-free transwell and Matrigel transwell assays, respectively. Changes of the key protein expression in Hippo and NOTCH signaling pathways, as well as epithelial-mesenchymal transition (EMT) markers, were analyzed using western blot. Interaction of *PVT1* with enhancer of zeste homolog 2 (EZH2) was verified by RNA pull-down, and their binding to the downstream targets was detected by Chromatin Immunoprecipitation (ChIP) assays.

Results: These results showed that *PVT1* was up-regulated in NSCLC tissue and cell lines, promoting NSCLC cell proliferation, migration and invasion. Knockdown of *PVT1* inhibited the expression of Yes-associated protein 1 (YAP1) and NOTCH1 signaling activation. Further, we have confirmed that *PVT1* regulated expression of YAP1 through EZH2-mediated *miR-497* promoter methylation resulting in the inhibition of *miR-497* transcription and its target YAP1 upregulation, and finally NOTCH signaling pathway was activated, which promoted EMT and invasion and metastasis.

Conclusions: These results suggested that lncRNA *PVT1* promotes NSCLC metastasis through EZH2-mediated activation of Hippo/NOTCH1 signaling pathways. This study provides a new opportunity to advance our understanding in the potential mechanism of NSCLC development.

Keywords: EZH2, miR-497, NSCLC, *PVT1*, YAP1

Cell Journal (Yakhteh), Vol 23, No 1, April-June (Spring) 2021, Pages: 21-31

Citation: Zeng ShG, Xie JH, Zeng QY, Dai SH, Wang Y, Wan XM, Liu JCh. lncRNA *PVT1* promotes metastasis of non-small cell lung cancer through EZH2-mediated activation of hippo/NOTCH1 signaling pathway. Cell J. 2021; 23(1): 21-31. doi: 10.22074/cellj.2021.7010.

This open-access article has been published under the terms of the Creative Commons Attribution Non-Commercial 3.0 (CC BY-NC 3.0).

Introduction

Lung cancer is the leading cause of cancer-related death worldwide (1). The most common type of that is non-small cell lung cancer (NSCLC), which accounts for approximately 85% of all lung cancer new cases (2). The average 5-year survival rate of NSCLC cancer patients is still very low, because of the limited therapeutic options, I addition to the higher rate of tumor metastasis and recurrence (2).

Yes-associated protein 1 (YAP1) is highly expressed in NSCLC tissues and cells. It can positively regulate expression of NOTCH1, affecting proliferation, invasion and metastasis ability as well as drug sensitivity in lung cancer cells (3). Our previous work proved that YAP, a core transcription co-activator in Hippo signaling pathway, was overexpressed in NSCLC tissues and cells, positively regulated expression of NOTCH1 and markedly promoted cell proliferation and invasion (4). These results indicated

that Hippo and NOTCH signaling pathways played an important role in development of NSCLC. However, the specific molecular mechanisms of these two signaling pathways in NSCLC tumorigenesis and development are not fully understood yet.

Long non-coding RNAs (lncRNAs) are non-coding transcripts with longer than 200 nucleotides, which exhibit various functions and regulate different processes by many molecular mechanisms (5). Growing evidences suggest that lncRNAs participate in the development and progression of NSCLC. *MALAT1* was reported to be a predictive marker for NSCLC metastasis development (6), while elevated expression of LINC00473 correlated with poor prognosis of NSCLC (7). Plasmacytoma variant translocation 1 (*PVT1*), a lncRNA that shares the location of chr8q24.21 with *c-Myc* (8). It is highly expressed and exerts a carcinogenic effect in many

tumors, such as NSCLC (9), colorectal cancer (10) and hepatocellular carcinoma (11). Recently, it was reported that *PVT1* recruited enhancer of zeste homolog 2 (*EZH2*) to the large tumor suppressor kinase 2 (*LATS2*) promoter and repressed its transcription (9). Therefore, *PVT1* knockdown could inhibit proliferation and induce apoptosis in NSCLC (9).

LATS2 plays a pivotal role in regulating Hippo growth inhibitory signaling (12). Recent study showed that *LATS2* inhibition decreased YAP1 phosphorylation. It promoted nuclear accumulation of YAP1 and upregulated the association of YAP1/ TEAD domain transcription factor 2 (*TEAD2*), which led to transcriptional activation of YAP1/*TEAD2* (12). These results indicated that lncRNA *PVT1* may inhibit Hippo signaling by silencing *LATS2*, and it plays a crucial role in promoting proliferation and anti-apoptosis. It was also reported that knockdown of lncRNA *PVT1* inhibited cell viability, invasion and induced apoptosis in NSCLC by regulating *miR-497* expression (13). However, the mechanism by which lncRNA *PVT1* inhibits *miR-497* still needs to be elucidated.

NOTCH signaling was reported to be altered in approximately one third of NSCLCs (14). Numerous studies have also suggested that activation of NOTCH correlates with poor clinical outcomes in NSCLC patients without *TP53* mutations and it is a biomarker for predicting survival time in patients with NSCLC (15). However, mechanism of NOTCH1 up-regulation is not well understood (14). An interacting network of the Hippo and NOTCH signaling pathways that control organ size and hepatocellular carcinoma (HCC) development was also identified (16). NOTCH and Hippo signaling was also showed to synergize to potentiate liver cell growth and remodel (17). Jagged-1 and NOTCH2, two NOTCH pathway components, are downstream targets of Hippo signaling. They lead to the dedifferentiation of hepatocytes into hepatic progenitors (18). Besides, YAP-dependent activity of Jag1 and Notch were also reported to correlate with survival times in human HCC and colorectal tumor samples (19). YAP1 can also contribute to progression and poor prognosis of NSCLC (4). Thus, we hypothesized that under the mediation of *TEAD1*, YAP1 is most likely a NOTCH1 upstream driver gene. We proposed hypotheses that lncRNA *PVT1* interacts with *EZH2* to silence the expression of *miR-497* and *LATS2* genes. Thus, it promotes YAP1 transcription and inhibits phosphorylation of YAP1, thereby activating NOTCH1 signaling and enhancing the invasion of NSCLC cells.

Materials and Methods

Tissue collection

This experimental study was approved by the Ethics

Committee (Code No.: 20180521) of the First Affiliated Hospital of Nanchang University (Nanchang, China). Written informed consents were obtained from all patients. Thirty paired primary tumor tissues and adjacent tissues from these NSCLC patients were obtained. Clinical-pathological characteristics were recorded. No local or systemic treatment was conducted in these patients before surgery. All samples were immediately snap-frozen in liquid nitrogen and stored at -80°C , until required.

Cell lines and cell culture

Human NSCLC cell lines A549, H1299, Calu-3, H1975 and PC-9 as well as human bronchial epithelial cells BEAS-2B were obtained from the American Type Culture Collection (ATCC, USA), cultured in their corresponding medium containing 10% FBS (Gibco, USA), 100 $\mu\text{g}/\text{ml}$ streptomycin (HyClone, USA) and 100 U/ml penicillin (HyClone) and incubated at 37°C in the presence of 5% CO_2 .

RNA extraction and quantitative reverse transcription PCR

Trizol reagent (Invitrogen, USA) was used to extract total RNA from tissue specimens and cell samples. First-strand cDNA was generated by ImProm-II Reverse Transcription System (Promega, USA). Then, SYBR Green qPCR assay (Takara, Japan) and gene-specific primers (Table 1) were used for quantitative reverse transcription PCR (qRT-PCR) analysis. *GAPDH* or *U6* was used as internal references for normalization. The relative expression levels of target genes were calculated using the comparative Ct method.

Plasmid generation and cell transfection

The *PVT1* sequence was synthesized and sub-cloned into the pcDNA3.1 vector (Invitrogen, USA) by GenePharma (Shanghai, China). The siRNAs directly against human

PVT1 gene (si-PVT1-1:

5'-CCTGTTACACCTGGGATT-3';

si-PVT1-2: 5'-GGACTTGAGAACTGTCCTT-3';

si-PVT1-3: 5'-CCTGGGATTTAGGCACTT-3'),

EZH2 gene (si-EZH2:

5'-CATCGAAAGAGAAATGGAATT-3'),

YAP1 gene (si-YAP1:

5'-AGAAGCTTTCGGCAGGAG-3')

were also designed and synthesized by GenePharma (Shanghai, China). si-NC (5'-UUCUCCGAACGUGU-CACGUTT-3') was used as a negative control. Plasmid vectors and siRNA oligonucleotides were transfected into H1299 or A549 cells with Lipofectamine 3000 (Invitrogen, USA) according to the manufacturer's instructions. Forty-eight hours after transfection, the cells were harvested for qRT-PCR or western blot analysis.

Table 1: Paired primer sequences used in qRT-PCR

Genes	Paired primers	Sequences (5'-3')
<i>PVT1</i>	sense	CTTGCGGAAAGGATGTTGGC
	antisense	GCCATCTTGAGGGGCATCTT
<i>YAP1</i>	sense	TTCGGCAGGCAATACGGAAT
	antisense	GTTGAGGAAGTCGTCTGGGG
<i>TEAD1</i>	sense	CCCTGGCTATCTATCCACCA
	antisense	AGGGCCTTATCCTTTGCAGT
<i>NOTCH1</i>	sense	GCACGTGTATTGACGACGTTG
	antisense	GCAGACACAGGAGAAGCTCTC
<i>LATS2</i>	sense	ACAAGATGGGCTTCATCCAC
	antisense	CTCCATGCTGTCCTGTCTGA
<i>EZH2</i>	sense	AAGCACAGTGCAACACCAAG
	antisense	CAGATGGTGCCAGCAATAGA
<i>GAPDH</i>	sense	CCAGGTGGTCTCCTCTGA
	antisense	GCTGTAGCCAAATCGTTGT
<i>miR-497</i>	RT	GTCGTATCCAGTGCAGGGTCCGAGGTATTTCGACTGGATACGACACAAAC
	sense	GCGCAGCAGCACACTGTG
	antisense	GTGCAGGGTCCGAGGT
<i>U6</i>	sense	CTCGCTTCGGCAGCACA
	antisense	AACGCTTACGAATTTGCGT

Methylation-specific PCR

Methylation analysis of miR-497 promoter was examined by Methylation-specific PCR (MSP). MethPrimer 1.0 was used to design MSP primers. A pair of methylation-specific primers (M-F: 5'-TTTGATTTAGGGAGAGGAAGGAC-3'; M-R: 5'-TAAACAAACA ACTAAAAACGACGA-3') and a pair of unmethylation-specific primers at the same site (U-F: 5'-TTTGATTTAGGGAGAGGAAGGAT-3'; M-R: 5'-TAAACAAACA ACTAAAAACAACAAA-3') were chosen. Briefly, the isolated genomic DNA was treated with sodium bisulfite using an EZ DNA Methylation Gold kit (Zymo Research, USA). They were then subjected to PCR assay using the specific primers. The PCR products were digested with a restriction endonuclease BstUI, recognizing sequences unique to the methylated alleles, but not unmethylated alleles. The digested products were next electrophoresed on 3% agarose gels and stained with ethidium bromide. The ratio of gray scale value of the methylated band was calculated as methylation levels.

In vitro transcription and RNA pull-down assay

In vitro transcription and RNA pull-down assay were performed as described before (20). Briefly, biotin-labeled lncRNA *PVT1* was transcribed with T7 RNA polymerase by TranscriptAid T7 High Yield Transcription Kit (Thermo Fisher Scientific, USA) *in vitro*. For RNA pull-down assay, 5 µg of biotin-labeled synthesized RNA was added to the RNA structure buffer (10 mM Tris pH=7, 0.1 M KCl, 10 mM MgCl₂) to ensure the formation of proper secondary structure. Following the indicated treatment, the cell samples were collected and their extracts were then mixed with biotin-labeled RNA. They were next rotated at room temperature for one hour, and then 50 µl of streptavidin-agarose beads were added to the mixture and rotated for one hour. After incubation, the beads were washed briefly twice with high-salt RNA Binding Protein Immunoprecipitation (RIP) buffer (containing 500 mM KCl, 25 mM Tris pH=7.4, 0.5 mM DTT, 0.5% NP40, 1 mM PMSF and protease inhibitor), then twice with low-salt RIP buffer (composed of 150 mM KCl, 25 mM Tris pH 7.4, 0.5 mM DTT, 0.5% NP40, 1 mM PMSF and protease

inhibitor), and lastly boiled in SDS-loading buffer for 10 minutes. The retrieved proteins were detected by means of western blotting.

Colony formation assay

Cells after transfection were collected at logarithmic growth phase. Then, they were placed in a 6-well plate (1×10^3 /well) for two weeks. 4% paraformaldehyde was used to fix the cells for 15 minutes after discarding the medium, and Giemsa solution was added to stain for 5 minutes. The cells were then quantified by photographing three independent visual fields under the microscope.

Chromatin immunoprecipitation assays

ChIP assays were conducted using the SimpleChIP® Plus Enzymatic Chromatin IP Kit, according to the manufacturer's instructions (CST, USA). H3 trimethyl Lys 27 antibody was obtained from Millipore (USA). EZH2 (5246) antibody was obtained from CST. Quantification of immunoprecipitated DNA was performed by quantitative PCR (qPCR). ChIP data were calculated as a percentage relative to the input DNA.

Transwell migration assay

8 mm pore 24-well transwell chambers (Corning, USA) were used for migration assay. 2×10^4 A549 or H1299 cells were seeded into the chambers and cultured with DMEM for 48 hours. Then, took out membranes at the bottom of chambers, and removed the cells on the upper membrane surface using a cotton swab. The cells on the lower surface of membrane surface were fixed with methanol and glacial acetic acid, at the ratio of (3:1) and they were stained with 10% Giemsa solution. Finally, five fields were selected randomly and counted for statistical analysis in each groups.

In vitro Matrigel invasion assay

Before seeding cells, the poly-carbonate membranes of the transwell upper chambers (8 μ m pore size; Corning, USA) was pre-coated with Matrigel (BD, USA). Then, 4×10^5 cells, re-suspended in 200 μ l serum-free medium, were placed in the upper chamber, followed by adding 600 μ l of the same medium to the lower chamber. Then, the cells on the upper membrane surface were removed after 48 hours incubation at 37°C. Meanwhile, the cells on the lower membrane surface were fixed with methanol and glacial acetic acid (3:1). They were next stained with 10% Giemsa solution. Finally, five fields selected randomly and counted for statistical analysis in each groups.

Western blot analysis

The cells were harvested and protein was isolated by IP lysis buffer (Thermo Fisher Scientific, USA) containing protease inhibitors (Roche, Switzerland). Then, the BCA Assay Kit (Thermo Fisher Scientific) was used to assess the concentration of proteins in the supernatants of cell lysates. Next, 10% SDS-PAGE gel electrophoresis was

applied for separation of equal amount of protein samples. Then, they were transferred to PVDF membranes, which was later incubated with a specific primary antibody followed by incubating with secondary antibody marked by horseradish peroxidase (goat anti-rabbit; Abcam) at room temperature for one hour. Optical density method was used for quantitative autoradiography with β -actin (1:3000; Proteintech, USA), as controls.

Statistical analysis

Prism 6.0 (GraphPad Software, USA) was used for statistical analysis of data. All experiments were performed at least three times in triplicate. Data were expressed as the mean \pm standard deviation (SD). Student's t test (two tailed) and one-way analysis of variance (ANOVA) were used to evaluate the significant difference. $P < 0.05$ was considered to be significantly different.

Results

lncRNA PVT1 was upregulated in NSCLC tissues and cell lines, promoting cell proliferation, migration and invasion

To investigate the role of *PVT1* in NSCLC, we first analyzed expression pattern of this lncRNA in 30 NSCLC and adjacent normal tissues using qRT-PCR. Results showed that *PVT1* level in NSCLC tissues was significantly higher than the adjacent normal tissues (Fig.1A), indicating that *PVT1* may be involved in NSCLC progression. Similar results were obtained in NSCLC cell lines. *PVT1* expression in A549, H1299, Calu-3, H1975 and PC-9 cells was much higher than in BEAS-2B cells (Fig.1B). To examine whether *PVT1* was functionally involved in NSCLC, we selected NSCLC cells A549 and H1299 for further explorations. qRT-PCR assay was performed to determine efficiency of *PVT1* siRNA (applied for knockdown) and *PVT1* plasmid (used for overexpression). The results showed that *PVT1* expression was sufficiently downregulated after transfecting with the three siRNAs, and it was successfully upregulated after *PVT1* plasmid transfection of both A549 and H1299 cells (Fig.1C). The most efficient si-PVT1-3 (collectively referred to as si-*PVT1* hereinafter) was selected for *PVT1* knockdown in the follow-up experiments. Then, colony formation assays were carried out to determine its effect on cell proliferation. It was determined that *PVT1* knockdown significantly inhibited cell proliferation, while *PVT1* overexpression significantly promoted cell proliferation (Fig.1D). Next, we evaluated the effects of *PVT1* on cell migration and invasion. As expected, the decreased expression of *PVT1* expression caused suppression of cell migration (Fig.1E) and invasion (Fig.1F), while *PVT1* overexpression promoted cell migration (Fig.1E) and invasion (Fig.1F). Taken together, these findings implied that lncRNA *PVT1* may function as an oncogene to promote tumorigenesis and development of NSCLC.

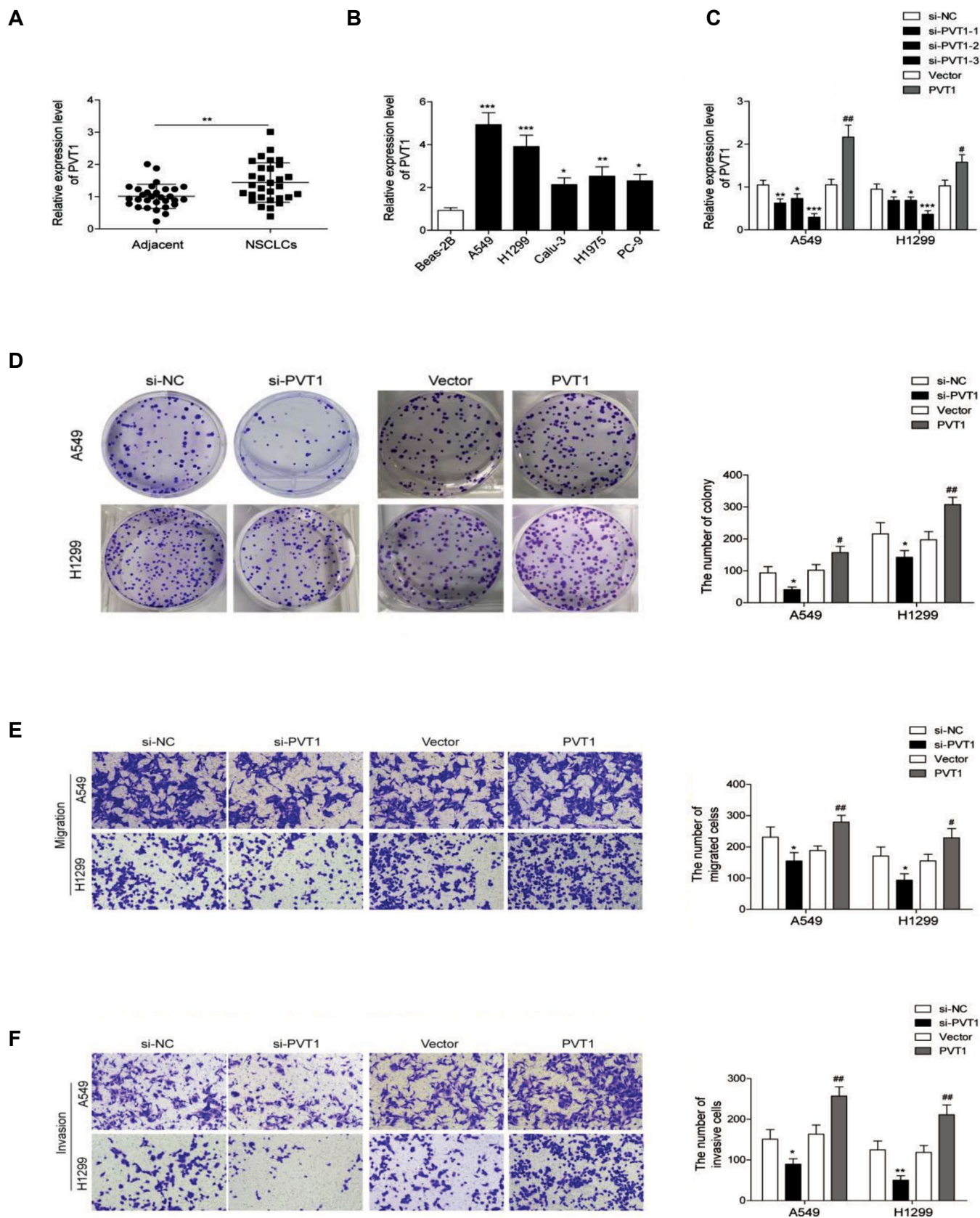


Fig.1: long non-coding RNAs (lncRNAs) plasmacytoma variant translocation 1(*PVT1*) was up-regulated in non-small cell lung cancer (NSCLC) tissues and cells, promoting NSCLC cell invasion and migration. **A.** quantitative reverse transcription polymerase chain reaction (qRT-PCR) analysis for the expression of *PVT1* in the NSCLC and adjacent normal tissues (n=30). **B.** qRT-PCR analysis for the expression of *PVT1* in five NSCLC cell lines compared to the normal lung epithelial cells, BEAS-2B. **C.** qRT-PCR analysis for the expression of *PVT1* in A549 and H1299 cells transfected with three siRNAs of *PVT1* (si-PVT1-1, si-PVT1-2 and si-PVT1-3) or the negative control (si-NC) as well as pcDNA-*PVT1* overexpression vector (*PVT1*) and pcDNA vector (vector). **D.** Colony formation assays were used to assess proliferation of A549 and H1299 cells after *PVT1* knockdown and *PVT1* overexpression. **E.** Matrigel-free transwell assay for cell migration and **F.** Matrigel transwell assay for cell invasion were confirmed in A549 and H1299 cells after *PVT1* knockdown by siRNAs transfection and *PVT1* overexpression. Data are mean \pm SD of three independent experiments. *, $P < 0.05$, **, $P < 0.01$, ***, $P < 0.001$ compared to si-NC group, #, $P < 0.05$, and ##, $P < 0.01$; #, $P < 0.01$ compared to the vector group. *PVT1* knockdown inhibited expression of yes-associated protein 1 (YAP1) and NOTCH1 signaling activation.

Hippo/YAP and NOTCH signaling pathways are associated with the occurrence and development of NSCLC (21). Western blot analysis demonstrated that protein levels of LAST2 and relative phosphorylated YAP1 were significantly down-regulated in NSCLC tissues than that of the adjacent tissues, while total YAP1, TEAD and NOTCH1 proteins were up-regulated in NSCLC tissues than that of the adjacent tissues (Fig.2A), indicating that the Hippo pathway was suppressed, promoting NOTCH signaling pathway activation in NSCLC tumorigenesis. Furthermore, we further investigated the effects of lncRNA *PVT1* on those pathways by siRNA knockdown experiments. Results of qRT-PCR analysis showed that mRNA expression levels of *YAP1*, *TEAD1* and *NOTCH1* were decreased obviously in A549 and H1299 cells after *PVT1* knockdown by siRNA treatment, except the mRNA level of *LAST2* which was up-regulated in si-*PVT1* group than the si-NC group in the A549 and H1299 cells (Fig.2B). Results of western blot analysis showed that LAST2 protein and phosphorylated YAP1 were significantly up-regulated while total YAP1, TEAD1 and NOTCH1

proteins were down-regulated after *PVT1* knockdown (Fig.2C). Taken together, our results demonstrated that *PVT1* knockdown could inhibit expression of YAP1 and NOTCH1 signaling activation.

Previous report found that knockdown of *PVT1* effectively promoted *miR-497* expression (13). To verify it, we detected *miR-497* expression levels after *PVT1* knockdown or overexpression in A549 and H1299 cells using qRT-PCR. Results showed that expression of *miR-497* was negatively regulated by *PVT1* (Fig.2D). To determine the role of lncRNA *PVT1* in regulating methylation, *miR-497* promoter methylation analysis was performed in the NSCLC and adjacent tissues by MSP. Results showed that methylation level of *miR-497* promoter was higher in the NSCLC tumor tissues than the adjacent tissues (Fig.2E), indicating that DNA methylation modification of *miR-497* promoter was occurred by tumorigenesis, which may be one reason for the low expression level of *miR-497* in NSCLC and it may also be one of results of lncRNA-mediated methylation.

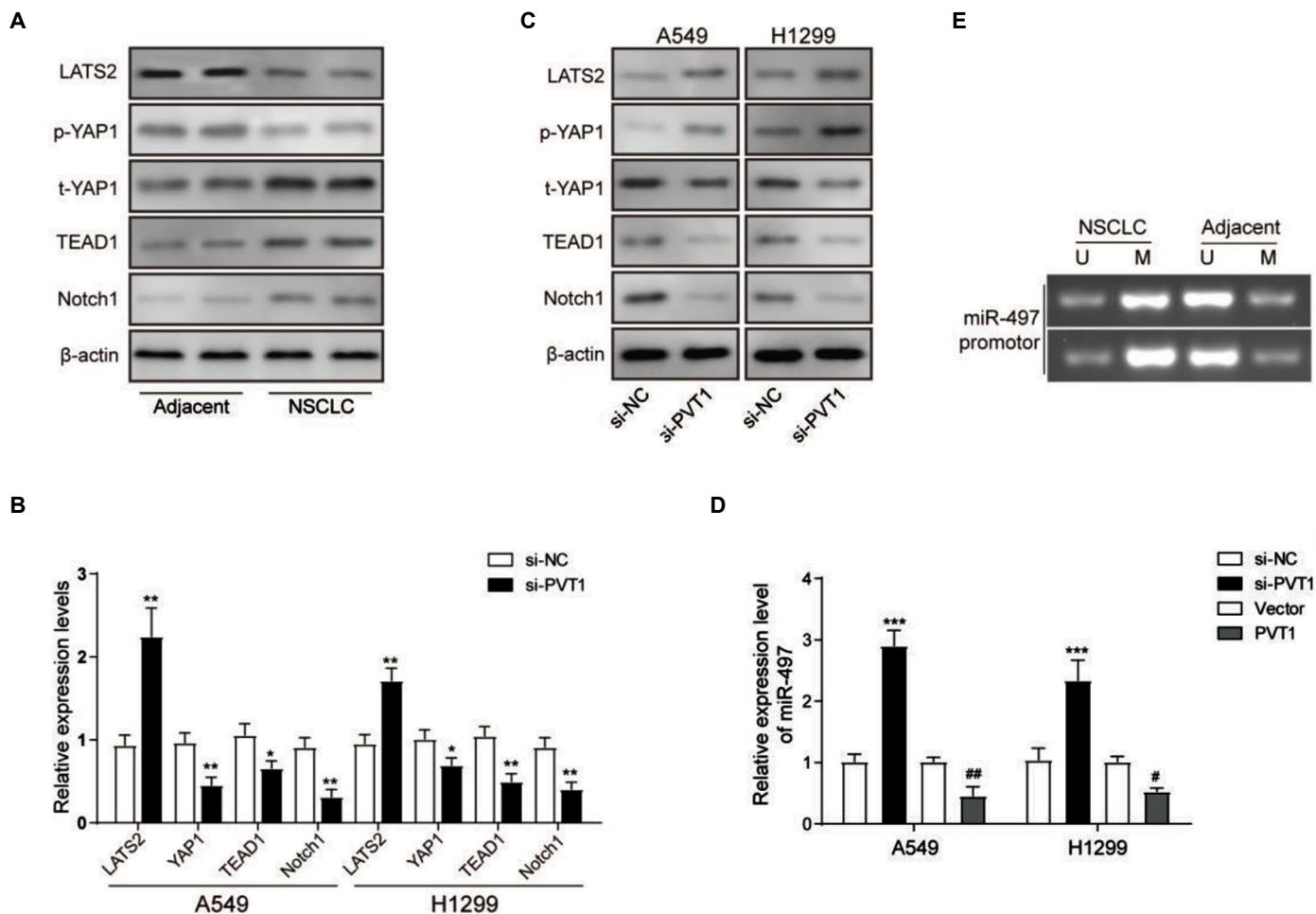


Fig.2: Plasmacytoma variant translocation 1(*PVT1*) knockdown inhibited yes-associated protein 1 (YAP1) expression and Notch1 signaling activation. Western blot analysis for protein levels of LAST2, p-YAP1, t-YAP1, TEAD and Notch1 in the NSCLC and adjacent normal tissues. **B.** Quantitative reverse transcription polymerase chain reaction (qRT-PCR) analysis for mRNA expression levels of *LAST2*, *YAP1*, *TEAD* and *Notch1* in A549 and H1299 cells after *PVT1* knockdown using the treatment with si-*PVT1* or si-NC. **C.** Western blot analysis for protein levels of LAST2, p-YAP1/t-YAP1, TEAD and Notch1 in A549 and H1299 cells after *PVT1* knockdown by treatment with si-lnc*PVT1* or siRNA negative control (si-NC). **D.** qRT-PCR analysis for the expression of microRNA-497(*miR-497*) in A549 and H1299 cells after *PVT1* knockdown or overexpression. **E.** MSP analysis for the methylation level of *miR-497* promoter. Data are mean \pm SD of three independent experiments. *, P<0.05, **, P<0.01 compared to si-NC group; ##, P<0.01 compared to vector group, p-YAP1; Phosphorylated YAP1 protein, t-YAP1; Total YAP1 protein, si-NC; siRNA negative control, si-*PVT1*; *PVT1* siRNA for knockdown, Vector; Empty pcDNA vector for negative control of overexpression, A549 and H1299; Two of human lung carcinoma cell lines, MSP; Methylation-specific polymerase chain reaction, LAST2; Large tumor suppressor kinase 2 protein, and SD; Standard deviation.

PVT1 directly interacted with *EZH2* in NSCLC cells

EZH2 is the functional enzymatic component of the polycomb repressive complex 2 (PRC2) and it has been linked to many forms of cancer. lncRNA *PVT1* was reported to modulate thyroid cancer cell proliferation by recruiting *EZH2*. To confirm whether *PVT1* could also interact with *EZH2* in NSCLC, expression profile of *EZH2* in clinic and cell levels were measured by qRT-PCR and western blot. The probable interaction between them was further verified using RNA pull-down assay. Results showed that *EZH2* was significantly up-regulated in NSCLC tissues and cell lines compared to the normal one in both mRNA and protein levels (Fig.3A, B). RNA pull-down analysis identified the interaction between *PVT1* and *EZH2* which was successfully pulled-down by a biotin-labeled *PVT1* probe in the A549 cell samples (Fig.3C). RNA pull-down experiments of the cell samples after transfecting with si-*PVT1* or siRNA-NC and culturing for 48 hours further proved these findings. Compared to the si-NC group, the level of *EZH2* in the si-*PVT1* group was reduced significantly along with *PVT1* knockdown (Fig.3D). All of these results have indicated that *PVT1* directly interacted with *EZH2* in NSCLC.

PVT1 regulated the expression of *YAP1* through *EZH2*-mediated *miR-497* promoter methylation

lncRNA *PVT1* was reported to recruit *EZH2* into the promoter of target genes to induce methylation, therefore inhibiting transcription of the target genes. As *PVT1* could down-regulate *LAST2* and up-regulate *YAP1*, we wondered whether it was involved in the regulation of methylation. First, we suppressed the expression of *EZH2* using siRNAs

in A549 and H1299 cells to confirm relationship of *EZH2* and *YAP1* expression levels. As results shown in Figure 4A, the mRNA expression level of *EZH2* was successfully suppressed by si-*EZH2* in the both cell lines, while expression of *miR-497* was inversely increased after *EZH2* knockdown, and *YAP1*, a known target gene of *miR-497*, was downregulated along with the upregulation of *miR-497* (Fig.4B). To verify the interaction between *EZH2* with *miR-497* promoter, ChIP assays using *EZH2* and H3K27me3 antibodies were performed. The qPCR results of *miR-497* promoter indicated that *EZH2* could directly bind to the *miR-497* promoter region and mediate H3K27me3 modification, and the *PVT1* overexpression promoted these interactions (Fig.4C). Moreover, we detected methylation modification of the *miR-497* promoter with MSP after *EZH2* knockdown or 5-Aza-dC treatment- an inhibitor commonly used for DNA methylation. Results showed that methylation level of the *miR-497* promoter was significantly decreased in A549 and H1299 cells in si-*EZH2* and 5-Aza-dC groups compared to the control group (Fig.4D), further suggesting that expression of the *miR-497* may be regulated by *EZH2* through DNA methylation of the corresponding microRNA promoter. Besides, after treatment with DNA methylation inhibitor 5-Aza-dC, expression of *miR-497* was increased obviously. This could be inverted by combined treatment with *PVT1* overexpression, while the changes of *YAP1* expression were on the contrary (Fig.4E). As expected, the protein levels of *LAST2* and phosphorylated *YAP1* were significantly upregulated after 5-Aza-dC treatment, which could be inverted by *PVT1* overexpression (Fig.4F). Taken together, these results indicated that *PVT1* regulated expression of *miR-497* and *YAP1* through *EZH2*/H3K27me3-mediated *miR-497* promoter methylation modification.

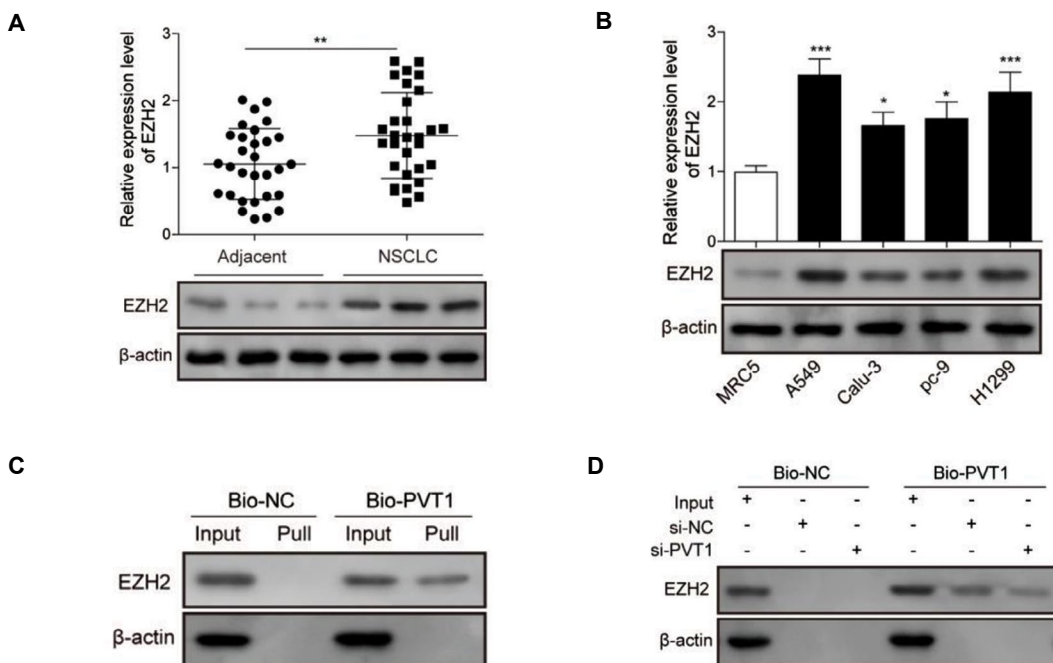


Fig.3: Long non-coding RNAs (lncRNAs)-plasmacytoma variant translocation 1(*PVT1*) directly interacted with enhancer of zeste homolog 2 (*EZH2*) in non-small cell lung cancer (NSCLC). **A.** Quantitative reverse transcription polymerase chain reaction (qRT-PCR) and western blot analysis, respectively for the mRNA and protein expression levels of *EZH2* in the NSCLC and adjacent normal tissues (n=30). **B.** qRT-PCR and western blot analysis, respectively for the mRNA and protein expression levels of *EZH2* in NSCLC cell lines compared to the normal lung epithelial cells, BEAS-2B. **C.** Relationship between lncRNA *PVT1* and *EZH2* verified in A549 cells by RNA pull-down and western blot assays using a biotin-labeled probe of *PVT1* (bio-*PVT1*). **D.** RNA pull-down and western blot assays used to verify the *PVT1* effect on *EZH2* level after *PVT1* knockdown by treating with si-*PVT1* or si-NC in A549 cells. Data are mean \pm SD of three independent experiments. *, $P < 0.05$, **, $P < 0.01$, ***, $P < 0.001$ compared to the adjacent group or MRC5 group. si-NC; siRNA negative control, Bio-NC; Biotin-labeled negative control, Pull; Pull-down group, and SD; Standard deviation.

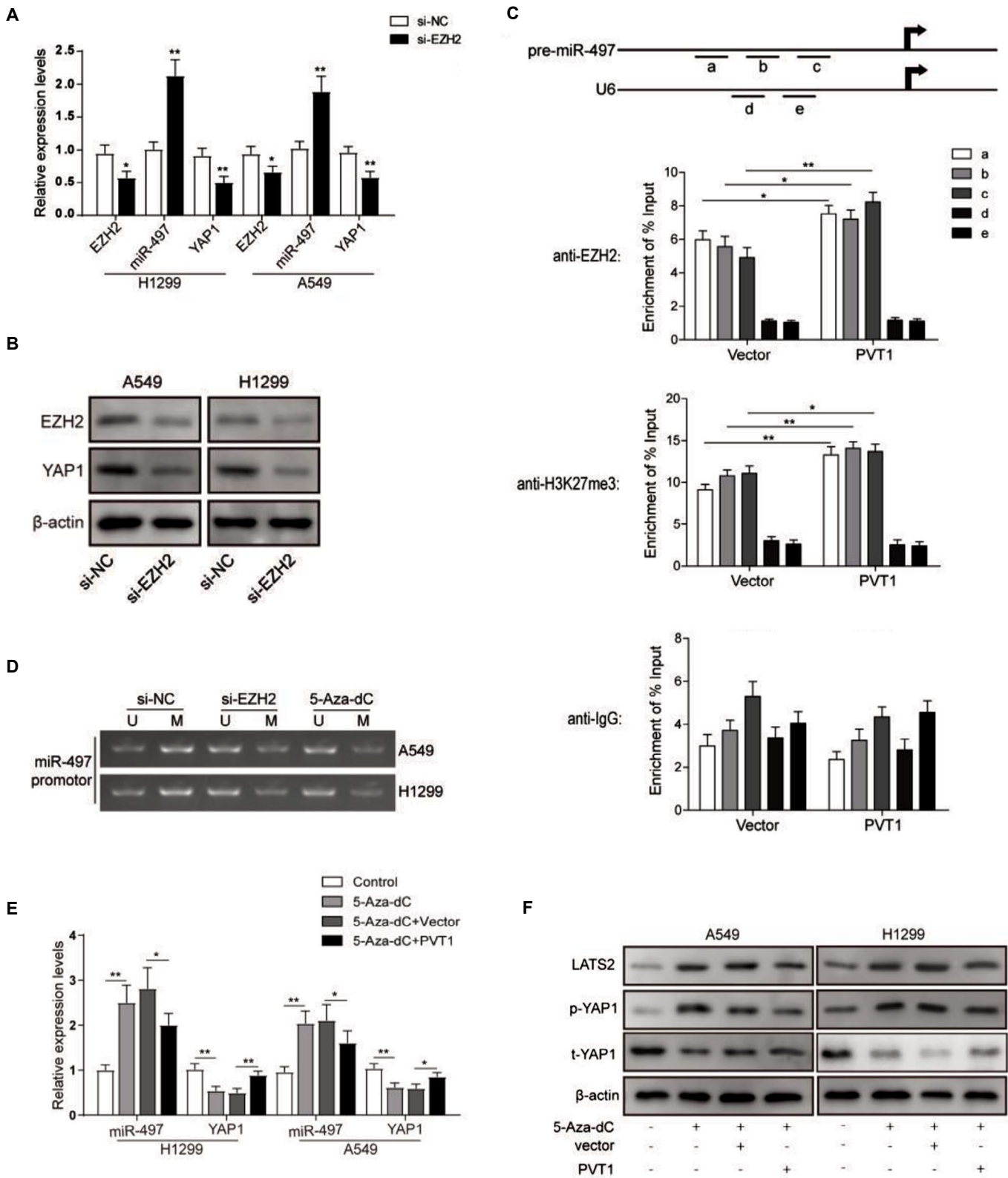
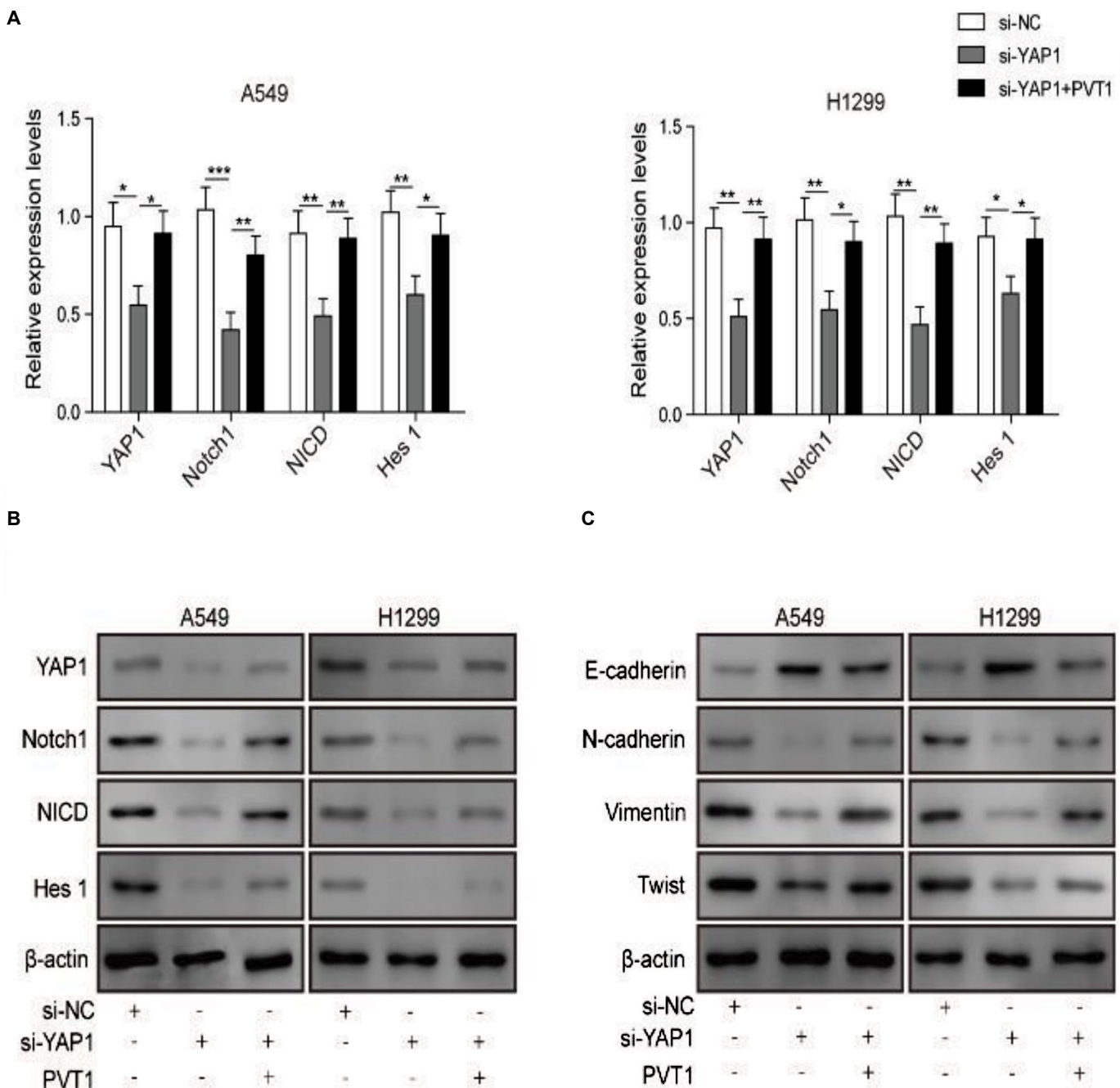


Fig.4: pcDNA-PVT1 vector for overexpression (PVT1) regulated expression of yes-associated protein 1 (YAP1) through enhancer of zeste homolog 2 (EZH2)-mediated microRNA-497(miR-497) promoter methylation. **A.** Quantitative reverse transcription polymerase chain reaction (qRT-PCR) analysis for the expression levels of *EZH2*, *miR-497* and *YAP1* in A549 and H1299 cells after *EZH2* knockdown, treated with si-EZH2 or si-NC. **B.** Western blot analysis for the protein levels of *EZH2* and *YAP1* in A549 and H1299 cells after *EZH2* knockdown, treated with *EZH2* siRNA for knockdown (si-EZH2) or si-NC. **C.** ChIP-qPCR of *EZH2* occupancy and H3K27me3 binding in the *miR-497* promoter in H1299 cells with or without PVT1 overexpression. a, b and c represented respectively three pairs of amplification primers for *miR-497* promoter; and d and e represented respectively two pairs of amplification primers for *U6* promoter as internal references. **D.** MSP analysis for the methylation level of *miR-497* promoter in A549 and H1299 cells treated with si-EZH2 or 5-Aza-dC. **E.** qRT-PCR analysis for the expression levels of *miR-497* and *YAP1* in A549 and H1299 cells treated with 5-Aza-dC or combined with PVT1 overexpression. **F.** Western blot analysis for the protein levels of *LAST2* and *YAP1* phosphorylation in A549 and H1299 cells treated with 5-Aza-dC or combined with PVT1 overexpression. Data are mean \pm SD of three independent experiments, *, $P < 0.05$, **, $P < 0.01$ compared between siRNA negative control (si-NC) and si-EZH2 groups or compared between groups as shown with a horizontal line. 5-aza-2-deoxycytidine; A549 and H1299; Two of human lung carcinoma cell lines, ChIP; Chromatin immunoprecipitation, MSP; Methylation-specific polymerase chain reaction, *LAST2*; Large tumor suppressor kinase 2 protein, and SD; Standard deviation.

PVT1 promoted NSCLC cells epithelial-mesenchymal transition and migration through activation of NOTCH1 signaling pathway

To test whether *PVT1* regulates invasion of NSCLC cells through activation of NOTCH1 signaling and epithelial-mesenchymal transition (EMT), expression of YAP1, NOTCH1, NICD and HES1 were assessed in A549 and H1299 cells after YAP1 knockdown with or without *PVT1* overexpression co-transfection. Results showed that YAP1 knockdown suppressed expressions of NOTCH1, NICD and HES1 (Fig.5A, B), indicating that activation of Hippo signaling pathway suppressed activation of NOTCH signaling pathway; while *PVT1* overexpression compensated these effects (Fig.5A, B), indicating that *PVT1* promoted activation of NOTCH

signaling pathway by suppressing Hippo signaling pathway through YAP1 overexpression. EMT markers (N-CADHERIN, VIMENTIN, E-CADHERIN and TWIST1) were downregulated in A549 and H1299 cells, while *PVT1* overexpression reversed these effects, indicating that *PVT1* promoted EMT of NSCLC cells through upregulated YAP1 (Fig.5C). Then, we further evaluated their effects on cell migration. Transwell assays demonstrated that YAP1 knockdown could significantly diminish migration and invasion abilities of A549 and H1299 cells. These effects were reversed by *PVT1* overexpression (Fig.5D). Taken together, our results demonstrated that lncRNA-*PVT1* promoted invasion and EMT of NSCLC cells through activation of NOTCH1 signaling.



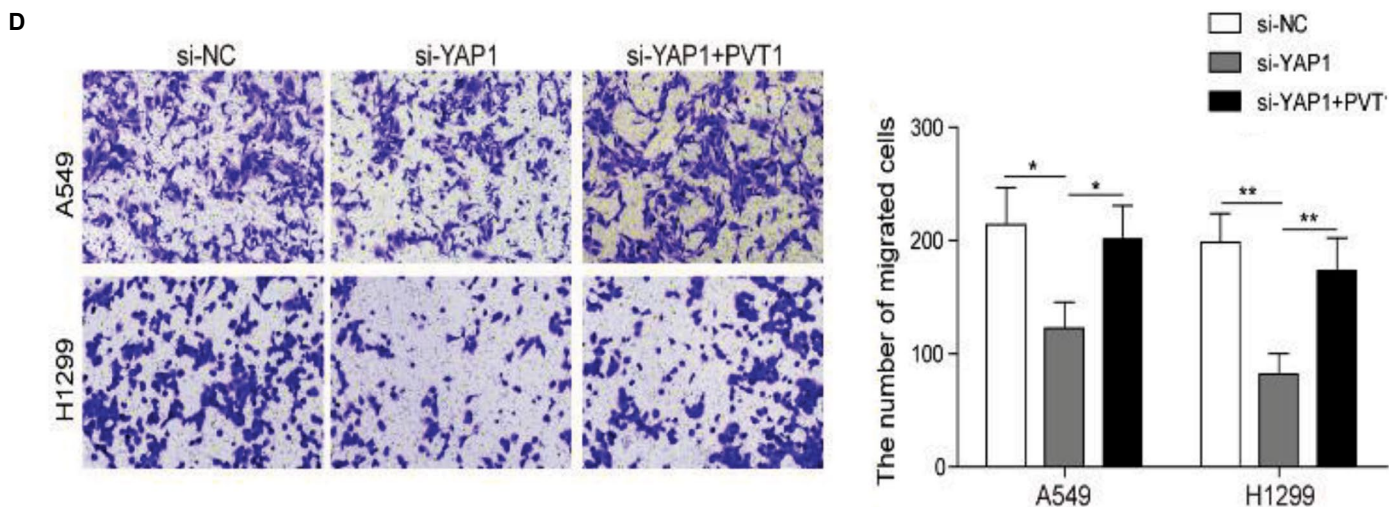


Fig. 5: Long non-coding RNAs (lncRNAs)-plasmacytoma variant translocation 1 (*PVT1*) promoted invasion and epithelial-mesenchymal transition (EMT) of non-small cell lung cancer (NSCLC) cells through activation of notch receptor 1 protein (Notch1) signaling via yes-associated protein 1 (YAP1). **A.** Quantitative reverse transcription polymerase chain reaction (qRT-PCR) analysis for the expression levels of the key protein molecules in Notch signaling pathway of A549 and H1299 cells, after YAP1 knockdown or co-transfection with *PVT1* overexpression. **B.** Western blot analysis for the key proteins in Notch signaling pathway and **C.** marker proteins of EMT in A549 and H1299 cells after YAP1 knockdown or co-transfection with *PVT1* overexpression. **D.** Matrigel-free transwell assay for cell migration were confirmed in A549 and H1299 cells, after YAP1 knockdown or co-transfection with *PVT1* overexpression. Data are mean \pm SD of three independent experiments, *, $P < 0.05$, **, $P < 0.01$, ***, $P < 0.001$ compared between groups as shown with a horizontal line, si-NC; siRNA negative control, si-YAP1; YAP1 siRNA for knockdown, A549 and H1299; The human lung carcinoma cell lines, and SD; Standard deviation.

Discussion

NSCLC accounts for almost 80% of lung cancer, as the leading cause of cancer mortality (22). Even though great progresses have been made in surgical resection, chemoradiotherapy or target drugs, its prognosis is still poor (2). Hence, it is of most importance to uncover the molecular mechanism of carcinogenesis. Accumulating studies have shown that some lncRNAs associate with NSCLC generation and they participate in different biological processes in NSCLC (23). Previously, *PVT1* was reported to function as an oncogenic lncRNA, a potential prognostic biomarker and therapeutic target in NSCLC (23-24). It was reported to act as a competing endogenous RNA (ceRNA) for *miR-497* in promoting NSCLC progression (13) and it could regulate expression of HIF1 α via functioning as ceRNA for *miR-199a* in NSCLC (25). It also facilitates NSCLC cell invasion through MMP9 (26). Besides, *PVT1* could promote NSCLC cell proliferation through epigenetically regulating *LATS2* expression (9). Here, consistent with previous study, we confirmed that *PVT1* was upregulated in NSCLC tissues and cells and it might promote proliferation and migration in NSCLC, indicating that *PVT1* may serve as an oncogene to promote NSCLC development and progression.

Hippo pathway is involved in the development of NSCLC. *LATS1*, the core component of Hippo pathway, was reported to suppress NSCLC cell proliferation and migration (27). While, *Tafazzin* (*TAZ*) was reported to be overexpressed in 70% NSCLC cell lines and it could cause transformation of non-tumorigenic lung epithelial cells (28). Besides, constitutively activated YAP, a *TAZ* paralog, was reported to drive NSCLC progression and metastasis (29). In this study, we found that *PVT1*

regulated expression of YAP1 through *EZH2*-mediated *miR-497* promoter methylation. These findings suggest that *PVT1* regulated Hippo-NOTCH1 signaling pathway through epigenetic regulation. Besides, *PVT1* activated NOTCH1 signaling through YAP1, indicating that YAP1 is most likely a NOTCH1 upstream driver gene and we, for the first time, revealed the molecular mechanism of NOTCH1 upregulation in NSCLC.

Increasing evidences showed that *EZH2* contributed to malignant transformation (30). *PVT1* and *EZH2* were also reported to have correlations. For example, *PVT1* modulates cell proliferation and apoptosis by recruiting *EZH2* in HCC (11). While, it represses *ANGPTL4* transcription through binding with *EZH2* in trophoblast cell (31). Besides, it can promote cell proliferation and invasion via targeting *EZH2* in glioma cells (32). In this study, RNA pull-down and RNA binding protein immunoprecipitation (RIP) assays were performed to verify the relationship between *PVT1* and *EZH2*. They demonstrated that *PVT1* could recruit *EZH2* to the promoter of *miR-497*, thus mediate H3K27me3 modification. We are the first to clearly elucidate the molecular mechanism by which *PVT1* inhibits *miR-497* in NSCLC.

EMT progression is of great importance for migration of NSCLC cells (33). Investigations on EMT will be of great benefit to the bulk of solid malignant tumors, as most of human malignancies arise from the epithelium tissues³³. However, the functional role of lncRNA in modulating EMT in NSCLC is still poorly understood. Here, we identified *PVT1* as a novel player in modulating EMT progress and we also revealed a previously unknown mechanism. Regarding that microRNAs may function

as oncogenes or tumor suppressors in almost all kind of tumors, including NSCLC (34), identifying and exploring their functions may do us a great favor to develop more effective biomarkers and therapies. Previously, *miR-497* was reported to suppress TGF- β induced EMT of NSCLC by targeting METADHERIN (MTDH) (35). Here, consistent with previous reports, we uncovered that *miR-497* inhibits EMT of NSCLC cells via targeting YAP1.

Conclusion

In summary, we demonstrated that *PVT1* is an oncogene in NSCLC, overexpression of which could promote cell proliferation, migration and EMT process via regulating the expression of YAP1 through EZH2-mediated *miR-497* promoter methylation. This novel mechanism will lead to a better understanding of EMT in NSCLC or even other cancers. Overall, these findings indicate that *PVT1* might be a potential target for NSCLC therapy.

Acknowledgments

There is no financially supported and conflict of interest.

Authors' Contributions

J.C.L., S.G.Z.; Contributed to conception and design. S.G.Z., J.H.X., Y.W.; Contributed to all experimental work, data and statistical analysis, and interpretation of data. J.C.L.; Were responsible for overall supervision. X.M.W.; Drafted the manuscript, which was revised by Q.Y.Z. and S.H.D. All authors read and approved the final manuscript.

References

- Bray F, Ferlay J, Soerjomataram I, Siegel RL, Torre LA, Jemal A. Global cancer statistics 2018: GLOBOCAN estimates of incidence and mortality worldwide for 36 cancers in 185 countries. *CA Cancer J Clin.* 2018; 68(6): 394-424.
- Zappa C, Mousa SA. Non-small cell lung cancer: current treatment and future advances. *Transl Lung Cancer Res.* 2016; 5(3): 288-300.
- Yu M, Chen Y, Li X, Yang R, Zhang L, Huangfu L, et al. YAP1 contributes to NSCLC invasion and migration by promoting Slug transcription via the transcription co-factor TEAD. *Cell Death Dis.* 2018; 9(5): 464.
- Wang Y, Dong Q, Zhang Q, Li Z, Wang E, Qiu X. Overexpression of yes-associated protein contributes to progression and poor prognosis of non-small-cell lung cancer. *Cancer Sci.* 2010; 101(5): 1279-1285.
- Fang Y, Fullwood MJ. Roles, Functions, and Mechanisms of Long Non-coding RNAs in Cancer. *Genomics Proteomics Bioinformatics.* 2016; 14(1): 42-54.
- Gutschner T, Hämmerle M, Eissmann M, Hsu J, Kim Y, Hung G, et al. The noncoding RNA MALAT1 is a critical regulator of the metastasis phenotype of lung cancer cells. *Cancer Res.* 2013; 73(3): 1180-1189.
- Chen Z, Li JL, Lin S, Cao C, Gimbrone NT, Yang R, et al. cAMP/CREB-regulated LINC00473 marks LKB1-inactivated lung cancer and mediates tumor growth. *J Clin Invest.* 2016; 126(6): 2267-2279.
- Liu Z, Zhang H. LncRNA plasmacytoma variant translocation 1 is an oncogene in bladder urothelial carcinoma. *Oncotarget.* 2017; 8(38): 64273-64282.
- Wan L, Sun M, Liu GJ, Wei CC, Zhang EB, Kong R, et al. Long noncoding RNA PVT1 promotes non-small cell lung cancer cell proliferation through epigenetically regulating LATS2 expression. *Mol Cancer Ther.* 2016; 15(5): 1082-1094.
- He F, Song Z, Chen H, Chen Z, Yang P, Li W, et al. Long noncoding RNA PVT1-214 promotes proliferation and invasion of colorectal cancer by stabilizing Lin28 and interacting with miR-128. *Oncogene.* 2019; 38(2): 164-179.
- Guo J, Hao C, Wang C, Li L. Long noncoding RNA PVT1 modulates hepatocellular carcinoma cell proliferation and apoptosis by recruiting EZH2. *Cancer Cell Int.* 2018; 18: 98.
- Guo C, Wang X, Liang L. LATS2-mediated YAP1 phosphorylation is involved in HCC tumorigenesis. *Int J Clin Exp Pathol.* 2015; 8(2): 1690-1697.
- Guo D, Wang Y, Ren K, Han X. Knockdown of LncRNA PVT1 inhibits tumorigenesis in non-small-cell lung cancer by regulating miR-497 expression. *Exp Cell Res.* 2018; 362(1): 172-179.
- Westhoff B, Colaluca IN, D'Ario G, Donzelli M, Tosoni D, Volorio S, et al. Alterations of the Notch pathway in lung cancer. *Proc Natl Acad Sci USA.* 2009; 106(52): 22293-22298.
- Zou B, Zhou XL, Lai SQ, Liu JC. Notch signaling and non-small cell lung cancer. *Oncol Lett.* 2018; 15(3): 3415-3421.
- Kim W, Khan SK, Yang Y. Interacting network of Hippo, Wnt/beta-catenin and Notch signaling represses liver tumor formation. *BMB Rep.* 2017; 50(1): 1-2.
- Yimlamai D, Fowl BH, Camargo FD. Emerging evidence on the role of the Hippo/YAP pathway in liver physiology and cancer. *J Hepatol.* 2015; 63(6): 1491-1501.
- Yimlamai D, Christodoulou C, Galli GG, Yanger K, Pepe-Mooney B, Gurung B, et al. Hippo pathway activity influences liver cell fate. *Cell.* 2014; 157(6): 1324-1338.
- Tschaharganeh DF, Chen X, Latzko P, Malz M, Gaida MM, Felix K, et al. Yes-associated protein up-regulates Jagged-1 and activates the Notch pathway in human hepatocellular carcinoma. *Gastroenterology.* 2013; 144(7): 1530-1542. e12.
- Shen Y, Liu S, Fan J, Jin Y, Tian B, Zheng X, et al. Nuclear retention of the lncRNA SNHG1 by doxorubicin attenuates hnRNPC-p53 protein interactions. *EMBO Rep.* 2017; 18(4): 536-548.
- Plouffe SW, Hong AW, Guan KL. Disease implications of the Hippo/YAP pathway. *Trends Mol Med.* 2015; 21(4): 212-222.
- Dela Cruz CS, Tanoue LT, Matthay RA. Lung cancer: epidemiology, etiology, and prevention. *Clin Chest Med.* 2011; 32(4): 605-644.
- Wei MM, Zhou GB. Long non-coding RNAs and Their roles in non-small-cell lung cancer. *Genomics Proteomics Bioinformatics.* 2016; 14(5): 280-288.
- Pan X, Zheng G, Gao C. LncRNA PVT1: a novel therapeutic target for cancers. *Clin Lab.* 2018; 64(5): 655-662.
- Wang C, Han C, Zhang Y, Liu F. LncRNA PVT1 regulate expression of HIF1alpha via functioning as ceRNA for miR199a5p in non-small cell lung cancer under hypoxia. *Mol Med Rep.* 2018; 17(1): 1105-1110.
- Chen W, Zhu H, Yin L, Wang T, Wu J, Xu J, et al. LncRNA-PVT1 facilitates invasion through upregulation of MMP9 in non-small cell lung cancer cell. *DNA Cell Biol.* 2017; 36(9): 787-793.
- Malik SA, Khan MS, Dar M, Hussain MU, Shah MA, Shafi SM, et al. Molecular alterations and expression dynamics of LATS1 and LATS2 Genes in non-small-cell lung carcinoma. *Pathol Oncol Res.* 2018; 24(2): 207-214.
- Noguchi S, Saito A, Horie M, Mikami Y, Suzuki HI, Morishita Y, et al. An integrative analysis of the tumorigenic role of TAZ in human non-small cell lung cancer. *Clin Cancer Res.* 2014; 20(17): 4660-4672.
- Yu J, Alharbi A, Shan H, Hao Y, Snetsinger B, Rauh MJ, et al. TAZ induces lung cancer stem cell properties and tumorigenesis by up-regulating ALDH1A1. *Oncotarget.* 2017; 8(24): 38426-38443.
- Chang CJ, Hung MC. The role of EZH2 in tumour progression. *Br J Cancer.* 2012; 106(2): 243-247.
- Xu Y, Lian Y, Zhang Y, Huang S, Zuo Q, Yang N, et al. The long non-coding RNA PVT1 represses ANGPTL4 transcription through binding with EZH2 in trophoblast cell. *J Cell Mol Med.* 2018; 22(2): 1272-1282.
- Yang A, Wang H, Yang X. Long non-coding RNA PVT1 indicates a poor prognosis of glioma and promotes cell proliferation and invasion via target EZH2. *Biosci Rep.* 2017; 37(6): pii: BSR20170871.
- Liang WC, Fu WM, Wong CW, Wang Y, Wang WM, Hu GX, et al. The lncRNA H19 promotes epithelial to mesenchymal transition by functioning as miRNA sponges in colorectal cancer. *Oncotarget.* 2015; 6(26): 22513-22525.
- Zhang B, Pan X, Cobb GP, Anderson TA. microRNAs as oncogenes and tumor suppressors. *Dev Biol.* 2007; 302(1): 1-12.
- Yin Q, Han Y, Zhu Y, Li Z, Shan S, Jin W, et al. miR-145 and miR-497 suppress TGF- β -induced epithelial-mesenchymal transition of non-small cell lung cancer by targeting MTDH. *Cancer Cell Int.* 2018; 18: 105.

Design and Microfabrication of An On-Chip Oocyte Maturation System for Reduction of Apoptosis

Behnaz Sadeghzadeh Oskouei, Ph.D.¹, Siavash Zargari, M.Sc.², Parviz Shahabi, Ph.D.³,

Marefat Ghaffari Novin, M.D., Ph.D.⁴, Maryam Pashaiasl, M.D., Ph.D.^{5*}

1. Department of Midwifery, School of Nursing and Midwifery, Tabriz University of Medical Sciences, Tabriz, Iran

2. Department of Electrical and Computer Engineering, University of Tabriz, Tabriz, Iran

3. Department of Physiology, School of Medicine, Tabriz University of Medical Sciences, Tabriz, Iran

4. Cellular and Molecular Biology Research Center, School of Medicine, Shahid Beheshti University of Medical Sciences, Tehran, Iran

5. Drug Applied Research Center, Tabriz University of Medical Sciences, Tabriz, Iran

*Corresponding Address: P.O.Box: 51656-65811, Drug Applied Research Center, Tabriz University of Medical Sciences, Tabriz, Iran
Email: pashaim@tbzmed.ac.ir

Received: 31/August/2019 Accepted: 13/November/2019

Abstract

Objective: In customary assisted reproductive technology (ART), oocyte culture occurs in static micro drops of Petri dishes with vast media volume; while, the *in vivo* condition is dynamic. In this study, we aimed to improve the maturation efficiency of mammalian oocytes by designing an optimal microchamber array to obtain the integration of oocyte trapping and maturation within a microfluidic device and evaluate the role of microfluidic culture condition in lipid peroxidation level of the culture medium, *in vitro* matured oocytes apoptosis, and its comparison with the conventional static system.

Materials and Methods: In this experimental research, immature oocytes were collected from ovaries of the Naval Medical Research Institute (NMRI) mice. Oocytes were randomly laid in static and dynamic (passive & active) *in vitro* maturation culture medium for 24 hours. The lipid peroxidation level in oocyte culture media was assessed by measuring the concentration of malondialdehyde (MDA), and the rate of apoptosis in *in vitro* matured oocytes was assessed by the TUNEL assay after a-24 hour maturation period.

Results: The MDA concentration in both dynamic oocyte maturation media were significantly lower than the static medium (0.003 and 0.002 vs. 0.13 $\mu\text{mol/L}$, $P < 0.01$). Moreover, the rate of apoptosis in matured oocytes after a-24 hour maturation period was significantly lower in passive dynamic and active dynamic groups compared with the static group (16%, 15% vs. 35%, $P < 0.01$).

Conclusions: The dynamic culture for *in vitro* oocyte maturation (IVM) improves the viability of IVM oocytes in comparison with the static culture condition.

Keywords: Assisted Reproductive Technology, Apoptosis, *In vitro* maturation, Microfluidics, Oocyte

Cell Journal (Yakhteh), Vol 23, No 1, April-June (Spring) 2021, Pages: 32-39

Citation: Sadeghzadeh Oskouei B, Zargari S, Shahabi P, Ghaffari Novin M, Pashaiasl M. Design and microfabrication of an on-chip oocyte maturation system for reduction of apoptosis. Cell J. 2021; 23(1): 32-39. doi: 10.22074/cellj.2021.7056.

This open-access article has been published under the terms of the Creative Commons Attribution Non-Commercial 3.0 (CC BY-NC 3.0).

Introduction

In vitro maturation (IVM) of mammalian oocytes is an important infertility treatment with substantial assurance. At present, IVM methods are very effective when used for mice and still regarded experimental in the human clinic due to suboptimal fertilization rates and embryo quality. Therefore, in order to achieve human embryos that have the same developmental potential as embryos resulting from standard IVF, assisted reproductive technology (ART) must improve increasingly in the field of IVM (1). Nevertheless, ART is quite expensive, and it has a generally low success rate (2). One of the considerable differences between *in vivo* and *in vitro* conditions for the oocyte/embryo is oxygen tension. Accordingly, *in vitro* culture is kept up with higher concentrations of O_2 in comparison with the *in vivo* culture, and therefore, it can result in the increased production of reactive oxygen species [ROS, (3)]. The relatively high oxygen

concentrations in the *in vitro* microenvironment of the cells may disturb the equilibrium between the formation of reactive oxygen species and antioxidants, causing a stressful condition called to oxidative stress (1).

Oxidative stress is involved in a wide range of biological events, including oxidation of amino acids and nucleic acids, apoptosis, necrosis, and membrane lipids peroxidation. The plasma membrane of the mammalian oocytes is a rich source of unsaturated fatty acids and vulnerable to ROS-related lipid peroxidation. The cellular structure and metabolic functions of the oocyte can be reduced as a result of lipid peroxidation, which is caused by ROS. The level of lipid peroxidation is defined by measuring the level of malondialdehyde (MDA), which is a stable lipid peroxidation product (4).

Cell death in the form of apoptosis is a physiologic phenomenon, occurring during several processes,

including gametogenesis/embryogenesis. Although apoptosis takes place as an ordinary component of *in vivo* development; however, it is more likely to occur during suboptimal *in vitro* culture conditions (1).

To date, all efforts and advances made in this area caused modifications in the ingredients of culture media, while there is no significant change in the physical instruments utilized for handling and manipulation of oocytes/embryos in ART research centers (5, 6).

Unfortunately, embryology laboratories still use petri dishes and fine-bore-glass-pipettes as static culture systems (2). Such conditions result in the induction of numerous alterations in oocytes and embryos. There are more controllable factors, such as media components, protein supplements, and embryo density. However, all of these compounds are static for several days and cells have to reside for a long time; therefore, cellular damages, such as epigenetic alterations may occur. It seems that simulating *in vivo* dynamic conditions in the culture medium increases its culture quality (7). Obviously, the dynamic environment of tubal/uterine produces a unique condition capable of supporting embryo development and it can also regulate gene expression (8) and interrupt cell-surface gradients on embryos (9). These gradients, such as potassium, calcium, and oxygen also exist in conventional static culture conditions, possibly through the secretion of trophic autocrine/paracrine factors; however, because of the nature of static conditions, the previously mentioned gradients cannot be disturbed, and therefore would not provide a more homogenous environment similar to *in vivo* dynamic culture systems [DCSs, (3)]. It is assumed that IVM of oocytes in a microfluidic environment can resemble *in vivo* conditions for oocyte development more closely and thus benefiting the maturation of efficient oocyte and subsequent embryo development. It is worth mentioning that each individual event during oocyte maturation can highly influence the subsequent embryonic development (10, 11).

Accordingly, the main goal of this study is to evaluate the effect of microfluidic culture condition on MDA concentration in culture media, *in vitro* matured oocytes apoptosis, and its correlation with conventional static system. A microfluidic device made (Patent No. 96301) by colleagues were used as dynamic culture condition (12). The success and applicability of the present device in the reduction of apoptosis and MDA production are the focus of this study.

Materials and Methods

Study design and animals

In this experimental study, immature oocytes were obtained from ovaries of the Naval Medical Research Institute (NMRI) mice (Pasteur Institute, Tehran, Iran) with an age range of 6-8 weeks, and sperm samples were acquired from male mice with an age range of 8-10 weeks. They were kept under a controlled condition with 12-hour light/dark cycle, constant temperature, and relative

humidity conditions with free access to water and food. All experiments procedures were carried out according to the Ethics Guidelines of Tabriz University of Medical Sciences (Registration number: 796973). Oocytes were randomly laid in static and dynamic (passive and active) *in vitro* maturation culture media for 24 hours. The lipid peroxidation level in oocyte culture media was assessed by measuring the MDA level, and the rate of apoptosis in the *in vitro* matured oocytes was assessed by the TUNEL assay after a-24 hour maturation period.

Computational model

COMSOL multiphysics software was employed for modeling and simulation of IVM microfluidic device to optimize the design, improve the performance, and reduce the process time. COMSOL is an interactive environment for modeling and simulating scientific and engineering problems. It permits conventional physics-based user interfaces and coupled systems of partial differential equations (PDEs) and enables the simulation of designs and devices dependent on electromagnetics, structural mechanics, acoustics, fluid flow, heat transfer, and chemical engineering behavior.

Herein, we built finite element models and used 2D and 3D simulations to study the flow behavior in microchannel and microchambers. The model is based on the steady-state Navier–Stokes equation for incompressible Newtonian fluid (13):

$$\partial\rho/\partial t + \nabla \cdot (\rho\mathbf{u}) = 0 \quad (1)$$

$$\rho \partial\mathbf{u}/\partial t + \rho(\mathbf{u} \cdot \nabla)\mathbf{u} + \nabla p - \mu \nabla^2 \mathbf{u} - (\lambda + \mu)\nabla(\nabla \cdot \mathbf{u}) = \mathbf{f} \quad (2)$$

Where \mathbf{u} is the velocity vector field, p the pressure, ρ the medium density, μ the dynamic viscosity, λ the molecular mean free path, and \mathbf{f} the body force.

In addition, the computational fluid dynamics was utilized to anticipate the wall shear stress as a function of the channel width and flow rate. Since the channel length was significantly large compared with the channel height, the system could be effectively modeled using a 2D simulation. Using these conditions, the maximum shear stress applied to the cell (τ_s) could also be assessed by this equation (14):

$$\tau_s = (6 \times 2.95 \mu Q)/H^2 \quad (3)$$

Where H is channel height, the medium viscosity, and Q the flow rate.

Device design and fabrication

The device was optimally designed using a finite element method (FEM) under the defined criteria and then fabricated using standard soft lithography procedures in our previously published work (15).

Master molds patterned with 200- μm thick resist were made by patterning a negative photoresist (SU-8 2050; Microchem, MA, USA) on a standard PCB substrate. The main biochip is then injection molded into the associated masters by pouring uncured PDMS pre-polymer (Sylgard 184; Dow Corning, MI, USA) solution over the masters. PDMS was chosen for this microfluidics system microfabrication because of its favorable mechanical properties, optical transparency, biocompatibility (16, 17), and straightforward manufacturing by rapid prototyping (12).

To remove microbubbles, the solution was then degassed in a desiccator using a single stage vacuum pump and kept in the oven at 70°C for 90 minutes, and then peeled off from the master. To improve the adhesion, the upper and lower PDMS layers were surface-treated utilizing a corona discharge gun for 4 minutes, and then bonded under the pressure. The bonded layers were then heated in the oven up to 70°C for 20 minutes to reinforce the bonding. Two sampler tips were then fixed on the upper layer as the inlet and outlet reservoirs.

Two types of devices (Passive and Active) consist of two PDMS layers, with a microchannel in the upper layer and a microchamber array in the lower one. The microchannel had a 7-mm length, 140- μm width, and 200- μm depth to transport oocytes, and the inlet and outlet were connected to the microchannel (Fig.1A). Square-shaped microchambers had a 120- μm width, 120- μm , 360- μm , 600- μm and 900- μm length, respectively, at a 250- μm interval distance to trap oocytes. The four microchambers were designed to compare their performance in oocyte capture and developmental competency of cumulus oocyte complexes (COCs) in groups of 1, 3, 5, and 7.

During the experiment, oocytes were loaded into the funnel shape inlet port, transported through the microchannel and lodged in the microchamber array. The design of the present culture microfunnels were selected rather than culture channels to minimize excessive fluid mechanical stress that may be associated with passage through narrow channels in previous studies (18). The illustration of the microfluidic device and microchamber array and the final assembled device are shown in Figure 1A, B.

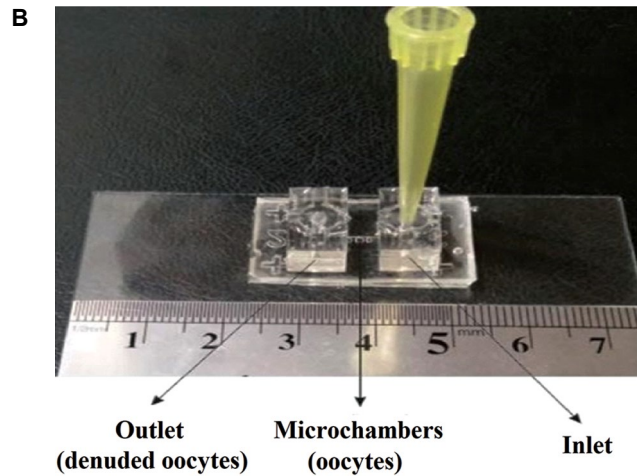
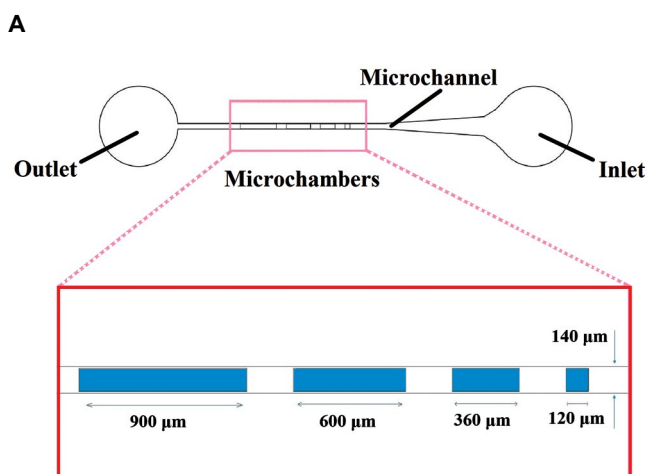


Fig.1: Schematic view of the proposed microfluidic device. A. Illustration of the microfluidic device and microchamber array (15), and B. Fabricated microfluidic device (12).

Superovulation, oocyte collection, and *in vitro* maturation

To obtain immature oocyte, female mice were induced by superovulation. They were injected intraperitoneally (i.p.) with 10 IU of PMSG (Gonaser®, Laboratorios Girona, Spain). Oocytes were retrieved 46–48 hours after PMSG injection.

Animals were sacrificed by cervical dislocation and their ovaries were removed and placed in tissue culture dishes (BD Falcon, 35 x 10 mm) containing human tubal fluid-HEPES buffered (GC-HTF W/HEPES; Genocell ideal, Iran) supplemented with 10% (v/v) qualified fetal bovine serum (FBS, Gibco, Invitrogen, South America). COCs were released by follicular puncturing with the aid of a pair of 28G needles under a stereomicroscope (Olympus, Japan) (19). Only cumulus intact oocytes in germinal vesicle (GV) stage evenly granulated cytoplasm were selected and moved to maturation medium (20). After several washes, just fully expanded COCs (19, 20) were divided into dynamic (passive and active) and static culture system groups, randomly and synchronously.

In dynamic groups, COCs were loaded into microfluidic chips pre-filled with 15-20 μL of human tubal factor (HTF) medium supplemented with 10% (v/v) qualified fetal bovine serum, 10 $\mu\text{g}/\text{mL}$ follicle stimulating hormone (FSH), 10 $\mu\text{g}/\text{mL}$ luteinizing hormone (LH), and 1 $\mu\text{g}/\text{mL}$ estradiol-17 β (Sigma Chemical company, St. Louis, MO, USA) as an IVM medium (5 oocytes/15 μL medium) and left to rest for 5 minutes. COCs were incubated in a humidified atmosphere with 5% CO_2 at 37°C for 20-24 hours (21).

As shown in Figure 2A, a syringe pump was connected to the inlet reservoir to generate a negative-pressure driven flow. The flow lasted for 2 minutes at an inlet velocity of 0.5 mm/s to guide oocytes into the microchamber array area.

In the active dynamic group, we utilized a low flow rate peristaltic pump (Langer Instruments, USA), which produced pulsatile fluid movement (1 $\mu\text{L}/\text{h}$), but in the passive dynamic group, we did not use any pump, and fluid movement was made by gravity.

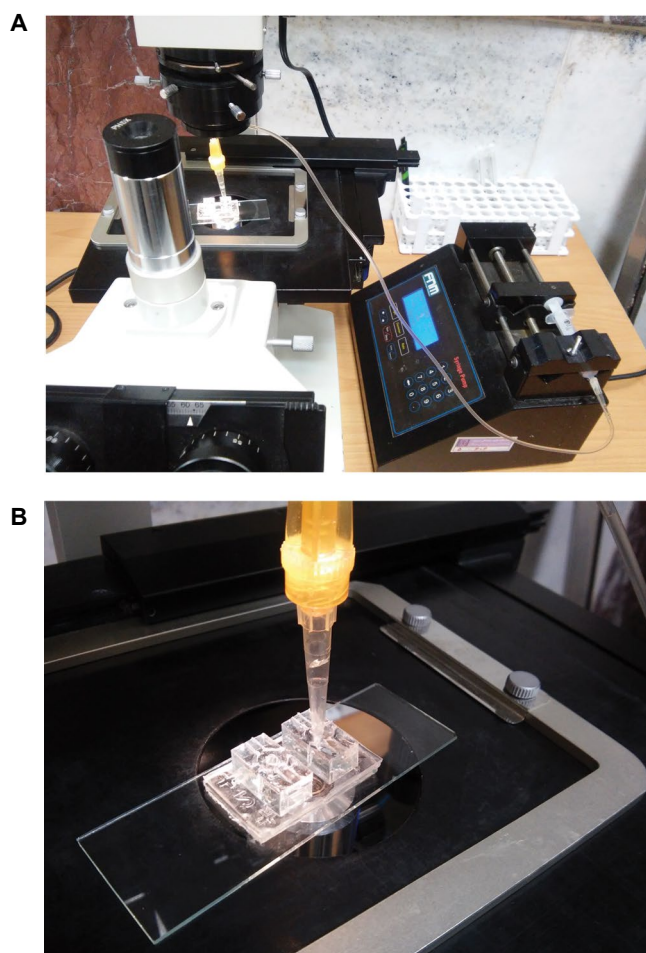


Fig.2: Schematic view of the experimental perfusion system comprising. **A.** a syringe pump and **B.** the fabricated microfluidic chip.

In the static group, COCs were set in several droplets of the IVM medium (15 oocytes/50 μ L medium under mineral oil) (20, 22) in tissue culture dishes and after that incubated in a similar condition used for experimental (dynamic) groups for 24 hours. Then, apoptosis in two groups was assessed under a fluorescent microscope (Labomed, USA).

TUNEL assay

The TUNEL assay and propidium iodide staining were performed to evaluate DNA fragmentation in oocytes. Following several washings in PBS (Gibco, Grand Island, NY, USA), oocytes were fixed in 3.7% paraformaldehyde solution (Wako, Japan), treated with 0.1% Triton X-100 solution (Sigma, Germany) for 40 minutes and exposed to the blocking solution at 4°C overnight. Then, oocytes were primarily incubated in TUNEL solution (Roche, Germany) at 37°C for an hour according to the manufacturer's guidelines. Negative control oocytes were incubated only in the fluorescent solution lacking the enzyme to ensure the absence of labeling. For the positive control, a number of oocytes prior to the incubation with TUNEL staining solution were incubated with 50 μ g/ml of the DNase I solution (Sigma, Germany) for one hour and then treated with the TUNEL solution. Oocytes were stained with 50 μ g/ml of the propidium iodide (Sigma, Germany) solution for 20 minutes to label nuclei and examined under a fluorescent microscope (Labomed, USA).

TUNEL assay

The TUNEL assay and propidium iodide staining were performed to evaluate DNA fragmentation in oocytes. Following several washings in PBS (Gibco, Grand Island, NY, USA), oocytes were fixed in 3.7% paraformaldehyde solution (Wako, Japan), treated with 0.1% Triton X-100 solution (Sigma, Germany) for 40 minutes and exposed to the blocking solution at 4°C overnight. Then, oocytes were primarily incubated in TUNEL solution (Roche, Germany) at 37°C for an hour according to the manufacturer's guidelines. Negative control oocytes were incubated only in the fluorescent solution lacking the enzyme to ensure the absence of labeling. For the positive control, a number of oocytes prior to the incubation with TUNEL staining solution were incubated with 50 μ g/ml of the DNase I solution (Sigma, Germany) for one hour and then treated with the TUNEL solution. Oocytes were stained with 50 μ g/ml of the propidium iodide (Sigma, Germany) solution for 20 minutes to label nuclei and examined under a fluorescent microscope (Labomed, USA).

MDA assay

In order to determine malondialdehyde (MDA) concentration in oocyte culture media, we used the MDA assay method. Lipid peroxidation was measured by the reaction of thiobarbituric acid (TBA) with MDA. The content of MDA was determined spectrophotometrically using a spectrofluorometer (PG instruments T70 UV/VIS, 532 nm).

The MDA fluorescence intensity of oocyte was evaluated utilizing different concentrations of tetraethoxy-propane as the standard. The results are expressed as μ mol MDA/L of the culture medium.

Statistical Analysis

All statistical analyses were implemented utilizing Service Provisioning System Software (SPSS) 22 for windows (SPSS, Chicago, IL, USA). The *in vitro* maturation and apoptosis rate in static and dynamic groups were compared by one-way analysis of variance (ANOVA) followed by Tukey's Post Hoc test. Data are expressed as means \pm SE. Differences at P-value of less than 0.05 were considered statistically significant.

Results

Computational analysis of the shear stress profile

We used computational fluid dynamics (CFD) features of COMSOL multiphysics to predict velocity profiles and shear stress patterns in our proposed structure. The culture medium (HTF) was modeled at a density of 1000 kg/m³ and a dynamic viscosity of 0.001 Pa.s (23). A uniform inlet velocity of 0.5 mm/s was used to simulate the experimental conditions. A zero pressure condition was applied to the outlet. No-slip boundary conditions were applied in the microchannel walls. Steady-state 2D velocity profiles and streamlines were obtained.

Figure 3 represent velocity contours and streamlines of the laminar flow, resulting from the 2D simulation under

an average inlet velocity of 0.5 mm/s. As shown in Figures, higher flow penetration in the chambers was achieved in larger chambers (600 and 900 μm in length) compared with the smaller ones (120 and 360 μm in length). This was supposed to have significant impacts on oocyte maturation due to better media circulation along the chambers.

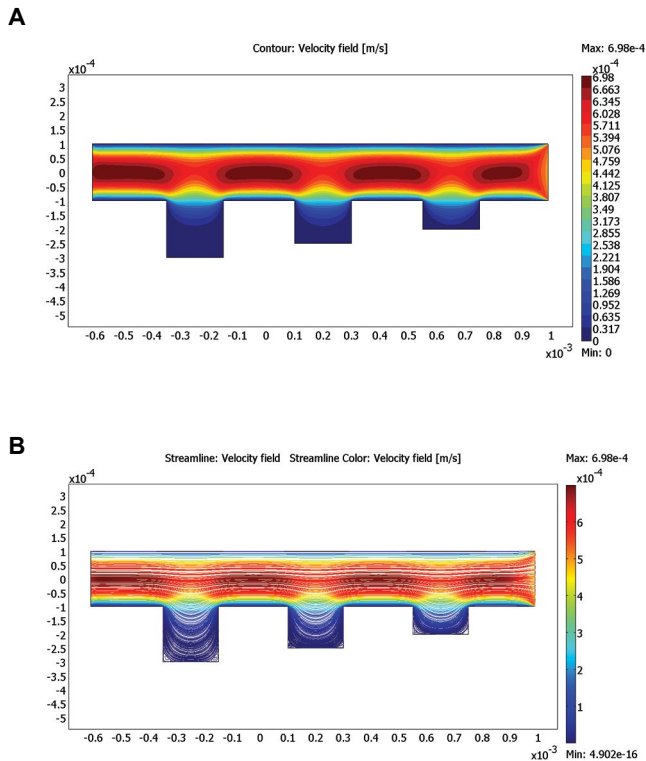


Fig.3: Simulation results obtained from COMSOL Multiphysics software. **A.** Velocity contours for microchambers with different lengths, and **B.** Streamlines for microchambers with different lengths.

Another vital parameter is the total stress parameters applied to the oocyte during maturation period. Extra tangential forces have degrading effects on the oocytes and could even cause degeneration (24). These forces could be measured in terms of the shear stresses from mechanical point of view. The resulting shear stress parameters within the microchambers are also calculated in the COMSOL using equation (3).

Figure 4 represents the shear stress profile for the different microchambers lengths. Here the extreme values (positive and negative peaks) correspond to chamber walls where an absolute maximum shear stress occurs over the oocytes and the sign of shear stress only explain changes in the direction of flow. For an inlet velocity of 0.5 mm/s, the maximum wall shear stress inside the microchannel was 0.04 dyne/cm², which was significantly lower than the average wall shear stress amplitude that an oocyte can tolerate (1.2 dyne/cm²) (24). According to the simulation results (Fig.3A, B), it can be deduced that the fluid velocity inside the microchambers is much lower than the fluid velocity inside the main channel (red and blue colors indicate the highest and lowest velocities, respectively). As a result, when oocytes are placed inside the microchambers, very

small shear stress is applied, and the maximum amount of shear stress is applied to the oocytes only at the beginning and end of each microchamber.

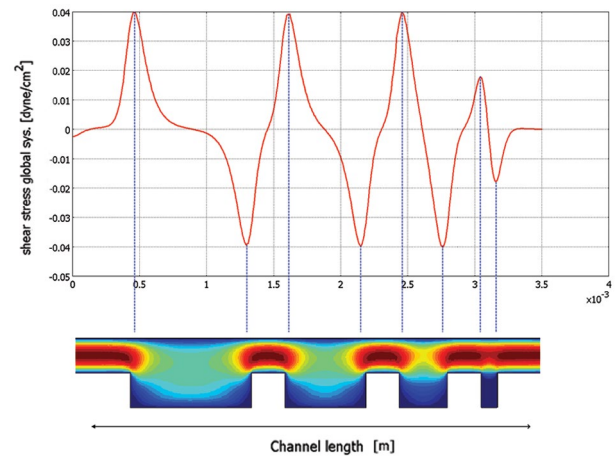


Fig.4: The shear stress profile in the microchannel.

Qualitative observations

Figure 5 indicates that all positive control oocytes were labeled by TUNEL assay solution and appeared as green-colored. None of the negative control oocytes were labeled by TUNEL assay solution and only counterstained by propidium iodide and observed as red-colored (Fig.5B). As shown in Figure 5C, *in vitro* matured oocytes were well labeled with TUNEL staining solution and quite distinct from the non-apoptotic cells (Fig.5D).

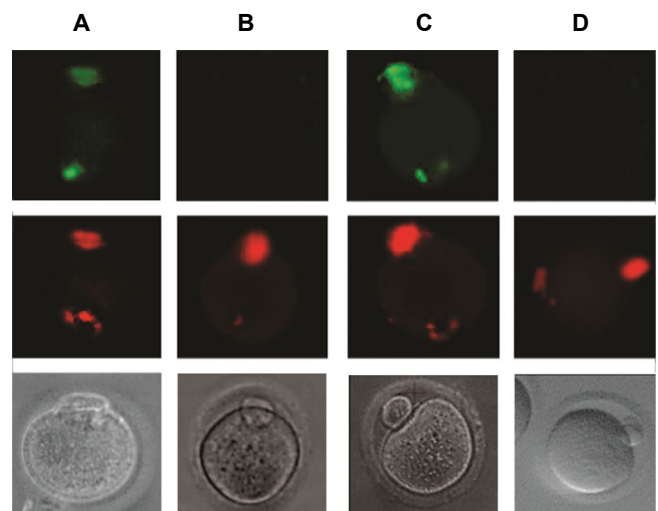


Fig.5: Microscopic view of mouse stage metaphase II oocytes under a fluorescent and stereo microscope. **A.** Cell nuclei were stained as green-colored after incubation with DNase I (positive control). **B.** Microscopic view of mouse oocytes under a fluorescent microscope; no cells were marked in the absence of terminal deoxy transferase but cells with stained nuclei with the propidium iodide (negative control). **C.** Microscopic view of an apoptotic cell. **D.** Microscopic view of a non-apoptotic cell. Upper figures were incubated with DNase I; middle figures were incubated with propidium iodide, and the below figures were not incubated.

The apoptosis rate in matured oocytes after a 24-hour maturation period

As shown in Figure 6A, the rate of apoptosis in matured oocytes after a 24-hour maturation period showed a significant difference in passive dynamic and active dynamic groups compared with the static group (16%, 15% vs. 35%, $P < 0.01$).

MDA assay

The means \pm SD of lipid peroxidation values, as determined by the MDA assay, in cultured oocytes are shown in Figure 6B.

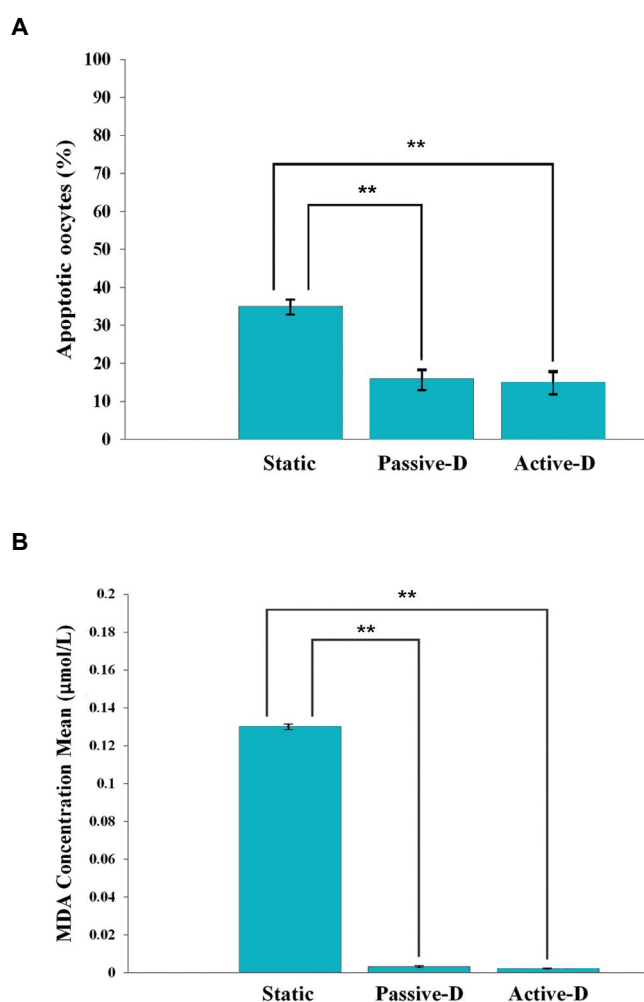


Fig.6: Graphical representation of the rate of apoptosis and MDA assay outcomes. **A.** The number of apoptotic oocytes in three groups. **B.** The concentration of MDA of three groups in oocyte culture media. Data are expressed as mean \pm SE. Asterisks indicate statistically significant differences relative to the static group. MDA; malondialdehyde, and **; ($P < 0.01$).

Discussion

This paper describes the effect of dynamic culture system on immature oocyte development by microfluidic chip, exclusively designed and constructed by the present authors (Patent No. 96301) (12). For having a good quality embryo, high quality matured oocyte is necessary.

It has been reported that a dynamic culture of pre-implanted embryos plays a role in successful implantation and ongoing normal pregnancies due to obtaining the developmental competence. However, few studies focused on the dynamic culture of immature oocytes (25). To do ART procedures, such as intracytoplasmic sperm injection (ICSI), the induction ovulation was performed. Frequently, a number of oocytes obtained after stripping contained at least one immature oocyte (i.e., oocytes at the metaphase I (MI) or GV stage of development) (26). Therefore, the rescue of immature oocytes would be critical. Conventional culture condition is static; however, the *in vivo* condition is dynamic. The dynamic condition is optimal for cell development (12). The present findings showed that the dynamic culture during IVM efficiently improved oocyte development. Embryos acquired from dynamic matured oocytes demonstrated higher development compared with the blastocyst stage, which is consistent with previous studies (27, 28).

Oocyte maturation is the most significant stage in ART protocols, since it determines subsequent successful fertilization, zygote formation, and suitable transition to the blastocyst stage, as well as appropriate implantation (8, 29).

For achieving a high quality embryo, efficient matured oocyte would be necessary. The application of the lab-on-a-chip (LOC) system in reproductive biology provides new possibilities for the development of techniques to assess the developmental competency of mammalian oocytes. This system may provide controllable microenvironments specialized for embryo development in addition to an automated platform for performing the multiple IVF steps (30-33).

Willadsen first reported on the importance of the microenvironment and embryo handling/culture in the 1970s (33). Choi developed a microfluidic device capable of selecting normal oocytes with relatively high specificity (34). Similarly, intrinsic sperm motility and microfluidic laminar flow were used to isolate motile spermatozoa from non-motile sperm, debris and seminal plasma (35, 36). Zeringue developed a microfluidic platform for the control of embryo positioning, movement, and zona pellucida removal for chimeric and transgenic production (37). Although these devices provide convenient handling properties for spermatozoa, oocytes, and embryos, they did not address the potential of microfluidics technology in their developmental competency. Therefore, the present research has been planned to investigate the oocyte maturation improvement.

Our results from this comparative controlled research proposed that the microenvironment obtained by microfluidics supports enhanced the immature oocyte development compared with the conventional static culture conditions and decreased apoptosis rate and MDA level in the dynamic condition in comparison with the static one. The greatest development of immature oocytes has been shown to occur in small volumes or in the presence of

multiple similar cells, which is likely due to the beneficial effects of autocrine oocyte secreted factors (OSFs) (38, 39). Oocyte culture in dynamic condition, due to small microenvironment, result in better effect of autocrine factors (12).

Our findings have also affirmed those of previous studies. We demonstrated that fluid movement and mechanical agitation of immature oocytes during dynamic culture could improve their development. We observed significantly lower apoptosis rate in dynamic culture groups compared to the static group ($P < 0.01$).

Moreover, the MDA level in dynamic groups was considerably low in comparison with the static group ($P < 0.01$). Previous studies did not provide strong evidence concerning oxidative stress in oocytes. The relatively high oxygen concentrations in the pre-implantation embryos disturb the balance between the formation of reactive oxygen species and antioxidants, leading to oxidative stress (40). Esfandiari et al. showed a significant correlation ($P < 0.0001$) between the level of ROS in different embryo culture media and they reported that a positive association between the levels of ROS at 24 hours and the blastocyst apoptosis rate (1). To date, no study compared the level of MDA and apoptosis rate in two culture media (static and dynamic) by the national production, but our results suggest such a survey would be warranted.

Conclusion

In this study, we utilized a microfluidic device for MDA assay and apoptosis rate of *in vitro* matured oocytes compared with the static system. Our results show that the utilization of microfluidic device in order to provide a dynamic culture condition has optimal effects on apoptosis and the decrease of MDA production. In present study, immature oocytes rescued in dynamic condition.

Acknowledgments

This report has been derived from a part of Ph.D. dissertation. The authors thank Electrical and Computer Engineering Faculty, University of Tabriz for excellent technical support and Professor Shuichi Takayama from the University of Michigan for his assistance with microfluidic chip microfabrication. Moreover, we thank Drug Applied Research Center, Tabriz University of Medical Sciences for present research funding. The authors declare no conflicts of interest.

Authors' Contributions

B.S.O.; Wrote the manuscript, carried out and study design the experiment. S.Z.; Designed and fabricated the microfluidic chip. P.S., M.GH.N., M.P.; Participated in evaluation, critical feedback and data analysis. B.S.O., S.Z.; Edited the manuscript. M.P.; Was responsible for

overall supervision. The authors read and approved the final manuscript.

References

1. Esfandiari N, Falcone T, Agarwal A, Attaran M, Nelson DR, Sharma RK. Protein supplementation and the incidence of apoptosis and oxidative stress in mouse embryos. *Obstet Gynecol.* 2005; 105(3): 653-660.
2. Beebe DJ, Glasgow IK, Wheeler MB. Microfluidic embryo and/or oocyte handling device and method. Google Patents; 2001. Available from: <https://patents.google.com/patent/US6193647B1/en> (27 Feb 2001).
3. Agarwal A, Gupta S, Sikka S. The role of free radicals and antioxidants in reproduction. *Curr Opin Obstet Gynecol.* 2006; 18(3): 325-332.
4. Agarwal A, Saleh RA, Bedaiwy MA. Role of reactive oxygen species in the pathophysiology of human reproduction. *Fertil Steril.* 2003; 79(4): 829-843.
5. Vajta G, Rienzi L, Cobo A, Yovich J. Embryo culture: can we perform better than nature? *Reprod Biomed Online.* 2010; 20(4): 453-469.
6. Smith GD, Takayama S, Swain JE. Rethinking in vitro embryo culture: new developments in culture platforms and potential to improve assisted reproductive technologies. *Biol Reprod.* 2012; 86(3): 62.
7. Gardner DK, Kelley RL. Impact of the IVF laboratory environment on human preimplantation embryo phenotype. *J Dev Orig Health Dis.* 2017; 8(4): 418-435.
8. da Rocha AM, Smith GD. Culture systems: fluid dynamic embryo culture systems (microfluidics). *Methods Mol Biol.* 2012; 912: 355-365.
9. Matsuura K, Naruse K. Use of silicone elastomer-based microfluidic devices and systems in reproductive technologies. *Advanced Elastomers-Technology, Properties and Applications: InTech;* 2012. Available from: <https://www.intechopen.com/books/advanced-elastomers-technology-properties-and-applications/use-of-silicone-elastomer-based-microfluidic-devices-and-systems-in-reproductive-technologies> (12 Sep 2012).
10. Hendriksen PJ, Vos PL, Steenweg WN, Bevers MM, Dieleman SJ. Bovine follicular development and its effect on the in vitro competence of oocytes. *Theriogenology.* 2000; 53(1): 11-20.
11. Spindler RE, Pukazhenthil BS, Wildt DE. Oocyte metabolism predicts the development of cat embryos to blastocyst in vitro. *Mol Reprod Dev.* 2000; 56(2): 163-171.
12. Sadeghzadeh Oskouei B, Pashaiasl M, Heidari MH, Salehi M, Veladi H, Ghaderi Pakdel F, et al. Evaluation of mouse oocyte in vitro maturation developmental competency in dynamic culture systems by design and construction of a lab on a chip device and its comparison with conventional culture system. *Cell J.* 2016; 18(2): 205-213.
13. Pelesko JA, Bernstein DH. *Modeling mems and nems.* Boca Raton, Florida: CRC press; 2002.
14. Gaver DP 3rd, Kute SM. A theoretical model study of the influence of fluid stresses on a cell adhering to a microchannel wall. *Biophys J.* 1998; 75(2): 721-733.
15. Zargari S, Veladi H, Sadeghzadeh B, Shahabi P, Frounchi J. A Microfluidic Chip for In Vitro Oocyte Maturation. *Sensor Lett.* 2016; 14(4): 435-440.
16. Quake SR, Scherer A. From micro-to nanofabrication with soft materials. *Science.* 2000; 290(5496): 1536-1540.
17. Johnson TJ, Ross D, Gaitan M, Locascio LE. Laser modification of preformed polymer microchannels: application to reduce band broadening around turns subject to electrokinetic flow. *Anal Chem.* 2001; 73(15): 3656-3661.
18. Heo YS, Cabrera LM, Bormann CL, Shah CT, Takayama S, Smith GD. Dynamic microfunnel culture enhances mouse embryo development and pregnancy rates. *Hum Reprod.* 2010; 25(3): 613-622.
19. Kawamura K, Kawamura N, Mulders SM, Sollewijn Gelpke MD, Hsueh AJ. Ovarian brain-derived neurotrophic factor (BDNF) promotes the development of oocytes into preimplantation embryos. *Proc Natl Acad Sci USA.* 2005; 102(26): 9206-9211.
20. Salimi M, Salehi M, Masteri Farahani R, Dehghani M, Abadi M, Novin MG, et al. The effect of melatonin on maturation, glutathione level and expression of H MGB1 gene in brilliant cresyl blue (BCB) stained immature oocyte. *Cell J.* 2014; 15(4): 294-301.
21. Eddings MA, Johnson MA, Gale BK. Determining the optimal PDMS-PDMS bonding technique for microfluidic devices. *Journal*

- of Micromechanics and Microengineering. 2008; 18(6): 067001.
22. Martin-Coello J, Gonzalez R, Crespo C, Gomendio M, Roldan ER. Superovulation and in vitro oocyte maturation in three species of mice (*Mus musculus*, *Mus spretus* and *Mus spicilegus*). *Theriogenology*. 2008; 70(6): 1004-1013.
 23. Singh H, Ang ES, Lim T, Huttmacher DW. Flow modeling in a novel non-perfusion conical bioreactor. *Biotechnol Bioeng*. 2007; 97(5): 1291-1299.
 24. Xie Y, Wang F, Zhong W, Puscheck E, Shen H, Rappolee DA. Shear stress induces preimplantation embryo death that is delayed by the zona pellucida and associated with stress-activated protein kinase-mediated apoptosis. *Biol Reprod*. 2006; 75(1): 45-55.
 25. Fauci LJ, Dillon R. Biofluidmechanics of reproduction. *Annu Rev Fluid Mech*. 2006; 38(1): 371-394.
 26. Johnson JE, Higdon HL 3rd, Boone WR. Effect of human granulosa cell co-culture using standard culture media on the maturation and fertilization potential of immature human oocytes. *Fertil Steril*. 2008; 90(5): 1674-1679.
 27. Smith GD, Takayama S. Gamete and embryo isolation and culture with microfluidics. *Theriogenology*. 2007; 68 Suppl 1: S190-S195.
 28. McDonald JC, Duffy DC, Anderson JR, Chiu DT, Wu H, Schueller OJ, et al. Fabrication of microfluidic systems in poly (dimethylsiloxane). *Electrophoresis*. 2000; 21(1): 27-40.
 29. Ghaffari Novin M, Noruzinia M, Allahveisi A, Saremi A, Fadaei Fathabadi F, Mastery Farahani R, et al. Comparison of mitochondrial-related transcriptional levels of TFAM, NRF1 and MT-CO1 genes in single human oocytes at various stages of the oocyte maturation. *Iran Biomed J*. 2015; 19(1): 23-28.
 30. Antosik P, Kempisty B, Jackowska M, Piotrowska H, Bukowska D, Wozna M, et al. Assessment of transcript and protein levels contributing to cell cycle control and gap junction connections in morphologically variable groups of porcine cumulus-oocyte complexes. *Vet Med-Czech*. 2010; 55(10): 512-521.
 31. Bukowska D, Kempisty B, Antosik P, Jaśkowski J, Olechnowicz J. Selected aspects of canine oocytes maturation, fertilization and embryo development in dogs. *Medycyna Weterynaryjna*. 2008; 64(5): 628-6231.
 32. Kempisty B, Antosik P, Bukowska D, Jackowska M, Lianeri M, Jaśkowski JM, et al. Assessment of zona pellucida glycoprotein and integrin transcript contents in porcine oocytes. *Reprod Biol*. 2009; 9(1): 71-78.
 33. Willadsen SM. A method for culture of micromanipulated sheep embryos and its use to produce monozygotic twins. *Nature*. 1979; 277(5694): 298-300.
 34. Choi W, Kim JS, Lee DH, Lee KK, Koo DB, Park JK. Dielectrophoretic oocyte selection chip for in vitro fertilization. *Biomed Microdevices*. 2008; 10(3): 337-345.
 35. Cho BS, Schuster TG, Zhu X, Chang D, Smith GD, Takayama S. Passively driven integrated microfluidic system for separation of motile sperm. *Anal Chem*. 2003; 75(7): 1671-1675.
 36. Schuster TG, Cho B, Keller LM, Takayama S, Smith GD. Isolation of motile spermatozoa from semen samples using microfluidics. *Reprod Biomed Online*. 2003; 7(1): 75-81.
 37. Zeringue HC, Rutledge JJ, Beebe DJ. Early mammalian embryo development depends on cumulus removal technique. *Lab Chip*. 2005; 5(1): 86-90.
 38. Hardy K, Spanos S. Growth factor expression and function in the human and mouse preimplantation embryo. *J Endocrinol*. 2002; 172(2): 221-236.
 39. Diaz-Cueto L, Gerton GL. The influence of growth factors on the development of preimplantation mammalian embryos. *Arch Med Res*. 2001; 32(6): 619-626.
 40. Guerin P, El Mouatassim S, Menezo Y. Oxidative stress and protection against reactive oxygen species in the pre-implantation embryo and its surroundings. *Hum Reprod Update*. 2001; 7(2): 175-189.

The Contribution of Y Chromosome Genes to Spontaneous Differentiation of Human Embryonic Stem Cells into Embryoid Bodies *In Vitro*

Simin Nafian Dehkordi, M.Sc.^{1,2}, Farzaneh Khani, M.Sc.^{1,2}, Seyedeh Nafiseh Hassani, Ph.D.³, Hossein Baharvand, Ph.D.^{3, 4},
Hamid Reza Soleimanpour-lichaei, Ph.D.^{1*}, Ghasem Hosseini Salekdeh, Ph.D.^{2, 5, 6*}

1. Department of Stem Cells and Regenerative Medicine, Institute of Medical Biotechnology, National Institute of Genetic Engineering and Biotechnology (NIGEB), Tehran, Iran
2. Department of Molecular Systems Biology, Cell Science Research Center, Royan Institute for Stem Cell Biology and Technology, ACECR, Tehran, Iran
3. Department of Stem Cells and Developmental Biology, Cell Science Research Center, Royan Institute for Stem Cell Biology and Technology, ACECR, Tehran, Iran
4. Department of Developmental Biology, University of Science and Culture, Tehran, Iran
5. Department of Systems Biology, Agricultural Biotechnology Research Institute of Iran, Karaj, Iran
6. Department of Molecular Sciences, Macquarie University, Sydney, NSW, Australia

*Corresponding Addresses: P.O.Box: 14965-161, Department of Stem Cells and Regenerative Medicine, Institute of Medical Biotechnology, National Institute of Genetic Engineering & Biotechnology (NIGEB), Tehran, Iran
P.O.Box: 16635-148, Department of Molecular Systems Biology, Cell Science Research Center, Royan Institute for Stem Cell Biology and Technology, ACECR, Tehran, Iran
Emails: hrs@nigeb.ac.ir, hsalekdeh@yahoo.com

Received: 10/September/2019, Accepted: 30/December/2019

Abstract

Objective: Sexual dimorphism in mammals can be described as subsequent transcriptional differences from their distinct sex chromosome complements. Following X inactivation in females, the Y chromosome is the major genetic difference between sexes. In this study, we used a male embryonic stem cell line (Royan H6) to identify the potential role of the male-specific region of the Y chromosome (MSY) during spontaneous differentiation into embryoid bodies (EBs) as a model of early embryonic development.

Materials and Methods: In this experimental study, RH6 cells were cultured on inactivated feeder layers and Matrigel. In a dynamic suspension system, aggregates were generated in the same size and were spontaneously differentiated into EBs. During differentiation, expression patterns of specific markers for three germ layers were compared with MSY genes.

Results: Spontaneous differentiation was determined by downregulation of pluripotent markers and upregulation of fourteen differentiation markers. Upregulation of the ectoderm markers was observed on days 4 and 16, whereas mesoderm markers were upregulated on the 8th day and endodermic markers on days 12-16. Mesoderm markers correlated with 8 MSY genes namely *DDX3Y*, *RPS4Y1*, *KDM5D*, *TBL1Y*, *BCORP1*, *PRY*, *DAZ*, and *AMELY*, which were classified as a mesoderm cluster. Endoderm markers were co-expressed with 7 MSY genes, i.e. *ZFY*, *TSPY*, *PRORY*, *VCY*, *EIF1AY*, *USP9Y*, and *RPKY*, which were grouped as an endoderm cluster. Finally, the ectoderm markers correlated with *TXLNGY*, *NLGN4Y*, *PCDH11Y*, *TMSB4Y*, *UTY*, *RBMY1*, and *HSFY* genes of the MSY, which were categorized as an ectoderm cluster. In contrast, 2 MSY genes, *SRY* and *TGIF2LY*, were more highly expressed in RH6 cells compared to EBs.

Conclusion: We found a significant correlation between spontaneous differentiation and upregulation of specific MSY genes. The expression alterations of MSY genes implied the potential responsibility of their gene co-expression clusters for EB differentiation. We suggest that these genes may play important roles in early embryonic development.

Keywords: Embryoid Bodies, Human Embryonic Stem Cells, Human Y Chromosome Proteome Project, RH6 Cell Line, Spontaneous Differentiation

Cell Journal(yakhteh), Vol 23, No 1, April-June (Spring) 2021, Pages: 40-50

Citation: Nafian Dehkordi S, Khani F, Hassani SN, Baharvand H, Soleimanpour-lichaei HR, Hosseini Salekdeh Gh. The contribution of y chromosome genes to spontaneous differentiation of human embryonic stem cells into embryoid bodies in vitro. Cell J. 2021; 23(1): 40-50. doi: 10.22074/cellj.2021.7145. This open-access article has been published under the terms of the Creative Commons Attribution Non-Commercial 3.0 (CC BY-NC 3.0).

Introduction

Immediately after fertilization, the sex of the human embryo is determined by the spermatozoon carrying either a Y or an X chromosome (1). The sex chromosomes induce specific aspects of organ development in the absence of gonadal sex hormones (2). There are fundamental metabolic differences between female and male preimplantation embryos (3, 4). Briefly, three main aspects of sexual dimorphism have been observed including gene expression profiles, kinetics of growth, and embryonic mortality (5). Male embryos have a greater

number of cells and metabolic activities than females with a significantly faster development (6-8).

Sexual dimorphisms are genetically initiated very early in embryonic development (9, 10); however the exact molecular mechanisms leading these differences remain to be comprehended. The sex chromosomes have conserved the essential sex-specific genes on a set of ancestral autosomes (11). Different chromosomal complements can display sexual dimorphism due to the different expression patterns of genes during preimplantation development

(12, 13). The X chromosome is inactivated in the differentiated state of human embryonic stem cells (hESCs), causing the same content of the X chromosome in both sexes (14). Otherwise, it typically results in premature abortion and fetal death (15). The Y chromosome is the major genetic difference between sexes and plays an important role in male embryos especially at the preimplantation stage of early fetus development. The Y chromosome size is approximately 60 Mb containing two distinct segments. The male-specific region of the Y chromosome (MSY) contains genes specific to sexual dimorphism and undergoes no meiotic crossing over with a homolog. Two pseudo-autosomal regions flank the MSY on both sides and frequently undergo X–Y crossing over at male meiosis. (16). There are 47 genes on the MSY region as described in NeXtProt, of which 26 genes are validated at protein level (PE1), 11 genes at transcript level (PE2), 3 genes at homology base (PE3) and 7 genes at uncertain level (PE5) (www.nextprot.org, v2.23.1).

The Chromosome-Centric Human Proteome Project (C-HPP) has been established to identify all proteins encoded by each human chromosome (17, 18). The Y-Chromosome Human Proteome Project (Y-HPP), as part of C-HPP, identifies and annotates protein products of the Y chromosome genes using many methods including the cell-based approach, as one of the most important approaches (19). By taking advantage of hESCs, we can show how Y-HPP has been conducted to gain a rich understanding of the MSY genes during development. Two individual characteristics of hESCs make them well-matched for this kind of studies. First, hESCs provide a unique self-renewal capacity and an abundant source for proteomics analysis. Second, hESCs offer an interesting opportunity for simulating human embryonic development *in vitro* by generating all cell types related to the three germ layers (20).

In hESCs, a range of tissue-specific differentiation is initiated via the formation of tissue-like spheroids called embryoid bodies (EBs) (21). EBs are 3-dimensional ESC aggregates that can determine the major genes involved in early embryogenesis following the lineage events to form three germ layers (mesoderm, endoderm, and ectoderm) (21-23). The lineage-specific differentiation of EBs *in vitro* recapitulates those seen in the developing embryo *in vivo* (24). On the other hand, EBs establish a model to simulate the *in vivo* differentiation process of ESCs under *in vitro* conditions to find the missing proteins by analyzing their expression levels and study possible effects of the human Y chromosome genes during spontaneous differentiation of hESCs (25-27). Although the expression profile of MSY genes has been transcriptionally detected in human pluripotent stem cells (28), a systematic expression profiling at the early developmental stages is needed. Here we aimed to determine a dynamic pattern of 38 MSY gene expressions at the early developmental stages of

hESCs into EBs by analyzing transcriptional data.

Materials and Methods

Cell culture

This experimental study was carried out in accordance with the guide for the care and use of laboratory animals and approved by the Local Ethical Committee of Royan Institute for Stem Cell Biology and Technology with a code number IR.ACECR.ROYAN.REC.1396.15.

In this study, Royan H6 (RH6), a human embryonic stem cell line, was cultured on a mouse embryonic fibroblast (MEF) feeder layer. MEFs were mitotically inactivated prior to the addition of the RH6 cells by adding mitomycin C (10 µg/mL, Sigma, Netherlands). The base media for hESC was prepared with a combination of DMEM / F12 (Gibco) supplemented with 20% knockout serum replacement (KOSR, Gibco), 1% nonessential amino acids (Gibco), 1% insulin-transferrin-selenium (ITS, Invitrogen), 0.1mM beta-mercaptoethanol (Sigma, Germany), and 100 units/mL penicillin and 100µg / mL streptomycin (Gibco). Human recombinant bFGF (Basic fibroblast growth factor) (Royan Biotech, Iran) was added to the hESC media (final concentration, 12 ng/ml) at the seeding time. The cell cultures were incubated at 37°C in a 5% CO₂ atmosphere with daily media changes. The cells were passaged upon reaching 70% confluence. Then, RH6 cells were cultured on a thin Matrigel layer in hESC media containing 100 ng/ml bFGF free of any feeder cells for induction of an efficient differentiation. Freshly coated-Matrigel plates were prepared at least 2 hours prior to seeding the cells, according to manufacturer's instructions. Briefly, for a 6-well plate, 500 µL of diluted Matrigel solution was used per well and incubated at 37°C to be polymerized. RH6 cells were directly seeded on the wet Matrigel coated plate and allowed to settle for 30-90 minutes in an incubator (5% CO₂, 37°C) before flooding them with culture media. The hESC media was carefully added to each sample well. The cultures were maintained for 7 days, with daily media changes to form the RH6 colonies.

Dynamic suspension of expanded RH6

After two passages on Matrigel, the RH6 cells were transferred to 125 mL spinner flask (Cellspin; Integra Biosciences AG, Switzerland) at a 40rpm agitation rate. For large-scale expansion, a 100-ml working volume was used as previously described (29). Briefly, undifferentiated RH6 cells were cultured with the optimal starting concentration of 2–3×10⁵ cells/mL at the hESC media, which was conditioned by MEFs, fresh 10 mM Rho-associated kinase inhibitor (ROCKi; Sigma, Netherlands) and 100 ng/mL bFGF. The spinner flask was placed on a magnetic stir plate in an incubator at 37°C and 5% CO₂ without changing media during the first two days. RH6 cells were expanded in a 3D-dynamic suspension culture after 4 days.

Spontaneous differentiation of RH6 into EBs

In the current study, RH6 cells were grown on inactivated

feeder layers to gain the growth factors, cytokines and nutrients required for maintaining pluripotency. The cells were then transferred onto Matrigel (Sigma, Germany) to be free of any feeder cells and were prepared for a successful differentiation. The same size aggregates were generated from single cells in a dynamic suspension system and spontaneously differentiated into three embryonic germ layers of EBs. RH6 3D aggregates were formed in controlled sizes and shapes by optimizing the agitation speed, the impeller type and the incubation density for 4 days. The homogeneously sized colonies ($175 \pm 25 \mu\text{m}$, approximately) were used to generate EBs by inducing spontaneous differentiation in static suspension condition for 20 days. The EB differentiation media consisted of KnockOut DMEM/F-12 base media, supplemented with 20% fetal bovine serum (FBS; Hyclone), 0.05 mM beta-

mercaptoethanol, 1% glutamine (Gibco), 1% essential amino acids, 100 units/mL penicillin and 100 $\mu\text{g/mL}$ streptomycin. For spontaneous differentiation, RH6 aggregates were cultured as a static suspension system in a 6-cm ultra-low attachment dish containing 5 ml of bFGF-free media for 8 days. The culture media was changed every 2 days. On day 8, RH6 aggregates were transferred into 0.1% gelatin-coated plates to maintain spontaneous differentiation in a 2D cell culture system for 12 days, hence undergoing a 20-day differentiation. Samples were collected at several time points (0, 4, 8, 12, 16 and 20 days) for expression analysis of the pluripotency and differentiation markers in comparison to the MSY genes in early embryonic development (Table 1, See supplementary online information at www.celljournal.org). A schematic summarizing the different steps to generate EBs is shown in Figure 1.

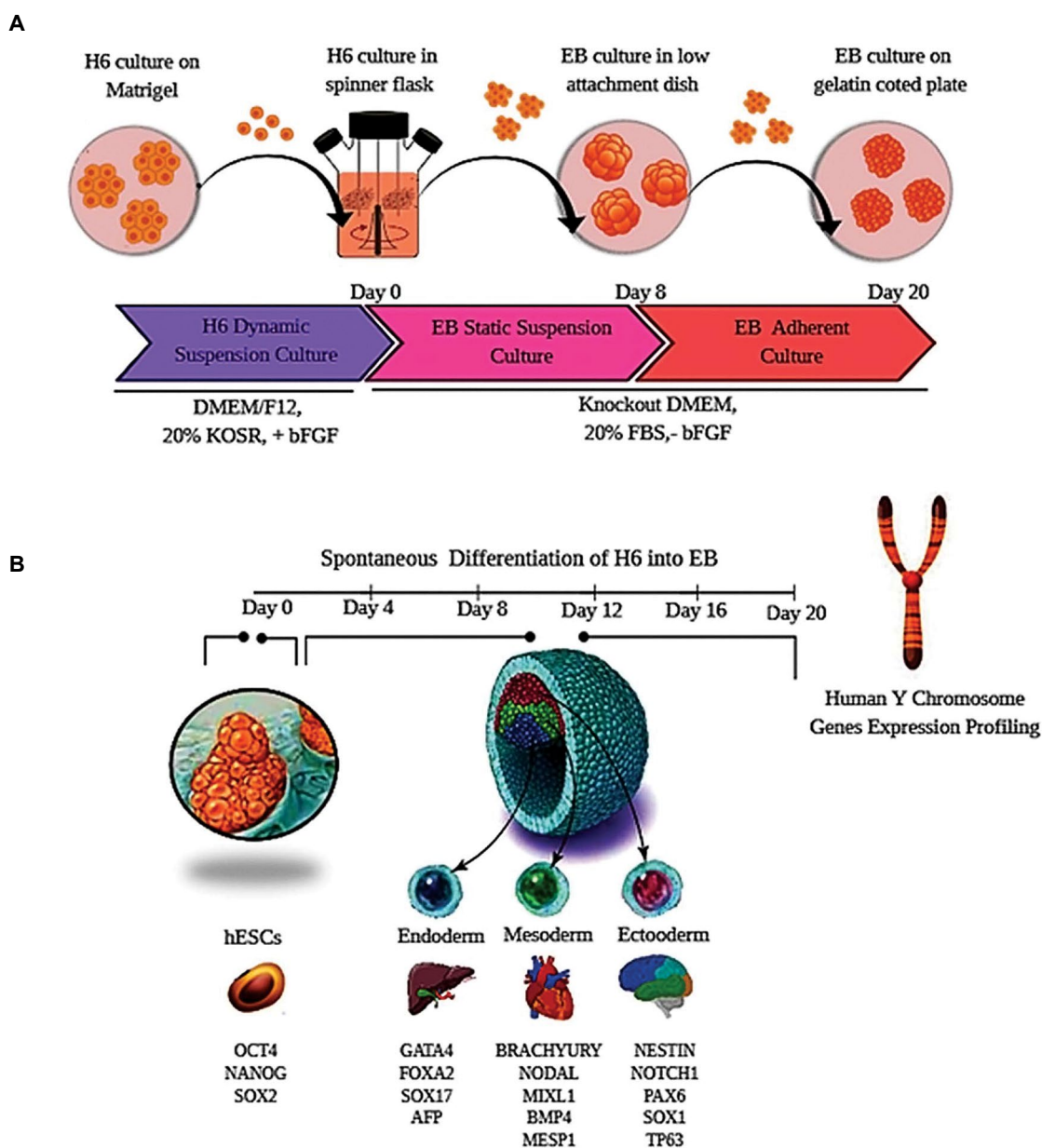


Fig. 1: Schematic view of spontaneous differentiation of RH6 cell suspension into EBs. **A.** Dynamic suspension culture of RH6 in spinner flasks was followed by a two-stage differentiation into EBs in static suspension and adherent cultures, sequentially. **B.** Several time points were found for expression analysis of the pluripotent and differentiation markers. The expression of MSY genes was also investigated to compare with the markers in three germ layers of EBs. RH6; Royan H6, EBs; Embryoid bodies, and MSY; The male-specific region of the Y chromosome.

Ribonucleic Acid Isolation and Quantitative Real-Time PCR (qRT-PCR)

According to the manufacturer's protocol, total Ribonucleic acid (RNA) was isolated using TRIzol reagent (Invitrogen, USA). The purified RNA was reverse-transcribed into cDNA. Quantitative real-time PCR (qRT-PCR) was performed in the Rotor Gene 6000 (Corbett, Australia). *GAPDH* was used as the housekeeping gene. Finally, relative changes in gene expression levels were calculated by the threshold (quantification) cycle. The primer sequences (pluripotent and the three layer-specific markers) are shown in a Table 2, See supplementary online information at www.celljournal.org). The highly specific primers were designed for MSY genes using Vector NTI software (Life Sciences, USA) and verified with NCBI Primer-BLAST (<https://www.ncbi.nlm.nih.gov/tools/primer-blast>) (30). The primer sequences (MSY genes and transcript variants) are shown in a Table 3, See supplementary online information at www.celljournal.org.

Statistical Analysis

Statistical analysis was performed for three biological replicates of each gene. Data are presented as mean \pm SEM. Statistical significance was detected using a two-way ANOVA (* $P < 0.05$) in Graphpad Prism software (Graphpad Software, USA). The relative expressions were compared to D0. Heatmap was generated using the heatmap.2 and g-plots libraries in the statistical software R (<http://www.r-project.org>). Heatmap was used to generate gene co-expression clusters based on pairwise Spearman correlations. Each square determined the correlation value between expression profiles of two genes. According to matched expression profiles, hierarchical clustering trees of the genes were shown in the top and left sides. The circo map was created with circo software (<http://www.circo.ca>).

Results

Generation of the three embryonic germ layers

To study the role of MSY genes in early embryonic development, RH6 cells were induced to differentiate spontaneously into the three embryonic germ layers of EBs. Stem cells were initially cultured on MEFs and Matrigel as a feeder layer and complex protein matrix, respectively, to maintain self-renewal and pluripotency (Fig.2A). Then, in a 3D dynamic suspension culture, RH6 single cells formed colonies with the same size and retained the characteristics of an undifferentiated hESC. Stem cell aggregates grew as a homogenous population of small cells forming spheroid clumps with distinct borders (Fig.2B). Differentiation was spontaneously induced through two sequential steps. At first, the aggregates with equal sizes made distinct cystic structures in a static suspension culture and closely compacted as a dark cavity in the center of the spheroid clumps like a solid ball. Therefore, EBs were well-organized with 3 germ layers which enlarged several times (Fig.2C). In the next step, EBs were cultured on a gelatin-coated plate as 2D

culture systems to sequentially generate endodermal and ectodermal layers (Fig.2D).

Expression of pluripotency and layer-specific markers during differentiation

We investigated the expression of some specific markers to evaluate cellular pluripotency and spontaneous differentiation at several time points (0, 4, 8, 12, 16 and 20 days). QRT-PCR was used to investigate the expressions of pluripotency markers (*OCT4*, *NANOG*, and *SOX2*), as well as some layer-specific markers including mesoderm (*NODAL*, *MIXL1*, *BMP4*, *MESPI*, and *BRACHYURY* (T)), endoderm (*GATA4*, *FOXA2*, *SOX17*, and *AFP*), and ectoderm (*NESTIN*, *NOTCH1*, *PAX6*, *TP63* and *SOX1*) markers.

For assessment of spontaneous differentiation, we also compared the expression of pluripotency and layer-specific markers in all samples. Although layer-specific markers showed very low expression levels in undifferentiated cells, they increased during RH6 differentiation (Fig.3A). Spearman correlation was applied by Heatmap to identify clusters with highly similar temporal expression patterns at several time points. Our analysis showed four distinct marker clusters (Fig.3B). The first cluster consisted of pluripotency markers including *OCT4*, *NANOG*, and *SOX2*, which are highly expressed in stem cells. The expression of pluripotency markers were significantly reduced or absent following the initiation of differentiation (Fig.3C). The second cluster consisted of 5 markers, including *NODAL*, *MIXL1*, *BMP4*, *MESPI*, and *BRACHYURY* (T), which were more expressed during spontaneous EB differentiation. It was indicated by an increased expression region for mesoderm markers on days 8, approximately, followed by a gradual decrease (Fig.3C). The third cluster consisted of 4 markers including *GATA4*, *FOXA2*, *SOX17*, and *AFP*, which are endoderm markers. Hierarchical clustering dendrogram of *GATA4*, *SOX17*, and *AFP* were more correlated than *FOXA2*. Endoderm markers showed a more identical pattern in comparison with the rest of the clusters (Fig.3C). The expression pattern of endoderm markers indicated a transient suppression until day 4 by differentiation initiation, following an enhancement on days 12-16 and ultimately a reduction on day 20 (Fig.3C). The fourth cluster including *NESTIN*, *NOTCH1*, *PAX6*, *TP63*, and *SOX1* were ectoderm markers. The expression pattern of *NESTIN*, *NOTCH1*, *PAX6*, and *TP63* were more correlated compared to *SOX1*. They were moderately upregulated at the beginning of differentiation and downregulated on day 8. However, the expression of the ectoderm markers slowly increased from day 12 up to day 16, when the maximum expression level was observed. Our results showed an upregulation of the ectoderm markers on days 4 and 16. From day 16 to 20, however, their expressions slowly decreased (Fig.3C).

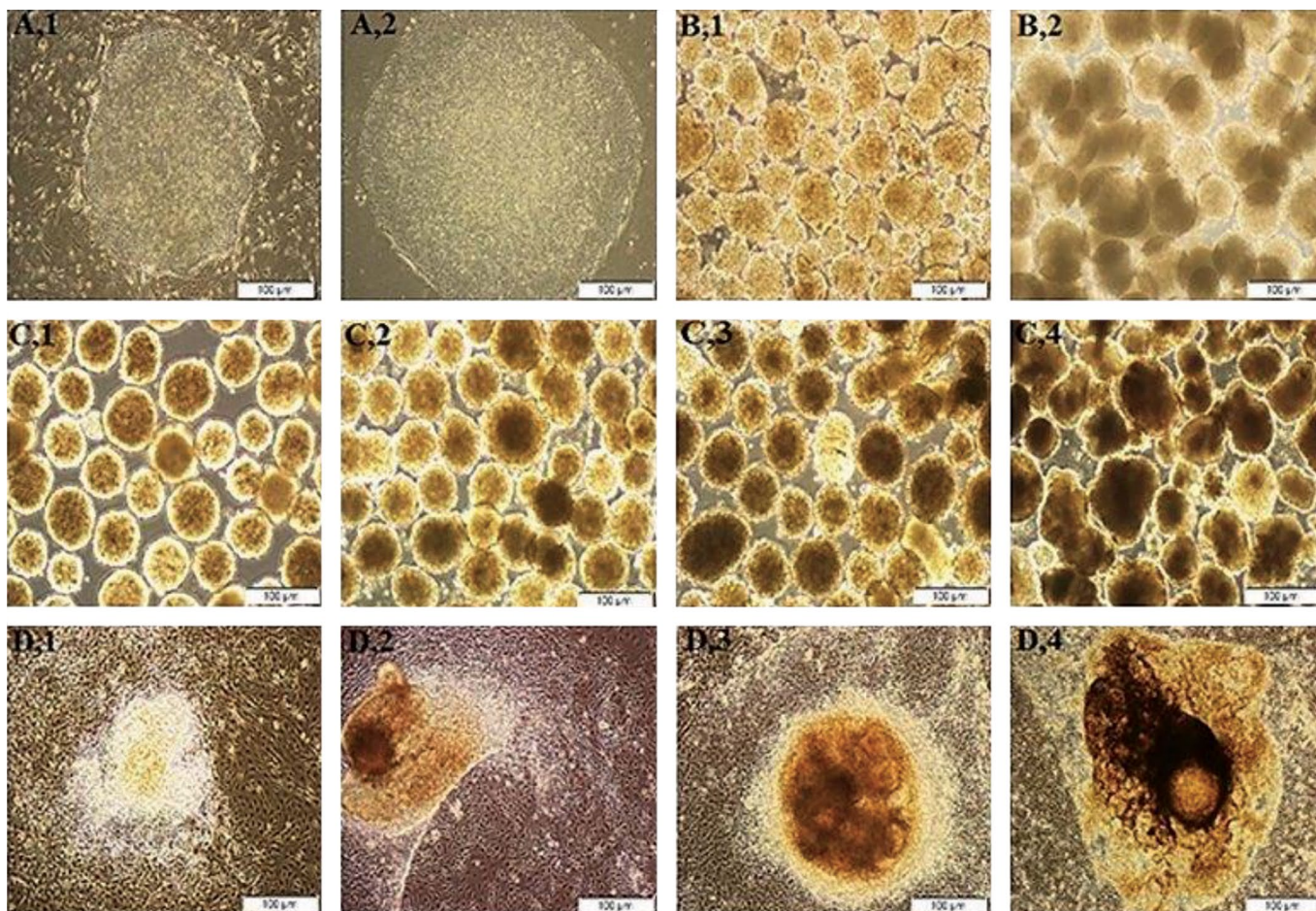


Fig.2: Morphology of RH6 colonies and EBs. **A.** Undifferentiated RH6 showed typical flat colonies with tight edge on the feeder layer (A1) and Matrigel (A2). **B.** The Single cells aggregated in a dynamic suspension culture for 4 days. On the first 3 days, RH6 created spheroid clumps or disc-like structures with a homogenous population of small cells (B1). On days 4, the aggregates were the same size (B2). **C.** In a static suspension culture, RH6 aggregates spontaneously differentiated into the EBs for 8 days. The aggregates of equal sizes on day 2 (C1) changed to the cystic and dense regions after 4 days (C2). EBs showed a dark cavity containing three germ layers on days 6 and 8, respectively (C3 and C4). **D.** 3D aggregates continued spontaneous differentiation in a 2D cell culture system for more than 12 days. Scale bar is 100µm. RH6; Royan H6, EBs; Embryoid bodies., 3D; Three dimensional (3D)-dynamic suspension culture, and 2D; Two dimensional (2D) cell culture system.

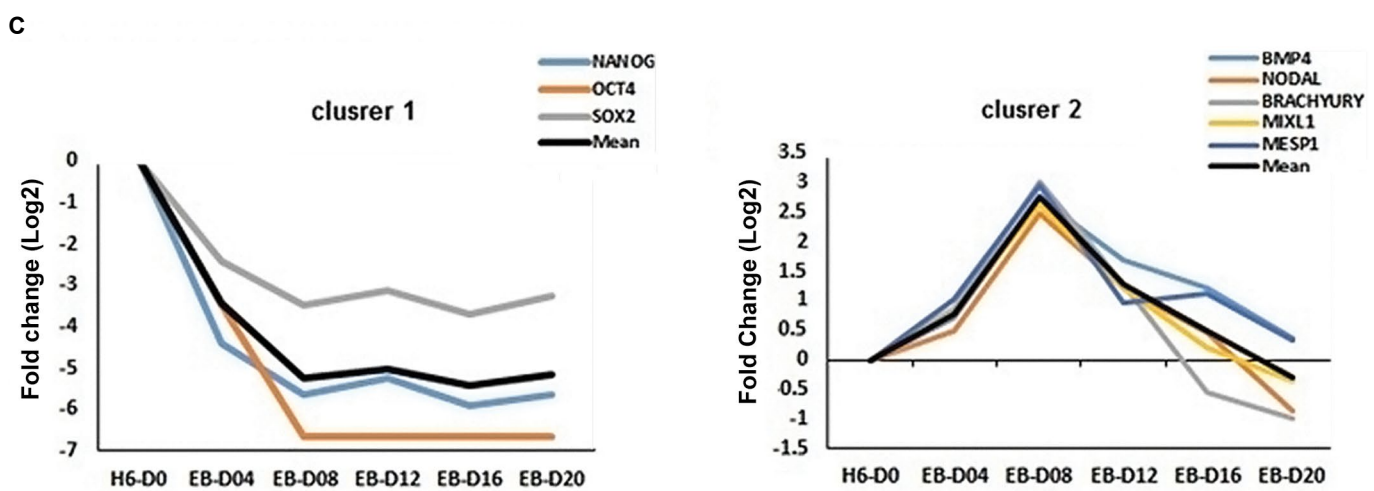
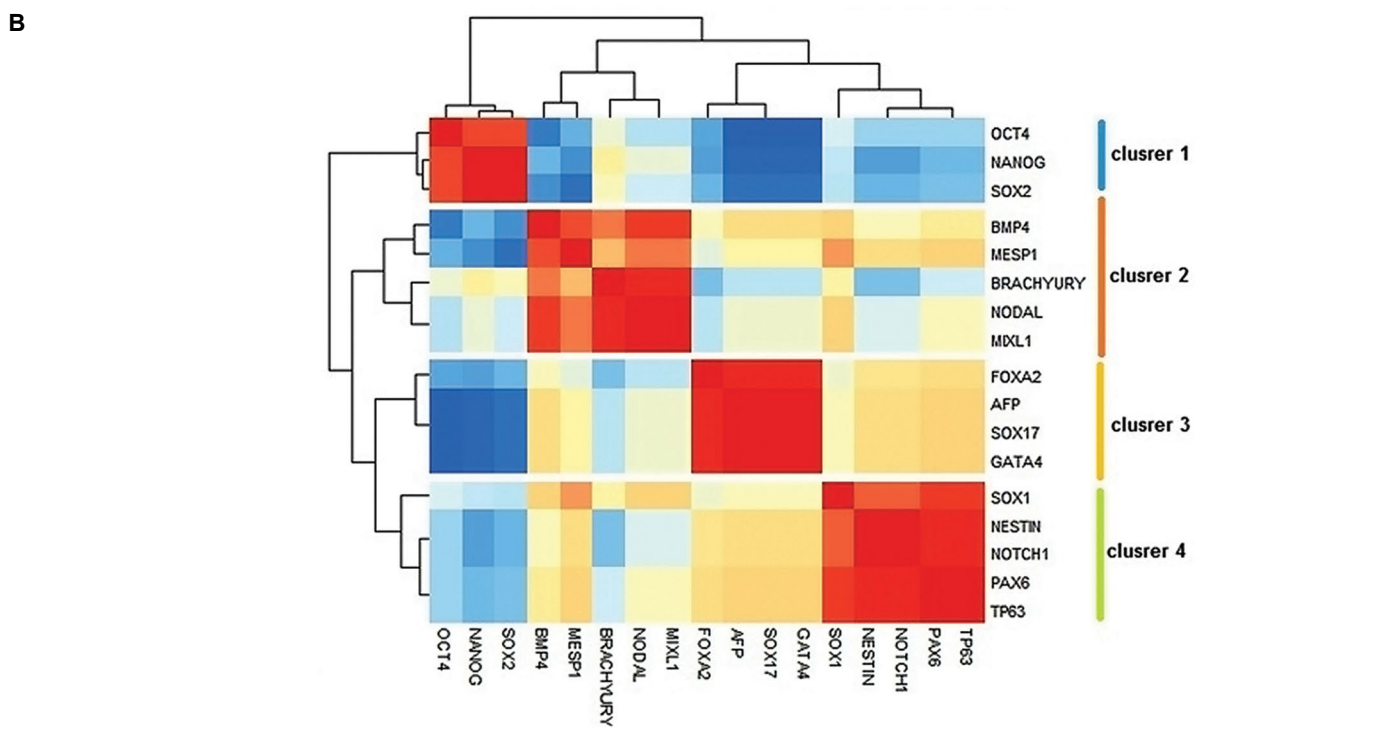
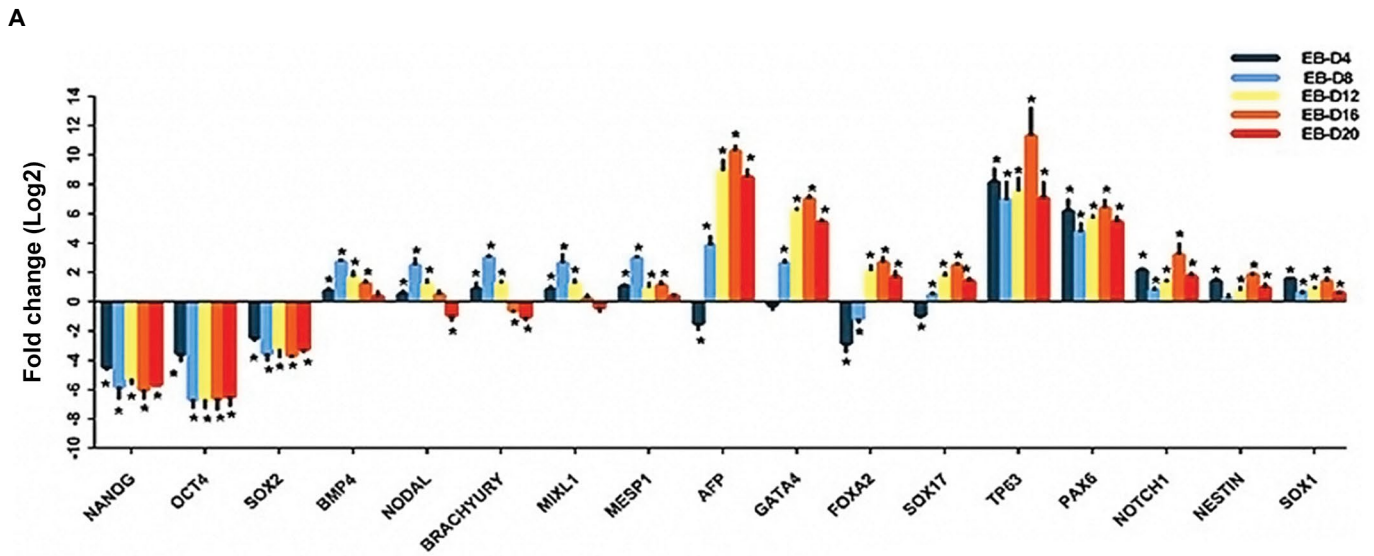
The expression pattern of MSY genes in EB

The X-degenerate, X-transposed and ampliconic segments are euchromatic sequences of the MSY region of the Y chromosome [16]. The *NLGN4Y*, *SRY*, *ZFY*, *TXLNGY*, *AMELY*, *EIF1AY*, *GYG2P1*, *DDX3Y*, *UTY*, *RPS4Y1*, *USP9Y*, *TBL1Y*, *KDM5D*, *TMSB4Y*, *PRKY*, and *RPS4Y2* genes are located on the X-degenerate segment. The X-transposed sequences encode the *TGIF2LY* and *PCDH11Y* genes, and the ampliconic segment encodes 8 gene families namely *DAZ*, *CDY*, *VCY*, *HSFY*, *RBMX*, *TSPY*, *BPY2*, and *PRY* (31, 32).

We investigated the expression pattern of Y chromosome genes to determine the genes involved in early EB differentiation. In general, our analysis was performed for 24 genes at protein evidence level (PE1), 8 genes at transcript evidence (PE2), 3 genes inferred from homology levels (PE3), as well as 3 genes at uncertain protein level (PE5), that have been

demonstrated in Figure S1, See supplementary online information at www.celljournal.org.

MSY genes showed altered expression levels during EB differentiation, as summarized in Figure 4. The expression pattern of 38 MSY genes was compared by Circos map at several time points (0, 4, 8, 12, 16 and 20 days, Fig.4). The inner colored segments were representative for each specific gene and the outer segments demonstrated the differentiation time points. The green segment, for example, was related to the *ZFY* transcript showing the maximum expression on days 16 (EB-D16, 85%), 12 (EB-D12, 5%) and 20 (EB-D20, 10%), respectively. The outside segment of differentiation time points represented the contribution of the Y chromosome genes in each group (i.e. in EB-D16, *ZFY* had the highest fold change ~ 35% among MSY genes). The inner segment of differentiation time points showed that most of the MSY genes were upregulated at EB-D16 (0-145).



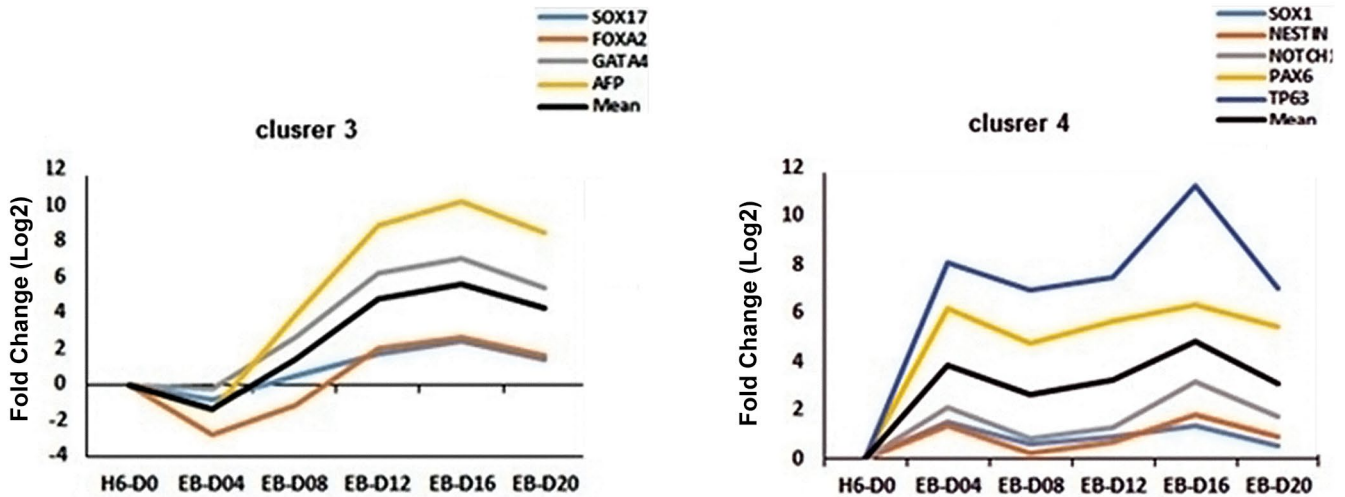


Fig.3: Analysis of expression patterns of pluripotent and layer-specific markers during EB differentiation. **A.** The expression pattern of pluripotent and three germ layer markers. **B.** Co-expressions of 17 markers in EB differentiation. **C.** Expression profiles for genes were shown in four clusters. Y-axis represents the difference between expression of the genes of a particular cluster and the mean expression of this cluster during time points suggesting the number of standard deviations that a particular data point differs from the mean. All data were presented as mean \pm SEM (* $P < 0.05$). EBs; Embryoid bodies.

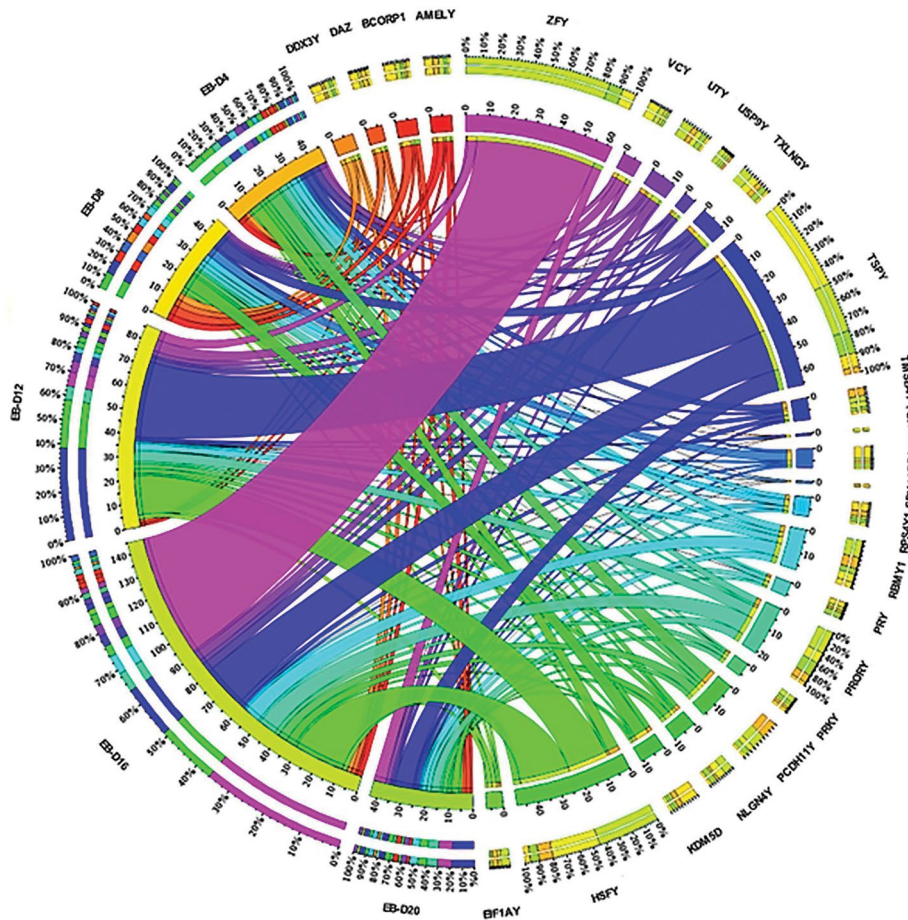


Fig.4: Schematic of dysregulated MSY transcripts during spontaneous differentiation. Circos map compared the expression pattern of 38 MSY genes at several time points (0, 4, 8, 12, 16 and 20 days). The expression of genes was related to time points of differentiation by inner arcs. The MSY genes were sorted in a descending order. Thus the *ZFY* gene, for example, had the maximal upregulation (0-60) at EB-D16 (~35%) while *SRY* and *TGIF2LY* indicated the maximal downregulation (0-2) during EB differentiation. MSY; The male-specific region of the Y chromosome and EBs; Embryoid bodies.

The expression of MSY genes and EB markers were compared by Spearman's Heatmap. The results detected four clusters, which contained highly correlated genes (Fig.5). The mesoderm markers showed high correlation with 8 MSY genes including *KDM5D*, *DDX3Y*, *RPS4Y1*, *TBL1Y*, *BCORP1*, *PRY*, *DAZ*, and *AMELY* (Fig.5). These genes were highly increased by differentiation initiation up to day 8 and were categorized as a mesoderm cluster (Fig.6A). The endoderm cluster was arranged based on a high correlation between endoderm markers and the 7 MSY genes: *ZFY*, *TSPY*, *PRORY*, *VCY*, *EIF1AY*, *USP9Y*, and *RPKY* (Fig.5). Among the mentioned genes, *VCY* and *TSPY* showed more correlation with endoderm markers by the Hierarchical clustering trees (Fig.6B). The ectoderm markers were grouped with 7 genes known as *TXLNGY*, *NLGN4Y*, *PCDH11Y*, *TMSB4Y*, *UTY*, *RBMY1*, and *HSFY* as an ectoderm cluster (Fig.5). The expression

pattern of *PCDH11Y* and *TMSB4Y* demonstrated a high correlation with *SOX1*, which was increased by differentiation initiation on day 4 followed by a severe downregulation by day 16. In contrast, the expression pattern of *RBMY1*, *HSFY*, *TXLNGY*, *NLGN4Y*, and *UTY*, which were upregulated from day 12 to the end, was similar to *NESTIN*, *NOTCH1*, *PAX6*, and *TP63* as ectoderm markers (Fig.6C). Some of the MSY genes including *EIF1AY*, *PRKY*, *RPS4Y1*, *SRY*, *USP9Y*, *UTY*, *TXLNGY*, *TBL1Y*, and *TGIF2LY* showed higher expression levels in RH6 cells (Fig.6D). The Spearman's analysis showed that pluripotency markers were more closely correlated with *SRY* and *TGIF2LY* genes, which were highly expressed in RH6 cells, but decreased by initiation of differentiation and remained at low levels throughout the differentiation period (Fig.6E). These genes were classified as a pluripotent cluster (Fig.5).

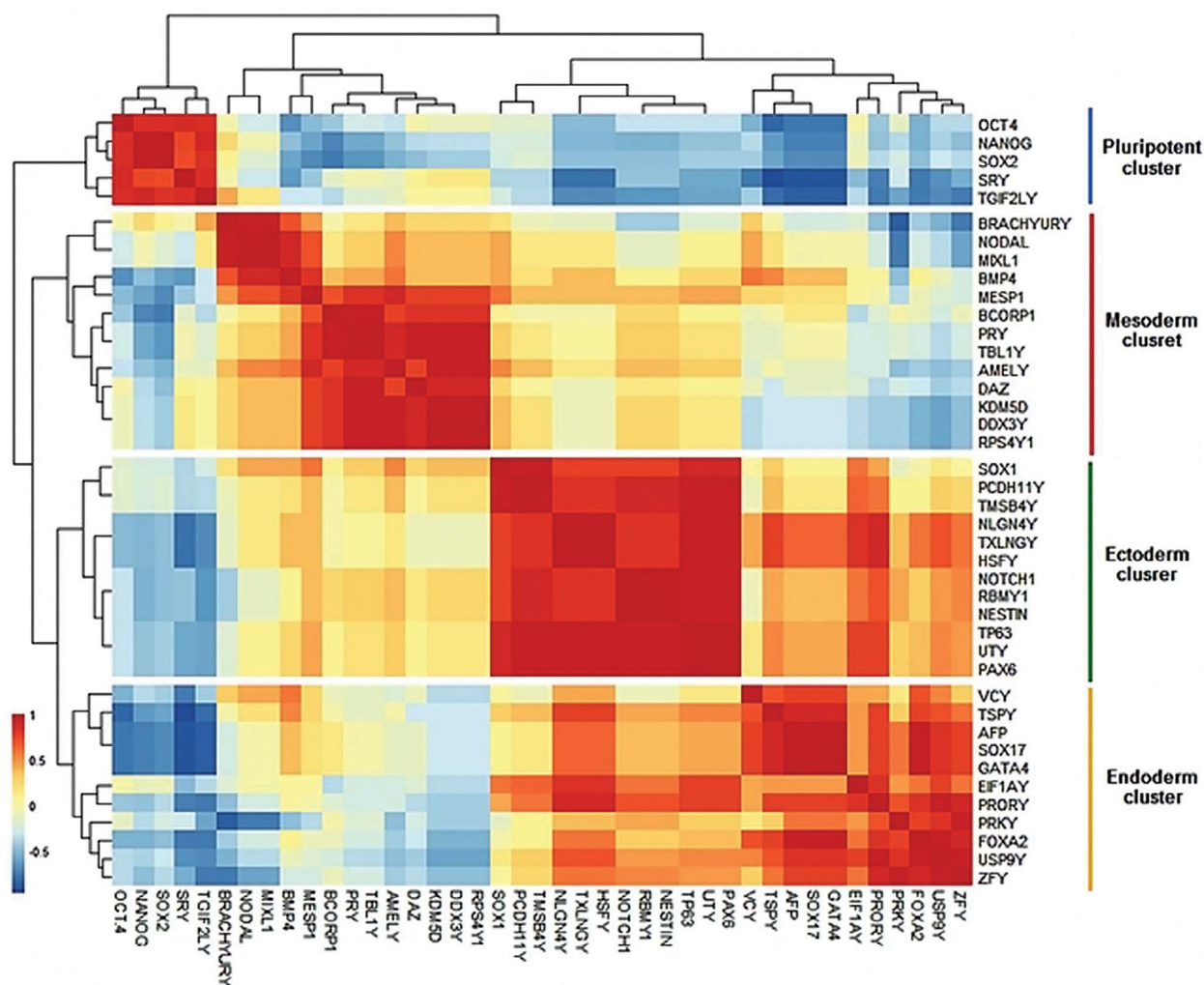


Fig.5: Co-expression of MSY genes and EB markers. The correlation of two expression profiles was determined by one square. Hierarchical trees were constructed based on matched profiles, shown on the top and left sides. Also, mesoderm, ectoderm, endoderm and pluripotent clusters were shown on the right side. MSY; The male-specific region of the Y chromosome and EBs; Embryoid bodies.

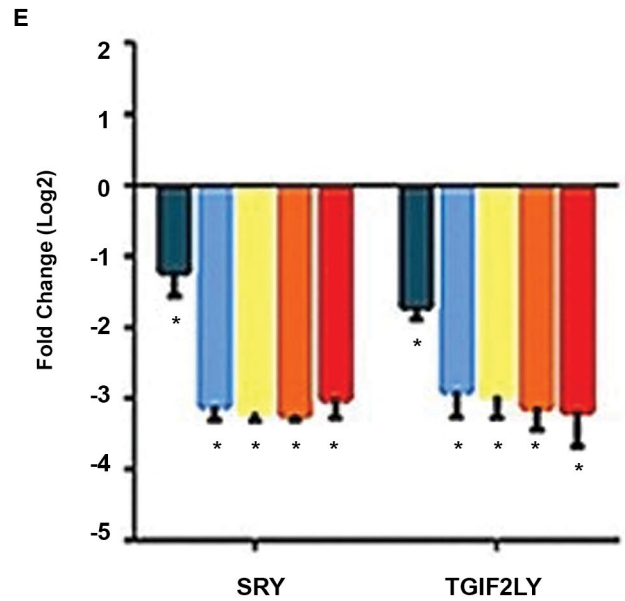
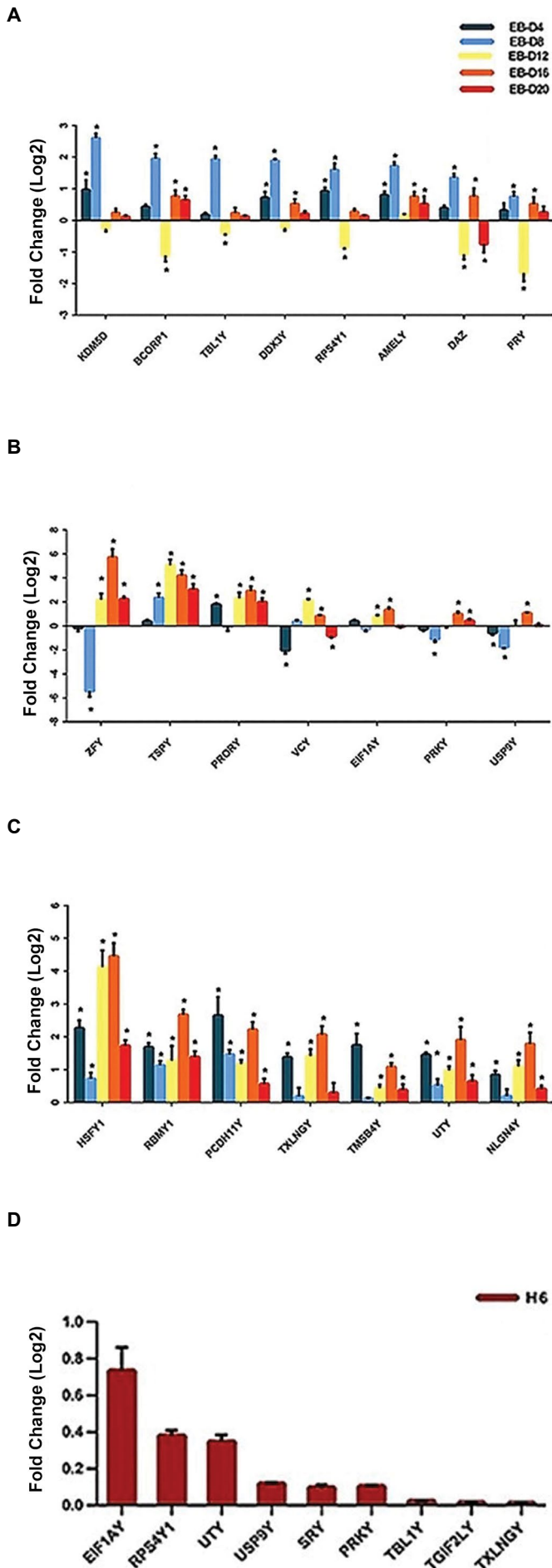


Fig.6: The expression pattern of MSY genes during spontaneous differentiation. **A.** The expression profile of MSY genes in the mesoderm cluster. **B and C.** The expression profile of MSY genes in the endoderm and ectoderm clusters, respectively. **D.** The expression profile of MSY genes in the pluripotency state in RH6 cells. **E.** The expression profile of MSY genes in the pluripotent cluster. All data were presented as mean \pm SEM. *; $P < 0.05$. MSY; The male-specific region of the Y chromosome and RH6; Royan H6.

Discussion

The Y-HPP was instituted to achieve a complete knowledge about the function, quantification, subcellular localization, and expression pattern of human Y chromosome protein and genes, especially during embryonic development. In the direction of one of the Y-HPP goals, we analyzed the expression pattern of most MSY genes in the process of male-ESCs (RH6) spontaneous differentiation into EBs as an *in vitro* model for early embryonic development. Our results indicated a higher expression of *SRY* and *TGIF2LY* genes in undifferentiated male embryonic stem cells compared to EBs. This observation is in agreement with previous studies showing the upregulation of *SRY* gene in fibroblasts reprogrammed to become induced pluripotent stem cells (iPSCs), and the downregulation of *SRY* following knockdown of both *OCT4* and *NANOG* genes (33, 34). Therefore, *SRY* promoter region has been shown to contain multiple putative *OCT4* and *NANOG* recognition sites. By starting of differentiation, we observed a significant reduction of *SRY* and *TGIF2LY*, following downregulation of *OCT4*, *NANOG* and *SOX2* markers corresponding to previous studies (28, 35).

Ronen and colleagues (2014) suggested that the MSY genes, including *RPS4Y1*, *DDX3Y*, *EIF1AY*, *TXLNGY*, *NLGN4Y*, *TMSB4Y*, *UTY*, *USP9Y*, *TTY15*, *PRKY*, and *ZFY* were highly expressed in male-hESCs and iPSCs [33]. Jangravi and colleagues (2012) also demonstrated that hESC lines were enriched for *NLGN4Y*, *PRKY*, *PCDH11Y*, *TMSB4Y*, *USP9Y*, *RPS4Y2*, *TXLNGY*, *AMELY*, *UTY*, and *RPS4Y1* transcripts (28). Consistent with these

studies, we showed that some of MSY genes including *EIF1AY*, *PRKY*, *RPS4Y1*, *SRY*, *USP9Y*, *UTY*, *TXLNGY*, *TBL1Y*, and *TGIF2LY* were specifically expressed in the pluripotent RH6 cells.

Petropoulos and colleagues (2016) indicated that the expression of Y chromosome genes increased in male embryos since day 8, whereas the X chromosome genes were more expressed in female embryos on days 3 and 4. Therefore, X genes were gradually downregulated after 5 days in return for the upregulation of Y genes starting on day 8. Petropoulos' study has shown that 10 of the Y chromosome genes, *DDX3Y*, *TXLNGY*, *TMSB4Y*, *PRKY*, *RPS4Y1*, *USP9Y*, *UTY*, *KDM5D*, *ZFY*, and *EIF1AY*, were upregulated at embryonic days and lineages, unlike *SRY* gene (35). Zhou and colleagues (2019) found that the Y chromosome is initially activated by *RPS4Y1* and *DDX3Y* genes in 8-day-old embryos when the two X chromosomes in females were widely activated in embryonic genome activation (36).

Torres and colleagues (2013) showed that *Utx* was not required for the proliferation of knockout mouse embryonic stem cells (mESCs), but this gene contributed to the establishment of ectoderm and mesoderm. In *Utx* knockout ESCs, *Uty* as a homologue of *Utx* could compensate for some of the functions of *Utx* during ectoderm and mesoderm differentiation (37). Vakilian and colleagues (2015) successfully differentiated a human embryonic carcinoma cell line (NTERA-2) into neuronal cells. They showed that the expression of 12 MSY genes, specifically *EIF1AY*, *RBMY1*, *DDX3Y*, *HSFY*, *BPY2*, *UTY*, *PCDH11Y*, *USP9Y*, *RPS4Y1*, *SRY*, *ZFY* and *PRY* were significantly upregulated during neural differentiation (38). Meyfour and colleagues (2017) performed a cardiac differentiation and reported an upregulation for the *TBL1Y*, *KDM5D*, *PCDH11Y*, *USP9Y*, *ZFY*, *RPS4Y*, *DDX3Y*, *XKRY*, *PRY*, and *UTY* genes at early mesoderm differentiation, and the *BCORP1*, *RBMY* and *HSFY* genes during late cardiogenesis. On the other hand, the expression of 5 MSY genes namely *VCY*, *SRY*, *TXLNGY*, *NLGN4Y* and *TMSB4Y* were decreased at early differentiation stages (39). Tsugata and colleagues (2015) performed differentiation of both male and female PSCs into insulin-producing cells and demonstrated that *RPS4Y1*, *DDX3Y*, *EIF1AY*, and *NLGN4Y* genes were expressed at higher levels in a male cell line compared to the female cells (40). In the current study, we found a significant correlation between spontaneous differentiation and upregulation of most MSY genes. Briefly, it appears that *KDM5D*, *TBL1Y*, *RPS4Y1*, *DDX3Y*, *PRY*, *DAZ*, *BCORP1*, and *AMELY* genes play key roles in mesoderm layer development. In the same manner, *TXLNGY*, *NLGN4Y*, *PCDH11Y*, *TMSB4Y*, *UTY*, *RBMY1*, and *HSFY* genes contribute to establishment of the ectoderm layer. Also, *ZFY*, *TSPY*, *PRORY*, *VCY*, *EIF1AY*, *USP9Y*, and *RPKY* genes were involved in the endoderm differentiation.

Conclusion

The present study is the first report to genetically

investigate MSY genes during spontaneous differentiation of RH6 into EBs. Using Spearman's Heatmap we identified distinct gene co-expression clusters to validate the correlation of MSY genes with each germ layer. The expression alterations characterized the potential responsibilities of each cluster for the differentiation of mesoderm, ectoderm and endoderm layers. We suggest that these genes may play important roles in early embryonic developments of males. Our results, along with future studies on directed differentiations, are potentially essential for a better understanding of gender-specific factors in embryonic developmental differences.

Acknowledgements

This work was financially supported by a grant (Code:95000131) from Royan Institute for Human Y Chromosome Proteome Project (Y-HPP) and the National Institute of Genetic Engineering & Biotechnology (NIGEB). There is no conflict of interest in this study.

Authors' Contributions

S.N.D., F.K.; Contributed to all experimental work, data and statistical analysis, and interpretation of data. S.N.D.; Wrote the manuscript. S.N.H.; Provided scientific advice throughout the project and performed cell culture. H.R.S.L., G.H.S.; Supervised the project scientifically and contributed to establishing the main idea of the presented work and designing the experimental study. H.R.S.L., G.H.S, H.B, S.N.H.; Contributed to financial support and final approval of the manuscript. All authors have read and approved the final version of this manuscript.

References

1. Setti AS, Figueira RC, Braga DP, Iaconelli A Jr, Borges E Jr. Gender incidence of intracytoplasmic morphologically selected sperm injection-derived embryos: a prospective randomized study. *Reprod Biomed Online*. 2012; 24(4): 420-423.
2. Arnold AP. Sex chromosomes and brain gender. *Nat Rev Neurosci*. 2004; 5(9): 701-708.
3. Kochhar HP, Peippo J, King WA. Sex related embryo development. *Theriogenology*. 2001; 55(1): 3-14.
4. Serdarogullari M, Findikli N, Goktas C, Sahin O, Ulug U, Yagmur E, et al. Comparison of gender-specific human embryo development characteristics by time-lapse technology. *Reprod Biomed Online*. 2014; 29(2): 193-199.
5. Legato M. Principles of gender-specific medicine. Gender in the genomic era. 3rd ed. Amsterdam: Elsevier Academic Press; 2017.
6. Ray PF, Conaghan J, Winston RM, Handside AH. Increased number of cells and metabolic activity in male human preimplantation embryos following in vitro fertilization. *Reproduction*. 1995; 104(1): 165-171.
7. Alfaraawati S, Fragouli E, Colls P, Stevens J, Gutiérrez-Mateo C, Schoolcraft WB, et al. The relationship between blastocyst morphology, chromosomal abnormality, and embryo gender. *Fertil Steril*. 2011; 95(2): 520-524.
8. Orzack SH, Stubblefield JW, Akmaev VR, Colls P, Munné S, Scholl T, et al. The human sex ratio from conception to birth. *Proc Natl Acad Sci USA*. 2015; 112(16): E2102-E2111.
9. Graves JA, Koina E, Sankovic N. How the gene content of human sex chromosomes evolved. *Curr Opin Genet Dev*. 2006; 16(3): 219-224.
10. Camerino G, Parma P, Radi O, Valentini S. Sex determination and sex reversal. *Curr Opin Genet Dev*. 2006; 16(3): 289-292.
11. Hughes JF, Rozen S. Genomics and genetics of human and primate Y chromosomes. *Annu Rev Genomics Hum Genet*. 2012; 13: 83-108.

12. Fleming A, Vilain E. The endless quest for sex determination genes. *Clin Genet*. 2005; 67(1): 15-25.
13. Bermejo-Alvarez P, Rizos D, Rath D, Lonergan P, Gutierrez-Adan A. Sex determines the expression level of one third of the actively expressed genes in bovine blastocysts. *Proc Natl Acad Sci USA*. 2010; 107(8): 3394-3399.
14. Bruck T, Benvenisty N. Meta-analysis of the heterogeneity of X chromosome inactivation in human pluripotent stem cells. *Stem Cell Res*. 2011; 6(2): 187-193.
15. Sullivan AE, Lewis T, Stephenson M, Odem R, Schreiber J, Ober C, et al. Pregnancy outcome in recurrent miscarriage patients with skewed X chromosome inactivation. *Obstet Gynecol*. 2003; 101(6): 1236-1242.
16. Skaletsky H, Kuroda-Kawaguchi T, Minx PJ, Cordum HS, Hillier L, Brown LG, et al. The male-specific region of the human Y chromosome is a mosaic of discrete sequence classes. *Nature*. 2003; 423(6942): 825-837.
17. Legrain P, Aebersold R, Archakov A, Bairoch A, Bala K, Beretta L, et al. The human proteome project: current state and future direction. *Mol Cell Proteomics*. 2011; 10(7): M111.009993.
18. Paik YK, Omenn GS, Uhlen M, Hanash S, Marko-Varga G, Aebersold R, et al. Standard guidelines for the chromosome-centric human proteome project. *J Proteome Res*. 2012; 11(4): 2005-2013.
19. Kelleher NL. A cell-based approach to the human proteome project. *J Am Soc Mass Spectrom*. 2012; 23(10): 1617-1624.
20. van Hoof D, Krijgsveld J, Mummery C. Proteomic analysis of stem cell differentiation and early development. *Cold Spring Harb Perspect Biol*. 2012; 4(3): a008177.
21. Bauwens CL, Peerani R, Niebruegge S, Woodhouse KA, Kumacheva E, Husain M, et al. Control of human embryonic stem cell colony and aggregate size heterogeneity influences differentiation trajectories. *Stem Cells*. 2008; 26(9): 2300-2310.
22. Pettinato G, Wen X, Zhang N. Formation of well-defined embryoid bodies from dissociated human induced pluripotent stem cells using microfabricated cell-repellent microwell arrays. *Sci Rep*. 2014; 4: 7402.
23. Burridge PW, Anderson D, Priddle H, Barbadillo Muñoz MD, Chamberlain S, Allegrucci C, et al. Improved human embryonic stem cell embryoid body homogeneity and cardiomyocyte differentiation from a novel V-96 plate aggregation system highlights interline variability. *Stem Cells*. 2007; 25(4): 929-938.
24. Gerecht-Nir S, Cohen S, Itskovitz-Eldor J. Bioreactor cultivation enhances the efficiency of human embryoid body (hEB) formation and differentiation. *Biotechnol Bioeng*. 2004; 86(5): 493-502.
25. Bratt-Leal AM, Carpenedo RL, McDevitt TC. Engineering the embryoid body microenvironment to direct embryonic stem cell differentiation. *Biotechnol Prog*. 2009; 25(1): 43-51.
26. Jadaliha M, Lee HJ, Pakzad M, Fathi A, Jeong SK, Cho SY, et al. Quantitative proteomic analysis of human embryonic stem cell differentiation by 8-plex iTRAQ labelling. *PLoS One*. 2012; 7(6): e38532.
27. Mekhoubad S, Bock C, de Boer AS, Kiskinis E, Meissner A, Eggan K. Erosion of dosage compensation impacts human iPSC disease modeling. *Cell Stem Cell*. 2012; 10(5): 595-609.
28. Ronen D, Benvenisty N. Sex-dependent gene expression in human pluripotent stem cells. *Cell Rep*. 2014; 8(4): 923-932.
29. Larijani MR, Seifinejad A, Pournasr B, Hajihoseini V, Hassani S-N, Totonchi M, et al. Long-term maintenance of undifferentiated human embryonic and induced pluripotent stem cells in suspension. *Stem Cells Dev*. 2011; 20(11): 1911-1923.
30. Ahmadi Rastegar D, Sharifi Tabar M, Alikhani M, Parsamatin P, Sahraneshin Samani F, Sabbaghian M, et al. Isoform-level gene expression profiles of human Y chromosome azoospermia factor genes and their X chromosome paralogs in the testicular tissue of non-obstructive azoospermia patients. *J Proteome Res*. 2015; 14(9): 3595-3605.
31. Jangravi Z, Alikhani M, Arefnezhad B, Sharifi Tabar M, Taleahmad S, Karamzadeh R, et al. A fresh look at the male-specific region of the human Y chromosome. *J Proteome Res*. 2012; 12(1): 6-22.
32. Bellott DW, Hughes JF, Skaletsky H, Brown LG, Pyntikova T, Cho TJ, et al. Mammalian Y chromosomes retain widely expressed dosage-sensitive regulators. *Nature*. 2014; 508(7497): 494-499.
33. Ross DG, Bowles J, Koopman P, Lehnert S. New insights into SRY regulation through identification of 5' conserved sequences. *BMC Mol Biol*. 2008; 9: 85.
34. Kang J, Shakya A, Tantin D. Stem cells, stress, metabolism and cancer: a drama in two acts. *Trends Biochem Sci*. 2009; 34(10): 491-499.
35. Petropoulos S, Edsgård D, Reinius B, Deng Q, Panula SP, Code-luppi S, et al. Single-cell RNA-seq reveals lineage and X chromosome dynamics in human preimplantation embryos. *Cell*. 2016; 165(4): 1012-1026.
36. Zhou Q, Wang T, Leng L, Zheng W, Huang J, Fang F, et al. Single-cell RNA-seq reveals distinct dynamic behavior of sex chromosomes during early human embryogenesis. *Mol Reprod Dev*. 2019; 86(7): 871-882.
37. Morales Torres C, Laugesen A, Helin K. Utx is required for proper induction of ectoderm and mesoderm during differentiation of embryonic stem cells. *PLoS One*. 2013; 8(4): e60020.
38. Vakilian H, Mirzaei M, Sharifi Tabar M, Pooyan P, Habibi Rezaee L, Parker L, et al. DDX3Y, a male-specific region of Y chromosome gene, may modulate neuronal differentiation. *J Proteome Res*. 2015; 14(9): 3474-3483.
39. Meyfour A, Ansari H, Pahlavan S, Mirshahvaladi S, Rezaei-Tavirani M, Gourabi H, et al. Y chromosome missing protein, TBL1Y, may play an important role in cardiac differentiation. *J Proteome Res*. 2017; 16(12): 4391-4402.
40. Tsugata T, Nikoh N, Kin T, Saitoh I, Noguchi Y, Ueki H, et al. Potential factors for the differentiation of ESCs/iPSCs into insulin-producing cells. *Cell Med*. 2015; 7(2): 83-93.

Inhibition of miR-200b Promotes Angiogenesis in Endothelial Cells by Activating The Notch Pathway

Tie-Ying Qiu, M.M.¹, Jin Huang, M.D.¹, Li-Ping Wang, M.M.¹, Bi-Song Zhu, M.D.^{2*}

1. Clinical Nursing Teaching and Research Section of the Second Xiangya Hospital, Changsha 410011, P.R. China
2. Organ Transplant Center, Xiangya Hospital, Central South University, Changsha 410008, P.R. China

*Corresponding Address: Organ Transplant Center, Xiangya Hospital, Central South University, Changsha 410008, P.R. China
Email: 277364307@qq.com

Received: 01/August/2019, Accepted: 5/November/2019

Abstract

Objective: Patients with diabetes mellitus frequently have chronic wounds or diabetic ulcers as a result of impaired wound healing, which may lead to limb amputation. Human umbilical vein endothelial cell (HUVEC) dysfunction also delays wound healing. Here, we investigated the mechanism of miR-200b in HUVECs under high glucose conditions and the potential of miR-200b as a therapeutic target.

Materials and Methods: In this experimental study, HUVECs were cultured with 5 or 30 mM glucose for 48 hours. Cell proliferation was evaluated by CCK-8 assays. Cell mobility was tested by wound healing and Transwell assays. Angiogenesis was analyzed *in vitro* Matrigel tube formation assays. Luciferase reporter assays were used to test the binding of miR-200b with Notch1.

Results: miR-200b expression was induced by high glucose treatment of HUVECs ($P < 0.01$), and it significantly repressed cell proliferation, migration, and tube formation ($P < 0.05$). Notch1 was directly targeted and repressed by miR-200b at both the mRNA and protein levels. Inhibition of miR-200b restored Notch1 expression ($P < 0.05$) and reactivated the Notch pathway. The effects of miR-200b inhibition in HUVECs could be reversed by treatment with a Notch pathway inhibitor ($P < 0.05$), indicating that the miR-200b/Notch axis modulates the proliferation, migration, and tube formation ability of HUVECs.

Conclusion: Inhibition of miR-200b activated the angiogenic ability of endothelial cells and promoted wound healing through reactivation of the Notch pathway *in vitro*. miR-200b could be a promising therapeutic target for treating HUVEC dysfunction.

Keywords: Angiogenesis, HUVEC Dysfunction, miR-200b, Notch Pathway

Cell Journal(Yakhteh), Vol 23, No 1, April-June (Spring) 2021, Pages: 51-60

Citation: Qiu TY, Huang J, Wang LP, Zhu BS. Inhibition of miR-200b promotes angiogenesis in endothelial cells by activating the notch pathway. Cell J. 2021; 23(1): 51-60. doi: 10.22074/cellj.2021.7080.

This open-access article has been published under the terms of the Creative Commons Attribution Non-Commercial 3.0 (CC BY-NC 3.0).

Introduction

Diabetes mellitus (DM) and complications from having DM are a threat to global health. Over 400 million adults have DM worldwide. This number is estimated to reach 640 million by 2040 (1). Type 2 diabetes mellitus (T2DM), which accounts for over 90% of DM cases, and complications from having T2DM have contributed tremendously to the global mortality and disability of this disease (2, 3). Traditionally, the complications of DM have been divided into two groups: macrovascular complications (such as cardiovascular diseases) and microvascular complications (those affecting the retina or the nervous system). Complications are very common in T2DM patients; almost 50% of patients have microvascular complications, and 30% have macrovascular complications, with rates that vary in different countries (4). Diabetic skin ulcers are non-healing and chronic wounds, and they are one of the most severe complications of DM (5), with up to 25% of DM patients developing these ulcers in their lifetime and 20% of these patients requiring amputations (6). Tremendous efforts have been made to explore the treatment for

diabetic ulcers, including bioengineered skin substitutes and negative pressure dressings (7). However, there is still no effective therapeutic method.

Wound healing is a dynamic and complex process involving multiple cellular activities, including inflammation, proliferation, angiogenesis, and tissue remodeling (8). In diabetes, however, the healing process is impaired by an excessive inflammatory response and decreased angiogenesis (9). Studies have shown that enhancers of angiogenesis, such as growth factors, can facilitate the proliferation and migration of endothelial cells, accelerating the wound healing process in DM (10). The importance of the Notch signaling pathway in wound healing has been thoroughly demonstrated. There are four Notch receptors in mammals (Notch1, Notch2, Notch3, and Notch4), all of which are single-pass transmembrane receptor proteins. Moreover, mammals possess five ligands for the Notch pathway (Delta-like 1, 3, 5, Jagged 1, 2). Once the ligand binds to the extracellular domain of Notch proteins, they undergo proteolytic cleavage, leading to the release of the Notch intracellular domain (NICD), which enters the nucleus and acts as a transcription

factor or forms a complex with other proteins to regulate the transcription of target genes (11, 12). The Notch signaling pathway plays a significant role in cell communication, regulating various biological processes during development and disease pathology (13, 14). Recent studies have found that Notch signaling promotes diabetic wound healing by regulating macrophage-mediated inflammation during the healing process (15). Additionally, the angiogenic ability of endothelial cells has been shown to be affected by Notch signaling, which could be due to the influence of vascular endothelial growth factor (VEGF) (16). The underlying molecular mechanism of Notch pathway-mediated wound healing is still unclear.

MicroRNAs (miRNAs) are small non-coding RNAs that are ~22 nt in length. miRNAs are post-transcriptional regulators that function by binding to the 3' untranslated region (3'UTR) of target mRNAs and inducing translational repression or mRNA degradation (17). miRNAs play significant roles in diverse biological processes, and they are dysregulated in numerous diseases (18, 19). Several miRNAs have been discovered to regulate angiogenesis in tumors or during wound healing (20, 21). miR-200b belongs to the miR-200 family and is widely expressed in various cell types, including cancer cells, stem cells, and endothelial cells (22-24). miR-200b has been demonstrated to regulate multiple cellular functions, such as migration, proliferation, and apoptosis (22). Moreover, inhibition of miR-200b has been linked with the promotion of angiogenesis by endothelial cells (25). However, the mechanism by which miR-200b acts and its downstream targets involved in the diabetic wound healing process are not quite clear.

In this work, we tried to demonstrate that miR-200b could target the Notch pathway, leading to the suppression of angiogenesis *in vitro*. We also aimed to evaluate the therapeutic properties of miR-200b inhibitors in facilitating the diabetic wound healing process.

Materials and Methods

Cell culture and treatment

In this experimental study, HUVECs were obtained from ScienCell Research Laboratories (Carlsbad, CA, USA). The HUVECs were cultured in F-12K medium supplemented with 1% antibiotics (100 U/ml penicillin and 100 mg/ml streptomycin, Cat. 15240062, Life Technologies, USA) and were maintained at 37°C in 5% CO₂. To mimic diabetic conditions, the HUVECs were incubated under high

glucose (30 mM glucose, HG) conditions for 12, 24, and 48 hours. Cells treated with 5 mM glucose as normal glucose (NG) were used as controls. Cells were then harvested for subsequent assays. The research purposes under protocols were approved by Xiangya Hospital.

Cell transfection

miRNA-negative controls and miR-200b inhibitors were purchased from GenePharma (Suzhou, China) and transfected into HUVECs at a concentration of 100 nM using Lipofectamine 2000 transfection reagent (Cat. 11668019, Invitrogen, USA) according to the manufacturer's instructions. After 48 hours, the cells were used for subsequent experiments.

Total RNA extraction and quantitative real-time PCR

Cells were dissolved in TRIzol reagent (Cat. 15596018, Invitrogen, USA), and total RNA was obtained according to the manufacturer's protocol. The RNA was then tested for quality and synthesized into cDNA using an iScript cDNA Synthesis Kit (Cat. 1708891, Bio-Rad, USA). qRT-PCR was performed using SYBR Green Supermixes (Cat. 1708882, Bio-Rad, USA). GAPDH and U6 were used as endogenous controls for normalization. Relative levels of expression were normalized and analyzed using the 2^{-ΔΔCt} method. Primer sequences are listed in Table 1.

Western blot analysis

Cells were washed with cold PBS and incubated with lysis buffer on ice for 30 minutes. Then, the cells were scraped, and after centrifugation, the supernatant containing the lysate was collected and stored at -80°C. A BCA assay kit (Cat. 5000001, Bio-Rad, USA) was used to determine protein concentrations. Protein samples were denatured and then separated by SDS-PAGE and transferred to PVDF membranes (Cat. IPVH00010, Millipore, USA). After blocking with non-fat milk for 1 hour, membranes were incubated overnight at 4°C with the following primary antibodies from Cell Signaling Technology (Danvers, USA): Notch1 (#3608), Jagged1 (#70109), Hes1 (#11988) and β-actin (#3700), and all were used at a 1:1000 dilution. After washing three times, the membranes were incubated with goat anti-mouse (#7076) or anti-rabbit (#7077) HRP-conjugated secondary antibodies (Cell Signaling Technology, USA). The signals were analyzed using an ECL detection kit (Cat. 32106, Pierce Biotechnology, USA).

Table 1: Primer sequences for quantitative real-time PCR

Gene	Forward sequence	Reverse sequence
<i>MiR-200b-3p</i>	5'-GCGGCTAATACTGCCTGGTAA-3'	5'-GTGCAGGGTCCGAGGT-3'
<i>Notch1</i>	5'-GCACGTGTATTGACGACGTTG-3'	5'-GCAGACACAGGAGAAGCTCTC-3'
<i>GAPDH</i>	5'-CCAGGTGGTCTCCTCTGA-3'	5'-GCTGTAGCCAAATCGTTGT-3'
U6	5'-CTCGCTTCGGCAGCAC-3'	5'-AACGCTTCACGAATTTGCGT-3'

Enzyme-linked immunosorbent assay

After the indicated treatments, the supernatants from the HUVECs were centrifuged at 1,000 x g for 5 minutes at 4°C prior to enzyme-linked immunosorbent assay (ELISA). The levels of VEGF (#DVE00) were measured using commercial ELISA kits (R&D Systems, Inc., Minneapolis, USA) according to the manufacturer's protocol. Each sample was evaluated in triplicate.

Cell viability assay

A Cell Counting Kit-8 (CCK8, Cat. CK04, Dojindo, Japan) assay was used to detect cell viability. Briefly, after the indicated treatment, 1×10^4 cells were seeded into 96-well plates, and CCK-8 solution was added to each well. After 2 hours of culture, the absorbance was measured at 450 nm using a spectrophotometer.

Wound-healing assay

The protocol was carried out as previously described (26). Briefly, HUVECs were seeded with the indicated treatments and then transfected with the indicated miRNA negative control or miRNA. Forty-eight hours later, the attached cells were scratched with a 10 μ l pipette tip, and images were captured under a microscope at 0 hours after the scratch. The plates were returned to the incubator and cultured for 24 hours. Then, another set of images of the same wounds was captured. The wound area was measured with ImageJ and was normalized and presented as a percentage of the initial wound measured at 0 hours.

Transwell assay

A Transwell assay was performed according to a reported protocol (27). After the indicated treatment, a total of 5×10^5 HUVECs were suspended in a serum-free culture medium and seeded into the upper insert of a 12-well Transwell plate (Cat. 3401, Corning Incorporated, USA), with or without Matrigel pretreatment. Medium with serum was added to the lower chamber. The plate was incubated in the incubator for 8 hours. Cells remaining in the upper insert were removed using cotton swabs, and the migratory cells were fixed with 4% paraformaldehyde for 10 minutes. After washing with PBS 3 times, the cells were stained with a crystal violet solution. Images were captured using brightfield microscopy (Olympus, Tokyo, Japan) and quantified.

In vitro Matrigel angiogenesis assays

In vitro Matrigel angiogenesis assays were performed to test the angiogenic abilities of cells. Briefly, 24 hours after the indicated treatment, HUVECs were seeded on normal Matrigel (Cat. 356234, BD Biosciences, USA) in 96-well plates (Sigma, USA). Tube lengths and branches were measured and quantified by ImageJ software.

Dual-luciferase reporter assay

The 3'UTR region of Notch1 mRNA was amplified by

PCR and cloned into a pGL3 vector (Promega, USA). HEK 293T cells were seeded into 24-well plates and were then cotransfected with a vector carrying either the wild type or mutant Notch1 3'-UTR and either a miR-200b mimic or a miR-negative control. Transfections were performed using Lipofectamine 2000 according to the manufacturer's protocol. Finally, luciferase activities were measured using a dual-luciferase reporter gene assay kit (Cat. E1910, Promega, USA).

Statistical analysis

Statistical analysis was performed using GraphPad Prism 5. All experiments were conducted at least three times. All data are presented as the mean \pm SD. The data were analyzed by one-way ANOVA, followed by Tukey's post hoc test or an independent sample t test. $P < 0.05$ was considered statistically significant.

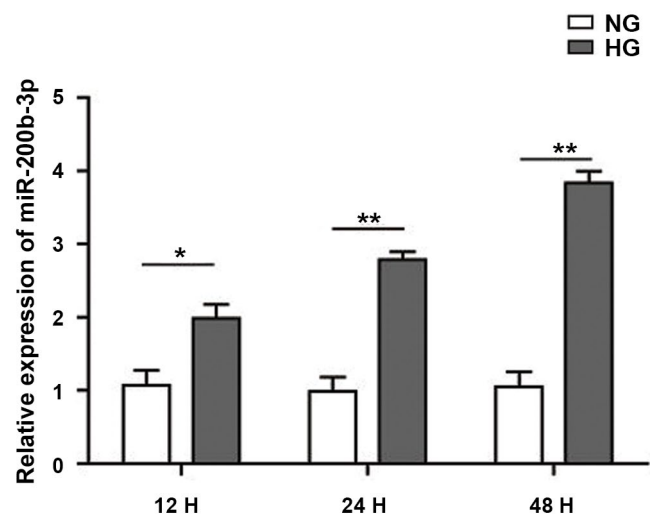
Results

miR-200b was upregulated in high glucose-treated HUVECs

To investigate the role of miR-200b in endothelial cell dysfunction, we first tested its expression in HUVECs grown in high glucose conditions. As shown in Figure 1A, the miR-200b level was significantly induced by high glucose treatment after just 12 hours ($P < 0.05$), and it continued to increase to a level that was 2-fold greater than the initial levels after 48 hours ($P < 0.01$).

Meanwhile, the tube formation ability of HUVECs was also impaired by high glucose treatment, as indicated by the decreased formation of tubes (Fig. 1B). Unsurprisingly, other genes related to angiogenesis also changed, which is exemplified by the decrease in VEGF (Fig. 1C, $P < 0.01$). In addition, high glucose treatment dramatically increased the level of IL-1 β (Fig. S1, See supplementary online information at www.celljournal.org). These results suggest a potential role for miR-200b in preventing endothelial cell angiogenesis *in vitro*.

A



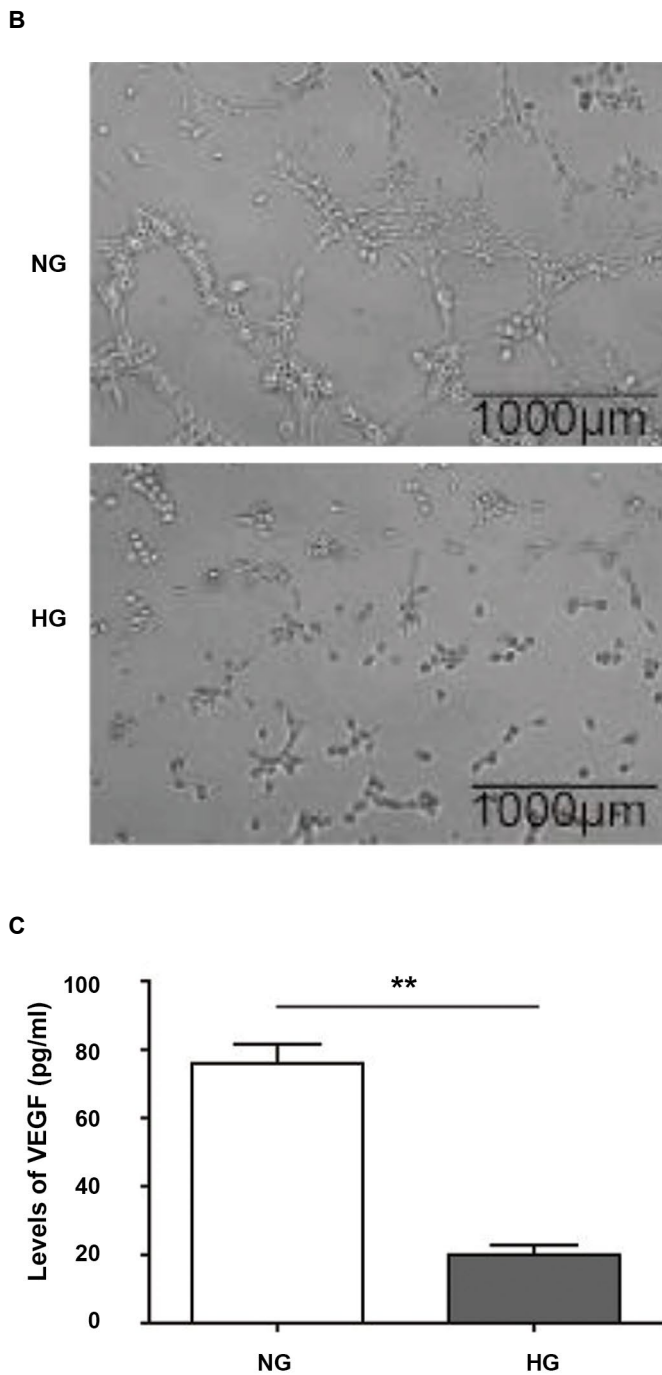


Fig.1: The high-glucose treatment induced the expression of miR-200b and impaired angiogenesis. **A.** Quantification of miR-200b by real-time PCR in Human umbilical vein endothelial cell (HUVECs) grown in normal glucose (NG) or high-glucose (HG) conditions for 12, 24, and 48 hours. U6 was used as an internal control for normalization. **B.** Representative images of HUVECs under different conditions during the *in vitro* angiogenesis assay. **C.** Quantification of secreted Vascular Endothelial Growth Factor (VEGF) from HUVECs, as determined by enzyme-linked immunosorbent assay (ELISA) after the indicated treatment. (N = 3). *, P<0.05, **, P<0.01, and H; Hour.

Knockdown of miR-200b promoted the proliferation and angiogenesis of HUVECs grown in high glucose conditions

To further explore the function of miR-200b in wound healing, we knocked down or overexpressed miR-200b and

subsequently studied how it affected the cellular activity of endothelial cells. miR-200b knockdown decreased miR-200b expression levels, while its overexpression increased miR-200b expression levels, indicating miR-200b knockdown and overexpression were transfected successfully (Fig. 2A and B). As shown in Figure.2C, high glucose treatment significantly inhibited the proliferation of HUVECs compared to cells grown in normal glucose conditions (P<0.01).

Moreover, when the miR-200b mimic was added, cell proliferation was further decreased (P<0.05). However, treatment with a miR-200b inhibitor remarkably rescued the impaired proliferation ability that was induced by high glucose treatment (P<0.05). In addition to cell proliferation, the migration ability of HUVECs was also affected. As demonstrated by wound healing and Transwell assays shown in Figure. 2D and E, compared to normal glucose conditions, high glucose treatment obviously inhibited the migration capacity of HUVECs (P<0.01) and further suppressed migration when combined with miR-200b overexpression (P<0.05). When miR-200b was suppressed by its inhibitor, the ability of the cells to migrate recovered significantly (P<0.05). The tube formation ability of HUVECs was also investigated. High glucose treatment alone or in combination with miR-200b overexpression dramatically impaired the tube formation ability, which was recovered by treatment with the miR-200b inhibitor (Fig.2F). These data indicate that miR-200b can affect the proliferation, migration, and tube formation ability of endothelial cells.

Notch1 was a direct target of miR-200b

Intriguingly, as one of the most important mediators in the wound healing process, the Notch pathway is potentially regulated by miR-200b. As shown in Figure.3A, we first performed prediction searches using StarBase to identify targets of miR-200b, which indicated that miR-200b may directly target the 3'UTR region of Notch1. To further determine whether miR-200b could target Notch1, we conducted a luciferase reporter assay, where the reporter contained either a wild type or a binding site mutated Notch1 3'UTR. As shown in Figure.3B, miR-200b remarkably inhibited luciferase activity from the Notch1 wild type 3'UTR (P<0.05) vector, but it did not have the same effect on the mutant. Consistently, when miR-200b was overexpressed in HUVECs, both the mRNA (Fig.3C) and protein (Fig.3D) of Notch1 were significantly suppressed (P<0.05). The downregulation of miR-200b by treatment with its inhibitor increased Notch1 expression (Fig.3C and D, P<0.05). Taken together, these results demonstrate that miR-200b could target and inhibit Notch1 directly in endothelial cells.

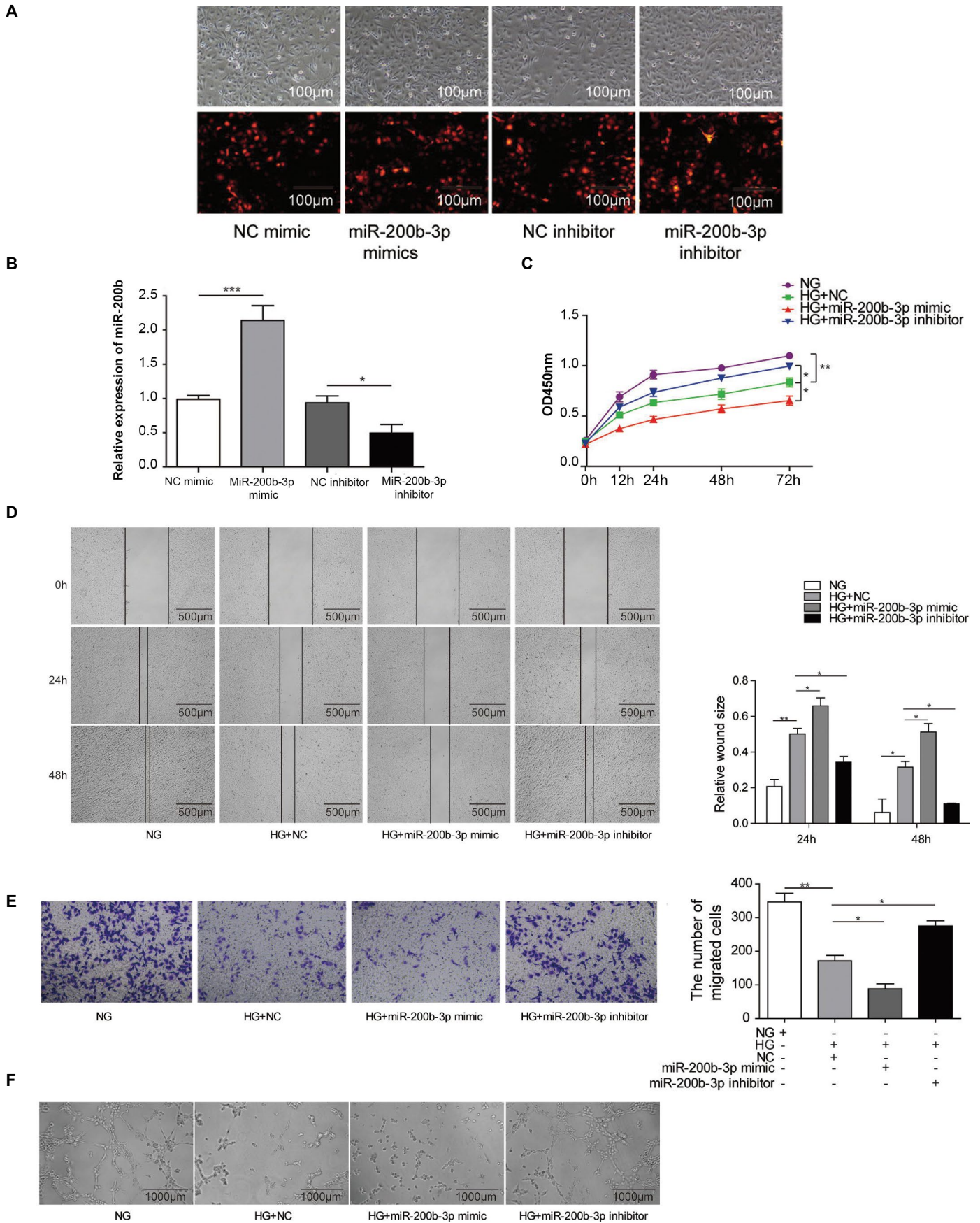


Fig.2: miR-200b affected the angiogenesis ability of Human umbilical vein endothelial cell (HUVECs). The HUVECs cells were transfected with NC mimic, miR-200b mimics, NC inhibitor, miR-200b inhibitor, and miR-200b transfection efficiency were analyzed by **A**. IF imaging and **B**. Real-time PCR. **C**. Quantification of HUVEC viability after the indicated treatment, as determined by CCK-8 assays. **D**. Representative images of HUVECs after the indicated treatments during the wound healing assay. **E**. Typical images and quantification of HUVECs with different treatments during the migration assay. **F**. Representative images of HUVECs under different conditions during the *in vitro* angiogenesis assay. (N = 3). NG; Normal glucose, HG; high-glucose, *, P<0.05, and **, P<0.01.

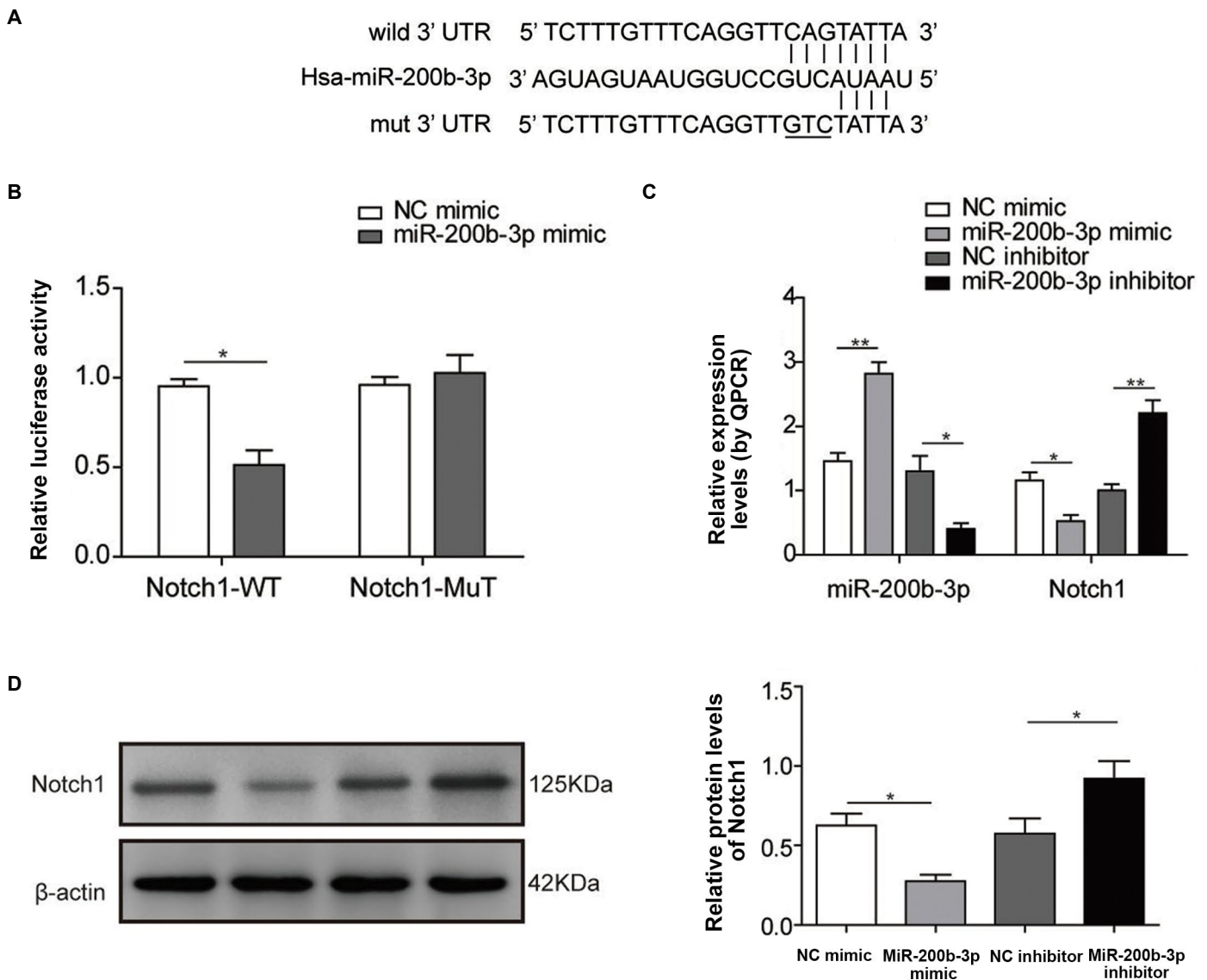


Fig.3: miR-200b directly targeted Notch1. **A.** Predicted miR-200b binding sites and induced mutations in the Notch1 3'UTR. **B.** Luciferase reporter assays show miR-200b-targeted Notch1 mRNA. **C.** miR-200b and Notch1 mRNA levels in Human umbilical vein endothelial cell (HUVECs) after the indicated treatments were quantified by real-time PCR. **D.** Representative images and quantification of Notch1 protein expression in HUVECs. (N=3), *, P<0.05, and **, P<0.01.

Inhibition of miR-200b could activate the Notch pathway and angiogenesis.

To evaluate whether miR-200b could regulate the Notch signaling pathway, we next examined downstream targets of the Notch pathway. Consistent with Notch1 expression, the mRNA and protein levels of Jagged1 and Hes1 were dramatically decreased by high glucose treatment (P<0.01), and they were recovered by miR-200b inhibition (P<0.05, Fig.4A and B). To further determine the role of the Notch pathway in miR-200b-mediated wound healing, we combined miR-200b downregulation with the Notch pathway inhibitor N-[N-(3,5-difluorophenacetyl)-l-alanyl]-S-phenylglycine t-butyl ester (DAPT) in high glucose conditions. Unsurprisingly, Notch pathway inhibition significantly repressed proliferation, which was upregulated by miR-

200b suppression (Fig.5A, P<0.05). Consistently, DAPT treatment could also obviously rescue the cell migration that was induced by miR-200b inhibition, as demonstrated by wound healing and Transwell assays (Fig.5B and C, P<0.05). For the tube formation function, treatment with the miR-200b inhibitor significantly increased the number of tubes formed by HUVECs, which was then decreased when DAPT was added. Downstream targets of the Notch pathway were also analyzed. As shown in Figure.5E, the protein levels of Jagged1, Notch1, and Hes1 were significantly upregulated in HUVECs grown in high-glucose conditions following the treatment with the miR-200b inhibitor. When DAPT treatment was added, their expression decreased (P<0.05). These data strongly indicate that inhibition of miR-200b could stimulate angiogenesis of endothelial cells by activating the Notch pathway.

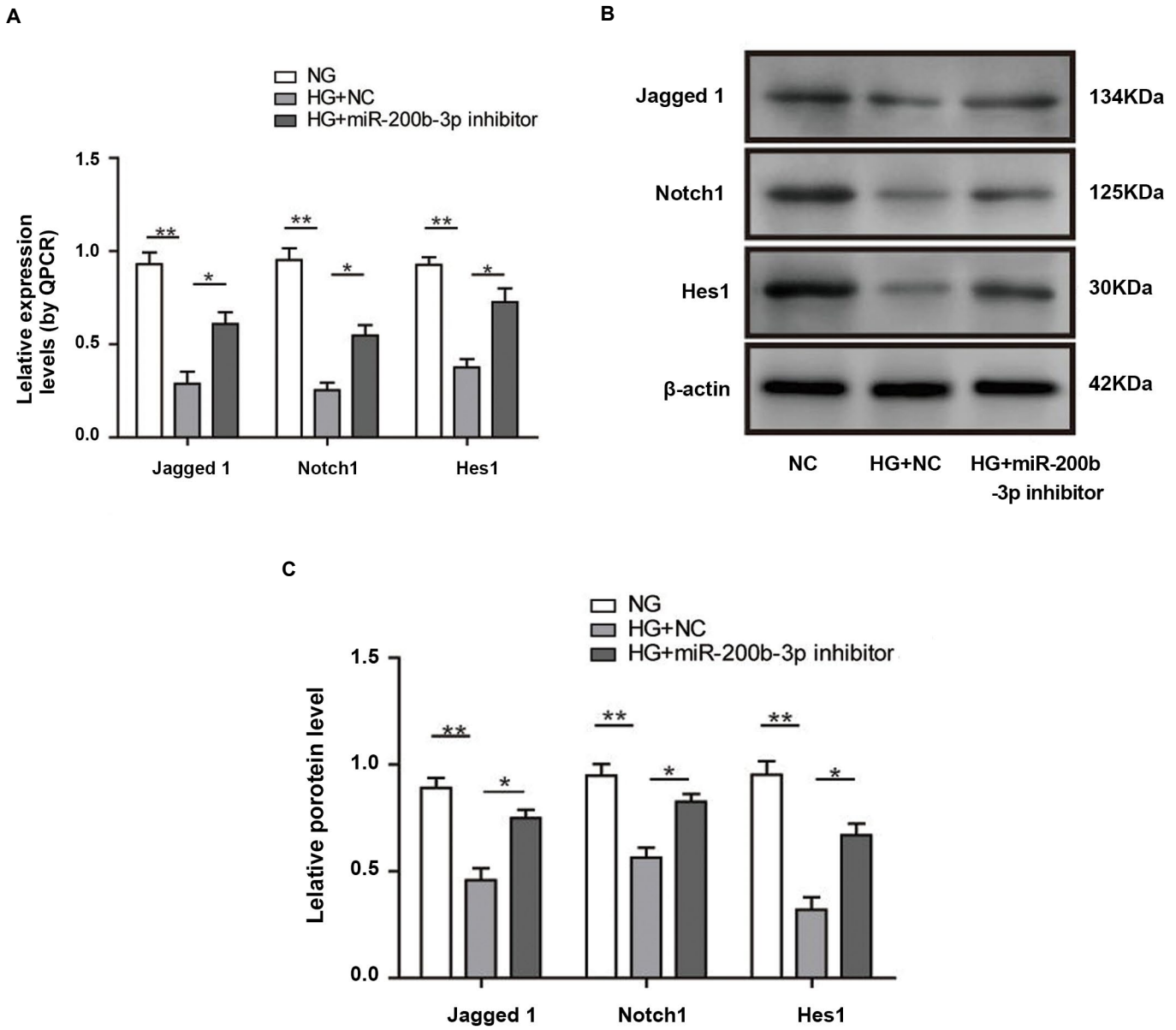
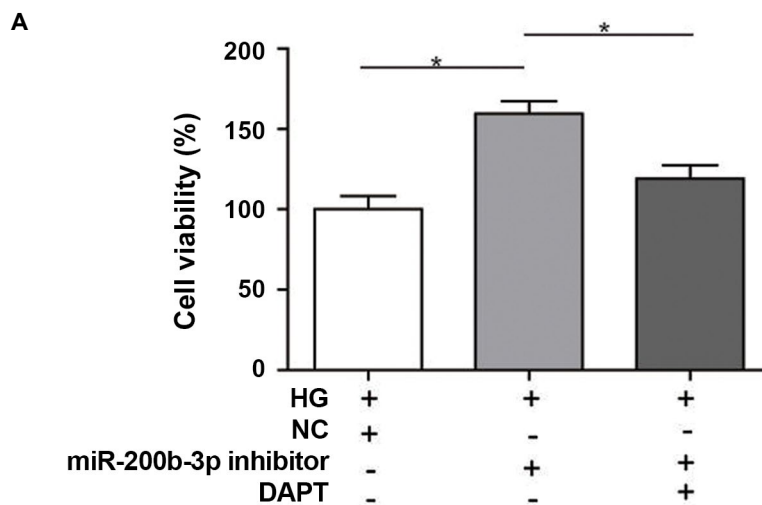


Fig.4: Inhibition of miR-200b could activate the Notch pathway. **A.** Quantification of Human umbilical vein endothelial cell (HUVEC) mRNA levels by real-time PCR. **B.** Representative images and quantification of Notch pathway protein expression in HUVECs. (N=3). NG; Normal glucose, HG; High-glucose, *, P<0.05, and **, P<0.01.



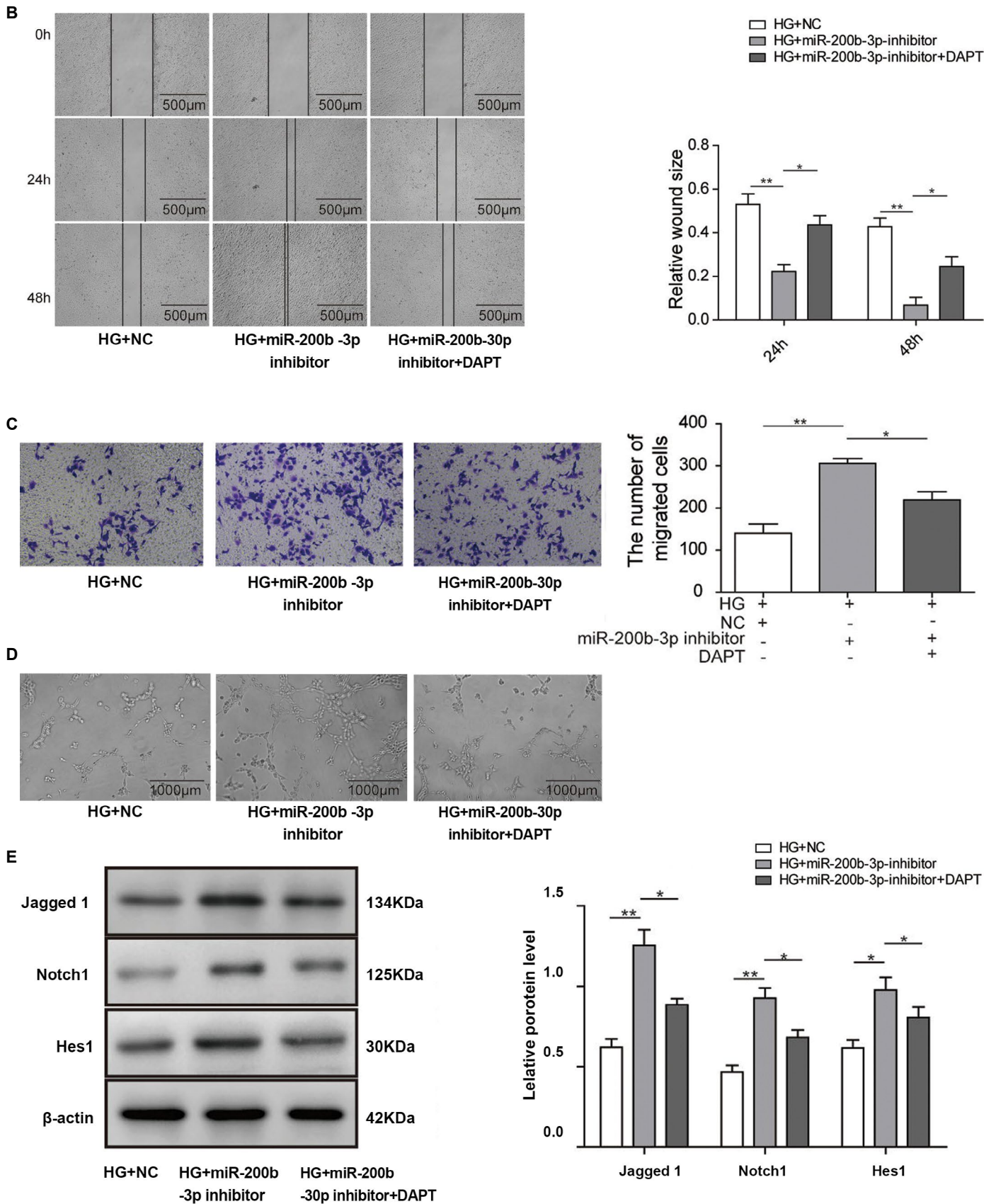


Fig.5: miR-200b affected angiogenesis by regulating Notch1. **A.** Quantification of human umbilical vein endothelial cell (HUVEC) viability was measured by CCK-8 assay after the indicated treatments. **B.** Representative images of HUVECs after the indicated treatments during the wound healing assay. **C.** Typical images and quantification of HUVECs with different treatments during the migration assay. **D.** Representative images of HUVECs under different conditions during *in vitro* angiogenesis assays. **E.** Representative images and quantification of Notch pathway protein expression in HUVECs. (N=3). NG; Normal glucose, HG; High-glucose, *, P<0.05, and **, P<0.01.

Discussion

Impaired wound healing is a major complication in diabetes patients, leading to morbidity and death (28). Skin wounds in diabetics have been linked to impaired antimicrobial activity in leukocytes, altered blood flow, and abnormal inflammatory state, all of which are related to the dysfunction of endothelial cells (29, 30). Recently, various methods have been used to treat diabetic wounds, such as tissue regeneration by stem cells or progenitor cells and administration of growth factors (31). However, the results have been very limited; since wound healing is a complex process, it is difficult to treat by targeting a single process. Due to their function in regulating multiple targets and pathological conditions, miRNAs have been considered promising therapeutic targets. The role of miRNAs in tumour angiogenesis has been widely explored, raising the potential for their use in wound healing.

Several studies have demonstrated the involvement of miRNA dysregulation in the angiogenesis process of diabetes mellitus. In a diabetic rat model, miR-320 suppressed the angiogenic response of microvascular endothelial cells by targeting insulin-like growth factor 1 (IGF1)(32). miR-93 was reported to be downregulated by high glucose treatment, and it also was found to suppress angiogenesis by targeting VEGF(33). Inhibition of miR-503 could stimulate angiogenesis in diabetic ischaemic muscle by upregulating cyclin E1 (34). miR-200b has been found to inhibit angiogenesis in tumour development by targeting interleukin-8 and CXCL1, which are secreted by cancer cells.

Moreover, miR-200b has also been reported to play an important role in endothelial cell function. Loss of miR-200b could enhance cell motility by activating epithelial-mesenchymal transition (EMT) (22). Additionally, transient inhibition of miR-200b in endothelial cells was sufficient to enhance angiogenesis during skin wound healing process (25). To explore the role of miR-200b in the wound healing process, we established a high glucose treatment assay and found a resultant upregulation of miR-200b in endothelial cells, which in turn negatively impacted proliferation, migration, and tube formation in these cells. Most importantly, the downregulation of miR-200b by treatment of cells with an inhibitor could significantly rescue the high glucose treatment-induced suppression of division, mobility, and angiogenesis in endothelial cells. While high-glucose treatment has been demonstrated to diminish the angiogenesis ability of endothelial cells by altering their biochemical and biophysical properties (36), our findings reveal the underlying molecular mechanism; further, our data are consistent with the reported function of miR-200b in other disease models.

It is well established that the Notch pathway is critical for wound healing. Overexpression of Jagged1, a Notch

ligand, in endothelial cells accelerated the wound healing process (37). Moreover, blocking the Notch pathway impaired wound healing by affecting the inflammatory response through the regulation of macrophages (20). Previous studies have demonstrated that miR-200b could regulate the Notch pathway in tumours by targeting Notch1 and suppressing tumour metastasis (38). The Notch ligands Jagged1 and Jagged2 were also found to be regulated by miR-200b in metastatic prostate cancer cells (39) and lung cancer (40). In the current work, Notch1 was found to be directly targeted for posttranscriptional regulation by miR-200b in endothelial cells. With the increase in miR-200b expression induced by high glucose treatment, Notch1 levels, and Notch pathway activity were significantly repressed.

On the other hand, miR-200b inhibition was proven to activate the Notch pathway and the wound healing process, which was blocked by treatment with DAPT, a Notch pathway inhibitor. Intriguingly, treatment with the miR-200b inhibitor could only partially return the expression of Notch pathway-related genes to the levels of expression observed control group, indicating the possibility that other angiogenesis-associated targets are regulated by miR-200b in high glucose conditions. This emphasizes the role of miR-200b in regulating the Notch pathway during diabetic wound healing.

Conclusion

In summary, this work demonstrates that miR-200b is upregulated by high glucose treatment in endothelial cells, impairing the wound healing process by suppressing cell proliferation, migration, and angiogenesis. The knockdown of miR-200b is sufficient to restore HUVEC dysfunction by stimulating the Notch pathway, which is shown to be directly regulated by miR-200b and plays a critical role in the wound healing process. Our findings illustrate the function of miR-200b in wound healing and highlight the potential of miR-200b as a promising therapeutic target in the treatment of diabetic complications. However, the current work is still based on an *in vitro* assay mimicking diabetic conditions by high glucose treatment. Further study on animal models is required to explore the function of miR-200b in the diabetic wound healing process and determine its potential as a treatment target.

Acknowledgment

There is no financial support in this study and there is no conflict of interest.

Author's Contributions

T.-Y.Q.; Contributed to conceptualization, data curation, formal analysis, project administration, validation, visualization, roles/writing - original draft, writing, reviewing, and editing. B.-S.Z.; Contributed to data curation, methodology, supervision, visualization,

writing, reviewing, and editing. L.-P.W. Participated in formal analysis and resources. J.H.; Contributed to investigation and software. All authors read and approved the final version of this manuscript.

References

- Zimmet PZ. Diabetes and its drivers: the largest epidemic in human history? *Clin Diabetes Endocrinol.* 2017; 3: 1.
- Bruno G, Runzo C, Cavallo-Perin P, Merletti F, Rivetti M, Pinach S, et al. Incidence of type 1 and type 2 diabetes in adults aged 30-49 years: the population-based registry in the province of Turin, Italy. *Diabetes Care.* 2005; 28(11): 2613-2619.
- Holman N, Young B, Gadsby R. Current prevalence of Type 1 and Type 2 diabetes in adults and children in the UK. *Diabet Med.* 2015; 32(9): 1119-1120.
- Litwak L, Goh SY, Hussein Z, Malek R, Prusty V, Khamseh ME. Prevalence of diabetes complications in people with type 2 diabetes mellitus and its association with baseline characteristics in the multinational A1chieve study. *Diabetol Metab Syndr.* 2013; 5(1): 57.
- Ramsey SD, Newton K, Blough D, McCulloch DK, Sandhu N, Reiber GE, et al. Incidence, outcomes, and cost of foot ulcers in patients with diabetes. *Diabetes Care.* 1999; 22(3): 382-387.
- Singh N, Armstrong DG, Lipsky BA. Preventing foot ulcers in patients with diabetes. *JAMA.* 2005; 293(2): 217-228.
- Sajid MT, Mustafa Qu, Shaheen N, Hussain SM, Shukr I, Ahmed M. Comparison of negative pressure wound therapy using vacuum-assisted closure with advanced moist wound therapy in the treatment of diabetic foot ulcers. *J Coll Physicians Surg Pak.* 2015; 25(11): 789-793.
- Kondo T, Ishida Y. Molecular pathology of wound healing. *Forensic Sci Int.* 2010; 203(1-3): 93-98.
- Wetzler C, Kampfer H, Stallmeyer B, Pfeilschifter J, Frank S. Large and sustained induction of chemokines during impaired wound healing in the genetically diabetic mouse: prolonged persistence of neutrophils and macrophages during the late phase of repair. *J Invest Dermatol.* 2000; 115(2): 245-253.
- Kolluru GK, Bir SC, Kevil CG. Endothelial dysfunction and diabetes: effects on angiogenesis, vascular remodeling, and wound healing. *Int J Vasc Med.* 2012; 2012: 918267.
- Bray SJ. Notch signalling: a simple pathway becomes complex. *Nat Rev Mol Cell Biol.* 2006; 7(9): 678-689.
- Gordon WR, Arnett KL, Blacklow SC. The molecular logic of Notch signaling—a structural and biochemical perspective. *J Cell Sci.* 2008; 121(Pt 19): 3109-3119.
- Fortini ME. Notch signaling: the core pathway and its posttranslational regulation. *Dev Cell.* 2009; 16(5): 633-647.
- Nye JS, Kopan R. Developmental signaling. Vertebrate ligands for Notch. *Curr Biol.* 1995; 5(9): 966-969.
- Kimball AS, Joshi AD, Boniakowski AE, Schaller M, Chung J, Allen R, et al. Notch regulates macrophage-mediated inflammation in diabetic wound healing. *Front Immunol.* 2017; 8: 635.
- Thurston G, Kitajewski J. VEGF and Delta-Notch: interacting signalling pathways in tumour angiogenesis. *Br J Cancer.* 2008; 99(8): 1204-1209.
- Sen CK, Gordillo GM, Khanna S, Roy S. Micromanaging vascular biology: tiny microRNAs play big band. *J Vasc Res.* 2009; 46(6): 527-540.
- Bonauer A, Boon RA, Dimmeler S. Vascular microRNAs. *Curr Drug Targets.* 2010; 11(8): 943-949.
- Sayed D, Abdellatif M. MicroRNAs in development and disease. *Physiol Rev.* 2011; 91(3): 827-887.
- Bonauer A, Carmona G, Iwasaki M, Mione M, Koyanagi M, Fischer A, et al. MicroRNA-92a controls angiogenesis and functional recovery of ischemic tissues in mice. *Science.* 2009; 324(5935): 1710-1713.
- Wang S, Aurora AB, Johnson BA, Qi X, McAnally J, Hill JA, et al. The endothelial-specific microRNA miR-126 governs vascular integrity and angiogenesis. *Dev Cell.* 2008; 15(2): 261-271.
- Brabletz S, Brabletz T. The ZEB/miR-200 feedback loop—a motor of cellular plasticity in development and cancer? *EMBO Rep.* 2010; 11(9): 670-677.
- Chan YC, Khanna S, Roy S, Sen CK. miR-200b targets Ets-1 and is down-regulated by hypoxia to induce angiogenic response of endothelial cells. *J Biol Chem.* 2011; 286(3): 2047-2056.
- Choi YC, Yoon S, Jeong Y, Yoon J, Baek K. Regulation of vascular endothelial growth factor signaling by miR-200b. *Mol Cells.* 2011; 32(1): 77-82.
- Chan YC, Roy S, Khanna S, Sen CK. Downregulation of endothelial microRNA-200b supports cutaneous wound angiogenesis by desilencing GATA binding protein 2 and vascular endothelial growth factor receptor 2. *Arterioscler Thromb Vasc Biol.* 2012; 32(6): 1372-1382.
- Rezabakhsh A, Rahbarghazi R, Malekinejad H, Fathi F, Montaseri A, Garjani A. Quercetin alleviates high glucose-induced damage on human umbilical vein endothelial cells by promoting autophagy. *Phytomedicine.* 2019; 56: 183-193.
- Matluobi D, Araghi A, Maragheh BFA, Rezabakhsh A, Soltani S, Khaksar M, et al. Carvacrol promotes angiogenic paracrine potential and endothelial differentiation of human mesenchymal stem cells at low concentrations. *Microvasc Res.* 2018; 115: 20-27.
- Kuo YR, Wang CT, Wang FS, Chiang YC, Wang CJ. Extracorporeal shock-wave therapy enhanced wound healing via increasing topical blood perfusion and tissue regeneration in a rat model of STZ-induced diabetes. *Wound Repair Regen.* 2009; 17(4): 522-530.
- Dasu MR, Thangappan RK, Bourgette A, DiPietro LA, Isseroff R, Jialal I. TLR2 expression and signaling-dependent inflammation impair wound healing in diabetic mice. *Lab Invest.* 2010; 90(11): 1628-1636.
- Wong SL, Demers M, Martinod K, Gallant M, Wang Y, Goldfine AB, et al. Diabetes primes neutrophils to undergo NETosis, which impairs wound healing. *Nat Med.* 2015; 21(7): 815-819.
- Borena BM, Martens A, Broeckx SY, Meyer E, Chiers K, Duchateau L, et al. Regenerative skin wound healing in mammals: state-of-the-art on growth factor and stem cell based treatments. *Cell Physiol Biochem.* 2015; 36(1): 1-23.
- Wang XH, Qian RZ, Zhang W, Chen SF, Jin HM, Hu RM. MicroRNA-320 expression in myocardial microvascular endothelial cells and its relationship with insulin-like growth factor-1 in type 2 diabetic rats. *Clin Exp Pharmacol Physiol.* 2009; 36(2): 181-188.
- Long J, Wang Y, Wang W, Chang BH, Danesh FR. Identification of microRNA-93 as a novel regulator of vascular endothelial growth factor in hyperglycemic conditions. *J Biol Chem.* 2010; 285(30): 23457-23465.
- Caporali A, Meloni M, Vollenkle C, Bonci D, Sala-Newby GB, Addis R, et al. Deregulation of microRNA-503 contributes to diabetes mellitus-induced impairment of endothelial function and reparative angiogenesis after limb ischemia. *Circulation.* 2011; 123(3): 282-291.
- Pecot CV, Rupaimoole R, Yang D, Akbani R, Ivan C, Lu C, et al. Tumour angiogenesis regulation by the miR-200 family. *Nat Commun.* 2013; 4: 2427.
- Rezabakhsh A, Nabat E, Yousefi M, Montazersaheb S, Cheraghi O, Mehdizadeh A, et al. Endothelial cells' biophysical, biochemical, and chromosomal aberrancies in high-glucose condition within the diabetic range. *Cell Biochem Funct.* 2017; 35(2): 83-97.
- Pedrosa AR, Trindade A, Fernandes AC, Carvalho C, Gigante J, Tavares AT, et al. Endothelial Jagged1 antagonizes Dll4 regulation of endothelial branching and promotes vascular maturation downstream of Dll4/Notch1. *Arterioscler Thromb Vasc Biol.* 2015; 35(5): 1134-1146.
- Yang X, Ni W, Lei K. miR-200b suppresses cell growth, migration and invasion by targeting Notch1 in nasopharyngeal carcinoma. *Cell Physiol Biochem.* 2013; 32(5): 1288-1298.
- Vallejo DM, Caparros E, Dominguez M. Targeting Notch signalling by the conserved miR-8/200 microRNA family in development and cancer cells. *EMBO J.* 2011; 30(4): 756-769.
- Yang Y, Ahn YH, Gibbons DL, Zang Y, Lin W, Thilaganathan N, et al. The Notch ligand Jagged2 promotes lung adenocarcinoma metastasis through a miR-200-dependent pathway in mice. *J Clin Invest.* 2011; 121(4): 1373-1385.

Elevated Secretion of Aldosterone Increases TG/HDL-C Ratio and Potentiates The Ox-LDL-Induced Dysfunction of HUVEC

Qian Zhang, Ph.D.¹, Yiwen Pan, M.Sc.^{2*}, Xiaochun Ma, Ph.D.¹, Hao Yang, B.Sc.², Jun Chang, B.Sc.², Ling Hong, M.Sc.², Huiwen Yan, Ph.D.^{2*}, Shubing Zhang, Ph.D.^{2,3,4*}

1. Department of Cardiovascular Surgery, Shandong Provincial Hospital Affiliated to Shandong First Medical University, Jinan, Shandong, China
2. Department of Cell Biology, School of Life Sciences, Central South University, Changsha, Hunan, China
3. Hunan Key Laboratory of Animal models for Human Diseases, Central South University, Changsha, Hunan, China
4. Breast Cancer Research Center, School of Life Sciences, Central South University, Changsha, Hunan, China

*Corresponding Address: Department of Cell Biology, School of Life Sciences, Central South University, Changsha, Hunan, China
Emails: yiwenpan@csu.edu.cn, huiwenyan1@hotmail.com, shubingzhang@csu.edu.cn

Received: 30/June/2019, Accepted: 28/September/2019

Abstract

Objective: Atherosclerosis (AS) is one of the most common causes of human death and disability. This study is designed to investigate the roles of aldosterone (Aldo) and oxidized low-density lipoprotein (Ox-LDL) in this disease by clinical data and cell model.

Materials and Methods: In this experimental study, clinical data were collected to investigate the Aldo role for the patients with primary aldosteronism or adrenal tumors. Cell viability assay, fluorescence-activated cell sorting (FACS) assay, apoptosis assay, cell aging analysis, and matrigel tube formation assay were performed to detect effects on human umbilical vein endothelial cells (HUVECs) treated with Aldo and/or Ox-LDL. Quantitative polymerase chain reaction (qPCR) and Western blot analysis were performed to figure out critical genes in the process of endothelial cells dysfunction induced by Aldo and/or Ox-LDL.

Results: We found that the Aldo level had a positive correlation with the TG/HDL-C ratio. Endothelial cell growth, angiogenesis, senescence, and apoptosis were significantly affected, and eNOS/Sirt1, the value of Bcl-2/Bax and Angiopoietin1/2 were significantly affected when cells were co-treated by Aldo and Ox-LDL.

Conclusion: Elevated Aldo with high Ox-LDL together may accelerate the dysfunction of HUVEC, and the Ox-LDL, especially for those patients with high Aldo should be well controlled. The assessment of the role of Aldo may provide a theoretical basis for the effective prevention and investigation of a new treatment of AS.

Keywords: Aldosterone, Atherosclerosis, Human Umbilical Vein Endothelial Cells, Oxidized Low-Density Lipoprotein, Triglyceride/High-Density Lipoprotein Cholesterol

Cell Journal(yakhteh), Vol 23, No 1, April-June (Spring) 2021, Pages: 61-69

Citation: Zhang Q, Pan Y, Ma X, Yan H, Chang J, Hong L, Yan H, Zhang Sh. Elevated secretion of aldosterone increases TG/HDL-C ratio and potentiates the Ox-LDL-induced dysfunction of HUVEC. Cell J. 2021; 23(1): 61-69. doi: 10.22074/cellj.2021.7033.

This open-access article has been published under the terms of the Creative Commons Attribution Non-Commercial 3.0 (CC BY-NC 3.0).

Introduction

Atherosclerosis (AS) is a chronic immune-inflammatory disease characterized by abnormal lipid metabolism in the arterial wall, which causes a variety of cardiovascular and cerebrovascular diseases and is one of the most common causes of human death and disability (1). Aldosterone (Aldo), the main mineralocorticoid hormone, belongs to the Renin-angiotensin-aldosterone-system and may play an important role in vascular injury and remodeling (2, 3). Excessive Aldo will cause hypertension, hypokalemia, vascular inflammation, injury, loss of vascular function, and the initiation and progression of AS (4, 5). In patients with known AS, higher Aldo levels predict a substantially increased risk of cardiovascular death, but the mechanisms are poorly understood (6).

Animal studies demonstrated that Aldo functions in atherosclerotic plaque formation, and Aldo infusion increased overall aortic plaque area with enhanced oxidative stress (7). Clinical trials showed that inhibition of Aldo production or inhibition of the mineralocorticoid receptor, which mediates Aldo's effects can reduce

cardiovascular ischemic events and mortality (8). Some studies suggest that Aldo can promote vascular inflammation, injury, and dysfunction. For example, nitric oxide (NO) functions as the relaxation factor of vascular smooth muscle and may have an anti-AS effect, while Aldo can reduce NO synthesis in the vascular wall (9, 10). Endothelial progenitor cells (EPC) are mainly involved in the renewal, vascular repair, and angiogenesis of VECs, while Aldo can lead to the dysfunction and damage of EPC (11). In addition, Aldo regulates vascular fibrosis and promotes insulin resistance by up-regulating insulin-like growth factor 1 receptor (IGF1R) in vascular smooth muscle cells (12). The above evidence suggests that Aldo probably function importantly in the occurrence of AS and mechanism involved need to be further clarified.

Vascular endothelial cells (VECs) dysfunction is found in the lesion-prone areas of arterial vasculature, resulting in the earliest detectable changes in the process of an atherosclerotic lesion (13). This leads into a complex pathogenic sequence, initially involving the selective recruitment of monocytes into the intima, where they

differentiate into macrophages and become foam cells; the released growth factors and chemokines then induce neighboring smooth muscle cells to proliferate and synthesize extracellular matrix components and then generate fibromuscular plaque (14, 15). During the development of AS, VECs are exposed to various damaging stimuli [such as oxidized low-density lipoprotein (Ox-LDL)], which trigger vascular endothelial injury (16). Angiogenesis has two kinds of functions on AS, which is induced in a hypoxic environment can be a reason to increase plaque of development and stability (17). However, it also has another function to repair damaged cells. Therefore, understanding the mechanism involved in VECs dysfunction induced by different factors will be helpful for better prevention and therapy of AS.

In this study, we analyzed the clinical data of these patients admitted to our department to explore the Aldo effects on the occurrence and progression of AS. At the same time, HUVECs were used to further explore the effect and mechanism of Ox-LDL and Aldo at the cellular level.

Materials and Methods

Patients' data

In this experimental study, human data were obtained from the basic diagnosis of patients from Shandong Provincial Hospital affiliated to Shandong University from January 2018 to January 2019. Consent has been obtained from each patient after a full explanation of the purpose and nature of all procedures used. The research purposes under protocols were approved by the Ethics Committee of our hospital (NO.2017536). It is considered to be excessive if the serum Aldo level is more than 300 pg/mL depending on clinical practice endorsed by our hospital. The patients were divided into 3 subgroups (Aldo<300, 300<Aldo<600, Aldo>600) or 2 subgroups (Aldo<300, Aldo>300) in different data analysis.

Chemicals

Aldo (ApexBio Technology, USA) was dissolved in dimethylsulfoxide (DMSO, Solarbio, Beijing, China) at 2 mM and stored at -20°C. Ox-LDL was obtained from Yiyuan Biotechnologies (Guangzhou, China). Cell Counting Kit-8 (CCK8) was obtained from YEASEN (Shanghai, China). Hoechst 33342 Staining Kit was obtained from Bioworld Technology (Nanjing, China). Senescence β -Galactosidase Staining Kit was obtained from Beyotime Biotechnology (Beijing, China).

Cell culture

HUVECs were obtained from the Department of Endocrinology, Xiangya Third Hospital, Central South University. Cells were grown at 37°C with RPMI 1640 (Hyclone, USA) medium supplemented with 100 μ g/mL streptomycin, 100 U/mL penicillin (Solarbio, Beijing, China) and 10% fetal bovine serum (PAN-Biotech, Germany) in a humidified incubator of 5% CO₂.

Cell counting assay kit-8 assay

Cell counting assay kit-8 (CCK8) was used to measure cell viability according to the manufacturer's instructions. The cells were seeded at a density of 3000 cells/well in 96-well plates and then treated for 24, 48, 72, and 96 h with Ox-LDL (120 μ g/mL) or/and Aldo (20 μ M) diluted to various concentrations in complete medium, control was incubated with DMSO. After treatment, CCK-8 reagent was mixed to the medium (1: 10) at 37°C for 2-4 hours and then measured absorbance at 490 nm using a microplate reader.

Fluorescence-activated cell sorting assay

After treated with Ox-LDL or/and Aldo for 48 hours, the cells were collected by Trypsin digestion to prepare a single cell suspension and then centrifuged for 5 minutes at 1000 r/minutes. After washed with phosphate buffer saline (PBS, Beijing Dingguo, China) twice, the cells were fixed at 4°C with 70% ice-ethanol overnight. Then, samples were stained with propidium iodide (PI) and measured using a flow cytometer.

Apoptosis assay by Hoechst33342

Cell apoptosis was measured using a Hoechst 33342 Staining Kit. The cells grew in 24-well plates treated with Ox-LDL (120 μ g/mL) or/and Aldo (20 μ M), as previously described. The control group was incubated with DMSO. After 48 hours treatment, the cells were incubated in dilution buffer with Chromogen (the final concentration was 5 μ g/mL) about 5 minutes in a dark incubator at 30°C, and then washed with PBS for 3 minutes for 3 times. The sample was then observed with the fluorescence microscope. The percentage of Hoechst staining was calculated by counting the positively stained cells within a sample of 100 cells.

Cell aging analysis

Cell aging was measured using a Senescence β -Galactosidase Staining Kit. HUVECs were treated with 20 μ M Aldo alone or combined with 120 μ g/mL of Ox-LDL for 48 hours. Cells were treated with the same amount of DMSO as control. The cells were rinsed using PBS and then fixed for 15 minutes with a fixation solution. After that, the cells were washed triplicate for 3 minutes and incubated with a staining solution overnight at 37°C. Then, the cells were observed and counted with the ordinary light microscope. The percentage of SA- β -gal was calculated by counting the positively stained cells within a sample of 100 cells.

Matrigel tube formation assay *in vitro*

After thawed on the ice overnight, Matrigel (Corning, USA) was added into a 96-well plate (50 μ L/well) and incubated for 30 minutes at 37°C to solidify. After trypsinized, the HUVECs were seeded into Matrigel-coated wells (2 \times 10⁴ cells per well). The cells were incubated with Ox-LDL (120 μ g/mL) or/and Aldo (20 μ M) for 6-12 hours in RPMI 1640 medium. Cells were treated with the same amount of DMSO as control. After 6-12 hours at 37°C, the tube formation in Matrigel was observed under a light microscope.

Quantitative polymerase chain reaction experiment

Total RNA extraction, reverse transcription, and quantitative polymerase chain reaction (qPCR) were performed using TRIzol Up Plus RNA Kit (Transgene Biotech, China), FastQuant RT Kit (Tiangen, China) and SuperReal PreMix Plus (Tiangen, China), respectively.

The primer sequences as followed:

eNOS was:

F: 5'-GTTTGTCTGCGGCGATGTT-3'

R: 5'-GCGTGAGCCCCGAAAATGTC-3'.

Sirt1 was:

F: 5'-TGACTGGACTCCAAGGCCACGG-3'

R: 5'-TCAGGTGGAGGTATTGTTTCCGGCA-3'.

Angiotensin-1 was:

F: 5'-AGCGCCGAAGTCCAGAAAAC-3'

R: 5'TACTCTCACGACAGTTGCCAT-3'.

Angiotensin-2 was:

F: 5'-CTCGAATACGATGACTCGGTG-3'

R: 5'TCATTAGCCACTGAGTGTGTTT-3'.

The relative abundance of mRNA was determined by the equation $2^{-\Delta CT}$ ($\Delta CT = \text{threshold cycle (CT)}_{\text{Tested Gene}} - \text{CT}_{\text{GAPDH}}$). For each sample, data were derived from three repeats.

Western blot analysis

The cells were treated with Aldo (20 μM), Ox-LDL (120 $\mu\text{g/mL}$), or Aldo plus Ox-LDL for 48 hours. The control group was incubated with DMSO. After lysed in RIPA buffer (Beyotime Biotechnology, China), the cells were centrifuged at $130000 \times g$ for 10 minutes at 4°C . Total proteins (25 μg) were resuspended in loading buffer and separated by 10% sodium dodecyl sulfate polyacrylamide gel electrophoresis (SDS-PAGE, Biosharp, China), followed by transferring onto a polyvinylidene fluoride membrane (18). The membranes were blocked with 5% nonfat dry milk and incubated with the primary antibody overnight. After incubated with secondary antibody and washed, blots were developed with the Efficient Chemiluminescence Kit (GENVIEW) and SageCapture imaging System (SAGECREATION). Primary antibodies are eNOS (1:1000; Cell Signaling Technology, No.9572), Bcl-2 (1:1000, Proteintech, No. 12789-1-AP), Bax (1:1000, Proteintech, No. 50599-2-Ig) and β -actin (1:2000, ABclonal, No. AC004). The second antibodies are Goat Anti-Mouse IgG (1:4000, ABclonal, No. AS003) and Goat Anti-Rabbit IgG (1:4000; Abbkine, No.A21020).

Statistics

All data were presented as mean \pm standard error. Statistical analysis was performed by the two-tailed Student t test, and it was considered statistically significant when the $P < 0.05$. (GraphPad Prism).

Results

A total of 327 patients (male 172, female 155) who had primary aldosteronism and adrenal tumors were examined retrospectively. The average age is 45.7 years old range from

16 to 77 years old. The demographic data of the cases were shown in Table 1.

Table 1: Demographic characteristics of cases

Characteristics	Male (n=172)	Female (n=155)
Age (Y)	44.29 \pm 12.69	47.35 \pm 11.60
Weight (kg)	80.06 \pm 12.18	66.45 \pm 10.74
Cholesterol (mmol/L)	4.88 \pm 1.18	5.16 \pm 1.15
HDL(mmol/L)	1.18 \pm 0.28	1.40 \pm 0.31
LDL (mmol/L)	4.00 \pm 14.98	3.00 \pm 0.94
TG (mmol/L)	1.88 \pm 1.33	1.52 \pm 0.88
ALD (pg/ml)	292.34 \pm 255.05	289.08 \pm 184.84

Data are presented as mean \pm SD. HDL; High-density lipoprotein cholesterol, LDL; Low-density lipoprotein.

Aldo level had a positive correlation with TG/HDL-C ratio

Our results confirm that excessive secretion of Aldo by the adrenal cortex is characterized by hypertension (Fig.1A, B). Interestingly, the serum Aldo level is relevant to the level of TG and HDL cholesterol (HDL-C). In excessive Aldo group (Aldo>300), 44.8% of patients were beyond the high limit value of TG, while only 26.1% in the normal group (Aldo<300). In the meantime, 1.7% of patients were beyond the low limit value of HDL-C in excessive Aldo group, while only 0.5% in the normal group (Fig.1C, D). TG/HDL-C ratio has been reported to be useful in predicting cardiovascular disease (19). It is surprising that 46.6% of patients with TG/HDL-C ratio were above the average in excessive Aldo group, while only 26.5% in the normal group (Fig.1E). Our data also show that Aldo is not significantly correlative to LDL-C (Fig.1F).

HUVECs growth was synergistically inhibited with the combined treatment of Aldo and Ox-LDL

Endothelial dysfunction plays a key role in AS (20). A common hallmark of these pathologic conditions is vascular dysfunction associated with endothelial cell growth inhibition, senescence, and death by apoptosis. HUVECs can be used as a cell model to understand further mechanisms involved in the endothelial dysfunction induced by the high level of Aldo and Ox-LDL. Our results showed that HUVECs growth can be inhibited by a high concentration of Aldo (Fig.2A). And cells growth was significantly inhibited even at a low concentration of Aldo when combined with the Ox-LDL together (Fig.2B). The cell cycle blockage may be the main reason for cell growth inhibition. Our results confirm that the cell cycle of HUVECs treated by Aldo and/or Ox-LDL can be blocked on the G1/S phase. The rate of G1/S increased significantly for the concomitant drugs group compared to the control group (Fig.2C, D). These data suggest that G1/S block is a major reason for inhibiting HUVECs growth, one kind of endothelial dysfunctions, which may be a mechanism for AS promoted by Aldo and Ox-LDL.

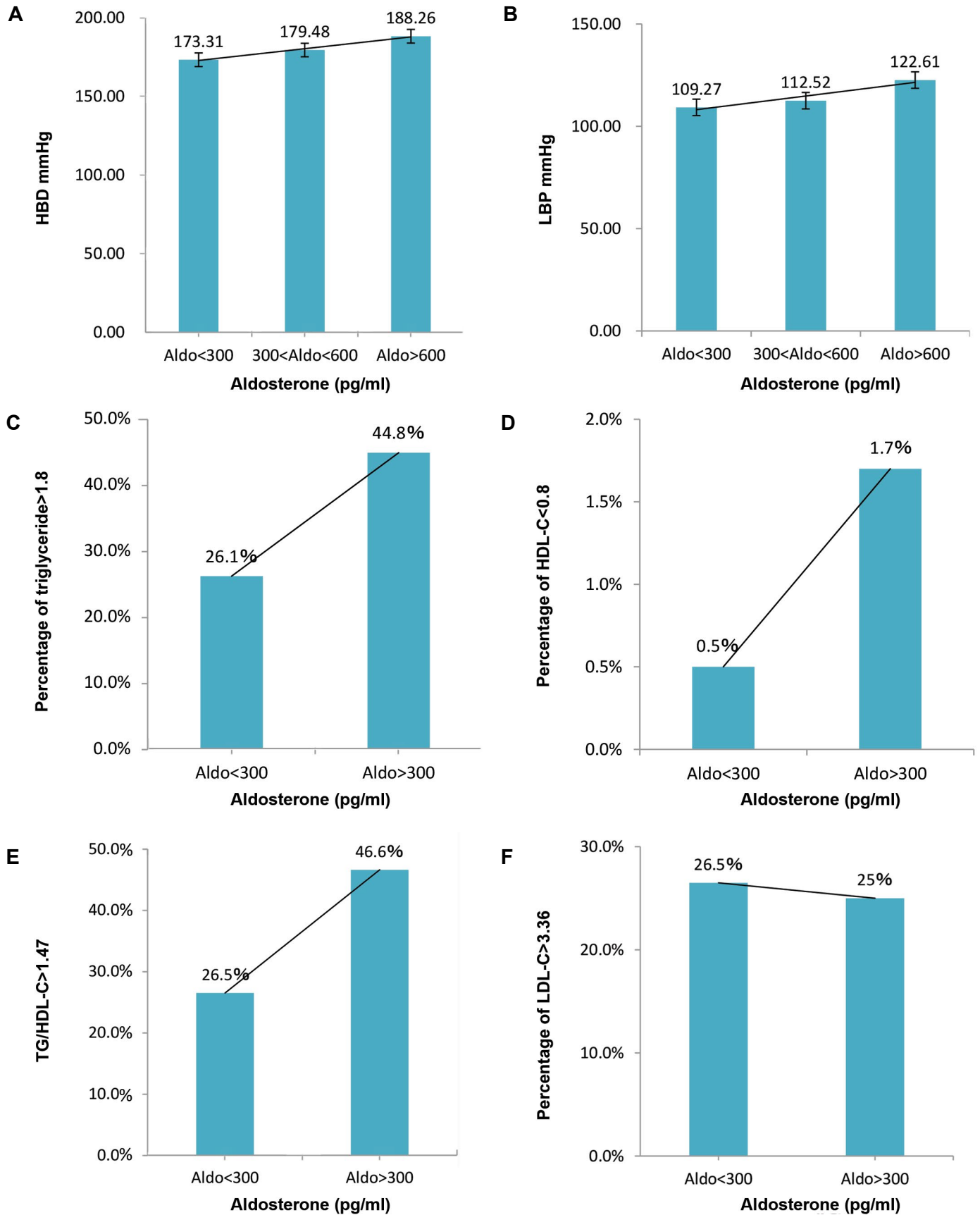


Fig.1: The correlation of serum Aldo level with blood pressure, TG, HDL-C, and LDL-C. The patients were divided into 3 subgroups (Aldo<300, 300<Aldo<600, Aldo>600) or 2 subgroups (Aldo<300, Aldo>300). **A.** The average vale of high blood pressure in Aldo<300, 300<Aldo<600, Aldo>600 groups. **B.** The average vale of low blood pressure in Aldo<300, 300<Aldo<600, Aldo>600 groups. **C.** The percentage of serum TG level above 1.8 mmol/L in Aldo<300 and Aldo>300 groups. **D.** The percentage of serum HDL-C level below 0.8 mmol/L in Aldo<300 and Aldo>300 groups. **E.** The percentage of TG/HDL-C ratio above the average in Aldo<300 and Aldo>300 groups. **F.** The percentage of serum LDL-C level above 3.36 mmol/L in Aldo<300 and Aldo>300 groups. TG; Triglyceride, HDL-C; High-density lipoprotein, cholesterol, LDL-C; Low-density lipoprotein, cholesterol, HBD; High blood pressure, LBP; Low blood pressure, and Aldo; Aldosterone.

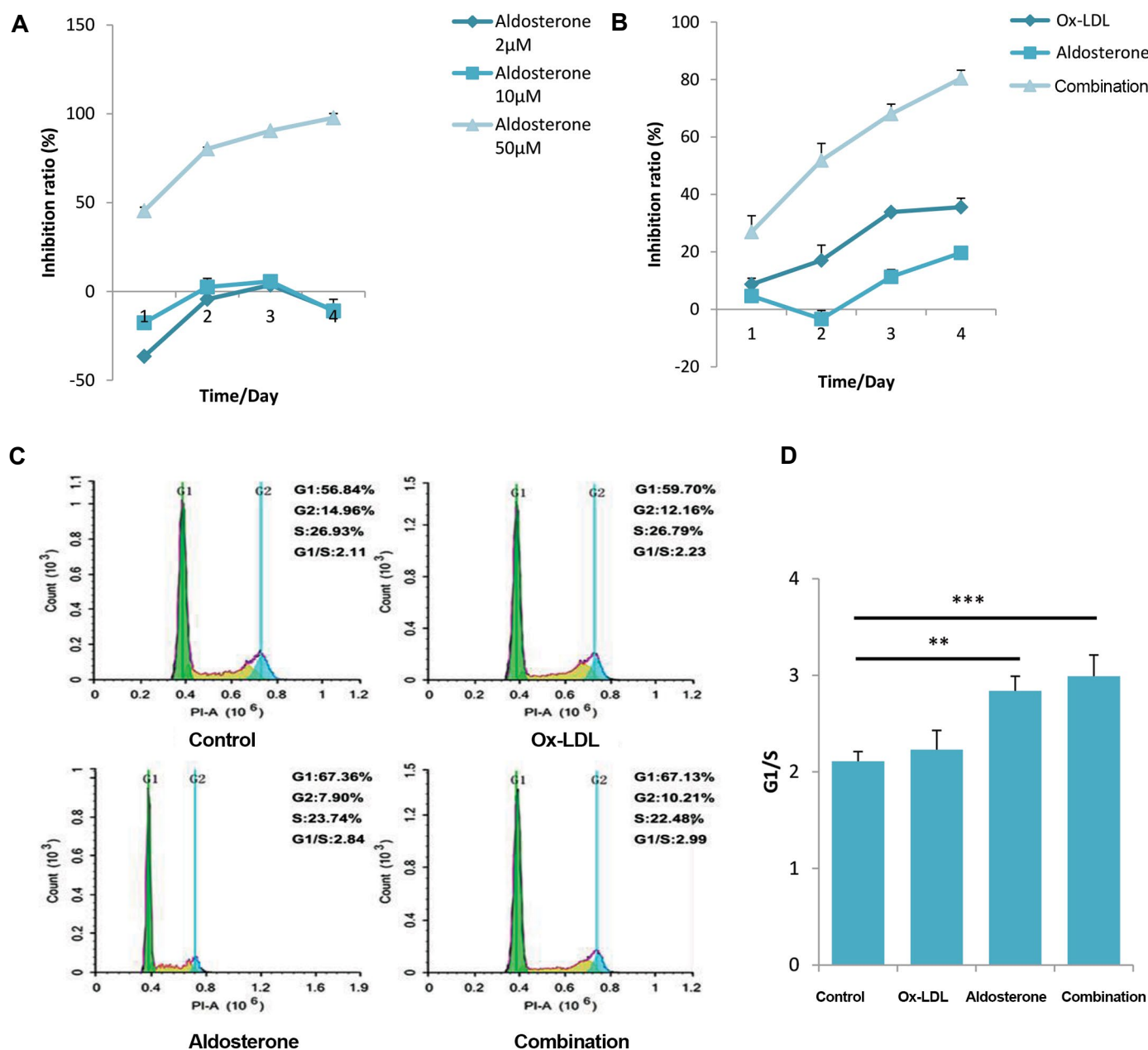


Fig.2: Aldo sterone and Ox-LDL block the cell cycle in the G1/S phase to inhibit proliferation of HUVECs. **A.** Cell growth curve of HUVECs under treatment of Aldo (2, 10 and 50 μ M). **B.** Cell growth curve of HUVECs which were treated with 20 μ M Aldo alone or combined with 120 μ g/mL of Ox-LDL. At each time point, relative numbers of viable cells were detected using CCK-8 assay. **C.** Cell cycle was detected by flow cytometry after treatment with Aldo (20 μ M), Ox-LDL (120 μ g/mL) or Aldo plus Ox-LDL. **D.** G1/S phase ratio of HUVECs which were treated with different drugs. DMSO used as control. Data are presented as mean values \pm standard errors from three experiments.

** $P < 0.005$, *** $P < 0.0005$ compared with the control group, Ox-LDL; Oxidized low-density lipoprotein, HUVECs; Human umbilical vein endothelial cells, Aldo; Aldosterone, and DMSO; Dimethylsulfoxide.

Aldo accelerated senescence and promoted apoptosis in HUVECs induced by Ox-LDL

Cell aging analysis results show that the senescence of HUVECs has been accelerated by the combined treatment of Aldo and Ox-LDL, but almost was not affected by the single drug (Fig.3A, B). qPCR results showed that eNOS RNA levels dramatically decreased, and the Sirt1 mRNA levels significantly increased when HUVECs were treated with Aldo and Ox-LDL (Fig.3C). Western blot results confirmed that the pattern of the eNOS protein level is similar to the mRNA level (Fig.3D, E). Apoptosis

assay results showed that the apoptosis rate of HUVECs significantly increased when combined treatment using both Aldo and Ox-LDL, compared with the control or single drug (Fig.4A, B). Western blot results suggested that the quantity of apoptosis-related critical protein Bcl-2 decreased, and Bax increased in HUVECs treated with single/combined drugs (Fig.4C-E), which suggested that the apoptosis is mediated by Bcl-2 family proteins through the mitochondria-dependent pathway. These above key factors, including eNOS, Sirt, Bcl-2, and Bax, may be useful targets for the better prevention and therapy of AS.

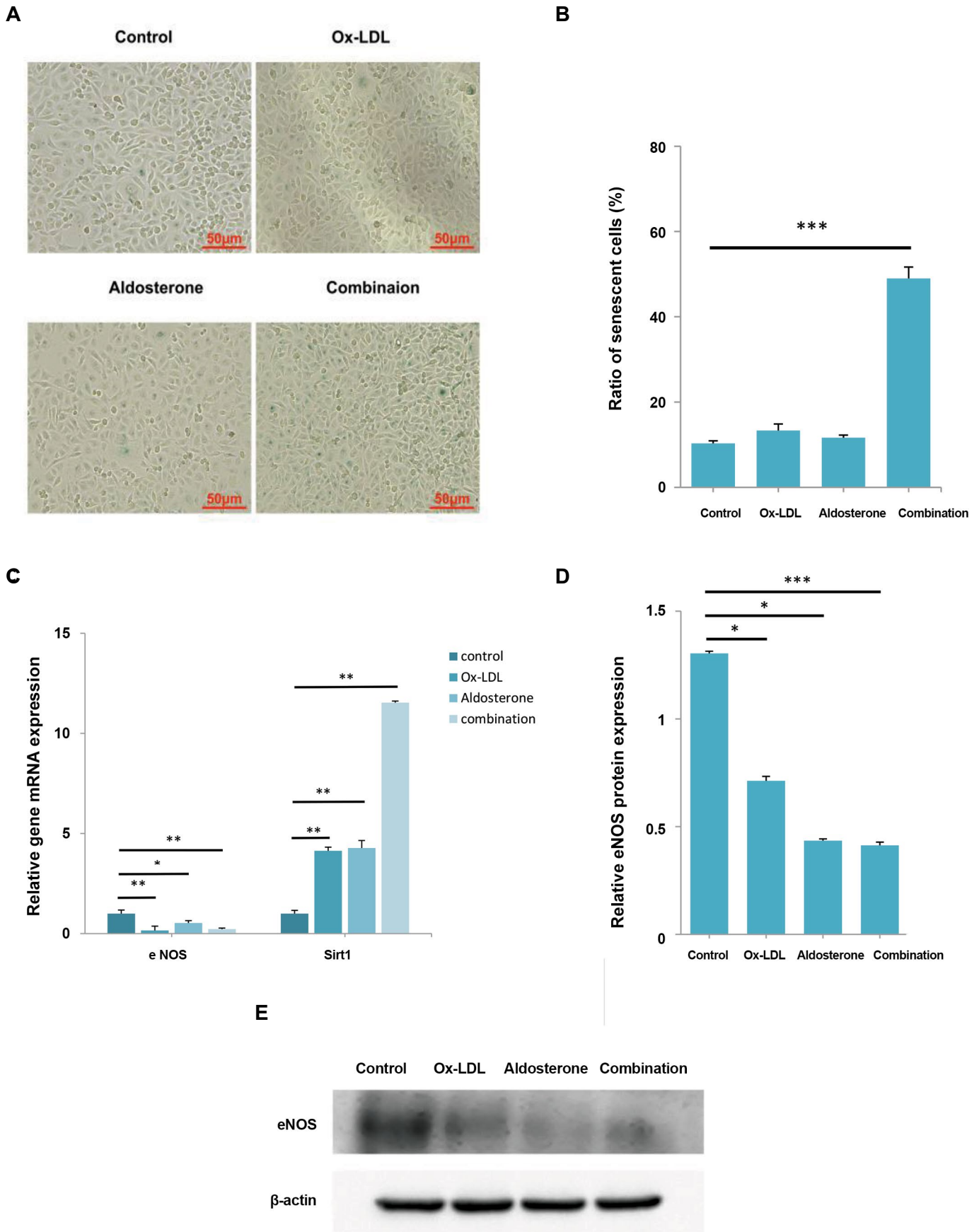


Fig.3: Aldo sterone accelerates senescence in HUVECs treated with Ox-LDL. HUVECs were treated with 20 µM Aldo alone or combined with 120 µg/mL of Ox-LDL for 48 hours. Cells were treated with the same amount of DMSO as control. **A.** Cell aging was detected by Senescence β-Galactosidase Staining Kit (scale bars: 50 µm). **B.** Ratio of SA-β galactosidase-positive HUVECs. **C-E.** Western blot and qPCR analysis of eNOS and Sirt1 in HUVECs. *, P<0.05, **, P<0.005, ***, P<0.0005, ****, P<0.0001 compared with the control group, HUVECs; Human umbilical vein endothelial cells, Ox-LDL; Oxidized low-density lipoprotein, DMSO; Dimethylsulfoxide, and qPCR; Quantitative polymerase chain reaction.

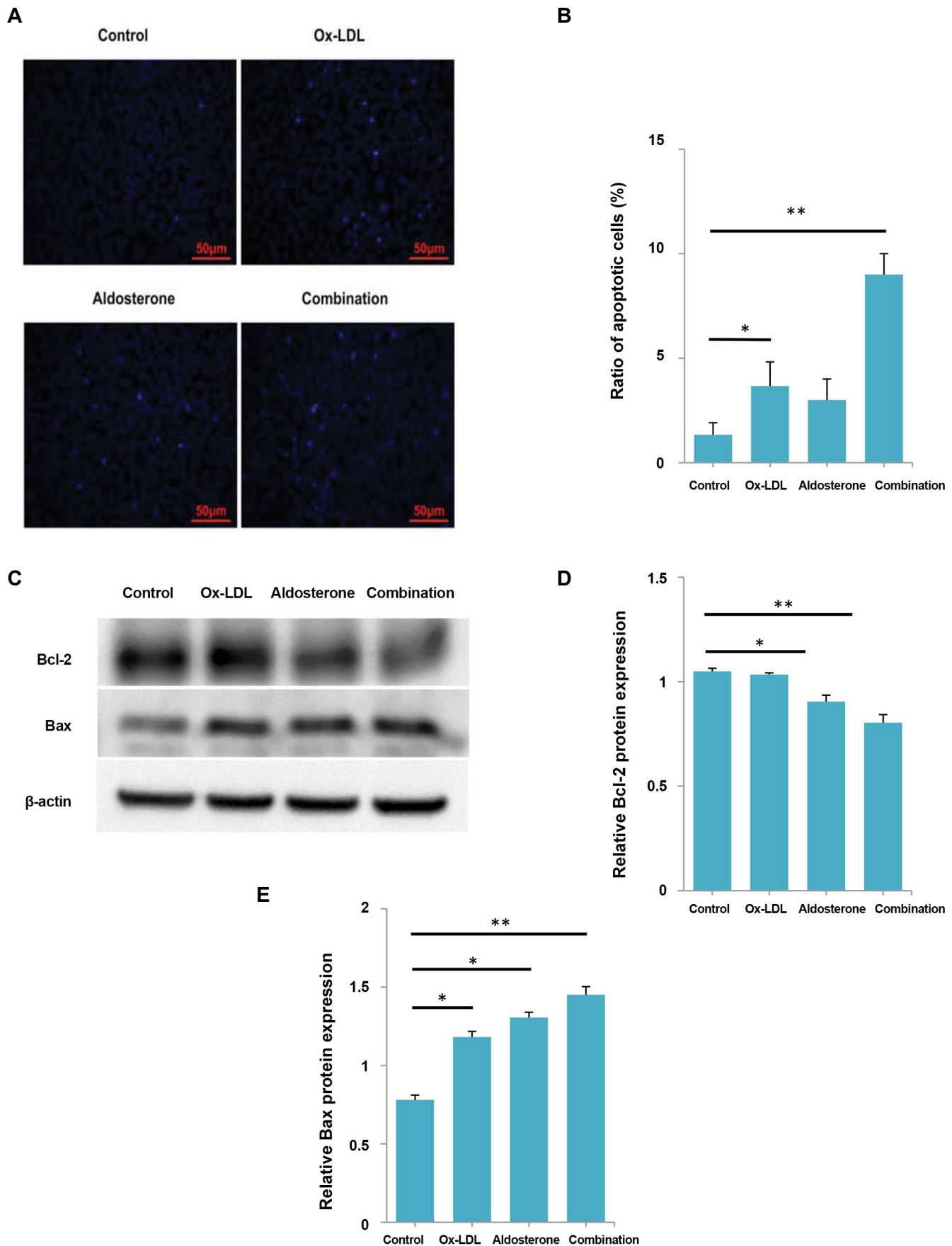


Fig.4: Aldo sterone promotes apoptosis in HUVECs induced by Ox-LDL. HUVECs were treated with 20 µM Aldo alone or combined with 120 µg/mL of Ox-LDL for 48 hours. Cells were treated with same amount of DMSO as control. **A.** The apoptosis of HUVECs was detected by Hoechst33342 staining (scale bars: 50 µm). **B.** Ratio of Hoechst33342 staining-positive HUVECs. **C-E.** Western blot analysis of Bcl-2 and Bax in HUVECs. β-actin is included as the loading control. Shown are mean values ± standard errors from three experiments. *, P<0.05, **, P<0.005 compared with the control group, HUVECs; Human umbilical vein endothelial cells, Ox-LDL; Oxidized low-density lipoprotein, and DMSO; Dimethylsulfoxide.

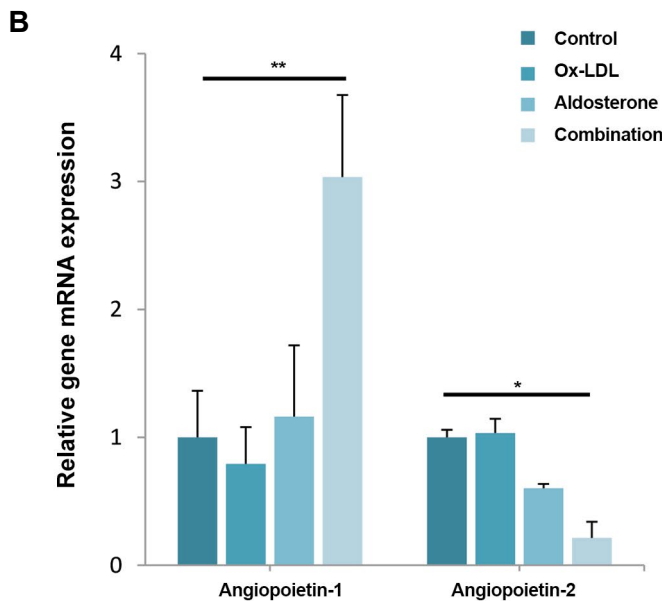
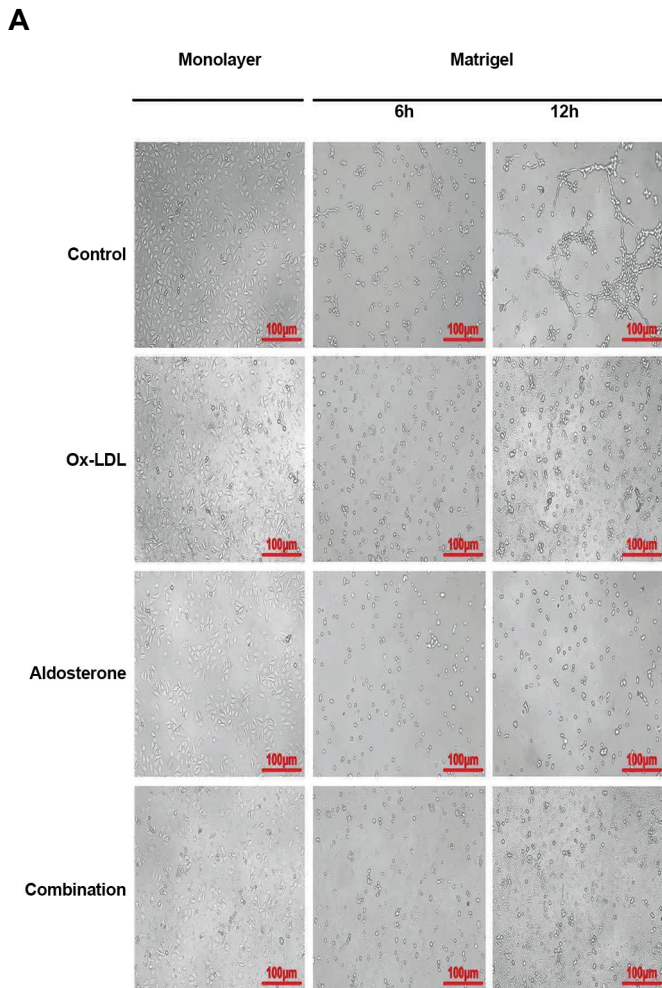


Fig.5: Aldo sterone and Ox-LDL inhibits tube formation *in vitro*. Cells were treated with Aldo (20 µM), Ox-LDL (120 µg/mL) or Aldo plus Ox-LDL for 48 hours, control was incubated with DMSO. **A.** Tube formation of HUVECs was examined by *in vitro* Matrigel tube formation assay (Scale bars: 100 µm). **B.** The relative expression of mRNA levels of Angiopoietin-1/2 in HUVECs was detected by qPCR. Shown are mean values ± standard errors from three experiments.

*, P<0.05, **, P<0.005 compared with the control group, Ox-LDL; Oxidized lowdensity lipoprotein, DMSO; Dimethylsulfoxide, HUVECs; Human umbilical vein endothelial cells, h; hours, and qPCR; Quantitative polymerase chain reaction.

Angiogenesis was inhibited in HUVECs treated with Aldo and/or Ox-LDL

Matrigel tube formation assay shows that angiogenesis of HUVECs was inhibited dramatically with the combined treatment of both Aldo and Ox-LDL (Fig.5A), which suggested that the ability to repair damaged cells attenuate. Both Angiopoietin1 and Angiopoietin2 are important in the process of Angiogenesis. qPCR results showed that Angiopoietin1 expression was promoted while Angiopoietin2 was inhibited in combined treatment (Fig.5B). The mechanism of angiogenesis regulated by Angiopoietin1/2 needs to be further clarified.

Discussion

Increasing evidence shows that Aldo plays crucial roles in the occurrence and progression of AS and promoting the formation of plaques (21). It is recognized that foam cell formation was a critical step, mainly according to the macrophages following exposure to Ox-LDL (22, 23). Patients' statistical data analysis results showed that excessive Aldo is related directly with TG/HDL-C ratio, which is a main predictive factor for cardiovascular disease, and this elucidates that excessive Aldo level may cause AS by affecting both TG and HDL-C. It is useful to continue to collect the patient's information.

An elevated level of plasma LDL-C is an important risk factor for AS. It is useful to decrease cardiovascular risk and prevent the progression of AS with controlling elevated LDL-C (24). Aldo has little effect on the LDL-C level in our patients. It is very interesting to investigate whether the progression of AS may be accelerated if Aldo affects the value of TG/HDL-C in the presence of a high level of LDL-C. There is a synergetic effect for the patient with excessive Aldo and Ox-LDL, which plays a central role in AS by acting on multiple cells, such as causing HUVECs in oxidative stress (25). Based on the HUVECs model, we found that cell growth and angiogenesis were synergistically inhibited. The rates of senescence and apoptosis were synergistically promoted when combined with both Aldo and Ox-LDL. Therefore, endothelial cells dysfunction, including growth, angiogenesis, senescence, and apoptosis, all of which were affected by Aldo in the presence of Ox-LDL. These findings provided more information for the clinical treatment of AS.

Human vascular endothelial cell senescence and apoptosis are initiating factors in numerous cardiovascular diseases (26). Activation of the renin-angiotensin-aldosterone (Aldo) system plays a critical role in endothelial dysfunction, vascular remodeling, and senescence (27). There are also many vital protein factors involved in the process of AS. eNOS/Sirt1 regulatory loops are the main factors in the ROS process, and Bcl-2/Bax are the main factor involved in the cell apoptosis (28). Angiopoietin2 attenuates AS, and its up-regulation may have potential therapeutic value in patients with this disease (29). Our study showed that eNOS/Sirt1, the value of Bcl-2/Bax and Angiopoietin2 are significantly

decreased with the concomitant treatment of Aldo and Ox-LDL. These factors play important roles in the process of endothelial cells dysfunction induced by Aldo and/or Ox-LDL. However, the mechanism of these key genes expression regulation by Aldo and Ox-LDL is still not clarified.

In summary, HUVECs growth, angiogenesis, senescence, and apoptosis were significantly affected when treated with both Ox-LDL and Aldo. The further study of Aldo will provide a theoretical basis for the effective prevention and investigation of a new treatment of AS. High concentrations of Aldo and LDL-C may accelerate the process of the disease, especially for those patients with increased level of Aldo who must control their LDL-C.

Acknowledgements

Funding from the Natural Science Foundation of Shandong Province (ZR2017BH017) and the Research Innovation Program for graduates of Central South University (grant no. 2018zzts400). This research work is also supported by the National Natural Science Foundation of China (grant no.81672632) and Science and Technology Major Projects of Hunan Province (grant no. 2018SK1020). The authors declare no conflict of interest.

Authors' Contributions

Q.Z., Y.P., H.Y., S.Z.; Contributed to conception and design. Q.Z., Y.P., X.M., H.Y., J.C., L.H.; Contributed to all experimental work, data and statistical analysis, and interpretation of data. H.Y., S.Z.; Were responsible for overall supervision. S.Z.; Drafted the manuscript, which was revised by H.Y. All authors read and approved the final manuscript.

References

- Libby P, Bornfeldt KE, Tall AR. Atherosclerosis: successes, surprises, and future challenges. *Circ Res*. 2016; 118(4): 531-534.
- McGraw AP, Bagley J, Chen WS, Galayda C, Nickerson H, Armani A, et al. Aldosterone increases early atherosclerosis and promotes plaque inflammation through a placental growth factor-dependent mechanism. *J Am Heart Assoc*. 2013; 2(1): e000018.
- Ames MK, Atkins CE, Pitt B. The renin-angiotensin-aldosterone system and its suppression. *J Vet Intern Med*. 2019; 33(2): 363-382.
- van der Heijden C, Deinum J, Joosten LAB, Netea MG, Riksen NP. The mineralocorticoid receptor as a modulator of innate immunity and atherosclerosis. *Cardiovasc Res*. 2018; 114(7): 944-953.
- Marzolla V, Armani A, Mammi C, Moss ME, Pagliarini V, Pontecorvo L, et al. Essential role of ICAM-1 in aldosterone-induced atherosclerosis. *Int J Cardiol*. 2017; 232: 233-242.
- Ivanov F, Susen S, Mouquet F, Pigny P, Cuilleret F, Sautiere K, et al. Aldosterone, mortality, and acute ischaemic events in coronary artery disease patients outside the setting of acute myocardial infarction or heart failure. *Eur Heart J*. 2012; 33(2): 191-202.
- Keidar S, Kaplan M, Pavlotzky E, Coleman R, Hayek T, Hamoud S, et al. Aldosterone administration to mice stimulates macrophage NADPH oxidase and increases atherosclerosis development: a possible role for angiotensin-converting enzyme and the receptors for angiotensin II and aldosterone. *Circulation*. 2004; 109(18): 2213-2220.
- Pitt B, Remme W, Zannad F, Neaton J, Martinez F, Roniker B, et al. Eplerenone, a selective aldosterone blocker, in patients with left ventricular dysfunction after myocardial infarction. *N Engl J Med*. 2003; 348(14): 1309-1321.
- Wu F, Lin Y, Liu Q. The emerging role of aldosterone/mineralocorticoid receptors in the pathogenesis of erectile dysfunction. *Endocrine*. 2018; 61(3): 372-382.
- Silva MA, Bruder-Nascimento T, Cau SB, Lopes RA, Mestriner FL, Fais RS, et al. Spironolactone treatment attenuates vascular dysfunction in type 2 diabetic mice by decreasing oxidative stress and restoring NO/GC signaling. *Front Physiol*. 2015; 6: 269.
- Marumo T, Uchimura H, Hayashi M, Hishikawa K, Fujita T. Aldosterone impairs bone marrow-derived progenitor cell formation. *Hypertension*. 2006; 48(3): 490-496.
- Sherajee SJ, Fujita Y, Rafiq K, Nakano D, Mori H, Masaki T, et al. Aldosterone induces vascular insulin resistance by increasing insulin-like growth factor-1 receptor and hybrid receptor. *Arterioscler Thromb Vasc Biol*. 2012; 32(2): 257-263.
- Stary HC. Natural history and histological classification of atherosclerotic lesions: an update. *Arterioscler Thromb Vasc Biol*. 2000; 20(5): 1177-1178.
- Gimbrone MA Jr, Garcia-Cardena G. Endothelial cell dysfunction and the pathobiology of atherosclerosis. *Circ Res*. 2016; 118(4): 620-636.
- Zheng B, Yin WN, Suzuki T, Zhang XH, Zhang Y, Song LL, et al. Exosome-mediated miR-155 transfer from smooth muscle cells to endothelial cells induces endothelial injury and promotes atherosclerosis. *Mol Ther*. 2017; 25(6): 1279-1294.
- Pacurari M, Kafoury R, Tchounwou PB, Ndebele K. The Renin-angiotensin-aldosterone system in vascular inflammation and remodeling. *Int J Inflamm*. 2014; 2014: 689360.
- Jaipersad AS, Lip GY, Silverman S, Shantsila E. The role of monocytes in angiogenesis and atherosclerosis. *J Am Coll Cardiol*. 2014; 63(1): 1-11.
- Zhang S, Liu J, Xu K, Li Z. Notch signaling via regulation of RB and p-AKT but not PIK3CG contributes to MIA PaCa-2 cell growth and migration to affect pancreatic carcinogenesis. *Oncol Lett*. 2018; 15(2): 2105-2110.
- Wen JH, Zhong YY, Wen ZG, Kuang CQ, Liao JR, Chen LH, et al. Triglyceride to HDL-C ratio and increased arterial stiffness in apparently healthy individuals. *Int J Clin Exp Med*. 2015; 8(3): 4342-4348.
- Zhang H, Wu S, Yang Y, Su R, Wen J, Ke X, et al. Crocin protects human umbilical vein endothelial cells from high glucose-induced injury via inhibiting the endoplasmic reticulum stress response. *Curr Mol Med*. 2018; 18(3): 166-177.
- Moss ME, Jaffe IZ. Mineralocorticoid receptors in the pathophysiology of vascular inflammation and atherosclerosis. *front endocrinol (Lausanne)*. 2015; 6: 153.
- Wei S, Zhang L, Bailu W, Zhao Y, Dong Q, Pan C, et al. ALDH2 deficiency inhibits Ox-LDL induced foam cell formation via suppressing CD36 expression. *Biochem Biophys Res Commun*. 2019; 512(1): 41-48.
- Liang SJ, Zeng DY, Mai XY, Shang JY, Wu QQ, Yuan JN, et al. Inhibition of orai1 store-operated calcium channel prevents foam cell formation and atherosclerosis. *Arterioscler Thromb Vasc Biol*. 2016; 36(4): 618-628.
- Pinkosky SL, Newton RS, Day EA, Ford RJ, Lhotak S, Austin RC, et al. Liver-specific ATP-citrate lyase inhibition by bempedoic acid decreases LDL-C and attenuates atherosclerosis. *Nat Commun*. 2016; 7: 13457.
- Kattoor AJ, Kanuri SH, Mehta JL. Role of Ox-LDL and LOX-1 in atherogenesis. *Curr Med Chem*. 2019; 26(9): 1693-1700.
- Song S, Wu S, Wang Y, Wang Z, Ye C, Song R, et al. 17 β -estradiol inhibits human umbilical vascular endothelial cell senescence by regulating autophagy via p53. *Exp Gerontol*. 2018; 114: 57-66.
- Savoia C, Battistoni A, Calvez V, Cesario V, Montefusco G, Filippini A. Microvascular alterations in hypertension and vascular aging. *Curr Hypertens Rev*. 2017; 13(1): 16-23.
- Carlomosti F, D'Agostino M, Beji S, Torcinaro A, Rizzi R, Zaccagnini G, et al. Oxidative stress-induced miR-200c Disrupts the regulatory loop among SIRT1, FOXO1, and eNOS. *Antioxid Redox Signal*. 2017; 27(6): 328-344.
- Yu H, Moran CS, Trollope AF, Woodward L, Kinobe R, Rush CM, et al. Angiotensin II attenuates angiotensin II-induced aortic aneurysm and atherosclerosis in apolipoprotein E-deficient mice. *Sci Rep*. 2016; 6: 35190.

Assessment of Atg7 and LC3II/LC3, as The Markers of Autophagy, in Sperm of Infertile Men with Globozoospermia: A Case-Control Study

Shaghayegh Foroozan-Boroojeni, M.Sc.¹, Marziyeh Tavalaei, Ph.D.¹, Zahra Zakeri, Ph.D.²,

Richard A. Lockshin, Ph.D.^{2,3}, Mohammad Hossein Nasr-Esfahani, Ph.D.^{1,4*}

1. Department of Animal Biotechnology, Reproductive Biomedicine Research Center, Royan Institute for Biotechnology, ACECR, Isfahan, Iran

2. Department of Biology, Queens College and Graduate Center of The City University of New York, Flushing, NY, USA

3. Department of Biological Sciences, St. John's University, Jamaica, NY, USA

4. Isfahan Fertility and Infertility Center, Isfahan, Iran

*Corresponding Address: P.O.Box: 8165131378, Department of Animal Biotechnology, Reproductive Biomedicine Research Center, Royan Institute for Biotechnology, ACECR, Isfahan, Iran
Email: mh.nasr-esfahani@royaninstitute.org

Received: 24/June/2019, Accepted: 11/Dec/2019

Abstract

Objective: Assessment of relationship between LC3II/LC3 and Autophagy-related 7 (Atg7) proteins, as markers of autophagy, as well as evaluating the sperm parameters and DNA fragmentation in spermatozoa of infertile men with globozoospermia.

Materials and Methods: In this case-control study, 10 semen samples from infertile men with globozoospermia and 10 fertile individuals were collected, and the sperm parameters, sperm DNA fragmentation, and main autophagy markers (Atg7 and LC3II/LC3) were assessed according to World Health Organization (WHO) criteria, TUNEL assay, and western blot technique, respectively.

Results: The mean of sperm concentration and motility were significantly lower, while the percentage of abnormal spermatozoa and DNA fragmentation were significantly higher in infertile men with globozoospermia compared to fertile individuals ($P < 0.01$). Unlike the relative expression of LC3II/LC3 that did not significantly differ between the two groups, the relative expression of ATG7 was significantly higher in infertile men with globozoospermia compared to fertile individuals ($P < 0.05$). There was a significantly negative correlation between the sperm concentration ($r = -0.679$; $P = 0.005$) and motility ($r = -0.64$; $P = 0.01$) with the expression of ATG7, while a significantly positive association was found between the percentage of DNA fragmentation and expression of ATG7 (0.841 ; $P = 0.018$).

Conclusion: The increased expression of ATG7 and unaltered expression of LC3II/LC3 may indicate that the autophagy pathway is initiated but not completely executed in spermatozoa of individuals with globozoospermia. A significant correlation of ATG7 expression with increased sperm DNA fragmentation, reduced sperm concentration, and sperm motility may associate with the activation of a compensatory mechanism for promoting deficient spermatozoa to undergo cell death by the autophagy pathway. Therefore, this pathway could act as a double-edged sword that, at the physiological level, is involved in acrosome biogenesis, while, at the pathological level, such as globozoospermia, could act as a compensatory mechanism.

Keywords: Acrosome, Autophagy, Chromatin, Globozoospermia, Infertility

Cell Journal (Yakhteh), Vol 23, No 1, April-June (Spring) 2021, Pages: 70-74

Citation: Foroozan-Boroojeni Sh, Tavalaei M, Zakeri Z, A. Lockshin R, Nasr-Esfahani MH. Assessment of Atg7 and LC3II/LC3, as the markers of autophagy, in sperm of infertile men with globozoospermia: a case-control study. Cell J. 2021; 23(1): 70-74. doi: 10.22074/cellj.2021.7023.

This open-access article has been published under the terms of the Creative Commons Attribution Non-Commercial 3.0 (CC BY-NC 3.0).

Introduction

Round-headed sperm syndrome or globozoospermia, is one of the types of monomorphic severe teratozoospermia (abnormal spermatozoa that are defective in terms of function and morphology), leading to a decrease or an absence of the acrosome in sperm cells. It is also characterized by the abnormal arrangement of mitochondria, aberrant nuclear membrane, and mid-piece defects (1,2). The absence of acrosome and lack of ability of these sperm to induce oocyte activation are considered the main reason for infertilization of these patients (3).

Globozoospermia has a genetic mode of inheritance as autosomal recessive (4). In this regard, three genes were identified related to globozoospermia namely, *SPATA16*, *PICK1*, and *DPY19L2* (5-7). These genes are somehow associated with the formation and localization of the acrosome

(7). In animal models, it is now known that the absence of the expression of other genes, such as Autophagy-related 7 (*Atg7*), HIV-1 Rev-binding protein (*HRB*), Golgi-associated PDZ, coiled-coil motif containing protein (*GOPC*), casein kinase 2, and α -prime polypeptide (*CSNK2A2*) induce a phenotype similar to globozoospermia (7-9). All of these genes are linked to biogenesis of the acrosome; the development of which commences with the formation and fusion of many pro-acrosomic granules from trans-Golgi stacks to create a single large acrosomic granule binding to the nucleus and subsequently covering this structure to form a mature acrosome (7). In addition, autophagy is also essential for acrosomal biogenesis, and the inactivation of testicular *Atg7* leads to deformity in acrosome structure (8).

Autophagy is considered one of the main intracellular process that can degrade and/or recycle long-lived

proteins and organelles. From a molecular point of view, Atg12-Atg5 and LC3-lipid/membrane, as two ubiquitin-like conjugation systems, form the core of autophagy machinery (10). For both of these conjugation systems, Atg7 is a key molecule, as it is able to activate both systems. The outcome of these molecular events can be observed at cellular levels, as the engulfment of cytoplasmic components is mediated by a double-membrane vesicle known as autophagosomes. The fusion of autophagosomes with lysosomes ultimately creates autolysosome. The autophagosome membrane, along with its contents is subsequently degraded by hydrolases enzymes, residing in autolysosome (10).

Considering autophagy plays a dual role in cell death and acrosomal biogenesis, and also, spermatozoa of infertile men with globozoospermia have low or no acrosome, we aimed to assess the two central markers of autophagy, namely Atg7 and LC3II/LC3, as well as the sperm parameters and DNA fragmentation in these individuals.

Materials and methods

This case-control study was approved by the review board of the Royan Institute (Ethical Code: IR.ACECR.ROYAN.REC.1397.15). The written informed consent was obtained from all individuals who participated in this study. Semen samples were collected from subjects who referred to Isfahan Fertility and Infertility Center. Totally 10 semen samples from infertile men with globozoospermia and 10 semen samples from fertile men were collected for this study. All globozoospermic samples had DPY19L2 deletion that was assessed according to our previous study (6). Couples with female factor infertility and men with leukocytospermia, genital infection, anatomical disorders, abnormal hormonal profile, varicocele, previous history of scrotal trauma or surgery, and age >40 years were excluded from this study.

Semen samples collection

Semen samples were collected after 3-5 days of sexual abstinence by masturbation in the sterile containers and kept for 30 minutes at room temperature to liquefy. In the first step, the sperm parameters (concentration, motility, and morphology) were evaluated according to guidelines provided by WHO (11). The sperm concentration and motility were determined by CASA (computer-assessed semen analysis; version Sperm 2.1# 1990-2004, Russia) system secured with a sperm processor chamber (Sperm meter; Sperm Processor, Aurangabad, India). Besides, sperm morphology was assessed by the Diff-Quick staining method and analyzed by CASA system. In the second step, we evaluated DNA fragmentation by the TUNEL assay and autophagy markers (Atg7 and LC3II/LC3I) by the western blot technique.

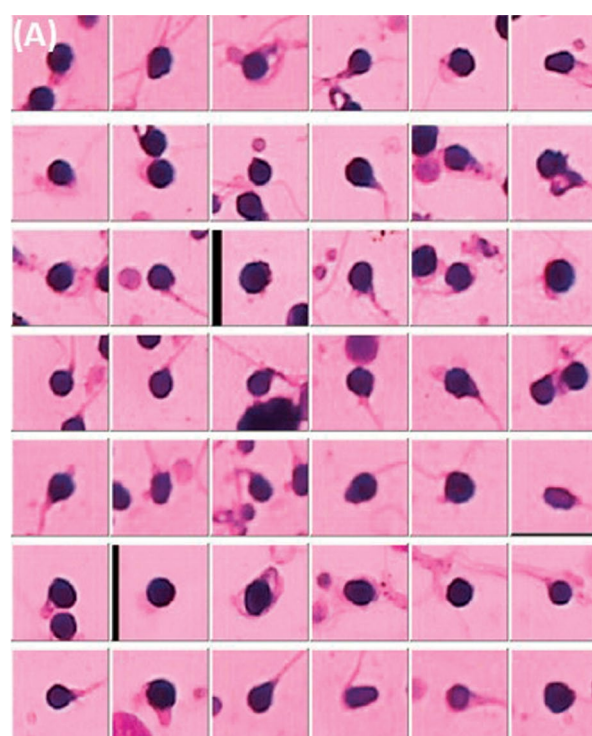
Diff-Quick staining

For the assessment of sperm morphology, we purchased a commercially available kit (Faradidpardaz Co, Iran), containing a fixative solution (methanol), eosin dye for

staining basic proteins (red), and thiazine dye for staining sperm DNA (blue). Briefly, 20 microlitres of the washed samples were smeared and air-dried. Then, slides were sequentially soaked in fixative, eosin, and thiazine solutions for 10-20 seconds, and finally rinsed in water to remove extra dye (11). Next, abnormalities in head, tail, acrosome, and neck of spermatozoa were evaluated (Fig.1A).

TUNEL assay

In this study, we determined DNA fragmentation of spermatozoa using a detection kit (Apoptosis Detection System Fluorescein, Promega, Germany), according to the manufacturer's instructions. Briefly, semen samples were washed twice with phosphate-buffered solution (PBS), and then for each sample, two smears were prepared. Then, slides were fixed in 4% paraformaldehyde for 25 minutes. Subsequently, slides were washed with PBS. Fixed spermatozoa were permeabilized with 0.2% Triton X-100 for 5 minutes. The next step was equilibration of slides with equilibration buffer for 7 minutes, and then incubation of slides with a mixture solution, containing nucleotide mix, rTdT, and equilibration buffer for 90 minutes at 37°C in a humidified chamber. Lastly, reactions were stopped by 2X SSC buffer and then the slides were washed with PBS. We stained slides with a freshly diluted propidium iodide solution (1 µg/ml in PBS) for 10 minutes and then slides were washed in PBS. For the evaluation of the percentage of DNA fragmentation, we used a fluorescence microscope (BX51, Tokyo, Japan). At least, 500 spermatozoa were counted for each sample. Spermatozoa with red nuclei were considered sperm with intact DNA, while those with green nuclei had damaged DNA, and they were reported as TUNEL-positive or DNA fragmented cells (Fig.1B and C).



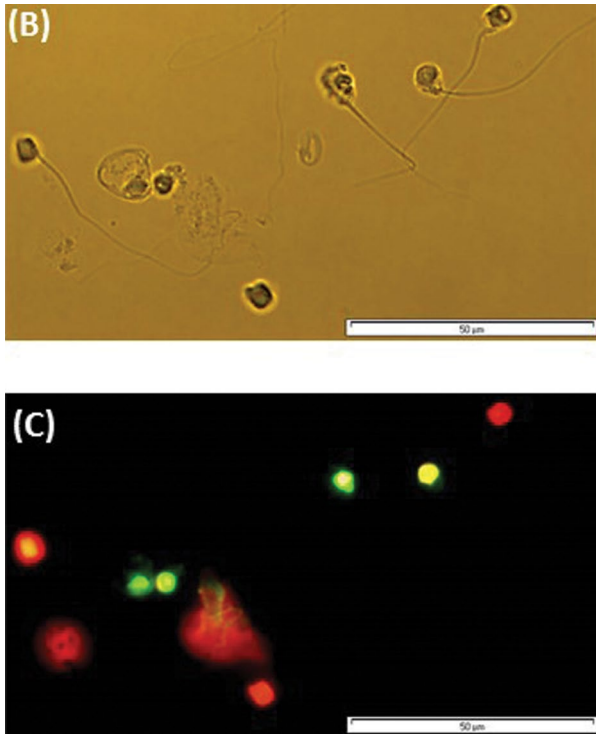


Fig.1: Assessment of sperm morphology and DNA fragmentation using Diff-Quick staining and TUNEL assay, respectively. **A.** Sperm sample from an infertile men with globozoospermia was satined with Diff-Quick method for assessment of sperm morphology and analyzed by CASA system (computer-assessed semen analysis; version Sperm 2.1# 1990-2004, Russia). **B** and **C.** Sperm sample from an infertile men with globozoospermia was assessed by TUNEL assay for evaluation of sperm DNA fragmentation (B: Light microscope; C: Floresecnce microscope).

Western blot

Protein extraction was performed from washed samples using TRI Reagent (Sigma-Aldrich; USA). Then, the protein concentration of each sample was evaluated by the Bradford assay (Bio-Rad; USA) to determine the amount of total proteins that should be loaded in each lane. For this aim, 40μg of protein of each sample were electrophoresed on 12% sodium dodecyl sulfate (SDS) polyacrylamide gels and then, the separated proteins were transferred onto PVDF membranes (Bio-Rad; USA). The membranes were blocked by PBS containing 5% skim milk powder (Merck, USA). For the detection of Atg7, LC3, and housekeeping glyceraldehyde-3-phosphate dehydrogenase (GAPDH), we used anti-Atg7 rabbit polyclonal antibody from Abcam company (Cambridge, MA, USA) with a dilution ratio of 1:1000, anti-LC3 rabbit polyclonal antibody from Novus Biologicals company (Littleton, CO, USA) with a dilution ratio of 1:4000, and monoclonal anti-glyceraldehyde GAPDH from Millipore company (USA) with a dilution ratio of 1:5000 as specific primary antibodies. For the first two proteins, membranes were incubated with primary antibodies overnight, while for the dtermination of the GAPDH protein, the membrane was incubated with the specific primary antibody for 90 minutes. Afterward, membranes were washed and incubated for an hour with appropriate secondary antibodies. For tracking anti-Atg7 and anti-LC3 antibodies, horseradish peroxidase (HRP) conjugated

anti-rabbit IgG (Dako, Japan) was applied, while for probing the GAPDH protein, horseradish peroxidase (HRP)-conjugated goat anti-mouse IgG (Dako, Japan) was utilized as secondry antibodies. Then, membranes were rinsed three times. The presence of specific proteins was identified using an Amersham ECL Advance Western Blotting Detection Kit (GE Healthcare, Germany). For the quantification of data, the density of protein bands was analyzed by Quantity One 1-D Analysis software v 4.6.9 (Bio-Rad, Munchen, Germany). Normalization of data was performed by dividing of band densities of Atg7 and LC3 to the band density of Glyceraldehyde GAPDH, and represented as the expression level of Atg7 and LC3. Moreover, the ratio of LC3-II level/LC3-I level was measured as an indicator of autophagic level (12).

Statistical analysis

For the comparison of the sperm parameters, DNA fragmentation, the expression of ATG7 and LC3II/LC3 proteins between fertile and globozoospermic men, independent t test was used. In this study, the values were expressed as the means and standard error (mean ± SE). The P values of less than 0.05 were statistically significant. For the evaluation of the relationship between different parameters, pearson correlation coefficient was employed. All statistical analyses were conducted using the SPSS software (V19.0; IDM, Chicago, IL, USA).

Results

The mean sperm concentrations (38.62 ± 8.63 vs. 82.64 ± 11.41 ; $P=0.005$) and sperm motility (32.85 ± 6.05 vs. 62 ± 4.27 ; $P= 0.001$) were significantly lower in infertile globozoospermic men compared to fertile men. The mean percentage of abnormal sperm morphology (100 ± 0.01 vs. 91.55 ± 2.44 ; $P=0.006$) was significantly higher in men with globozoospermia compared to fertile individuals. Also, the mean percentage of DNA fragmentation was significantly higher in men with globozoospermia compared to fertile individuals (18.18 ± 7.8 vs. 5.35 ± 1.9 ; $P<0.05$).

The role of autophagy flux in globozoospermia was studied by the western blot analysis to detect ATG7 and LC3II/LC3 proteins. The relative expression of ATG7 was significantly higher in infertile men with globozoospermia compared to fertile subjects (at a ratio of ATG7/GAPDH 3.1 ± 0.94 vs. 0.71 ± 0.2 ; $P=0.04$). However, the ratio of LC3II/LC3I shows no significant difference between the two groups (0.07 ± 0.04 vs. 0.06 ± 0.03 ; $P=0.8$) (Fig.2).

In this study, the correlations between measured parameters and markers in total population were analyzed as depicted in Table 1. The results showed significantly negative associations of sperm concentration and motility with the expression of ATG7 ($P<0.05$). Besides, a significantly positive correlation was found between the percentage of DNA fragmentation and expression of ATG7 ($P<0.05$). There were also significant negative correlations among the percentage of DNA fragmentation, sperm concentrations, and motility ($P<0.05$).

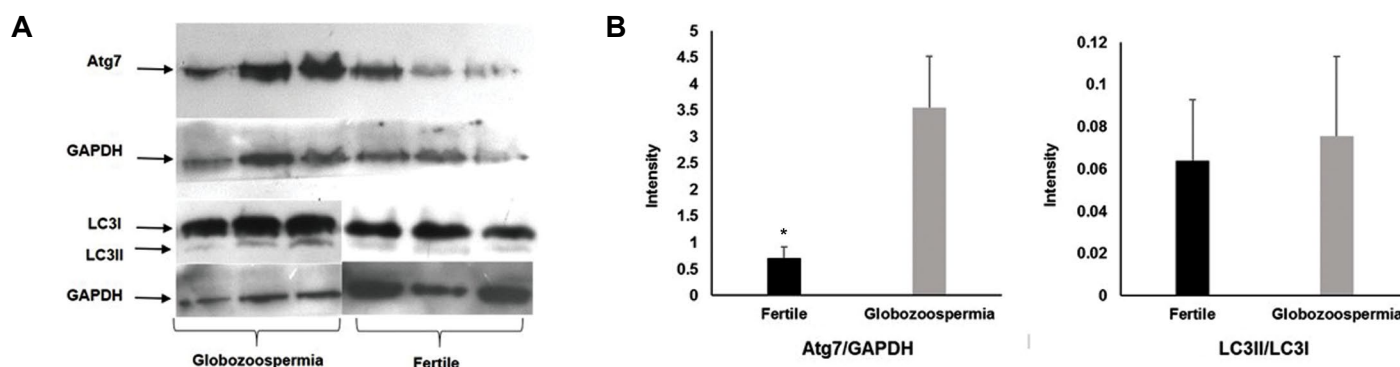


Fig.2: Western blot of autophagy markers Atg7 and LC3. **A.** Western blot image of three fertile individuals and three infertile men with globozoospermia. **B.** Intensity of Atg7 relative to GAPDH and LC3II/LC3I ratio between infertile men with globozoospermia and fertile individuals. Data are presented as mean \pm SEM and analyzed by independent-samples t test (* $P < 0.05$). GAPDH; Glyceraldehyde 3-phosphate dehydrogenase; and Atg7; Autophagy-related 7.

Table 1: Correlations between autophagy markers, semen parameters and DNA damage.

Parameters	ATG7	LC3II/LC3I	Concentration (10 ⁶ /ml)	Motility (%)	Abnormal sperm morphology (%)	TUNEL (%)
ATG7	1	-0.223	-0.679** (P=0.005)	-0.640* (P=0.01)	0.421	0.841* (P=0.018)
LC3II/LC3I	-0.223	1	-0.302	-0.204	0.232	-0.179
Concentration (10 ⁶ /ml)	-0.679** (P=0.005)	-0.302	1	0.722** (P<0.001)	-0.207	-0.663* (P= 0.026)
Motility (%)	-0.640* (P=0.01)	-0.204	0.722** (P<0.001)	1	-0.316	-0.693* (P= 0.018)
Abnormal sperm morphology (%)	0.421	0.232	-0.207	-0.316	1	0.264

*; Correlation is significant at the 0.05 level (2-tailed), **; Correlation is significant at the 0.01 level (2-tailed), ATG7; Autophagy-related 7, and TUNEL; Terminal deoxynucleotidyl transferase dUTP nick end labeling.

Discussion

Globozoospermia is a type of primary infertility in men with a prevalence of less than 0.1% among all types of male infertilities (1). Recent studies demonstrated that autophagy is involved in acrosomal biogenesis, and testis specific inactivation of Atg7 leads to deformation of the acrosome (8,9). Therefore, we aimed to analyze some markers involved in autophagy in spermatozoa of individuals with globozoospermia. The present study demonstrated that the expression of ATG7 was significantly higher in globozoospermic individuals compared to the control group. However, no difference was found in LC3II/LC3 expression between the two groups. According to a study conducted by Lee et al., to induce autophagy and achieve acrosome biogenesis, the LC3 protein has to be deacetylated by Sirt1, allowing the de-acetylated LC3 protein to be transferred from the nucleus to the cytoplasm (13). Regarding our obtained results, it is possible that due to defects in the expression of other genes involved in the acrosomal biogenesis, such as DPY19L2 (5-7), spermatozoa increase the activation of autophagy which is perceptible by the increased expression of ATG7. However, because of the deletion of DPY19L2

gene, the acrosome biogenesis does not completely occur. Our findings also suggest that autophagy is initiated but not completed, as we observed no change in a ratio of LC3II/LC3 expression. The confirmation of this hypothesis requires further studies.

Considering that autophagy may be induced in the form of cell death (14), another reason for the increase in ATG7 expression in infertile men with globozoospermia may be an increased rate of cell death. In this regard, higher sperm DNA fragmentation, as one of the causes of cell death and chromatin damage, has been reported in these individuals (2, 15, 16) even in Dpy19L2-deficient globozoospermic spermatozoa (17). On the other hand, autophagy normally helps cells survive in stressful conditions; however it can ultimately result in cell death. Also, a previous study demonstrated a low fertilization rate in men with higher 10% thresholds, as measured by the TUNEL assay (18). In this regard, we also observed that the mean sperm DNA fragmentation was higher than 10% in infertile men with globozoospermia compared to fertile men. Therefore, we suggested that one of the possible causes of failure in assisted reproduction techniques in these individuals may be owing to the high percentage of sperm DNA fragmentation in the semen samples.

The observed significant negative correlations among ATG7 expression, sperm concentration, and motility in the present study suggest that in some sperm cells, autophagy and cell death are completed, led to the reduced sperm concentrations. Moreover, a significantly positive correlation between sperm DNA fragmentation and the expression of ATG7, as well as a significant positive association between abnormal sperm chromatin packaging (protamine deficiency) and the expression of ATG7 (19) may confirm the activation of the ATG7 pathway, as a promoter of cell death. Regardless of a significantly negative correlation between sperm motility and the expression of ATG7 (20) in this study, our results were consistent with findings obtained in a study carried out Zhang et al. who showed that the sperm motility of zebrafish would be improved upon the inhibition of autophagy (21). These differences between studies may be related to sample size, species, and type of samples.

Conclusion

Sperm samples from globozoospermic men show high expression of ATG7 which would be expected to remove a number of abnormal spermatozoa, as defined by chromatin abnormal packaging and/or damaged DNA in this condition. A significantly negative correlation among sperm concentration, and motility, and the expression of ATG, along with a significantly positive correlation among sperm DNA fragmentation, the sperm parameters, and the expression of ATG7 might be linked with the activation of the autophagy pathway, as a compensatory mechanism for driving deficient spermatozoa to undergo cell death. Autophagy can act as a double-edged sword that, at the physiological level, is involved in acrosome biogenesis, while, at the pathological events, such as globozoospermia and varicocele it possibly acts as a compensatory mechanism for promoting deficient spermatozoa to undergo cell death. One of the limitations of this study was small sample size. Therefore, further studies are needed to confirm this hypothesis in different pathologies of male infertility.

Acknowledgments

The authors declare no conflict of interest. This study was supported by the Royan Institute, and we would like to express our gratitude to staff members of Isfahan Fertility and Infertility for their full support.

Authors' Contributions

Sh.F-B.; Acquisition and assembly of data, data analysis, interpretation and manuscript writing. M.T.; Conception, design, collection and/or assembly of data, data analysis, interpretation, manuscript writing and final approval of manuscript. R.A.L., Z.Z.; Conception, design, interpretation and manuscript writing. M.H.N-E.; Conception, design, data analysis, interpretation, manuscript writing and final approval of manuscript. All authors read and approved the final manuscript.

References

1. Dam AH, Feenstra I, Westphal JR, Ramos, L, van Golde RJ, Kremer JA. Globozoospermia revisited. *Hum Reprod Update*. 2007; 13(1): 63-75.

2. Perrin A, Coat C, Nguyen MH, Talagas M, Morel F, Amice J, et al. Molecular cytogenetic and genetic aspects of globozoospermia: a review. *Andrologia*. 2013; 45(1): 1-9.
3. Hotaling JM, Smith JF, Rosen M, Muller CH, Walsh TJ. The relationship between isolated teratozoospermia and clinical pregnancy after in vitro fertilization with or without intracytoplasmic sperm injection: a systematic review and meta-analysis. *Fertil Steril*. 2011; 95(3): 1141-1145.
4. De Braekeleer M, Nguyen MH, Morel F, Perrin A. Genetic aspects of monomorphic teratozoospermia: a review. *J Assist Reprod Genet*. 2015; 32(4): 615-623.
5. Elinati E, Kuentz P, Redin C, Jaber S, Vanden Meerschaut F, Makarian J, et al. Globozoospermia is mainly due to DPY19L2 deletion via non-allelic homologous recombination involving two recombination hotspots. *Hum Mol Genet*. 2012; 21(16): 3695-3702.
6. Kuentz P, vanden Meerschaut F, Elinati E, Nasr-Esfahani MH, Gurgan T, Kilani Z, et al. Assisted oocyte activation overcomes fertilization failure in globozoospermic patients regardless of the DPY19L2 status. *Hum Reprod*. 2013; 28(4): 1054-1061.
7. Khawar MB, Gao H, Li W. mechanism of acrosome biogenesis in mammals. *Front Cell Dev Biol*. 2019; 7: 195.
8. Wang H, Wan H, Li X, Liu W, Chen Q, Wang Y, et al. Atg7 is required for acrosome biogenesis during spermatogenesis in mice. *Cell Res*. 2014; 24(7): 852-869.
9. Liu C, Song Z, Wang L, Yu H, Liu W, Shang Y, et al. Sirt1 regulates acrosome biogenesis by modulating autophagic flux during spermiogenesis in mice. *Development*. 2017; 144(3): 441-451.
10. Nakatogawa H. Two ubiquitin-like conjugation systems that mediate membrane formation during autophagy. *Essays Biochem*. 2013; 55: 39-50.
11. Cao XW, Lin K, Li CY, Yuan CW. A review of WHO laboratory manual for the examination and processing of human semen (5th edition). *Zhonghua nan ke xue=(National Journal of Andrology)*. 2011; 17(12): 1059-1063.
12. Zhang M, Jiang M, Bi Y, Zhu H, Zhou Z, Sha J. Autophagy and apoptosis act as partners to induce germ cell death after heat stress in mice. *PLoS One*. 2012; 7(7): e41412.
13. Lee IH, Cao L, Mostoslavsky R, Lombard DB, Liu J, Bruns NE, et al. A role for the NAD-dependent deacetylase Sirt1 in the regulation of autophagy. *Proc Natl Acad Sci USA*. 2008; 105(9): 3374-3379.
14. Yonekawa T, Thorburn A. Autophagy and cell death. *Essays Biochem*. 2013; 55: 105-117.
15. Hosseinfar H, Yazdanikhah S, Modarresi T, Totonchi M, Sadighi Gilani MA, Sabbaghian M. Correlation between sperm DNA fragmentation index and CMA 3 positive spermatozoa in globozoospermic patients. *Andrology*. 2015; 3(3): 526-531.
16. Eskandari N, Tavalae M, Zohrabi D, Nasr-Esfahani MH. Association between total globozoospermia and sperm chromatin defects. *Andrologia*. 2018; 50(2).
17. Yassine S, Escoffier J, Martinez G, Coutton C, Karaouzene T, Zouari R, et al. Dpy19l2-deficient globozoospermic sperm display altered genome packaging and DNA damage that compromises the initiation of embryo development. *Mol Hum Reprod*. 2014; 21(2): 169-185.
18. Simon L, Liu L, Murphy K, Ge S, Hotaling J, Aston KI, et al. Comparative analysis of three sperm DNA damage assays and sperm nuclear protein content in couples undergoing assisted reproduction treatment. *Hum Reprod*. 2014; 29(5): 904-917.
19. Foroozan-Broojeni S, Tavalae M, Lockshin RA, Zakeri Z, Abbasi H, Nasr-Esfahani MH, et al. Comparison of main molecular markers involved in autophagy and apoptosis pathways between spermatozoa of infertile men with varicocele and fertile individuals. *Andrologia*. 2019; 51(2): e13177.
20. Aparicio IM, Espino J, Bejarano I, Gallardo-Soler A, Campo ML, Salido GM, et al. Autophagy-related proteins are functionally active in human spermatozoa and may be involved in the regulation of cell survival and motility. *Sci Rep*. 2016; 6: 33647.
21. Zhang J, Zhang X, Liu Y, Su Z, Dawar FU, Dan H, et al. Leucine mediates autophagosome-lysosome fusion and improves sperm motility by activating the PI3K/Akt pathway. *Oncotarget*. 2017; 8(67): 111807-111818.

Proteomics Analyses Reveal Functional Differences between Exosomes of Mesenchymal Stem Cells Derived from The Umbilical Cord and Those Derived from The Adipose Tissue

Bin Liu, Ph.D.^{1,2}, Guanglei Qiao, M.Sc.³, Wen Cao, M.Sc.⁴, Chenlu Li, M.Sc.⁵, Shaojun Pan, Ph.D.⁶,
Lirui Wang, Ph.D.^{1,2}, Yanlei Liu, Ph.D.^{1,2}, Lijun Ma, Ph.D.^{3*}, Daxiang Cui, Ph.D.^{1,2,3*}

1. Institute of Nano Biomedicine and Engineering, Shanghai Engineering Research Center for Intelligent Diagnosis and Treatment Instrument, Department of Instrument Science and Engineering, School of Electronic Information and Electrical Engineering, Shanghai Jiao Tong University, China
2. National Center for Translational Medicine, Collaborative Innovative Center for System Biology, Shanghai Jiao Tong University, China
3. Department of Oncology, Tongren Hospital, Shanghai Jiao Tong University School of Medicine, China
4. Bio-X Institutes, Key Laboratory for the Genetics of Developmental and Neuropsychiatric Disorders (Ministry of Education), Shanghai Jiao Tong University, China
5. School of Laboratory Medicine and Life Science, Wenzhou Medical University, University Town, Chashan, China
6. School of Biomedical Engineering, Shanghai Jiao Tong University, China

*Corresponding Addresses: P.O. Box: 200336, 1111 Xian Xia Road, Department of Oncology, Tongren Hospital, Shanghai Jiao Tong University School of Medicine, Shanghai, P.R. China

P.O.Box: 20040, 800 Institute of Nano Biomedicine and Engineering, Shanghai Engineering Research Center for Intelligent Diagnosis and Treatment Instrument, Department of Instrument Science and Engineering, School of Electronic Information and Electrical Engineering, Shanghai Jiao Tong University, China
Emails: ljma56@126.com, dxcui@sjtu.edu.cn

Received: 26/May/2019, Accepted: 30/October/2019

Abstract

Objective: We aimed to identify the differentially expressed proteins (DEPs) and functional differences between exosomes derived from mesenchymal stem cells (MSCs) derived from umbilical cord (UC) or adipose tissue (AD).

Materials and Methods: In this experimental study, the UC and AD were isolated from healthy volunteers. Then, exosomes from UC-MSCs and AD-MSCs were isolated and characterized. Next, the protein compositions of the exosomes were examined via liquid chromatography tandem mass spectrometry (LC-MS/MS), followed by evaluation of the DEPs between UC-MSC and AD-MSC-derived exosomes. Finally, functional enrichment analysis was performed.

Results: One hundred and ninety-eight key DEPs were identified, among which, albumin (ALB), alpha-II-spectrin (SPTAN1), and Ras-related C3 botulinum toxin substrate 2 (RAC2) were the three hub proteins present at the highest levels in the protein-protein interaction network that was generated based on the shared DEPs. The DEPs were mainly enriched in gene ontology (GO) items associated with immunity, complement activation, and protein activation cascade regulation corresponding to 24 pathways, of which complement and coagulation cascades as well as platelet activation pathways were the most significant.

Conclusion: The different functions of AD- and UC-MSC exosomes in clinical applications may be related to the differences in their immunomodulatory activities.

Keywords: Complement and Coagulation Cascades, Exosomes, Mesenchymal Stem Cells, Proteomics Analysis

Cell Journal (Yakhteh), Vol 23, No 1, April-June (Spring) 2021, Pages: 75-84

Citation: Liu B, Qiao G, Cao W, Li Ch, Pan Sh, Wang L, Liu Y, Ma L, Cui D. Proteomics analyses reveal functional differences between exosomes of mesenchymal stem cells derived from the umbilical cord and those derived from the adipose tissue. Cell J. 2021; 23(1): 75-84. doi: 10.22074/cellj.2021.6969. This open-access article has been published under the terms of the Creative Commons Attribution Non-Commercial 3.0 (CC BY-NC 3.0).

Introduction

Mesenchymal stem cells (MSCs) are pluripotent stem cells with the abilities of self-renewing and differentiating into various cell types, such as osteoblasts, chondrocytes, myocytes, and adipocytes, under appropriate conditions (1). MSCs have specific immune properties that allow them to survive in a heterogeneous environment (2). Umbilical cord-derived MSCs (UC-MSCs) are the most primitive MSCs, and they have been proven to be effective in disease therapy, such as in lupus erythematosus (3), psoriasis (4), and rheumatoid arthritis (5). Adipose tissue-derived mesenchymal stem cells (AD-MSCs), which can differentiate into osteoblasts, chondroblasts, adipose precursor cells, and cardiomyocytes, hold great promise for use in wound healing and treating kidney injuries (6, 7). Although the clinical applications of UC-MSCs and AD-MSCs are extensive, their applications are somewhat different. Additionally, there are various

limitations for the clinical applications of MSCs on the whole. For instance, except for UC-MSCs, MSC collection procedures are invasive and laborious. Furthermore, proliferation and differentiation abilities of MSCs decrease in culture after several passages (8, 9). In spite of the function of MSCs that has been confirmed in regenerative medicine and immunomodulatory diseases, the wide application of MSCs is restricted owing to the limitations in their source and stability (8).

Exosomes are small bilayer vesicles of 30-100 nm in diameter that are released from cells. They are involved in intercellular communication by transferring cellular components between cells (10). Many studies have shown that MSC-derived exosomes have functions similar to those of MSCs, such as immune regulation and promoting regeneration of damaged tissues (11). Relative to MSCs,

exosomes are more stable and retainable in the host following their allogeneic administration due to a lower host-versus-graft reaction (10). Exosomes derived from MSCs may provide an alternative therapy for various diseases, especially for degenerative diseases. Li et al. (12) have reported that transplantation of exosomes derived from UC-MSCs alleviates liver fibrosis induced by CCl_4 . Similarly, exosomes from UC-MSCs repair cisplatin-induced acute kidney injury and acute myocardial ischemic injury (13, 14). In addition, in a previous study exosomes derived from UC-MSCs showed immunomodulatory effects on *in vitro* stimulated T cells and promoted cell migration in a breast cancer cell model through the Wnt signaling pathway (15, 16). Combination of AD-MSCs- and AD-MSC-derived exosomes also significantly reduced the brain infarct volume in stroke rats, and protected the kidneys from acute ischemia-reperfusion injury (17, 18).

Exosomes usually contain lipids, miRNAs, mRNAs, and proteins that can recognize their target cells and modulate their functions. In recent years, exosome proteomes have been at the center of attention in biomedical research. Thousands of proteins have been found in exosomes, several hundreds of which are common in at least two sets, and only two proteins are shared by more than four sets (11). It is well known that exosomes are membranous vesicles released by cells, which exist in blood, breast milk, saliva, malignant effusions, and also in the supernatants of cell cultures (20). In recent years, exosomes derived from MSCs have been applied in the clinics. As proteins mediate most of the intracellular physiological processes and communication between cells, mass spectrometry proteomics methods and proteomics have been widely used in elucidating biological processes (21). In the present study, exosomes from UC-MSCs and AD-MSCs were isolated and their protein compositions were examined by liquid chromatography-tandem mass spectrometry (LC-MS/MS). Then, functional enrichment analysis of the differentially expressed proteins (DEPs) between the two exosomes was performed. The purpose of this research was to evaluate the DEPs and potential functional differences between the exosomes derived from UC-MSCs and those derived from AD-MSCs.

Materials and Methods

Materials

In this experimental study, MSCs serum-free medium was ordered from Shanghai Puma Biotechnology (Shanghai, China), and trypsin and Dulbecco's phosphate buffered saline (DPBS) were ordered from Gibco (Grand Island, NY, USA). The antibodies of APC-anti-human CD73, FITC-anti-human CD90, PerCP-Cy5.5-anti-human CD105, PE-anti-human CD34, PE-anti-human CD45, and PE-anti-human HLA-DR were purchased from BD Pharmingen (NJ, USA). The CD63 and β -actin antibodies were ordered from Absin Bioscience (Shanghai, China) and Cell Signaling Technology (Danvers, MA, USA), respectively.

Cell culture and supernatant collection

The collection and use of all human umbilical cords

or adipose tissues from healthy volunteers in this study was approved by Ethics Committee of Shanghai Tongren Hospital (No.201501801). UC-MSCs were acquired by through direct explant method using umbilical cords donated by healthy women immediately after giving birth (22). AD-MSCs were acquired from the adipose tissues of healthy volunteers using the enzymatic digestion method (23). All the donors provided their informed consents prior to tissue donation. Cellular morphologies of the UC- and AC-MSCs were examined and photographed using a light microscope (Nikon TS100). The UC- and AD-MSCs were plated at the density of 8000 cells/cm² in T175 flasks for 3-5 passages in serum-free medium. The supernatants of the cultures were collected after 72 hours for exosome collection. The total supernatant volume collected for each cell type was 50 mL.

Characterization of the surface markers on UC-MSCs and AD-MSCs

Surface marker characterization was performed by flow cytometry. Briefly, the UC-MSCs and AD-MSCs were detached with trypsin and washed with DPBS. Afterward, APC-anti-human CD73, FITC-anti-human CD90, PerCP-Cy5.5-anti-human CD105, PE-anti-human CD34, PE-anti-human CD45, and PE-anti-human HLA-DR were added into the tubes containing $5-10 \times 10^5$ cells. After twenty minutes of incubation in the dark, the cells were washed with DPBS and processed with FACS Calibur system (BD Bioscience, USA).

Extraction and identification of exosomes

To remove the residual cells and fragments, the supernatants of both cell types were consecutively centrifuged at 800 g for ten minutes and 12,010 g for twenty minutes at 4°C. Then the samples were centrifuged at 100,010 g for two hours at 4°C. After washing, the precipitates were resuspended in 100 μL DPBS. Finally, the exosomes were stored at -80°C for future usage.

The morphologies of the exosomes were examined using a transmission electron microscope (TEM) JEM 2100F (JEOL, Japan). The particle size distribution of the exosomes was assessed by the particle analysis system: qNano (Izon science, Oxford, UK). The expression level of CD63 on the exosomes was evaluated by the BCA Protein Assay Kit (Sangon Biotech, Shanghai, China) and western blotting assay.

Mass spectrometry analysis

Exosome-associated proteins were studied using LC-MS/MS. Briefly, the supernatant and exosome solutions of UC- and AD-MSCs were all sonicated before the protein contents were extracted. Afterward, 1M dithiothreitol and 1 M iodoacetamide were included to reduce and alkylate the extracted proteins, respectively. The samples were then digested using 20 ng/ μL trypsin overnight at 37°C. Next, the mixtures were centrifuged at 12,010 rpm for twenty minutes. Then the filtrate was collected and dried at 55°C to obtain the polypeptides. The dried polypeptide samples were reconstituted in 0.1% aqueous formic acid, followed

by desalting via ZipTip C18 columns (Thermo Scientific, Waltham, MA, USA). The samples were recovered from the columns with water containing 2% acetonitrile and 0.1% formic acid. Finally, the samples were analyzed with Nano Liquid Chromatography–Orbitrap Mass Spectrometry (Easy-nLC1200, Q-Exactive Plus, ThermoFisher Scientific). In the present study, 16 samples were analyzed, comprising 4 replicates from each supernatant and exosome sample derived from UC-MSCs or AD-MSCs (Sup UC, Sup AD, Exosome UC, and Exosome AD).

For the mass spectrometric analysis, an electrospray positive ion source and secondary data-dependent acquisition (data-dependent acquisition, DDA) mode (Target SIM-dd MS2) were used. The parameters of full mass were as follows: 2.0 KV spray voltage, 320°C capillary temperature, 350–1500 m/z scan range, 70,000 resolution, 3e6 AGC target, and 50 ms maximum ion injection time (MIT). The parameters of dd-MS2/dd-SIM were as follows: 20–2000 m/z scan range, 17,500 resolution, 1e5 AGC target, 45 ms MIT, and 1.6 m/z isolation window. The most abundant 20 peptides were subjected to a secondary fragmentation using high energy collisional dissociation (loop count=20, MSX count=1, TopN=20). The normalized collision energy (NCE) was 28. Likewise, the ions with a charge number of 1 and those ≥ 8 were excluded. The dynamic exclusion time was 30 seconds.

Data preprocessing

Data were obtained by Nano-ESI-LC-MS/MS by searching the Sequest HT engine, and the proteins of each group were identified by the Proteome Discoverer software (2.2.0.388, ThermoFisher Scientific). Protein analysis was performed using UniProt analysis software (<https://www.uniprot.org/>) with fixed carbamidomethyl-cysteine, variable methionine-oxidation asparagine/glutamine deamidation, and N-terminal acetyl that was allowed against the complete human proteome. The precursor mass tolerance was 10 ppm and the fragment mass tolerance was 0.02 Da, with the maximum missed cut site allowed being 2. The cut-off value for false discovery rate (FDR) was $\leq 1\%$.

Identification of the differentially expressed proteins

The log fold change (log FC) was calculated based on the total abundance ratio and the P value. The DEPs between Exosome UC vs. Exosome AD and Sup UC vs. Sup AD were selected with the P value < 0.05 and $|\log_2FC| > 0.585$ (1.5 fold) as the threshold of DEPs. In addition, the volcano and Veen maps were constructed.

Protein-protein interaction network of the differentially expressed proteins

Search tool for the retrieval of interacting genes/proteins (STRING) database was applied to analyze the protein-protein interaction (PPI) of the DEPs (23). The PPI relationship pairs, of which the threshold Required Confidence > 0.4 were used in the formation of the PPI network by Cytoscape (<http://www.cytoscape.org/>). Moreover, CytoNCA plugin

(Version 2.1.6) was selected to study the topological features of the nodes in the PPI network with the "without weight" parameter. Based on the order of the degree centrality (DC), betweenness centrality (BC), and closeness centrality (CC) of the nodes, the top 10 key nodes (also named hub proteins) were identified.

Functional enrichment analysis of the DEPs

The clusterProfiler of R package (Version 3.2.11) was used to perform the KEGG pathway and gene ontology (GO) enrichment analyses. P values < 0.05 were considered significant, and the top 20 of the GO and pathway items were taken into account in the analysis. ClueGO and CluePedia plugins of cytoscape were used for functional clustering analysis of the target proteins. The network map of all target functional proteins was constructed by cytoscape. In the ClueGO plugin, the value of kappa showed the relationship between the GO terms according to the overlapping genes. Meanwhile, GO functions were grouped according to the kappa coefficients. A high kappa coefficient indicates a stronger correlation between the GO items.

Mapping the key pathway

Key pathways were mapped by the KEGG MAPPER, and the key proteins were marked.

Results

Cell surface markers of MSCs derived from UC and AD

UC-MSCs and AD-MSCs were characterized based on the International Society for Cellular Therapy (ISCT) minimal definition criteria flow cytometry (24). In culture, UC-MSCs had a long fusiform morphology with vortex-like adherent projections. On the other hand, although AD-MSCs were also fusiform, they grew in parallel to each other or in a spiral pattern (Fig.1A, B). In addition, the majority of both UC- and AD-MSCs expressed CD73 (98.24 and 100.00%, respectively), CD90 (98.61 and 99.36%), and CD105 (99.94 and 99.93%) (Fig.1C, D). In contrast, only a few UC-MSCs and AD-MSCs were positive for CD34 (0.37 and 2.22%, respectively), CD45 (1.04 and 0.32%), and HLA –DR (0.31 and 0.30%). All the results indicated that the cell morphology and surface markers of the UC- and AD-MSCs were in agreement with the ISCT standards.

Morphological characterization of the exosomes

The exosome morphologies were examined by TEM. The vesicles observed had a well-defined circular structure with a lipid bilayer membrane and a diameter of approximately 100 nm (Fig.2A). There was no obvious morphological difference between the exosomes derived from UC-MSCs and AD-MSCs. The results of particle size distribution (Fig.2B) were consistent with the TEM results. In addition, the membrane-specific protein CD63 (28–29 kDa) was detected on the vesicles (Fig.2C). These results confirmed successful isolation of the exosomes.

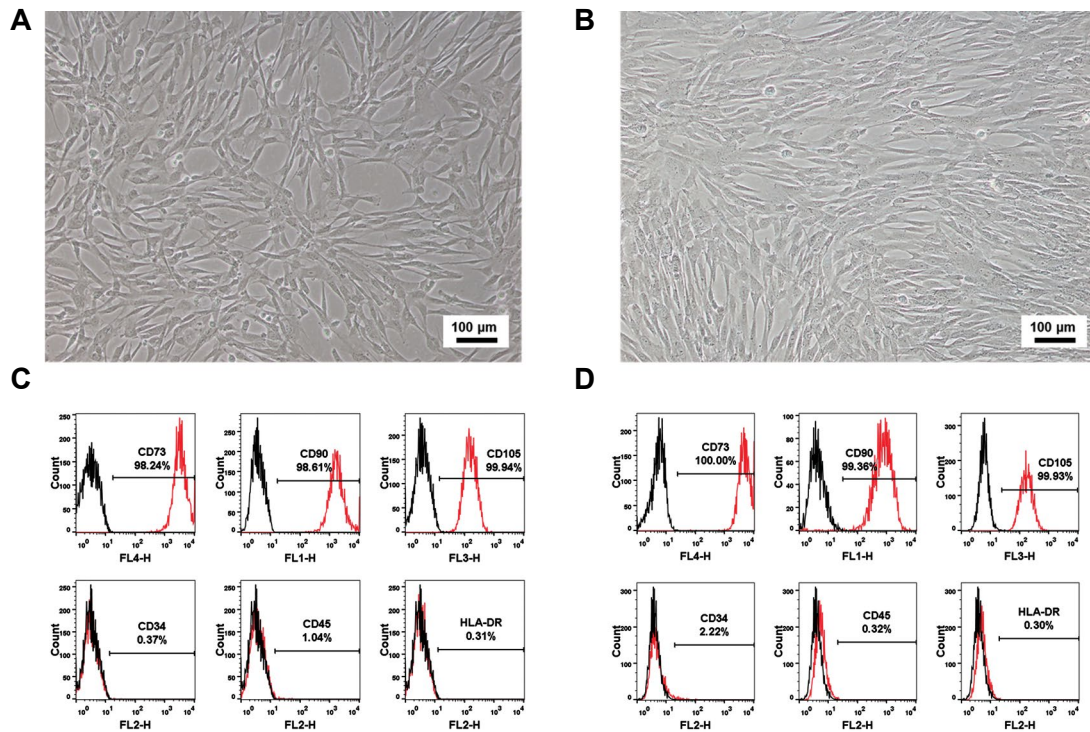


Fig.1: The morphology and surface biomarkers of UC- and AD- MSCs. **A** and **B**. show the morphologies of UC- and AD-MSCs with a magnification of 10X. **C** and **D**. show the surface markers of UC- and AD-MSCs. AD; Adipose tissue, UC; Umbilical cord, and MSCs; Mesenchymal stem cells.

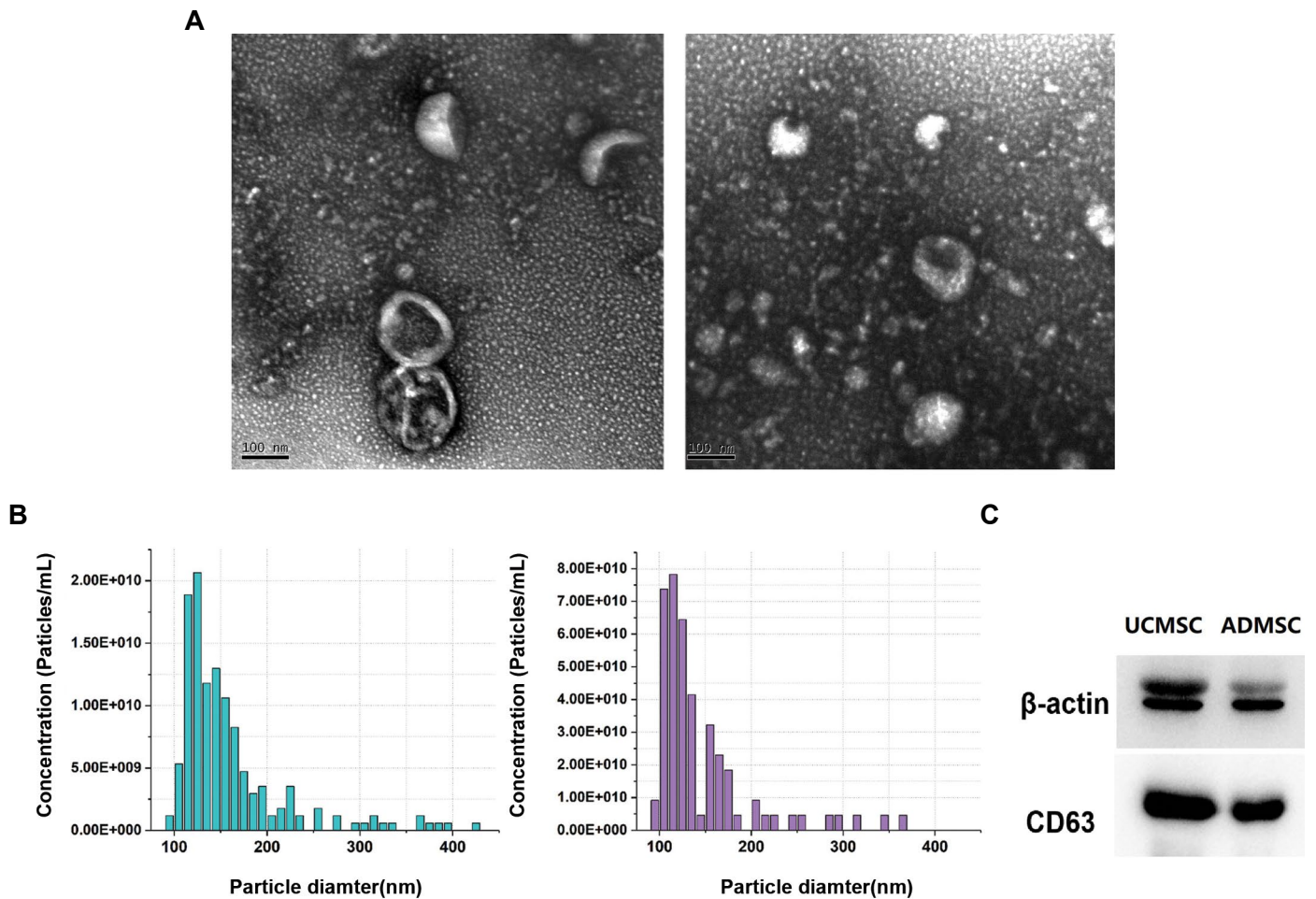


Fig.2: Sizes and protein characteristics of exosomes. **A**. The TEM images of exosomes derived from UC- and AD- MSCs. **B**. The particle size distribution of exosomes derived from UC- and AD- MSCs. **C**. Western blot results of exosomes from UC- and AD- MSCs. AD; Adipose tissue, UC; Umbilical cord, and MSCs; Mesenchymal stem cells.

DEPs between exosome UC and exosome AD, and between Sup UC and Sup AD

There were 458 DEPs between Exosome UC and Exosome AD comprising 430 upregulated and 55 downregulated proteins (Fig.3A, B). Furthermore, 439 DEPs were identified between Sup UC and Sup AD, comprising 296 upregulated and 143 downregulated proteins. There were 198 members in the intersection of the DEPs between exosome UC and exosome AD, and between Sup UC and Sup AD (Fig.3C), of which 163 DEPs were synergistically expressed proteins. Exosomes were present in the supernatants in sufficient quantities to assess for functional differences between the two exosome types by studying the intersection of the two DEPs.

Protein-protein interaction network analysis

The PPI network was formed based on the 198 common DEPs mentioned above. This study found that the PPI network contained 92 nodes and 210 interaction pairs (Fig.4). The topological property analysis of the nodes revealed that albumin (ALB), alpha-II-spectrin (SPTAN1), and Ras-related C3 botulinum toxin substrate 2 (RAC2) had higher scores compared to other proteins. Based on the topological property analysis, the top 5 proteins (also named hub proteins) of the PPI network were ALB, SPTAN1, RAC2, protein phosphatase 2, regulatory subunit A (PPP2R1A), and alpha-centractin (ACTR1A).

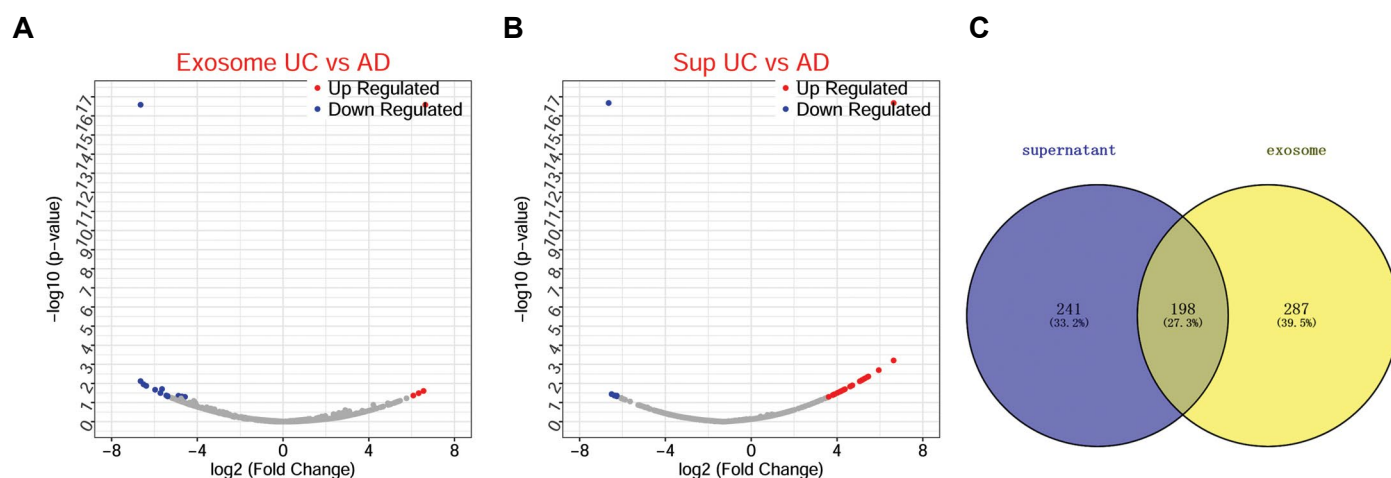


Fig.3: DEPs between exosomes derived from the UC- and AD- MSCs. **A.** The volcano figure of the DEPs between exosomes from the UC- and AD- MSCs. **B.** The volcano figure of the DEPs between supernatant from the UC- and AD- MSCs. **C.** Venn diagram of the DEPs. Blue and red dots represent downregulated and upregulated proteins, respectively. The gray color represents the normally regulated proteins, abscissa is \log_2FC , and ordinate is $\log_{10}P$. AD; Adipose tissue, UC; Umbilical cord, DEPs; Differentially expressed proteins, and MSCs; Mesenchymal stem cells.

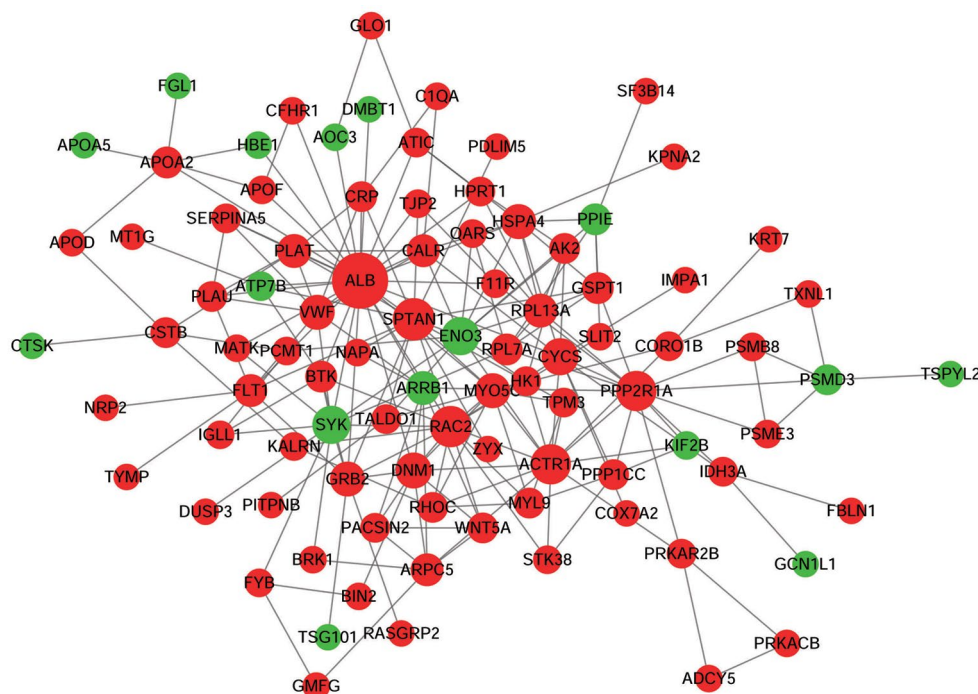


Fig.4: The PPI network based on 198 shared DEPs. The green and red colors represent downregulated and upregulated proteins, respectively. The dot size represents the degree of connectivity, as the higher the degree of connectivity, the larger the dot. DEPs; Differentially expressed proteins, and PPI; Protein-Protein interaction.

Functional enrichment analysis

A total of 438 GO items were obtained based on the functional enrichment analysis, which was performed on the 163 synergistically expressed DEPs. The DEPs were mainly enriched in the GO items associated with immunity, complement activation, and protein activation cascade regulation (Fig.5A). Additionally, the DEPs were enriched in 24 pathways, including those associated with insulin signaling, focal adhesion, complement and coagulation cascades, and platelet activation (Fig.5B). Among these, the complement and coagulation cascade pathway and platelet activation were the most significant pathways in the whole 24 pathways.

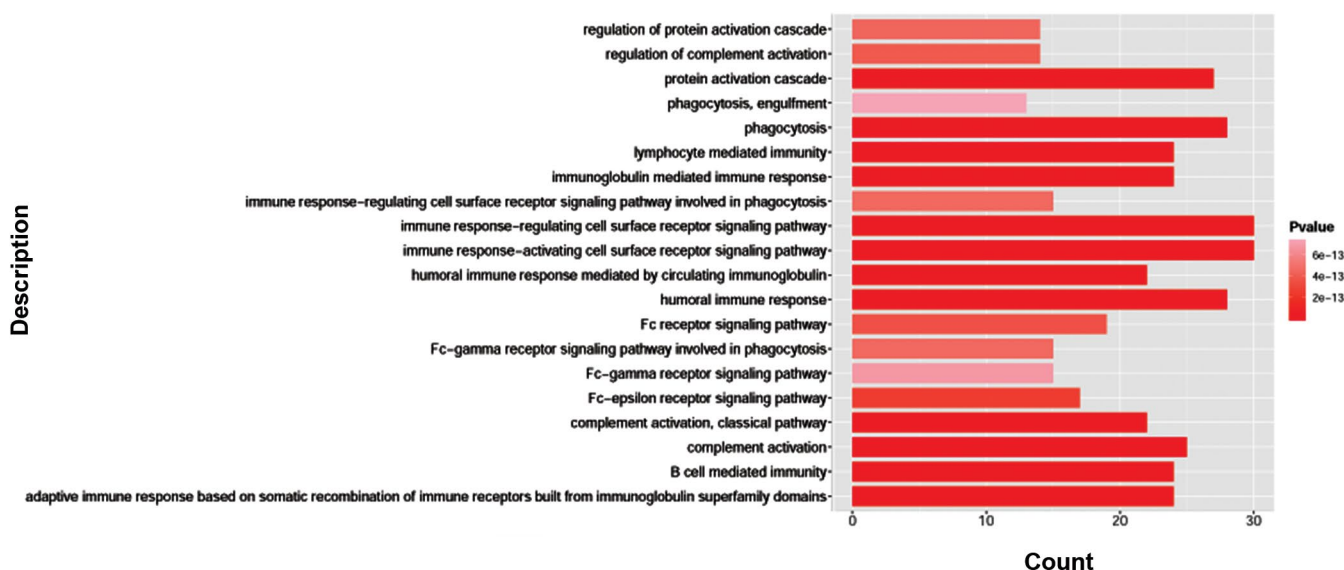
Functional clustering analysis performed by the ClueDO plugin revealed that the enriched functions were divided into 15 categories. Figure 5C shows the representative functional items of each category, such as smooth muscle cell migration, lamellipodium organization, peptidyl tyrosine autophosphorylation, negative regulation of GTPase activity, and intestinal absorption (denoted by **, if the term/group was greater than significant, P value<0.001). In addition, correlation analysis was performed on the functional categories to obtain a functional clustering network (Fig.5D). The colors in Figures 5 C and D correspond to each other, and the same color represents the same type of GO function. The number of GO terms connected to the protein nodes (red markers) and the thickness of the links indicates the significance of each protein. Microfilament-associated proteins BRK1, recombinant rabbit coronin-1B (CORO1B), slit homolog 2 protein N-product (SLIT2), apolipoprotein

A-II precursor (APOA2), apolipoprotein A-5 precursor (APOA5), and β -arrestin-1 (ARRB1) were more significant than others. Figure 5D also shows the correlation between the GO items—the smaller the P value, the larger the dot, indicating a stronger correlation. It is clear from these results that intestinal absorption, positive regulation of endocytosis, regulation of the meiotic cell cycle, and smooth muscle cell migration are processes where protein function is substantial.

Mapping the key pathway

To further study the function of exosomes, the potential regulatory networks of the key pathways, the complement and coagulation cascade and platelet activation, were mapped. Figure 6A shows the complement and coagulation cascade pathway, which contains both extrinsically and intrinsically regulated cascades. When compared with the Exosome AD, the expressions of protein C inhibitor (PCI), von Willebrand Factor (vWF), urokinase type plasminogen activator (uPA), plasminogen activator (tPA), complement regulatory protein C1qrs, and human mannan-binding lectin-associated serine protease 1/2 (MASP1/2) in the Exosome UC were significantly upregulated. Figure 6B shows the platelet activation pathway, which has a significant association with the complement and coagulation cascade pathway. Adenylate cyclase (AC), Ras-guanine nucleotide releasing factor (RASGRP), von willebrand factor (vWF), and tyrosine protein kinase Btk were upregulated in the Exosome UC, whereas tyrosine kinase Syk was downregulated.

A



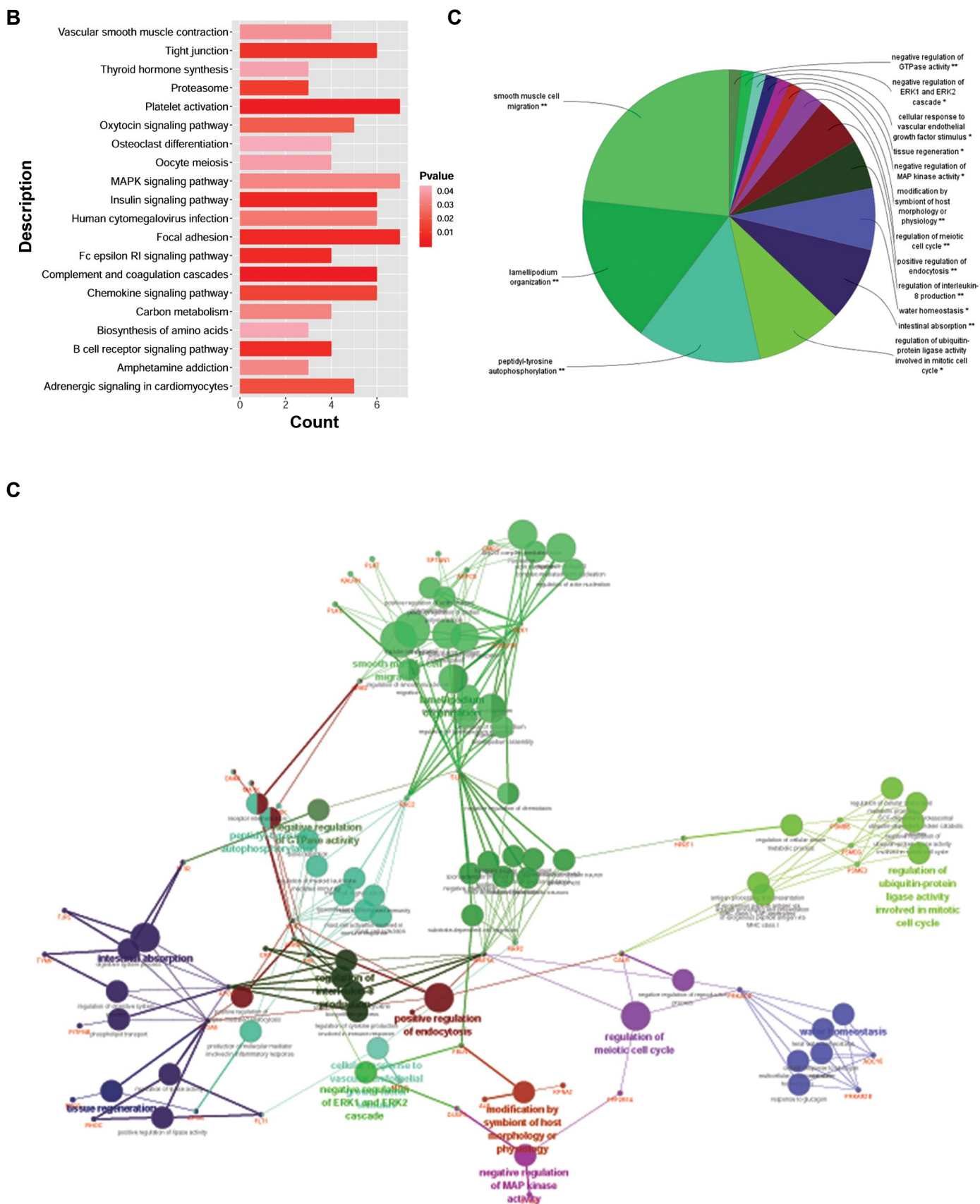
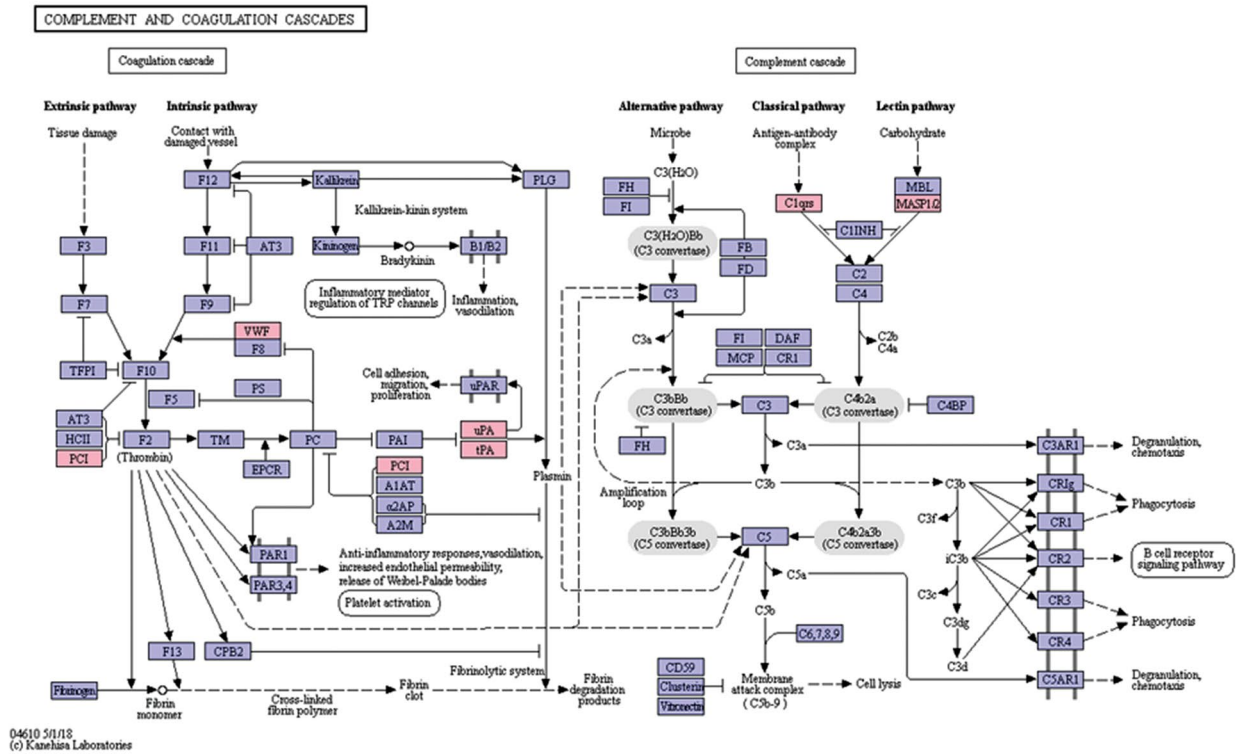


Fig.5: The functional enrichment analyses of the DEPs. **A.** The histogram of GO enrichment analysis based on the DEPs. **B.** KEGG pathway of DEPs. The vertical axis in A and B is the functional item and the horizontal axis is the count, which is the number of enriched proteins. The deeper the red color, the smaller the P value, indicating a higher significance. **C.** The Pie chart of functional classification. Different colors represent different types of functions, and the labels are representative function items. **D.** The network of ClueGO function. The red label is the target protein and the other dots are GO functional terms. The two-point line represents the correlation between different functions. Different colors represent different groups, and the smaller the P value, the larger the dot. Meanwhile the larger the kappa coefficient, the thicker the line. DEPs; Differentially expressed proteins, Go; Gene ontology, and KEGG; kyoto encyclopedia of genes and genomes.

A



B

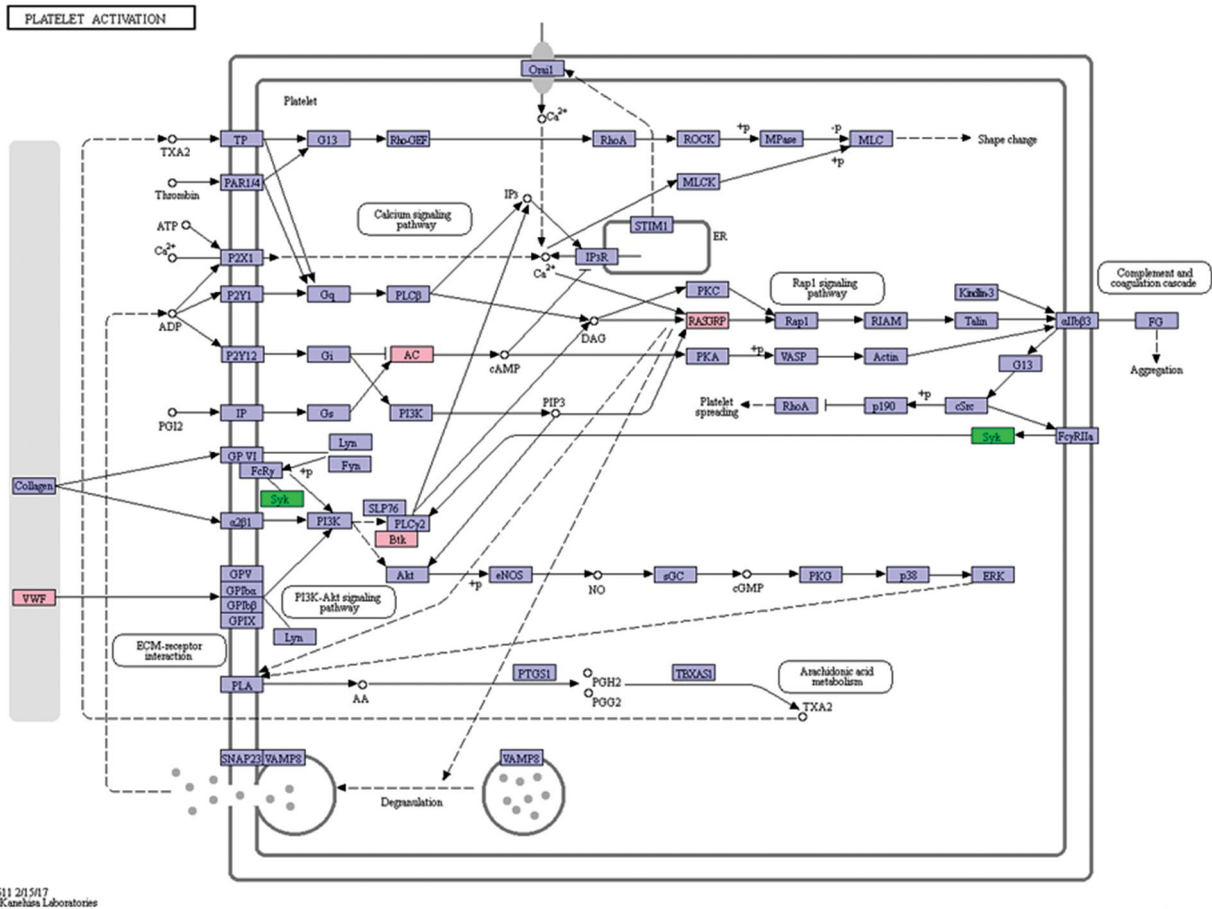


Fig.6: The regulatory network of different pathways. **A.** The regulatory network of the complement and coagulation cascade pathway. **B.** The regulatory network of the platelet activation pathway. Pink represents the differential protein that is upregulated in the pathway, and green is the downregulated protein in UC-MSC exosomes compared with AD-MSC exosomes. AD-MSCS; Adipose mesenchymal stem cells, and UC; Umbilical cord.

Discussion

The widespread use of MSC exosomes in the repair and regeneration of damaged tissues is closely related to immune regulation (25). According to Neerukonda et al. (26), MSC exosomes can regulate innate and adaptive immune responses during infection, inflammation, and virus-associated pathology (27). The immunoregulatory effect of MSC exosomes may be associated with suppression of T lymphocyte function, natural killer cell cytotoxic activity, and B cell activation, proliferation and secretion. It may also be associated with modulation of macrophage differentiation and dendritic cell maturation (28). Proteomic analyses have shown that MSC exosomes contain various cytokines, such as interleukin-10 (IL-10), interleukin-6 (IL-6), macrophage stimulating factor (MSF), transforming growth factor β (TGF β), prostaglandin E2, platelet-derived growth factor (PDGF), vascular endothelial growth factor (VEGF), and fibroblast growth factor (FGF) among others, indicating that MSC exosomes have immunomodulatory functions (29).

In this study, the DEPs of exosomes from UC- and AD-MSCs were mainly enriched in immune functions, suggesting that these two exosome types highly differ in immune regulation. The complement and coagulation cascades and the platelet activation pathway were the most important among the 24 pathways related with GO items. The proteins BRK1, CORO1B, SLIT2, APOA2, APOA5, and ARRB1 in the functional clustering network were considered more significant than other proteins based on the Main GOs. Taken together, these results suggest that these two exosome types may be used for different clinical applications.

The complement cascade has serum proteins that are activated by antigen-antibody complexes, causing pathogenic microorganisms to be cleaved or phagocytosed, thereby mediating immune and inflammatory responses (30, 31). The complement system has an important role in exosome-related biological functions. Neuronal exosomes promote synaptic pruning through upregulation of complement cascade factors (32). Moreover, astrocyte-derived exosomes in Alzheimer patient cells has shown high complement levels (33). In addition, the complement and coagulation cascade was the star signaling pathway in the proteomic research of exosomes. Wong et al. (34) reported that in the serum exosomes of acute ulcerative colitis mice, caused by dextran sulfate sodium, the complement and coagulation cascade pathway was activated. A proteomic profile analysis on the pathology of preeclampsia also revealed that cord exosome proteins might play an important role via the complement and coagulation cascades (34). In our study, the DEPs were obviously enriched in the complement and coagulation cascade pathway, indicating that the different functions of exosomes of AD- and UC-MSCs were related to the complement and coagulation cascades.

Platelet activation was another significant signaling pathway in our study. It has been reported that exosomes

are novel effectors of human platelet lysate activity (35). There are many studies focusing on bioactivities of exosomes derived from different platelets. For instance, exosomes from septic shock patients can induce myocardial dysfunction (36). Guo et al. (37) revealed that exosomes from plasma that contain large amounts of platelets may improve re-epithelialization of chronic skin wounds in diabetic rats. However, there are few studies on the activating effects of exosomes on platelets, especially in various types of MSCs (38). In our study, we found that the DEPs were mainly involved in platelet activation, which gave us a new perspective to assess the different functions between AD- and UC-MSC exosomes.

Conclusion

The DEPs between AD- and UC-MSC exosomes were significantly enriched in immunity, complement system, coagulation cascade, and platelet activation pathways. The different functions of AD- and UC-MSC exosomes in clinical applications may be related to their immunomodulatory activities.

Acknowledgements

This research was supported by 973 Project (2015CB931802 and 2017YFA0205301), Chinese National Natural Scientific Fund (No.81327002 and No.81803094), China Postdoctoral Science Foundation (No. 2017M621486), Shanghai Jiaotong University Medical Professionals Cross Fund (No. YG2016ZD10) and Shanghai Engineering Research Center for Intelligent diagnosis and treatment instrument (No.15DZ2252000). The authors declare no conflicts of interest.

Authors' Contributions

B.L.; Contributed to all experimental work, statistical analysis, interpretation of data, and drafted the manuscript. G.Q., W.C., C.L.; Contributed extensively in the data collection and the discussion. S.P., L.W., Y.L.; Advised on the project and participated in study design. L.M., D.C.; Contributed to the conception and design. All authors read and approved the final manuscript.

References

1. Pittenger MF, Mackay AM, Beck SC, Jaiswal RK, Douglas R, Mosca J D, et al. Multilineage potential of adult human mesenchymal stem cells. *Science*. 1999; 284(5411):143-147.
2. Liechty KW, MacKenzie TC, Shaaban AF, Radu A, Moseley AM, Deans R, et al. Human mesenchymal stem cells engraft and demonstrate site-specific differentiation after in utero transplantation in sheep. *Nat Med*. 2000; 6(11): 1282-1286.
3. Wang D, Li J, Zhang Y, Zhang M, Chen J, Li X, et al. Umbilical cord mesenchymal stem cell transplantation in active and refractory systemic lupus erythematosus: a multicenter clinical study. *Arthritis Res Ther*. 2014; 16(2): R79.
4. Chen H, Niu J-W, Ning H-M, Pan X, Li X-B, Li Y, et al. Treatment of psoriasis with mesenchymal stem cells. *Am J Med*. 2016; 129(3): e13-e14.
5. Wang L, Wang L, Cong X, Liu G, Zhou J, Bai B, et al. Human umbilical cord mesenchymal stem cell therapy for patients with active rheumatoid arthritis: safety and efficacy. *Stem Cells Dev*. 2013; 22(24): 3192-3202.
6. Maharlooei MK, Bagheri M, Solhjoui Z, Jahromi BM, Akrami M, Ro-

- hani L, et al. Adipose tissue derived mesenchymal stem cell (AD-MSC) promotes skin wound healing in diabetic rats. *Diabetes Res Clin Pract*. 2011; 93(2): 228-234.
7. Gao J, Liu R, Wu J, Liu Z, Li J, Zhou J, et al. The use of chitosan based hydrogel for enhancing the therapeutic benefits of adipose-derived MSCs for acute kidney injury. *Biomaterials*. 2012; 33(14): 3673-3681.
 8. Xin Y, Wang YM, Zhang H, Li J, Wang W, Wei YJ, et al. Aging adversely impacts biological properties of human bone marrow-derived mesenchymal stem cells: implications for tissue engineering heart valve construction. *Artif Organs*. 2010; 34(3): 215-222.
 9. Mirakabad FST, Hosseinzadeh S, Abbaszadeh HA, Khoramgah MS, Ghanbarian H, Ranjbari J, et al. The comparison between the osteogenic differentiation potential of clay-polyacrylonitrile nanocomposite scaffold and graphene-polyacrylonitrile scaffold in human mesenchymal stem cells. *Biomedical Engineering*. 2019; 11(3): 238-253.
 10. Yu B, Zhang X, Li X. Exosomes derived from mesenchymal stem cells. *Int J Mol Sci*. 2014; 15(3): 4142-4157.
 11. Phinney DG, Pittenger MF. Concise review: MSC-derived exosomes for cell-free therapy. *Stem Cells*. 2017; 35(4): 851-858.
 12. Li T, Yan Y, Wang B, Qian H, Zhang X, Shen L, et al. Exosomes derived from human umbilical cord mesenchymal stem cells alleviate liver fibrosis. *Stem Cells Dev*. 2013; 22(6): 845-854.
 13. Zhou Y, Xu H, Xu W, Wang B, Wu H, Tao Y, et al. Exosomes released by human umbilical cord mesenchymal stem cells protect against cisplatin-induced renal oxidative stress and apoptosis in vivo and in vitro. *Stem Cell Res Ther*. 2013; 4(2): 34.
 14. Zhao Y, Sun X, Cao W, Ma J, Sun L, Qian H, et al. Exosomes derived from human umbilical cord mesenchymal stem cells relieve acute myocardial ischemic injury. *Stem Cells Int*. 2015; 2015: 761643.
 15. Blazquez R, Sanchez-Margallo FM, de la Rosa O, Dalemans W, Álvarez V, Tarazona R, et al. Immunomodulatory potential of human adipose mesenchymal stem cells derived exosomes on in vitro stimulated T cells. *Front Immunol*. 2014; 5: 556.
 16. Lin R, Wang S, Zhao RC. Exosomes from human adipose-derived mesenchymal stem cells promote migration through Wnt signaling pathway in a breast cancer cell model. *Mol Cell Biochem*. 2013; 383(1-2): 13-20.
 17. Lin KC, Yip HK, Shao PL, Wu SC, Chen KH, Chen YT, et al. Combination of adipose-derived mesenchymal stem cells (ADMSC) and ADMSC-derived exosomes for protecting kidney from acute ischemia-reperfusion injury. *Int J Cardiol*. 2016; 216: 173-185.
 18. Chen K-H, Chen C-H, Wallace CG, Yuen C-M, Kao G-S, Chen Y-L, et al. Intravenous administration of xenogenic adipose-derived mesenchymal stem cells (ADMSC) and ADMSC-derived exosomes markedly reduced brain infarct volume and preserved neurological function in rat after acute ischemic stroke. *Oncotarget*. 2016; 7(46): 74537-74556.
 19. Raimondo F, Morosi L, Chinello C, Magni F, Pitto M. Advances in membranous vesicle and exosome proteomics improving biological understanding and biomarker discovery. *Proteomics*. 2011; 11(4): 709-720.
 20. Choi DS, Kim DK, Kim YK, Gho YS. Proteomics, transcriptomics and lipidomics of exosomes and ectosomes. *Proteomics*. 2013; 13(10-11): 1554-1571.
 21. Zhang H, Zhang B, Cheng M, Tao Y, Hu J, Xun M, et al. Isolation and characterization of mesenchymal stem cells derived from whole human umbilical cord by applying a direct explant technique. *J Basic Clin Med*. 2012 (1):17.
 22. Zhang W, Li G, Chen Y, Ma L, Han J. Isolation, culture and genetic stability of adult adipose-derived mesenchymal stem cells. *Journal of Clinical Rehabilitative Tissue Engineering Research*. 2009;13(40):7833-7837.
 23. Szklarczyk D, Franceschini A, Wyder S, Forslund K, Heller D, Huerta-Cepas J, et al. STRING v10: protein-protein interaction networks, integrated over the tree of life. *Nucleic Acids Res*. 2015; 43(Database issue): D447-D452.
 24. Dominici M, Le Blanc K, Mueller I, Slaper-Cortenbach I, Marini F, Krause D, et al. Minimal criteria for defining multipotent mesenchymal stromal cells. The International Society for Cellular Therapy position statement. *Cytotherapy*. 2006; 8(4): 315-317.
 25. Zhang S, Chuah SJ, Lai RC, Hui JHP, Lim SK, Toh WS. MSC exosomes mediate cartilage repair by enhancing proliferation, attenuating apoptosis and modulating immune reactivity. *Biomaterials*. 2018; 156: 16-27.
 26. Neerukonda S, Egan NA, Parcels M. Exosomal communication during infection, inflammation and virus-associated pathology. *J Cancer Ther Sci*. 2017; 1(1): 1-13.
 27. Uccelli A, Rosbo NK. The immunomodulatory function of mesenchymal stem cells: mode of action and pathways. *Ann N Y Acad Sci*. 2015; 1351: 114-126.
 28. Han R, Li L, Wang R, Hou Z. Immunomodulatory effects of mesenchymal stem cells-derived exosomes. *Chinese Journal of Tissue Engineering Research*. 2019; 23(17): 2762-2769.
 29. Kim H-S, Choi D-Y, Yun SJ, Choi S-M, Kang JW, Jung JW, et al. Proteomic analysis of microvesicles derived from human mesenchymal stem cells. *J Proteome Res*. 2012; 11(2): 839-849.
 30. Ricklin D, Lambris JD. Complement in immune and inflammatory disorders: pathophysiological mechanisms. *J Immunol*. 2013; 190(8): 3831-3838.
 31. Ricklin D, Hajishengallis G, Yang K, Lambris JD. Complement: a key system for immune surveillance and homeostasis. *Nat Immunol*. 2010; 11(9): 785-797.
 32. Bahrini I, Song JH, Diez D, Hanayama R. Neuronal exosomes facilitate synaptic pruning by up-regulating complement factors in microglia. *Sci Rep*. 2015; 5: 7989.
 33. Goetzl EJ, Schwartz JB, Abner EL, Jicha GA, Kapogiannis D. High complement levels in astrocyte-derived exosomes of Alzheimer disease. *Ann Neurol*. 2018; 83(3): 544-552.
 34. Wong WY, Lee MML, Chan BD, Kam RK, Zhang G, Lu AP, et al. Proteomic profiling of dextran sulfate sodium induced acute ulcerative colitis mice serum exosomes and their immunomodulatory impact on macrophages. *Proteomics*. 2016; 16(7): 1131-1145.
 35. Torreggiani E, Perut F, Roncuzzi L, Zini N, Baglio SR, Baldini N. Exosomes: novel effectors of human platelet lysate activity. *Eur Cell Mater*. 2014; 28: 137-151.
 36. Azevedo LC, Janiszewski M, Pontieri V, Pedro Mde A, Bassi E, Tucci PJ, et al. Platelet-derived exosomes from septic shock patients induce myocardial dysfunction. *Crit Care*. 2007; 11(6): R120.
 37. Guo SC, Tao SC, Yin WJ, Qi X, Yuan T, Zhang CQ. Exosomes derived from platelet-rich plasma promote the re-epithelization of chronic cutaneous wounds via activation of YAP in a diabetic rat model. *Theranostics*. 2017; 7(1): 81-96.
 38. Zhang H, Zhang B, Cheng M, Tao Y, Hu J, Xun M, et al. Isolation and characterization of mesenchymal stem cells derived from whole human umbilical cord by applying a direct explant technique. *J Basic Clin Med*. 2012 (1):17.

Long-Term Effects of Hippocampal Low-Frequency Stimulation on Pro-Inflammatory Factors and Astrocytes Activity in Kindled Rats

Razieh Rohani, M.Sc.¹, Abbas Aliaghaei, Ph.D.¹, Mohammad-Amin Abdollahifar, Ph.D.¹, Yousef Sadeghi, Ph.D.¹,
Leila Zare, Ph.D.², Samaneh Dehghan, Ph.D.², Mohammad Hassan Heidari, Ph.D.^{1*}

1. Department of Biology and Anatomical Sciences, School of Medicine, Shahid Beheshti University of Medical Sciences and Health Services (SBMU), Tehran, Iran
2. Department of Physiology, Faculty of Medical Sciences, Tarbiat Modares University, Tehran, Iran

*Corresponding Address: P.O.Box: 985717443, Department of Biology and Anatomical Sciences, School of Medicine, Shahid Beheshti University of Medical Sciences and Health Services (SBMU), Tehran, Iran
Email: hdr@sbmu.ac.ir

Received: 05/September/2019, Accepted: 21/October/2019

Abstract

Objective: Epilepsy is accompanied by inflammation, and the anti-inflammatory agents may have anti-seizure effects. In this investigation, the effect of deep brain stimulation, as a potential therapeutic approach in epileptic patients, was investigated on seizure-induced inflammatory factors.

Materials and Methods: In the present experimental study, rats were kindled by chronic administration of pentylenetetrazol (PTZ; 34 mg/Kg). The animals were divided into intact, sham, low-frequency deep brain stimulation (LFS), kindled, and kindled +LFS groups. In kindled+LFS and LFS groups, animals received four trains of intra-hippocampal low-frequency deep brain stimulation (LFS) at 20 minutes, 6, 24, and 30 hours after the last PTZ injection. Each train of LFS contained 200 pulses at 1 Hz, 200 μ A, and 0.1 ms pulse width. One week after the last PTZ injection, the Y-maze test was run, and then the rats' brains were removed, and hippocampal samples were extracted for molecular assessments. The gene expression of two pro-inflammatory factors [interleukin-6 (IL-6) and tumor necrosis factor-alpha (TNF- α)], and glial fibrillary acidic protein (GFAP) immunoreactivity (as a biological marker of astrocytes reactivation) were evaluated.

Results: Obtained results showed a significant increase in the expression of interleukin-6 (IL-6), tumor necrosis factor (TNF)- α , and GFAP at one-week post kindling seizures. The application of LFS had a long-lasting effect and restored all of the measured changes toward normal values. These effects were gone along with the LFS improving the effect on working memory in kindled animals.

Conclusion: The anti-inflammatory action of LFS may have a role in its long-lasting improving effects on seizure-induced cognitive disorders.

Keywords: Deep Brain Stimulation, Epilepsy, GFAP, Interleukin-6, TNF- α

Cell Journal (Yakhteh), Vol 23, No 1, April-June (Spring) 2021, Pages: 85-92

Citation: Rohani R, Aghaei AA, Abdollahifar MA, Sadeghi Y, Zare L, Dehghan S, Heidari MH. Long-term effects of hippocampal low-frequency stimulation on pro-inflammatory factors and astrocytes activity in kindled rats. *Cell J.* 2021; 23(1): 85-92. doi: 10.22074/cellj.2021.7139.

This open-access article has been published under the terms of the Creative Commons Attribution Non-Commercial 3.0 (CC BY-NC 3.0).

Introduction

Epilepsy is among the most prevalent brain diseases, has widespread distribution, and about 1% of people suffer from it. Medicinal therapy is the main therapeutic manner in epileptic patients. However, approximately 20-30% of patients suffer from epilepsy that is resistant to medicinal therapy (1). In addition, about 50% of epileptic patients have variable degrees of cognitive impairments that seriously influence the quality of life of patients (2). Therefore, there are a lot of efforts to find new therapeutic methods to reduce the severity of seizures in these patients.

Application of deep brain stimulation (DBS) is a possible treatment for drug-resistant epileptic patients. U.S. food and drug administration (FDA) has approved the DBS applying in some brain areas, including anterior thalamus and hippocampus, as a new therapy in epileptic patients (3). The pattern of DBS, especially its frequency, is an important factor in its effectiveness. DBS has been applied in a wide range of frequency (from 1-190 Hz)

in epileptic patients [reviewed in: (4)] and laboratory animals (5-10). Applying DBS at low-frequency (named low-frequency stimulation; LFS) exerts anticonvulsant effects. Interestingly, the neuronal damage induced by low-frequency stimulation (LFS) application in the epileptic and its surrounding areas is less than the damage caused by high-frequency stimulation. Accordingly, LFS may be considered as an appropriate choice for epileptic patients (11). In addition to its anticonvulsant effect, LFS restores the learning and memory impairment following seizures (12, 13).

Finding the precise mechanisms of antiepileptic and anticonvulsant actions of DBS is required before its application as an anticonvulsant method. Different mechanisms, such as changes in neuronal excitability and gene expression, have been suggested to be involved in DBS anticonvulsant effects (14). In addition, recently, it has been reported that high-frequency stimulation of

thalamus has an anti-inflammatory effect in epileptic models (15). The plasma concentrations of IL-1, TNF- α , and IL-6, as important inflammatory agents, are increased in individuals with temporal lobe epilepsy. These agents have also detected from resected brain tissue from people with intractable epilepsy (16). In line with the role of inflammatory agents in epilepsy, the induction of IL-1 α , TNF- α , and IL-6 has been shown in both neurons and glia before epilepsy onset. There is an increase in inflammatory cytokines levels (IL-1 β , IL-6, and TNF- α) in the hippocampus of PTZ-induced kindling (17). Inflammatory agents increase in a laboratory model of seizure, including PTZ kindling. It has been shown that PTZ-induced kindling causes significant neuronal injury and expression of the pro-inflammatory TNF- α in the cerebral cortex (18).

It is hypothesized that focal or systemic impaired inflammatory processes lead to unusual connectivity in the central nervous system and may increase the excitability of neuronal networks. Therefore, inflammation can mediate the onset of epilepsy (19). Instead, it has been reported that the LFS application reduced the seizure-induced hyperexcitability (20). Considering the fact that, PTZ kindling profoundly affects the hippocampus, and the hippocampus is a vital structure for the acquisition of new memories (21), in the present study we applied LFS in the CA1 region of the hippocampus (as an important area in generation and propagation of kindled seizures). Then we investigated the effect of LFS on inflammatory factors and working memory following PTZ kindling in rats.

Materials and Methods

Animals

Male Sprague-Dawley rats (weighed 200-220 g) were used in the present experimental study. Animals were prepared from the animal house of Shahid Beheshti University of Medical Sciences. All experiments and research protocols were in accordance with the guidelines established by the Animal Care Commission of Shahid Beheshti University of Medical Sciences (the ethical approval number was: IR.SBMU.MSP.REC.1395.447). All efforts performed to reduce the pain and discomfort during experiments. Animals were caged in groups of four and had free access to food and water. The light-dark cycle was adjusted for 12-hours (lights from 07:00 A.M. to 7:00 P.M.), and the temperature was controlled in the range of 22-24°C. The number of animals and their distress were kept minimized during the experiments.

Experimental procedure

The animals were divided into intact, sham, LFS, kindled (K), and kindled +LFS (KLFS) groups. In the kindled group, animals received PTZ until three sequential stages 4 or 5 seizures were observed, and these animals were considered as fully kindled. A similar protocol was performed for the animals in the KLFS group; however,

after achieving the fully kindled state, animals received LFS at four-time points. LFS was applied in LFS group animals similar to the KLFS group but did not receive kindling stimulation. In the sham group, the animals underwent a surgical procedure, without receiving LFS or kindling stimulations. The intact group did not undergo any surgery, LFS, or kindling stimulations.

Animal surgery

Rats were anesthetized by intraperitoneal injection of ketamine and xylazine (100 and 10 mg/kg, respectively) before surgery. The animal head was fixed in a stereotaxic instrument. A tripolar stimulating/recording electrode was implanted into the hippocampal CA1 region of the right hemisphere coordinated as follows: 3.2 mm posterior and 2 mm to the right from bregma and 2.3 mm below dura (22). The electrode consisted of twisted Teflon-coated stainless steel strands, insulated except at their tips, with a diameter of 127 μ m (A-M Systems, USA). Three miniature stainless steel screws were also fixed on the skull to secure the electrode assembly. One screw was connected to an insulated stainless steel wire and served as a monopolar ground and reference electrode. Implanted electrodes were attached to pins of a small plastic multi-channel socket. The plastic socket was attached to the skull with dental acrylic as a head stage.

PTZ kindling procedure

Chemical kindling was induced by intraperitoneal injection of a sub-threshold dose of PTZ (34 mg/Kg; 0.1 ml/100 g) every other day. The convulsive behaviors of each animal were observed immediately following PTZ injection for 20 minutes when the rat was put in a transparent plexiglass box (30×30×30 cm). The Seizure intensity was evaluated using a modified Racine scale. In stage 0, no response was observed. In stage 1, ear and facial twitching occurred. Stage 2 was distinguished by convulsive twitching axially through the body. In stage 3, rats showed myoclonic jerks and rearing. Stage 4 was accompanied by wild running and jumping, and finally, in stage 5, generalized tonic-clonic seizures were observed (23). PTZ was dissolved in sterile isotonic saline as a vehicle exactly before the injections. In the sham group, animals received the vehicle and were handled similar to the animals of the kindled group. All animals weighed before each injection.

Low-frequency stimulation application

LFS was administered at four different time points. The 1st LFS was applied at 20 minutes, and the 2nd LFSs was applied at 6 hours after the last PTZ injection. The 3rd and 4th LFSs were applied the next day at the same time (i.e., there was a 6-hour interval between third and fourth LFSs). Each LFS contained four trains of 200 square monophasic pulses at 0.1 ms duration and 1 Hz. LFS trains were applied at 5 minutes intervals. The LFS intensity (200 μ A) adjusted according to previous experiments (12). Using a PC-based stimulating and

recording system (D3111 ScienceBeam instrument Co., Iran), LFS parameters were determined. During LFS administration, local field potentials were recorded from the hippocampal CA1 using a custom-designed software, eTrace analysis (version 2 ScienceBeam instrument Co., Iran), to confirm the LFS pulses were applied at the site.

Y-maze test

The spatial working memory was assessed by the Y-maze test. The apparatus had three arms separated by 120° angles. Each arm was made of black Plexiglass (30 cm long × 8 cm wide × 15 cm high). There were also different cues outside the maze to make different spacial properties for each arm. Each animal was randomly placed in an apparatus arms and could freely explore the maze for 5 minutes. The consecutive entrance of animals (without repetition) into three different arms was considered as a spontaneous alternation. The spontaneous alternation percentage was measured as the ratio of actual (total alternations) to possible (total arm entries - 2) number of alternations × 100.

Quantitative real-time polymerase chain reaction

The expression of IL-6 and TNF- α genes was measured by quantitative real-time polymerase chain reaction (qRT-PCR). One week after the last PTZ injection, animals were anesthetized with CO₂, sacrificed, and their dorsal hippocampi were isolated and preserved in RNAlater solution at -20°C. According to the manufacturer's instructions, we used the High Pure RNA Tissue Kit (Roche, Basel, Switzerland) to extract total RNA. In the presence of random hexamers and RNase inhibitor, 1 μ g of total RNA was transcribed to cDNA using murine leukemia virus (MuLV) reverse transcriptase (Fermentas, Lithuania). The qRT-PCR analysis was run using specific primers for IL-6 and TNF- α genes. GAPDH & ribosomal RNA 18s were used as internal controls (Table 1). Reactions were performed using SYBR® Premix Ex Taq™ II (TAKARA BIO INC.) on a Rotor-Gene™

6000 real-time PCR machine (Corbett Research, Qiagen, Germany). Initial denaturation was performed at 95°C for 15 minutes. Then, 40 denaturation cycles were run at 95°C for 5 seconds, under primer specific conditions (Table 1), and extension at 60°C for 20 seconds. Comparative qRT-PCR quantitation was performed between candidate groups using REST 2009 (Relative Expression Software Tool, Qiagen).

Immunofluorescence investigations

Animals were anesthetized with CO₂, sacrificed, and their brain was removed for Immunofluorescence study at one week after the last kindling stimulation. The paraffin blocks of the brains were processed and sectioned by a Leica semi-motorized rotary microtome (Leica RM 2145, Germany) with 10 μ m thickness. The slides with tissue sections were immersed into xylene (3 changes, 10 minutes each), and were transferred from xylene into 100% ethanol (3 changes, 10 minutes each). Then, they were immersed into 95, 80, and 70% ethanol (1 change, 5 minutes each). At the next step, slides were immersed in a retrieval solution (sodium citrate, pH: 6) jar and autoclaved at 95°C for 20 minutes. Then, they were let cool to room temperature for 25-30 minutes and were transferred into washing buffer (phosphate buffer solution; PBS). 0.2% Triton X-100 was used to make the samples permeabilized. Then, samples were blocked with 10% normal goat serum for 1 hour. The sections were incubated with chicken anti-GFAP primary antibodies (aVeS Co.; USA) overnight at 4°C. After extensive washing with PBS and 1-hour incubation with an appropriate fluorescent-labeled rabbit anti-chicken IgY H & L (Cat No: ab6751; Texas Red®) secondary antibody. The prepared samples were washed with PBS. Tissue sections were counterstained with 4,6-diamidino-2-phenylindole (DAPI) as a nuclear dye and were coverslipped, then examined under a fluorescence microscope. To quantify the immunostaining data, we used the ImageJ software. The mean gray value of the desired area was subtracted by the mean gray value of the background.

Table 1. Sequences of primers used in real-time polymerase chain reactions

Primer Name	3'-Sequence-5'	Annealing	NCBI Accession number
18s rRNA	F: GAGAAACGGCTACCACATCC	55°C × 25	NR_046237.1
	R: TTTTTCGTCACTACCTCCCC	second	
GAPDH	F: GAACATCATCCCTGCATCCA	60°C × 25	NM_017008.4
	R: GCCAGTGAGCTTCCC GTTCA	second	
IL-6	F: TCTCTCCGCAAGAGACTTCCA	55°C × 25	NM_012589.2
	R: ATACTGGTCTGTTGTGGGTGG	second	
TNF α	F: ACCACGCTCTTCTGTCTACTG	60°C × 25	NM_012675.3
	R: CTTGGTGGTTTGCTACGAC	second	

IL-6; interleukin-6, TNF- α ; Tumor necrosis factor- alpha, and GAPDH; Glyceraldehyde-3-phosphate dehydrogenase.

Statistics

Statistical analysis was done using GraphPad Prism version 6.01 for Windows (GraphPad Software, Ca, USA). Data were averaged and expressed as mean \pm SEM. The normality of distribution of data was checked by the Kolmogorov-Smirnov test, and the p-values were calculated for all experimental groups. Obtained results showed the normal distribution of data. To evaluate the effect of kindling and LFS application on different parameters in experimental groups, one-way ANOVA was used, followed by Tukey's post hoc test. The values of spontaneous alternation in all groups were also compared with a chance level of 50% by using a one-sample t test. P-value of less than 0.05 was considered to represent a significant difference.

Results

Animals showed fully kindled seizures (i.e., the consecutive stage 4 or 5 seizures) after receiving 10.44 ± 1.04 PTZ injections in kindled and after receiving 11.33 ± 0.91 PTZ injections in kindled+LFS groups. There was no significant difference in the kindling rate between these two groups, showing similar neuronal excitability in the animals of these two groups. As there was no significant difference in intact and sham groups, their data were merged and were considered as the control group. In addition, previous experiments showed that the applied pattern of LFS exerted an anticonvulsant effect in fully kindled animals (24, 25).

When the working memory was evaluated in fully kindled animals ($n=7$) at one week after the last PTZ injection, there was a significant ($P<0.05$) reduction in their spontaneous alternation compared to the control group ($n=6$, Fig.1A). Applying LFS in fully kindled animals restored the working memory impairment. There was no significant difference in spontaneous alternation between kindled + LFS ($n=7$) and control groups (Fig.1A). Administration of LFS alone ($n=5$) had no effect on working memory. In addition, there was not any significant difference in the number of total entries among experimental groups in the Y-maze test (Fig.1B).

In the next step, we tried to find the effects of LFS on inflammatory mediators. The gene expression of both TNF- α and IL-6 increased in the hippocampus of kindled animals ($n=3$; $P<0.001$). When LFS was applied in full kindled animals (kindled + LFS group; $n=3$), there was a lower increase in the expression of these genes compared to the kindled group, and there was a significant difference between kindled and kindled + LFS groups ($P<0.001$). However, there was a significant increase in the gene expression level of both TNF- α and IL-6 in kindled + LFS compared to control animals ($P<0.001$; Fig.2). Thus, LFS could not completely return the level of gene expression of

TNF- α and IL-6 toward control situations. Interestingly, while LFS reduced TNF- α and IL-6 gene expression in kindled animals, applying LFS alone ($n=3$) in the control group significantly increased the expression of these two genes (Fig.2).

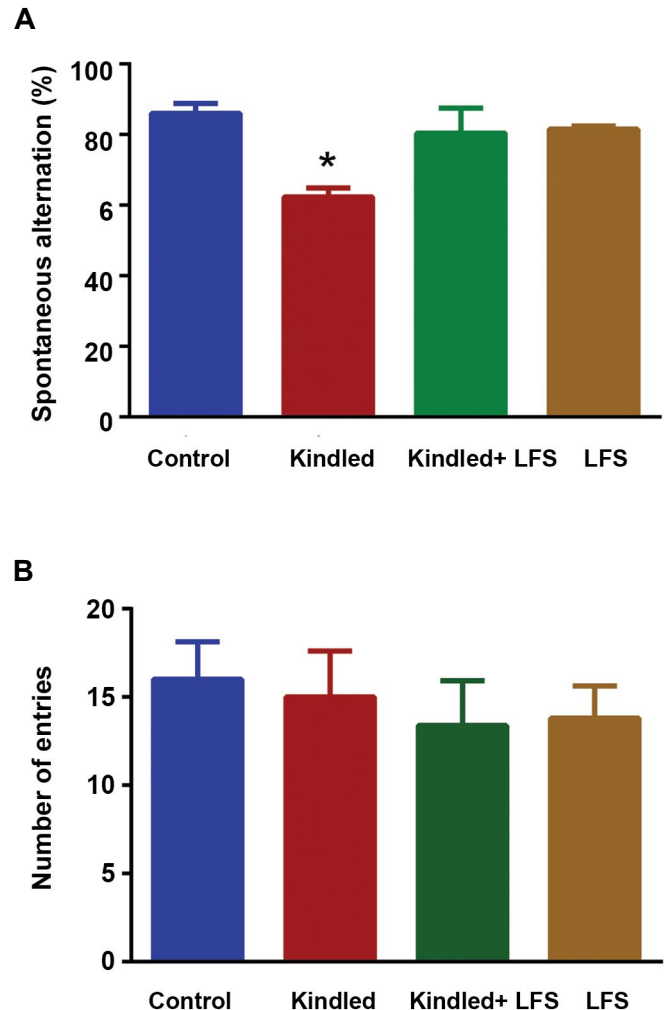


Fig.1: Effect of low-frequency stimulation (LFS) on kindling-induced impairment in working memory. **A.** Spontaneous alternations were measured as an index of working memory in rats. Applying LFS in kindled animals restored the reduction of spontaneous alternations at one week post its application. LFS alone had no significant effect on this parameter. **B.** There was no significant difference in the number of entries between experimental groups. * $P<0.05$ when compared to control group. Data are presented as mean \pm SEM (Control $n=6$, LFS $n=5$, Kindled $n=7$, Kindled+LFS $n=6$).

To confirm the effect of LFS on seizure-induced changes in the inflammatory system, we also compared the amount of glial fibrillary acidic protein (GFAP) in different experimental groups by immunofluorescence method. Obtained results showed a significant increase in the expression of GFAP in the hippocampal CA1 area of the kindled animals ($n=6$; $P<0.01$). The application of LFS in the CA1 region decreased the expression of GFAP compared to kindled group ($P<0.05$). There was no significant difference between kindled+LFS ($n=4$) and control ($n=5$) groups (Fig.3).

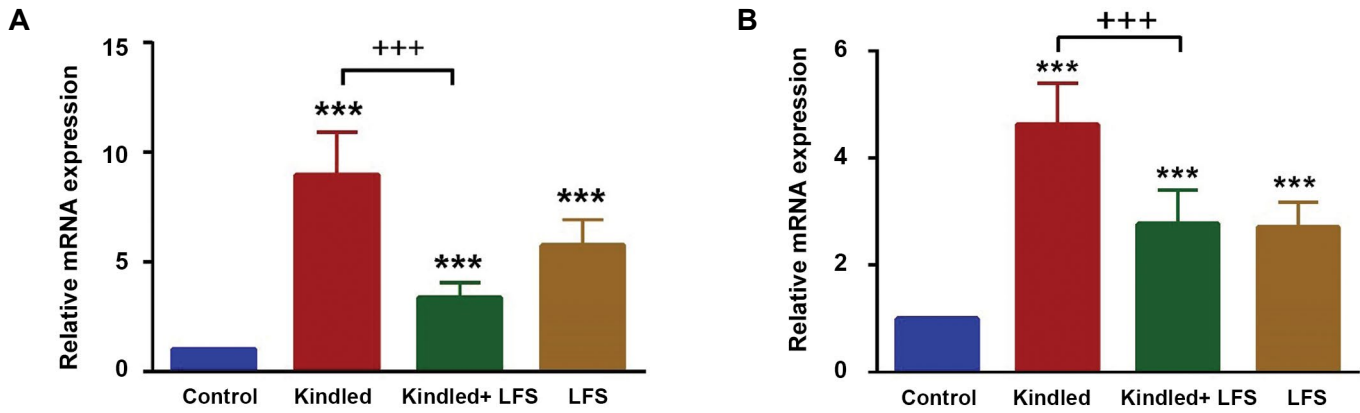


Fig.2: Effect of low-frequency stimulation (LFS) on kindling-induced increment in pro-inflammatory factors. **A.** Tumor necrosis factor- alpha (TNF- α) and **B.** interleukine -6 (IL-6) were significantly increased in kindled animals. Applying LFS in kindled animals reduced the gene expression of TNF- α and IL-6 at one week post its application significantly. LFS alone had also significant effect on these parameters. *** $P < 0.001$ when compared to control group and +++ $P < 0.001$ compared with the related group. Data are presented as mean \pm SEM (Control n=3, Kindled n=3, KLFS n=3, LFS n=3). mRNA; Messenger ribonucleic acid.

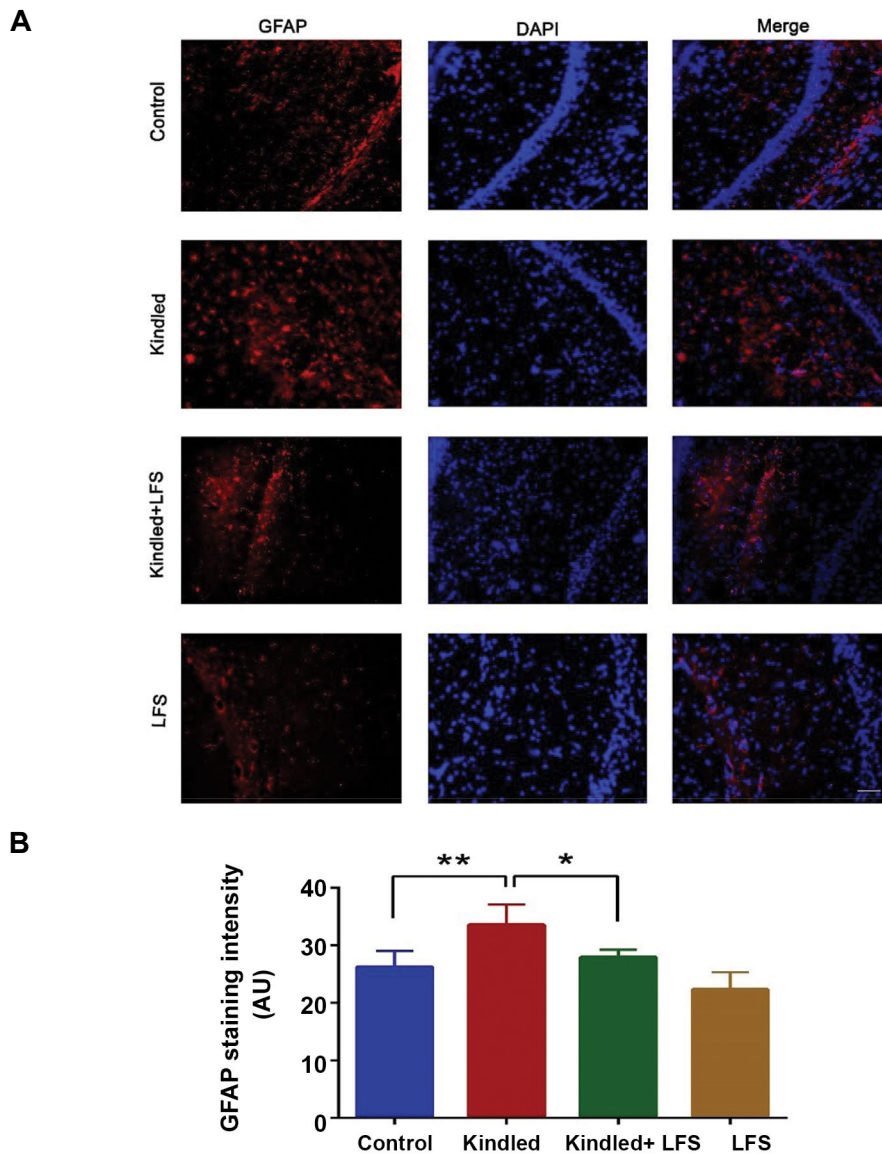


Fig.3: Effect of low-frequency stimulation (LFS) on kindling-induced increment glial fibrillary acidic protein (GFAP). **A.** Representative immunofluorescence images for GFAP (red), nucleus (DAPI, blue), and merged in the hippocampal CA1 subfield. **B.** Quantification of GFAP signals in different experimental groups. GFAP was significantly increased in kindled animals. Applying LFS in kindled animals reduced GFAP expression at one week post its application significantly. LFS alone had no significant effect on these parameters. * $P < 0.05$ and ** $P < 0.01$ when compared to control group. Data are presented as mean \pm SEM (Control n=5, LFS n=4, Kindled n=6, KLFS n=4).

Discussion

Obtained results demonstrated that LFS applying in the hippocampal CA1 region of full PTZ kindled rats had a long-lasting effect and reduced the inflammatory agents in the hippocampus at one-week post kindled seizures. It was previously shown that the LFS pattern used in the present study had an anticonvulsant effect on the kindled animals (25, 24).

There is a strong relationship between epilepsy and inflammation, and recently, the anti-inflammatory agents are thought to reduce and control the seizure attacks (26), although it is not completely clear whether inflammation causes epilepsy or is a result of epilepsy. Similar to previous reports, our data showed a significant increase in inflammatory factors, including IL-6 and TNF- α . During seizure development, the production of IL-6 and TNF- α is increased significantly (27). The increment of IL-6 and TNF- α may be involved in the epileptogenesis via different mechanisms including exerting a modulatory effect on glutamatergic transmission (28), potentiating the function of N-methyl-D-aspartic acid (NMDA) receptors via activation of non-receptor tyrosine kinases (29), and changing the synaptic transmission through GABAergic neurons (30). Therefore, the decrement of inflammatory agents may be partly considered as a mechanism of the anticonvulsant effect of LFS. Of course, it must be considered that the expression levels of IL-6 and TNF- α genes were related to both hippocampal neurons and glial cells.

In line with the results of the present study, it has been reported that the application of deep brain stimulation exerts anticonvulsant and anti-inflammatory effects (31). However, there are many differences between these studies and ours: a. in these studies the researchers used high-frequency stimulation (130 Hz at the intensity of 400 μ A) while we used LFS at lower intensity (1 Hz at the intensity of 200 μ A); b. they stimulated the anterior nucleus of thalamus while we stimulated the CA1 region of the dorsal hippocampus and c. they measured the changes in inflammatory factors while stimulation was switched on. However, in the present study, we assessed the inflammatory agents at a one-week post-LFS. On the other hand, we evaluated the long-lasting effect of LFS on the brain inflammatory system. Thus, considering the fact that the amount of neuronal damage in response to LFS is less than damage resulted from high-frequency stimulation (11). LFS may be suggested as a better pattern of stimulation in epileptic patients.

Changes in the expression of GFAP also confirmed the protective effect of LFS on the inflammatory system in kindled animals. GFAP is expressed by and is an index of astroglial activation. Epileptic seizures lead to an increment in GFAP expression in different brain areas, including the hippocampus (32). In addition, astrocyte dysfunction contributes to the generation or spread of seizure activity. Accordingly, astrocytes should be regarded as important targets for

the new alternative antiepileptic strategies, including deep brain stimulation (33). Our present study showed that LFS applying in fully kindled animals restored the GFAP expression toward its normal values. Of course, as we showed the fluorescent intensity and not the number of cells (neurons and glia) in the immunostaining experiment, the probable changes in neuronal numbers in different experimental groups may be related to an increase in GFAP expression. Therefore, it is better to count the number of cells in future experiments.

The increment in the activity of astrocytes, and therefore over-expression of GFAP can be observed in many brain diseases. In the first step, the activation of astrocytes may protect the brain through different mechanisms such as repairing the blood-brain barrier, limitation of the damaged area, and the release of neurotrophic factors (34). However, following their activation, astrogliosis has neurotoxic effects and increases the progression of the disease, since it exacerbates the inflammatory reactions through producing the cytokines and promoting the glutamate release (35). These mechanisms may be suggested to exacerbate of seizure-induced brain damage. Accordingly, reducing the biological activity of astrocytes following the LFS application may have a role in the long-lasting protective effects of LFS. Of course, it must be emphasized that, considering the growing data about the impact of the glial cells in the mechanisms of the DBS therapies, more studies needed to find the time-course of the brain tissue inflammatory reaction following deep brain stimulation (36).

The activation of astrocyte is regulated and be controlled by many factors, including IL-6 and TNF- α (37). Therefore, the observed increase in IL-6 and TNF- α in our study are in line and can be considered as a reason for increasing of GFAP expression. On the other hand, the inhibitory effect of LFS on GFAP may be due to its inhibitory effects on these pre-inflammatory factors, but not its direct effect on astrocytes themselves. It must be considered that other important cells involved in brain inflammation are microglial cells. Therefore, it is recommended to measure Iba-1 (as a molecular index of neuroglial activities) in future research.

Considering that the ameliorating effect of LFS is applied through different mechanisms, it cannot be concluded from the presented results that whether LFS directly affects inflammatory responses or it influences them indirectly by modulating the neurotransmitter and/or neuromodulatory systems.

Another finding of the present study was the restoring effect of LFS on working memory in kindled animals. This finding was in line with our previous study in which the application of LFS had an improving effect on working memory at 24 hours after the last kindling stimulation (12). However, our present study confirmed that this improving effect lasts for at least one week after the last kindled seizures. Many

experimental models of seizures are accompanied by cognitive abnormalities. In addition, many epileptic patients have also memory impairment (12, 38).

Many factors can be considered as the mechanisms involved in these kinds of memory impairments; however, one probable reason for these comorbidities may be the chronic activation of inflammatory agents. Some investigators showed that the increase in cytokines and increment of their signaling resulted in memory impairment, and there are many reports about the role of inflammatory cytokines, such as IL-6 and TNF- α in the molecular mechanisms underlying learning and memory consolidation (39). Our data showed that LFS' improvement of working memory was accompanied by decreasing the inflammation in rat brains. Thus, obtained results are in line with the previous studies suggesting the seizure-induced inflammatory factors may potentially be involved in memory impairment following seizure behaviors.

In our experiments, the animals were chronically implanted with the electrodes. Therefore, it may be suggested that the inserted electrodes were partly the reason for inflammation in the brain of rats. It has been shown that the implanted electrodes, used for deep brain stimulation, result in glial scars. However, this damage is restricted to a very small area in nearby the electrodes (40). Therefore, all of the observed changes in inflammatory actions in the present study can be related to seizure induction.

Conclusion

Obtained results showed that LFS applying in the dorsal hippocampus of kindled animals reduced the seizure-dependent inflammatory reactions and restored the memory impairment at a long-lasting time (one week) post-seizure. This protective effect was observed both in the gene expression of pro-inflammatory factors and astrocyte activation and in working memory as an important cognitive behavior. However, more studies need to shed light on the precise mechanisms of LFS, finding the best pattern of LFS and the best brain region of stimulation.

Acknowledgments

This study was supported by a grant (#14970) from Shahid Beheshti University of Medical Sciences, Faculty of Medicine. The authors declare no conflict of interest.

Authors' Contributions

R.R.; Contributed to all experimental work, data and statistical analysis, interpretation of data, writing and editing the manuscript. A.A.A.; Participated in study design, obtaining funding, technical and material support. and statistical analysis. M-A.A.; Participated

in study design, technical and material support. M.H.H.; Supervision and revision of the manuscript. Y.S.; Supervision. S.D.; Participated in data analysis. L.Z.; Contributed in technical support. All authors read and approved the final version of the manuscript.

References

- Dalic L, Cook MJ. Managing drug-resistant epilepsy: challenges and solutions. *Neuropsychiatr Dis Treat*. 2016; 12: 2605-2616.
- Erdoğan F, Göğeli A, Arman F, Ersoy AO. The effects of pentylenetetrazole-induced status epilepticus on behavior, emotional memory, and learning in rats. *Epilepsy Behav*. 2004; 5(3): 388-393.
- Tröster AI, Meador KJ, Irwin CP, Fisher RS; SANTE Study Group. Memory and mood outcomes after anterior thalamic stimulation for refractory partial epilepsy. *Seizure*. 2017; 45: 133-141.
- Laxpati NG, Kasoff WS, Gross RE. Deep brain stimulation for the treatment of epilepsy: circuits, targets, and trials. *Neurotherapeutics*. 2014; 11(3): 508-526.
- Gharib A, Sayyahi Z, Komaki A, Barkley V, Sarihi A, Mirnajafi-Zadeh J. The role of 5-HT1A receptors of hippocampal CA1 region in anticonvulsant effects of low-frequency stimulation in amygdala kindled rats. *Physiol Behav*. 2018; 196: 119-125.
- Mohammad-Zadeh M, Mirnajafi-Zadeh J, Fathollahi Y, Javan M, Jahanshahi A, Noorbakhsh SM, et al. The role of adenosine A(1) receptors in mediating the inhibitory effects of low frequency stimulation of perforant path on kindling acquisition in rats. *Neuroscience*. 2009; 158(4): 1632-1643.
- Namvar S, Fathollahi Y, Javan M, Zeraati M, Mohammad-Zadeh M, Shojaei A, et al. The antiepileptogenic effect of low-frequency stimulation on perforant path kindling involves changes in regulators of G-protein signaling in rat. *J Neurosci*. 2017; 37(5): 450-459.
- Mardani P, Oryan S, Sarihi A, Alaei E, Komaki A, Mirnajafi-Zadeh J. Endocannabinoid CB1 receptors are involved in antiepileptogenic effect of low frequency electrical stimulation during perforant path kindling in rats. *Epilepsy Res*. 2018; 144: 71-81.
- Rohani R, Piryaei A, Jahanshahi A, Sadeghi Y, Mirnajafi-Zadeh J. Effect of low-frequency stimulation on kindling induced changes in rat dentate gyrus: an ultrastructural study. *Acta Neurol Belg*. 2014; 114(1): 47-53.
- Kille KB, Tian N, Durand DM. Low frequency stimulation decreases seizure activity in a mutation model of epilepsy. *Epilepsia*. 2010; 51(9): 1745-1753.
- Goodman JH, Berger RE, Tchong TK. Preemptive low-frequency stimulation decreases the incidence of amygdala-kindled seizures. *Epilepsia*. 2005; 46(1): 1-7.
- Ghafari S, Fathollahi Y, Javan M, Shojaei A, Asgari A, Mirnajafi-Zadeh J. Effect of low frequency stimulation on impaired spontaneous alternation behavior of kindled rats in Y-maze test. *Epilepsy Res*. 2016; 126: 37-44.
- Gharib A, Komaki A, Manoochehri Khoshinani H, Saidijam M, Barkley V, Sarihi A, et al. Intrahippocampal 5-HT1A receptor antagonist inhibits the improving effect of low-frequency stimulation on memory impairment in kindled rats. *Brain Res Bull*. 2019; 148: 109-117.
- Jahanshahi A, Mirnajafi-Zadeh J, Javan M, Mohammad-Zadeh M, Rohani R. The antiepileptogenic effect of electrical stimulation at different low frequencies is accompanied with change in adenosine receptors gene expression in rats. *Epilepsia*. 2009; 50(7): 1768-1779.
- Chen YC, Zhu GY, Wang X, Shi L, Du TT, Liu DF, et al. Anterior thalamic nuclei deep brain stimulation reduces disruption of the blood-brain barrier, albumin extravasation, inflammation and apoptosis in kainic acid-induced epileptic rats. *Neurol Res*. 2017; 39(12): 1103-1113.
- Fiala M, Avagyan H, Merino JJ, Bernas M, Valdivia J, Espinosa-Jefrey A, et al. Chemotactic and mitogenic stimuli of neuronal apoptosis in patients with medically intractable temporal lobe epilepsy. *Pathophysiology*. 2013; 20(1): 59-69.
- Singh N, Saha L, Kumari P, Singh J, Bhatia A, Banerjee D, et al. Effect of dimethyl fumarate on neuroinflammation and apoptosis in pentylenetetrazol kindling model in rats. *Brain Res Bull*. 2019; 144: 233-245.
- Frantz AL, Regner GG, Pflüger P, Coelho VR, da Silva LL, Viau CM, et al. Manual acupuncture improves parameters associated

- with oxidative stress and inflammation in PTZ-induced kindling in mice. *Neurosci Lett*. 2017; 661: 33-40.
19. Musto AE, Rosencrans RF, Walker CP, Bhattacharjee S, Raulji CM, Belayev L, et al. Dysfunctional epileptic neuronal circuits and dysmorphic dendritic spines are mitigated by platelet-activating factor receptor antagonism. *Sci Rep*. 2016; 6: 30298.
 20. Ghotbedin Z, Janahmadi M, Mirnajafi-Zadeh J, Behzadi G, Semnani S. Electrical low frequency stimulation of the kindling site preserves the electrophysiological properties of the rat hippocampal CA1 pyramidal neurons from the destructive effects of amygdala kindling: the basis for a possible promising epilepsy therapy. *Brain Stimul*. 2013; 6(4): 515-523.
 21. Samokhina E, Samokhin A. Neuropathological profile of the pentylenetetrazol (PTZ) kindling model. *Int J Neurosci*. 2018; 128(11): 1086-1096.
 22. Paxinos G, Watson C. *The rat brain in stereotaxic coordinations*. 7th ed. Academic Press; 2013; 472.
 23. Becker A, Grecksch G, Schröder H. N omega-nitro-L-arginine methyl ester interferes with pentylenetetrazol-induced kindling and has no effect on changes in glutamate binding. *Brain Res*. 1995; 688(1-2): 230-232.
 24. Asgari A, Semnani S, Atapour N, Shojaei A, Moradi H, Mirnajafi-Zadeh J. Combined sub-threshold dosages of phenobarbital and low-frequency stimulation effectively reduce seizures in amygdala-kindled rats. *Neurol Sci*. 2014; 35(8): 1255-1260.
 25. Esmaeilpour K, Sheibani V, Shabani M, Mirnajafi-Zadeh J. Effect of low frequency electrical stimulation on seizure-induced short- and long-term impairments in learning and memory in rats. *Physiol Behav*. 2017; 168: 112-121.
 26. Paudel YN, Shaikh MF, Shah S, Kumari Y, Othman I. Role of inflammation in epilepsy and neurobehavioral comorbidities: Implication for therapy. *Eur J Pharmacol*. 2018; 837: 145-155.
 27. Wang ZH, Mong MC, Yang YC, Yin MC. Asiatic acid and maslinic acid attenuated kainic acid-induced seizure through decreasing hippocampal inflammatory and oxidative stress. *Epilepsy Res*. 2018; 139: 28-34.
 28. Młodzikowska-Albrecht J, Steinborn B, Zarowski M. Cytokines, epilepsy and epileptic drugs--is there a mutual influence? *Pharmacol Rep*. 2007; 59(2): 129-138.
 29. Viviani B, Bartesaghi S, Gardoni F, Vezzani A, Behrens MM, Bartfai T, et al. Interleukin-1beta enhances NMDA receptor-mediated intracellular calcium increase through activation of the Src family of kinases. *J Neurosci*. 2003; 23(25): 8692-8700.
 30. Roseti C, van Vliet EA, Cifelli P, Ruffolo G, Baayen JC, Di Castro MA, et al. GABAA currents are decreased by IL-1 β in epileptogenic tissue of patients with temporal lobe epilepsy: implications for ictogenesis. *Neurobiol Dis*. 2015; 82: 311-320.
 31. Chen YC, Shi L, Zhu GY, Wang X, Liu DF, Liu YY, et al. Effects of anterior thalamic nuclei deep brain stimulation on neurogenesis in epileptic and healthy rats. *Brain Res*. 2017; 1672: 65-72.
 32. Thom M. Review: Hippocampal sclerosis in epilepsy: a neuropathology review. *Neuropathol Appl Neurobiol*. 2014; 40(5): 520-543.
 33. Steinhäuser C, Seifert G, Bedner P. Astrocyte dysfunction in temporal lobe epilepsy: K⁺ channels and gap junction coupling. *Glia*. 2012; 60(8): 1192-1202.
 34. Sofroniew MV, Vinters HV. Astrocytes: biology and pathology. *Acta Neuropathol*. 2010; 119(1): 7-35.
 35. Takano T, Oberheim N, Cotrina ML, Nedergaard M. Astrocytes and ischemic injury. *Stroke*. 2009; 40 Suppl 3: S8-S12.
 36. Fenoy AJ, Goetz L, Chabardès S, Xia Y. Deep brain stimulation: are astrocytes a key driver behind the scene? *CNS Neurosci Ther*. 2014; 20(3): 191-201.
 37. Parpura V, Heneka MT, Montana V, Oliet SH, Schousboe A, Haydon PG, et al. Glial cells in (patho)physiology. *J Neurochem*. 2012; 121(1): 4-27.
 38. Leeman-Markowski BA, Schachter SC. Treatment of cognitive deficits in epilepsy. *Neurol Clin*. 2016; 34(1): 183-204.
 39. Rosenblat JD, Cha DS, Mansur RB, McIntyre RS. Inflamed moods: a review of the interactions between inflammation and mood disorders. *Prog Neuropsychopharmacol Biol Psychiatry*. 2014; 53: 23-34.
 40. Orłowski D, Michalis A, Glud AN, Korshøj AR, Fitting LM, Mikkelsen TW, et al. Brain tissue reaction to deep brain stimulation-A longitudinal study of DBS in the goettingen minipig. *Neuromodulation*. 2017; 20(5): 417-423.

Impact of Methyl- β -Cyclodextrin and Apolipoprotein A-I on The Expression of ATP-Binding Cassette Transporter A1 and Cholesterol Depletion in C57BL/6 Mice Astrocytes

Shirin Azizidoost, M.Sc., Hossein Babaahmadi-Rezaei, Ph.D., Zahra Nazari, M.Sc., Maryam Cheraghzadeh, Ph.D.,
Alireza Kheirollah, Ph.D.*

Cellular and Molecular Research Center, Department of Biochemistry, Medical School, Ahvaz Jundishapur University of Medical Sciences, Ahvaz, Iran

*Corresponding Address: P.O.Box: 61357- 15794, Cellular and Molecular Research Center, Department of Biochemistry, Medical School, Ahvaz Jundishapur University of Medical Sciences, Ahvaz, Iran
Email: akheirollah@ajums.ac.ir

Received: 17/July/2019, Accepted: 25/November/2019

Abstract

Objective: Dysregulation of cholesterol metabolism in the brain is responsible for many lipid storage disorders, including Niemann-Pick disease type C (NPC). Here, we have investigated whether cyclodextrin (CD) and apolipoprotein A-I (apoA-I) induce the same signal to inhibit cell cholesterol accumulation by focusing on the main proteins involved in cholesterol homeostasis in response to CD and apoA-I treatment.

Materials and Methods: In this experimental study, astrocytes were treated with apoA-I or CD and then lysed in RIPA buffer. We used Western blot to detect protein levels of 3-hydroxy-3-methyl-glutaryl coenzyme A reductase (HMGCR) and ATP-binding cassette transporter A1 (ABCA1). Cell cholesterol content and cholesterol release in the medium were also measured.

Results: ApoA-I induced a significant increase in ABCA1 and a mild increase in HMGCR protein level, whereas CD caused a significant increase in HMGCR with a significant decrease in ABCA1. Both apoA-I and CD increased cholesterol release in the medium. A mild, but not significant increase, in cell cholesterol content was seen by apoA-I; however, a significant increase in cell cholesterol was detected when the astrocytes were treated with CD.

Conclusion: CD, like apoA-I, depletes cellular cholesterol. This depletion occurs in a different way from apoA-I that is through cholesterol efflux. Depletion of cell cholesterol with CDs led to reduced protein levels of ABCA1 along with increased HMGCR and accumulation of cell cholesterol. This suggested that CDs, unlike apoA-I, could impair the balance between cholesterol synthesis and release, and interfere with cellular function that depends on ABCA1.

Keywords: ATP Binding Cassette Transporter 1, Apolipoprotein A-I, Astrocytes, Beta-cyclodextrin, 3-hydroxy-3-methyl-glutaryl Coenzyme A Reductase

Cell Journal(yakhteh), Vol 23, No 1, April-June (Spring) 2021, Pages: 93-98

Citation: Azizidoost Sh, Babaahmadi-Rezaei H, Nazari Z, Cheraghzadeh M, Kheirollah A. Impact of methyl- β -cyclodextrin and apolipoprotein A-I on the expression of ATP-binding cassette transporter A1 and cholesterol depletion in C57BL/6 mice astrocytes. Cell J. 2021; 23(1): 93-98. doi: 10.22074/cellj.2021.7061. This open-access article has been published under the terms of the Creative Commons Attribution Non-Commercial 3.0 (CC BY-NC 3.0).

Introduction

Beta-cyclodextrin (β -CD) is reported to be effective in exit of cholesterol from the plasma membrane (1, 2); however, relatively few studies have investigated its mechanism of action in influencing either *in vivo* or *in vitro* cholesterol metabolism, especially in diseases such as Niemann-Pick disease type C (NPC). A number of candidate proteins involved in cholesterol synthesis/trafficking and efflux have been introduced. In this research, we focused on two proteins of this type, ATP-binding cassette subfamily A member 1 (ABCA1) as the main protein for cholesterol efflux and 3-hydroxy-3-methyl-glutaryl coenzyme A reductase (HMGCR) as an important and rate limiting enzyme in cholesterol synthesis (3).

There is increasing evidence that deregulation of lipoprotein and/or lipid metabolism is coupled to the progression of neurodegenerative diseases like Alzheimer's disease (AD) and NPC (4, 5). Cholesterol is a primary lipid that regulates brain cell structure and

function during the developmental period and adult life (4). The blood brain barrier (BBB) separates the brain's cholesterol metabolism from the periphery (6); therefore, maintaining the steady-state content of cholesterol in the brain is of particular importance for its physiological function (4). HMGCR acts as a rate-limiting enzyme in cholesterol synthesis and is the primary site of feedback regulation in the biosynthesis of cholesterol (7). ABCA1, a member of the ATP-binding cassette transporters family, is responsible for the majority of cholesterol efflux to deliver cholesterol to an acceptor like apolipoprotein A-I (apoA-I) for high-density lipoprotein (HDL) generation (8). There is abundant evidence that ABCA1-mediated cholesterol efflux to apoA-I can occur at the plasma membrane (9). Thus, the mentioned enzymes are targets of the highly successful blood cholesterol-lowering drugs and their inhibition is a rapid mechanism for switching off the cholesterol synthesis.

Altered brain lipid metabolism, such as cholesterol, has

been implicated in the progression of neurodegenerative diseases like NPC and AD (10). Cholesterol reduction in experimental animal models delays the progression of Alzheimer's pathology. These findings raise the possibility that treating humans with cholesterol lowering medications might reduce the risk of developing AD (11). In other words, it has been reported that the loss of cholesterol shuttling in NPC disease is associated with reduced activity of ABCA1, which is responsible for low HDL cholesterol levels in NPC patients (12).

ApoA-I, a natural cholesterol lowering agent, is one of the main apolipoproteins in the brain. It is an HDL cholesterol transporter that prevents brain cholesterol deposition and holds neuroprotective properties. Decreased serum HDL cholesterol and apoA-I concentration is shown to be highly correlated with AD severity (13). In the human brain, an association has been found between apoA-I with amyloid beta deposits; complexes between apoA-I and amyloid beta can be detected in cerebrospinal fluid (CSF) from AD patients (14).

Cyclodextrins (CDs), namely synthetic cholesterol lowering agents, are a family of cyclic polysaccharide compounds widely used to bind cholesterol. The use of CDs, in particular β -CDs, is increasing in biomedical research because they are able to interact with cell membranes and are known to extract cholesterol and other lipids from these membranes (15). β -CD is a biologically active molecule, and studies have shown that β -CD and its derivatives significantly reduce intracellular cholesterol levels in NPC mutants (16). CDs may also be useful for AD because of intriguing parallels between NPC1 and AD, including neurofibrillary tangles and prominent lysosome system dysfunction (17).

β -CD has been reported to play a role in cholesterol exit from the plasma membrane (1) but relatively few studies have dealt with its mechanism of action to influence *in vivo* or *in vitro* cholesterol metabolism, especially in certain diseases such as NPC (18, 19). There are a number of candidate proteins implicated in cholesterol synthesis/trafficking and efflux. Here we focused on two of them: ABCA1, as the main protein of cholesterol efflux, and HMGCR as an essential rate-limiting enzyme in cholesterol synthesis. In the present study, we used a cell culture model to elucidate and compare the mechanism of CD-mediated cholesterol depletion with apoA-I mediated cholesterol efflux from astrocytes through investigating the protein expressions of ABCA1 and HMGCR.

Materials and Methods

Materials

Beta-cyclodextrin (C4805) and a cholesterol quantitation kit (MAK043-1KT) were purchased from Sigma-Aldrich (USA). Dulbecco's Modified Eagle's Medium (DMEM; low glucose) and 0.25% trypsin-EDTA were obtained from Bio-Idea (Iran). Mouse anti-ABCA1 monoclonal antibody (cat. no. HJ1) was obtained from Invitrogen (USA), and rabbit anti-HMGCR monoclonal antibody

(cat. no.174830) and rabbit anti-GAPDH antibody (Cat. no. 181603) were purchased from Abcam (USA). ApoA-I was a generous gift from Dr. JI. Ito (Biochemistry Dept., Nagoya City University Graduate School of Medical Sciences, Nagoya, Japan). Fetal bovine serum bovine serum (FBS) and penicillin/streptomycin were purchased from Gibco (USA). Hexane and isopropanol were obtained from Merck (Germany).

Primary isolation and culture of astrocytes

In this experimental study, 18 mice were housed in a temperature-controlled room ($24 \pm 1^\circ\text{C}$) under 12 hours light/dark conditions with free access to food and water. The mice were fed with a standard commercial chow diet and water for a week to stabilize their metabolic condition. The animal procedures were in accordance with the guidelines for animal care prepared by the Committee on Care and Use of Laboratory Animal Resources, National Research Council (USA), and approved by the Institute of Animal Ethics Committee (IAEC) in Ahvaz Jundishapur University of Medical Sciences (AJUMS) for the Purpose of Control and Supervision of Experiments on Animals (IR.AJUMS.REC.1395.637). Astrocytes were isolated from P0 C57BL/6J wild-type mice based on a previously described protocol (20). Briefly, after brain dissection and removal of the meninges, the minced brain pieces were incubated with 0.1% trypsin solution in Dulbecco's phosphate-buffered saline (DPBS) for 3 minutes at 37°C to obtain single cells. The cell suspension was centrifuged at 1000 rpm for 1 minute and the cell pellet was cultured in DMEM, low glucose + 10% FBS + 1% penicillin/streptomycin for one week for the primary culture and a subsequent week for the secondary culture (21).

Experimental design and treatment

Astrocytes were plated at a density of 3×10^6 in DMEM/10% FBS medium, incubated at 37°C and 5% CO_2 , and allowed to adhere. Astrocytes that were 75% confluent were treated with 5 $\mu\text{g/ml}$ apoA-I or 5 μM beta-cyclodextrin for 24 hours. Vehicle-treated cells were used as the control dish.

Immunoblotting

An equal amount of proteins (150 μg protein/lane) in the cell lysate were separated by 10% sodium dodecyl sulphate-polyacrylamide gel electrophoresis (SDS-PAGE) and then transferred to a polyvinylidene difluoride membrane. Bands of HMGCR and ABCA1 were detected after overnight immunostaining of the membrane with specific primary antibodies against HMGCR (1:5000 dilution, Abcam) and ABCA1 (1:2000 dilution, Invitrogen), followed by a subsequent incubation for 2 hours with the corresponding HRP-conjugated anti-IgG (1:4000 dilution, Sigma) as secondary antibodies. Rabbit anti-GAPDH (1:4000 dilution, Abcam) was used as an internal control for equal loading, and immunoreactive proteins were quantified with enhanced chemiluminescence (ECL) reagent followed by densitometric analysis with ImageJ software.

Extraction of lipid from astrocytes

To determine the cellular cholesterol content, the culture medium was removed and the cells were washed with DPBS. Next, the cell plates were dried with a dryer. We added 1.5 ml of hexane: isopropanol (3:2) solution to each culture plate to extract lipids by shaking the samples for 1.5 hours at room temperature. Then, the supernatant was transferred to a tube and this step was repeated with the same volume of hexane: isopropanol (3:2) for another hour. After evaporating the organic solvent in a 40°C water bath under nitrogen gas, the dried lipids were dissolved in 200 µl cholesterol assay buffer and vortexed until the mixture was homogenized and stored at -20°C for further cholesterol assay.

Cholesterol assay in cell and conditioned media

We determined the cholesterol content of the astrocytes and conditioned media based on the protocol presented in the Sigma cholesterol quantitation kit (MAK043-1KT). Briefly, a set of cholesterol standards were prepared by diluting 2 µg/µl stock solution of standard cholesterol provided with the kit. Reaction mixtures were set up according to the kit's protocol and the absorbance of samples was measured at 570 nm. All samples and standards were run in triplicate and the cholesterol content of the samples was determined from a standard curve.

Statistical analysis

Statistical analysis of this experimental study was performed with SPSS (version 18) software. Descriptive statistics presented data as mean ± SD and analysis of variance (ANOVA) was used to check significant differences between groups in the results from Western blotting analysis. In all triplicate experiments, significant differences were noted at * $P \leq 0.05$ and ** $P \leq 0.01$.

Results

Characterization of astrocytes

In the previous study, astrocytes isolated by the same method were characterized immunohistochemically with specific anti-glial fibrillary acidic protein (GFAP) antibody. The results showed that the cellular population contained 95% GFAP-positive cells, which are a marker for astrocyte characterization (20, 21). No morphology changes were detected before and after treatment (Fig. S1). (See Supplementary Online Information at www.celljournal.org).

Effects of apolipoprotein A-I and beta-cyclodextrin on protein levels of 3-hydroxy-3-methyl-glutaryl coenzyme A reductase

In order to check the effect of apoA-I and β-CD on the protein level of HMGCR, which is the main rate-limiting enzyme involved in cholesterol synthesis,

we treated the cultured astrocytes with 5 µg/ml of apoA-I or 5 µM of β-CD for 24 hours. Once the cells were harvested, cell lysates were subjected to SDS-PAGE and HMGCR was detected by western blot. As indicated in Figure 1, both apoA-I and β-CD increased the protein level of HMGCR, which was only significant for β-CD treatment with a 51% increase in comparison to the control group (Fig.1).

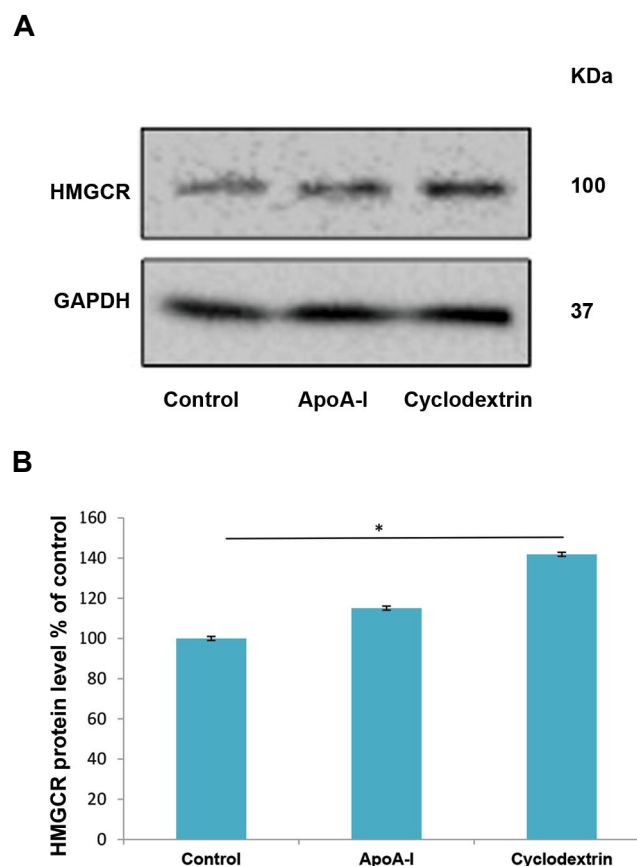


Fig.1: Effects of apoA-I and β-CD on HMGCR protein levels in a primary culture of astrocytes. Mouse astrocytes were incubated with 5 µg/ml of apoA-I and 5 µM of β-CD. After 24 hours of incubation, the cells were harvested with RIPA buffer. **A.** Then, 150 µg/lane of cell lysate was subjected to SDS-PAGE and western blot analysis against the HMGCR antibody. **B.** The bands were scanned and normalized with β-actin as an internal control. Data were analysed with SPSS and represent mean ± SD of triplicate samples. * $P < 0.05$ indicates statistical significance. apoA-I; Apolipoprotein A-I, β-CD; Beta-cyclodextrin, HMGCR; 3-hydroxy-3-methylglutaryl coenzyme A reductase, and SDS-PAGE; Sodium dodecyl sulphatepolyacrylamide gel electrophoresis.

Effect of apolipoprotein A-I and beta-cyclodextrin on protein levels of ATP-binding cassette transporter A1

We sought to investigate the effects of β-CD and apoA-I on protein level of ABCA1 as the main protein involved in cholesterol efflux. Cultured astrocytes were treated with 5 µg/ml of apoA-I or 5 µM of β-CD for 24 hours. Following cell lysis, the lysates were loaded into SDS-PAGE and the protein level of ABCA1 was analysed by western blot. We found a significant increase in the ABCA1 protein (52%) after apoA-I treatment. However, β-CD significantly down

regulated the protein level of ABCA1 compared with the control group (Fig.2).

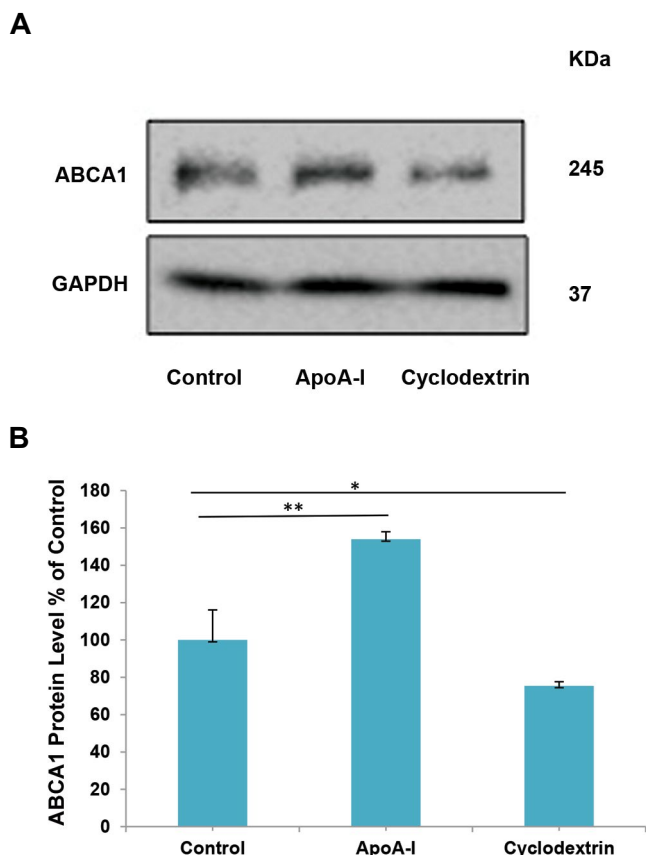


Fig.2: Effect of apoA-I and β -CD on protein level of ABCA1 in primary culture of astrocytes. Mouse astrocytes were incubated with 5 μ g/ml of apoA-I and 5 μ M of β -CD. After 24 hours of incubation, the cells were harvested with RIPA buffer and **A**. 150 μ g/lane of cell lysate was subjected to SDS-PAGE and Western blot analysis against the ABCA1 antibody. **B**. The bands were scanned and normalized with β -actin as an internal control. Data were analysed with SPSS and represent mean \pm SD of the triplicate samples. * P <0.05 indicates statistical significance. apoA-I; Apolipoprotein A-I, β -CD; Beta-cyclodextrin, ABCA1; ATP-binding cassette transporter A1, SDS-PAGE; Sodium dodecyl sulphate-polyacrylamide gel electrophoresis.

Cholesterol content in the cell and conditioned medium

To determine the effect of apoA-I and β -CD on cholesterol release in conditioned medium and on cellular cholesterol content, a quantitative cholesterol kit (Sigma) was used following treatment with 5 μ g/ml of apoA-I or 5 μ M of β -CD for 24 hours. Cholesterol from both cells and media were extracted and further measured based on the protocol provided in the Sigma quantitative kit for the three experimental groups. Figure 3A shows a significant increase of approximately 66% in cholesterol level in the conditioned medium when the astrocytes were treated with apoA-I. β -CD increased cholesterol release to approximately 24%; however, it was still significant.

Our western blot data showed a significant increase in HMGCR after the astrocytes were treated with either apoA-I or β -CD. We checked to see if the HMGCR enhancement caused an abundance of cholesterol by

assessing the cell cholesterol content in the treated astrocytes. Results shown in Figure 3B indicated an increase in cell cholesterol level by both apoA-I (about 15%) and β -CD (about 33%) in astrocytes compared with the control group. However, this increase was significant for β -CD, but not apoA-I (Fig.3B).

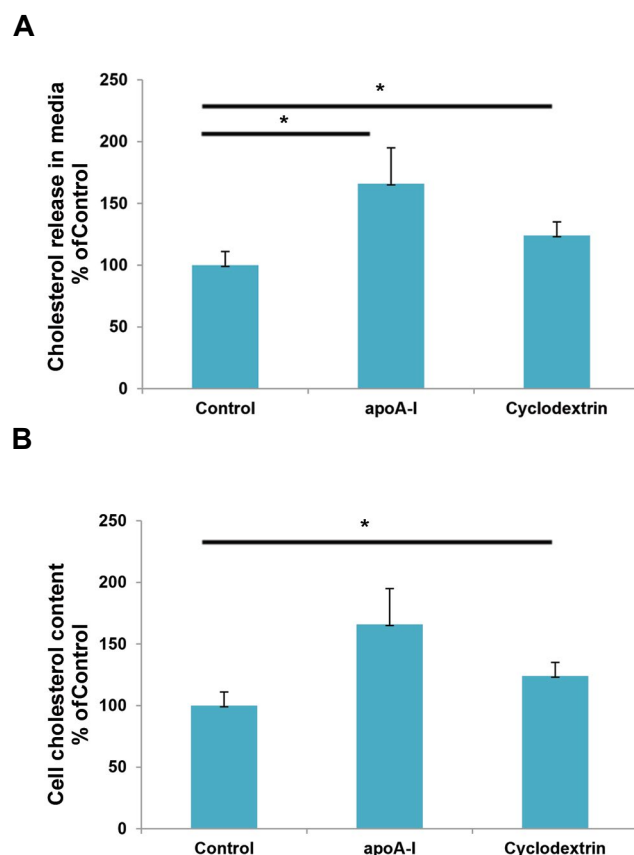


Fig.3: Effect of apoA-I and β -CD on the cell cholesterol content and cholesterol release in the media of astrocytes. Astrocyte-isolated newborn mice were incubated in the presence or absence of 5 μ g/ml of apoA-I and 5 μ M of β -CD. After 24 hours of incubation, **A**. we measured cholesterol release in the media and **B**. the cell cholesterol content according to the protocol in the Sigma cholesterol quantitation kit. Data were analysed with the student's t-test and represent mean \pm SD of triplicate samples. * P <0.05 and ** P <0.01 indicate statistical significance. apoA-I; Apolipoprotein A-I, β -CD; Beta-cyclodextrin.

Discussion

Abnormal accumulation of intracellular cholesterol results from impaired cholesterol trafficking/efflux (22). In healthy cells there are pathways involved in cholesterol delivery to the extracellular acceptors like apoA-I to provide a balance between cholesterol synthesis, trafficking, and efflux. This process regulates the cell cholesterol content and is mediated by many proteins, including HMGCR and ABCA1 as the two pivotal members of cholesterol homeostasis (7, 8). β -CD has been reported to be effective in regulating cholesterol metabolism (23), but relatively few studies have investigated its mechanism of action to influence *in vivo* or *in vitro* cholesterol metabolism, especially in the brain (24). The present study was carried out to investigate

the effects of apoA-I, as a natural and well-established signal inducer for cell cholesterol homeostasis, and β -CD, as a cholesterol-lowering synthetic reagent, on protein levels of HMGCR and ABCA1 as a possible regulatory mechanism for cellular cholesterol depletion.

Based on many reports, it is worth noting that apoA-I signalling activates the entire cholesterol metabolic cycle in astrocytes through promotion of cholesterol synthesis/trafficking, and its subsequent efflux in order to inhibit cellular cholesterol accumulation. Here, we first checked the apoA-I signalling on protein level of ABCA1, HMGCR, and on cell cholesterol content and release.

Our data showed that the ABCA1 protein level was significantly increased. There was a mild increase in HMGCR observed in astrocytes treated with apoA-I. Consistent with this finding, several studies have shown that apoA-I initially interacts with ABCA1 to generate HDL through promotion of cholesterol efflux (8). This interaction is believed to subsequently contribute to an increase in cellular content of ABCA1, suggesting the effect of apoA-I on stability of ABCA1 protein levels, which is in line with our results. HMGCR, along with cell cholesterol content and release were up regulated by apoA-I treatment, which suggested that the entire cell cholesterol pathway was under the control of apoA-I signalling in astrocytes. Astrocytes are the most abundant and supporting cells in the central nervous system (CNS). They should provide enough cholesterol to deliver cholesterol in the form of HDL cholesterol to the neurons (25). These results supported the findings of Ito et al. who reported increased synthesis of cholesterol and phospholipids in rat astrocytes after apoA-I treatment (26).

β -CD, like apoA-I, is an acceptor for excess cell cholesterol (27); therefore, it is believed to be used as a cholesterol-lowering medicine in some neurodegenerative disease such as NPC to reduce cell overload cholesterol (19). Unlike the apoA-I effect, we observed an increased level of HMGCR and a decreased ABCA1 protein level in comparison to the control group in astrocytes treated with β -CD. In support of our findings, Coisne et al. reported a significant decrease of ABCA1 protein level in β -CD-treated bovine smooth muscle cells (24). Also, compared to apoA-I and in agreement with our western blot data, we observed a reduction in cholesterol release in conditioned media of astrocytes-treated with β -CD. This confirmed that ABCA1, which is the main protein responsible for cholesterol release, is affected by β -CD treatment.

In contrast to the report showing that CD treatment blocked cholesterol efflux (28), our data demonstrated that CD, which is the cholesterol acceptor, significantly increased cholesterol secretion in conditioned media. β -CD could possibly deplete cholesterol just from plasma membrane because at the same time the cell cholesterol content is increased. Depletion of cholesterol from the plasma membrane may induce a positive feedback to increase HMGCR protein expression, and result in increased cholesterol synthesis.

Overall, apoA-I regulates not only cholesterol efflux but also intracellular cholesterol trafficking and regulates all elements in cholesterol metabolism. However, due to the accumulation of cellular cholesterol, CD only releases cholesterol from the plasma membrane and does not support intracellular cholesterol trafficking. We have suggested that this regulation may be due to the decreased protein level of ABCA1 after CD treatment.

Since ABCA1 is involved in a variety of cell functions, its protein levels are tightly controlled by transcriptional and post-translational regulatory pathways (29). The cell cholesterol content in particular has a regulatory effect on ABCA1 abundance through the post-translational regulatory pathways. Although both apoA-I and β -CD are cholesterol acceptors that can deplete cell cholesterol (30) and increase cholesterol secretion in conditioned media, they have a different effect on ABCA1 abundance. Our findings suggest that, unlike apoA-I, β -CD lacks the ability to stabilize ABCA1, a crucial mediator of cholesterol efflux. Thus, it is likely that the action of β -CD inhibits ABCA1 signalling pathways, including cholesterol efflux, which results in abnormal cholesterol accumulation with long-term exposure. (31).

Conclusion

Our study provides new evidence that β -CD, like apoA-I, can increase the HMGCR protein. Unlike apoA-I, it can reduce ABCA1, which may interfere with many cell functions and signalling that originate from ABCA1. Our findings are of great importance in the understanding of cellular events related to β -CD treatment. Further studies are necessary to clarify all unrecognized aspects of using CDs in treating neurodegenerative disorders like NPC and AD.

Acknowledgements

We wish to thank all of our colleagues at the Cellular and Molecular Research Center of Ahvaz Jundishapur University of Medical Sciences. This work is part of a PhD thesis and was supported financially by the Vice Chancellor for Research Affairs, Cellular and Molecular Research Center of Ahvaz Jundishapur University of Medical Sciences under grant reg. no. CMRC-9516. There is no conflict of interest in this study.

Authors' Contributions

A.Kh., H.B-R.; Contributed to the conception and study design. Sh.A.; Helped with the manuscript preparation and contributed to all experimental work and animal care. Z.N., M.Ch.; Were involved in data analysis and manuscript revision. All authors read and approved the final manuscript.

References

1. Zidovetzki R, Levitan I. Use of cyclodextrins to manipulate plasma membrane cholesterol content: evidence, misconceptions and control strategies. *Biochim Biophys Acta*. 2007; 1768(6): 1311-1324.
2. Simons M, Keller P, De Strooper B, Beyreuther K, Dotti CG, Si-

- mons K. Cholesterol depletion inhibits the generation of β -amyloid in hippocampal neurons. *Proc Natl Acad Sci U S A*. 1998; 95(11): 6460-6464.
3. Röhrl C, Stangl H. Cholesterol metabolism—physiological regulation and pathophysiological deregulation by the endoplasmic reticulum. *Wien Med Wochenschr*. 2018; 168(11-12): 280-285.
 4. Zhang J, Liu Q. Cholesterol metabolism and homeostasis in the brain. *Protein Cell*. 2015; 6(4): 254-264.
 5. Vance JE. Lipid imbalance in the neurological disorder, Niemann-Pick C disease. *FEBS Lett*. 2006; 580(23): 5518-5524.
 6. Jeske DJ, Dietschy JM. Regulation of rates of cholesterol synthesis in vivo in the liver and carcass of the rat measured using [3 H] water. *J Lipid Res*. 1980; 21(3): 364-376.
 7. DeBose-Boyd RA. Feedback regulation of cholesterol synthesis: sterol-accelerated ubiquitination and degradation of HMG CoA reductase. *Cell Res*. 2008; 18(6): 609-621.
 8. Lee JY, Parks JS. ATP-binding cassette transporter A1 and its role in HDL formation. *Curr Opin Lipidol*. 2005; 16(1): 19-25.
 9. Denis M, Landry YD, Zha X. ATP-binding cassette A1-mediated lipidation of apolipoprotein A1 occurs at the plasma membrane and not in the endocytic compartments. *J Biol Chem*. 2008; 283(23): 16178-16186.
 10. Gamba P, Testa G, Sottero B, Gargiulo S, Poli G, Leonarduzzi G. The link between altered cholesterol metabolism and Alzheimer's disease. *Ann N Y Acad Sci*. 2012; 1259(1): 54-64.
 11. McGuinness B, Passmore P. Can statins prevent or help treat Alzheimer's disease? *J Alzheimers Dis*. 2010; 20(3): 925-933.
 12. Choi HY, Karten B, Chan T, Vance JE, Greer WL, Heidenreich RA, et al. Impaired ABCA1-dependent lipid efflux and hypoalphalipoproteinemia in human Niemann-Pick type C disease. *J Biol Chem*. 2003; 278(35): 32569-32577.
 13. Merched A, Xia Y, Visvikis S, Serot JM, Siest G. Decreased high-density lipoprotein cholesterol and serum apolipoprotein A1 concentrations are highly correlated with the severity of Alzheimer's disease. *Neurobiol Aging*. 2000; 21(1): 27-30.
 14. Slot RE, Van Harten AC, Kester MI, Jongbloed W, Bouwman FH, Teunissen CE, et al. Apolipoprotein A1 in cerebrospinal fluid and plasma and progression to Alzheimer's disease in non-demented elderly. *J Alzheimers Dis*. 2017; 56(2): 687-697.
 15. Kilsdonk EP, Yancey PG, Stoudt GW, Bangerter FW, Johnson WJ, Phillips MC, et al. Cellular cholesterol efflux mediated by cyclodextrins. *J Biol Chem*. 1995; 270(29): 17250-17256.
 16. Singhal A, Szente L, Hildreth JE, Song B. Hydroxypropyl-beta and-gamma cyclodextrins rescue cholesterol accumulation in Niemann-Pick C1 mutant cell via lysosome-associated membrane protein 1. *Cell Death Dis*. 2018; 9(10): 1019.
 17. Nixon RA. Niemann-Pick Type C disease and Alzheimer's disease: the APP-endosome connection fattens up. *Am J Pathol*. 2004; 164(3): 757-761.
 18. Tanaka Y, Yamada Y, Ishitsuka Y, Matsuo M, Shiraishi K, Wada K, et al. Efficacy of 2-hydroxypropyl- β -cyclodextrin in Niemann-Pick disease type C model mice and its pharmacokinetic analysis in a patient with the disease. *Biol Pharm Bull*. 2015; 38(6): 844-851.
 19. Kondo Y, Tokumaru H, Ishitsuka Y, Matsumoto T, Taguchi M, Motoyama K, et al. In vitro evaluation of 2-hydroxyalkylated β -cyclodextrins as potential therapeutic agents for Niemann-Pick Type C disease. *Molecular genetics and metabolism*. 2016; 118(3): 214-219.
 20. Ito Ji, Nagayasu Y, Lu R, Kheirollah A, Hayashi M, Yokoyama S. Astrocytes produce and secrete FGF-1, which promotes the production of apoE-HDL in a manner of autocrine action. *J Lipid Res*. 2005; 46(4): 679-686.
 21. Ueno S, Ito Ji, Nagayasu Y, Furukawa T, Yokoyama S. An acidic fibroblast growth factor-like factor secreted into the brain cell culture medium upregulates apoE synthesis, HDL secretion and cholesterol metabolism in rat astrocytes. *Biochim Biophys Acta*. 2002; 1589(3): 261-272.
 22. Ory D. Niemann-Pick type C: a disorder of cellular cholesterol trafficking. *Biochim Biophys Acta*. 2000; 1529(1-3): 331-339.
 23. Mahammad S, Parmryd I. Cholesterol depletion using methyl- β -cyclodextrin. *Methods Mol Biol*. 2015; 1232: 91-102.
 24. Coisne C, Hallier-Vanuxeem D, Boucau M-C, Hachani J, Tilloy S, Bricout H, et al. β -Cyclodextrins decrease cholesterol release and ABC-associated transporter expression in smooth muscle cells and aortic endothelial cells. *Front Physiol*. 2016; 7: 185.
 25. Pfrieger FW, Ungerer N. Cholesterol metabolism in neurons and astrocytes. *Prog Lipid Res*. 2011; 50(4): 357-371.
 26. Ito Ji, Nagayasu Y, Kato K, Sato R, Yokoyama S. Apolipoprotein A1 induces translocation of cholesterol, phospholipid, and caveolin-1 to cytosol in rat astrocytes. *J Biol Chem*. 2002; 277(10): 7929-7935.
 27. Low H, Hoang A, Sviridov D. Cholesterol efflux assay. *J Vis Exp*; 2012; 61: e3810.
 28. Wang N, Silver DL, Thiele C, Tall AR. ATP-binding cassette transporter A1 (ABCA1) functions as a cholesterol efflux regulatory protein. *J Biol Chem*. 2001; 276(26): 23742-23747.
 29. Camargo F, Erickson RP, Garver WS, Hossain GS, Carbone PN, Heidenreich RA, et al. Cyclodextrins in the treatment of a mouse model of Niemann-Pick C disease. *Life Sci*. 2001; 70(2): 131-142.
 30. Ren B, Jiang B, Hu R, Zhang M, Chen H, Ma J, et al. HP- β -cyclodextrin as an inhibitor of amyloid- β aggregation and toxicity. *Phys Chem Chem Phys*. 2016; 18(30): 20476-20485.
 31. Berry-Kravis E, Chin J, Hoffmann A, Winston A, Stoner R, LaGorio L, et al. Long-term treatment of Niemann-Pick type C1 disease with intrathecal 2-hydroxypropyl- β -cyclodextrin. *Pediatr Neurol*. 2018; 80: 24-34.

Ovulation Induction Changes Epigenetic Marks of Imprinting Genes in Mice Fetus Organs

Anahita Oveisi, M.Sc.^{1,2}, Akbar Vahdati, Ph.D.^{1,2}, Maryam Shahhoseini, Ph.D.^{3,4}, Raha Favaedi, M.Sc.³, Saman Maroufizadeh, Ph.D.⁵, Bahar Movaghar, Ph.D.^{6*}

1. Department of Biology, Fars Science and Research Branch, Islamic Azad University, Fars, Iran

2. Department of Biology, Shiraz Branch, Islamic Azad University, Shiraz, Iran

3. Department of Genetics, Reproductive Biomedicine Research Center, Royan Institute for Reproductive Biomedicine, ACECR, Tehran, Iran

4. Department of Cell and Molecular Biology, School of Biology, College of Science, University of Tehran, Iran

5. School of Nursing and Midwifery, Guilan University of Medical Sciences, Rasht, Iran

6. Department of Embryology, Reproductive Biomedicine Research Center, Royan Institute for Reproductive Biomedicine, ACECR, Tehran, Iran

*Corresponding Address: P.O.Box: 19395-4644, Department of Embryology, Reproductive Biomedicine Research Center, Royan Institute for Reproductive Biomedicine, ACECR, Tehran, Iran
Email: b.movaghar@royaninstitute.org

Received: 16/May/2019, Accepted: 3/November/2019

Abstract

Objective: Genomic imprinting is an epigenetic phenomenon that plays a critical role in normal development of embryo. Using exogenous hormones during assisted reproductive technology (ART) can change an organism hormonal profile and subsequently affect epigenetic events. Ovarian stimulation changes gene expression and epigenetic pattern of imprinted genes in the organs of mouse fetus.

Materials and Methods: For this experimental study, expression of three imprinted genes *H19*, *Igf2* (Insulin-like growth factor 2) and *Cdkn1c* (Cyclin-dependent kinase inhibitor 1C), which have important roles in development of placenta and embryo, and the epigenetic profile of their regulatory region in some tissues of 19-days-old female fetuses, from female mice subjected to ovarian stimulation, were evaluated by quantitative reverse-transcription PCR (qRT-PCR) and Chromatin immunoprecipitation (ChIP) methods.

Results: *H19* gene was significantly lower in heart ($P<0.05$), liver ($P<0.05$), lung ($P<0.01$), placenta ($P<0.01$) and ovary ($P<0.01$). It was significantly higher in kidney of ovarian stimulation group compared to control fetuses ($P<0.05$). *Igf2* expression was significantly higher in brain ($P<0.05$) and kidney ($P<0.05$), while it was significantly lower in lung of experimental group fetuses in comparison with control fetuses ($P<0.05$). *Cdkn1c* expression was significantly higher in lung ($P<0.05$). It was significantly decreased in placenta of experimental group fetuses rather than the control fetuses ($P<0.05$). Histone modification data and DNA methylation data were in accordance to the gene expression profiles.

Conclusion: Results showed altered gene expressions in line with changes in epigenetic pattern of their promoters in the ovarian stimulation group, compared to normal cycle.

Keywords: Epigenetic, Fetus, Imprinted Gene, Histone Modification, Ovarian Stimulation

Cell Journal (Yakhteh), Vol 23, No 1, April-June (Spring) 2021, Pages: 99-108

Citation: Oveisi A, Vahdati A, Shahhoseini M, Favaedi R, Maroufizadeh S, Movaghar B. Ovulation induction changes epigenetic marks of imprinting genes in mice fetus organs. Cell J. 2021; 23(1): 99-108. doi: 10.22074/cellj.2021.6953.

This open-access article has been published under the terms of the Creative Commons Attribution Non-Commercial 3.0 (CC BY-NC 3.0).

Introduction

During prenatal stages of development, specific parental gene or cluster of genes are widely expressed mono-allelically and termed "imprinted genes" (1). Expression of these genes is down-regulated after birth (1). Although imprinted genes occupied a small subset of the genome, they play critical roles for normal development of organisms (1). *H19*, *Igf2* (Insulin-like growth factor 2) as well as *Cdkn1c* (Cyclin-dependent kinase inhibitor 1C) are the most frequently studied imprinted genes (2). *H19* gene produces a non-coding RNA as a trans-regulator of a group of co-expressed imprinted genes, to control fetal and early postnatal growth in mice (3). One of these co-expressed imprinted genes is *Igf2* gene, which plays major role in promoting embryonic/ placental growth and development (4). Like *Igf2*, *Cdkn1c* is expressed in trophoblast cells. It is a cell cycle inhibitor and a negative regulator of cell proliferation. It is clear that orchestrated regulation of the imprinted genes network promotes and

guarantees normal embryo development (5).

Imprinted genes mainly are regulated by epigenetic mechanisms including DNA methylation, interfering RNAs (including miRNA, piRNA, siRNA) and histone modification to promote normal development of embryo. It has also been shown that some defects in genomic imprinting can cause infertility (6, 7).

The major epigenetic process that is recognized to be associated with imprinted genes in both gametes and developing embryos is DNA methylation (8). It is one of the most studied epigenetic mechanisms that can affect activity of DNA segment and gene expression without changing its sequence. There are three epigenetic mechanisms that control gene expression:

1. DNA methylation is a process in which the methyl group is added to specific dinucleotide CpG sites in the genome. Hypermethylation of these sites in the genome leads to gene suppression, while hypomethylation of

them can cause gene over-expression. Sites of DNA methylation are engaged by various proteins, containing methyl-CpG binding domain (MBD) proteins which recruit enzymatic machinery to create silent chromatin (9). Among them, Methyl CpG binding protein 2 (MeCP2) as a DNA methylation "reader" protein specifically binds to methylated DNA regions and typically can be detected by chromatin immunoprecipitation techniques, as an epigenetic marker for DNA methylation (10). 2. interfering RNAs (including miRNA, piRNA, siRNA), which describes epigenetic and posttranscriptional regulation of transposons and genes (7). 3. histone modification which describes posttranslational modifications altering interaction of the histones with DNA and nuclear proteins (11).

H3K9 (lysine 9 of histone 3) is an important position in the genome, as balance between its acetylation (H3K9ac) and deacetylation can regulate gene expression. H3K9ac and H3K9 trimethylation (H3K9me3) could have critical roles in epigenetic regulation of gene expression. Acetylation of this position causes opening of chromatin and mediating gene transcriptional activity. In contrast, its deacetylation (which is usually simultaneous with methylation) results in gene transcriptional repression. These two situations cause chromatin structure to be accessible or inaccessible for transcription. In addition, "bivalent marks" of H3K4me3 and H3K27me3 (trimethylated lysine 4 and 27 on histone H3) are respectively activating and repressing histone marks that regulate gene expression level (12).

Histone codes like H3K9ac and H3K4me3 cause gene up-regulation and others such as H3K9me2 and H3K27me3 lead to gene repression (11). Some studies have shown a link between transcription of imprinted differentially methylated regions and removal insertion of histone modifications (13).

Patients undergo ovarian stimulation through *in vitro* fertilization (IVF) procedures, using high doses of exogenous gonadotropins, to enable retrieval of multiple oocytes in one cycle and this stimulation may affect oogenesis, oocyte/embryo quality and prenatal outcomes (14).

In vitro studies showed that ovarian stimulation disrupts and delays development of one- or two-cell mouse embryos into blastocysts (15, 16). *In vivo* studies are concordant, indicating that ovarian stimulation delays embryo development (16, 17). Study of Sato et al. in the human and mouse suggest that ovarian stimulation/superovulation can lead to the production of oocytes without correct primary imprint. They demonstrated that the results of studies on human are inconsistent with mouse studies (18).

Ovarian stimulation is the most important cause of multiple pregnancies and consequently low birth weight, increased risk of miscarriage, growth retardation and preterm delivery (14).

Finally, ovarian stimulation has been shown to be the cause for imprinting defects. For example, over-expression of gene *IGF2* with paternal imprinting in the placenta have been correlated with fetal growth restriction in humans (14).

Manipulations in hormonal profile, reproductive system and gametes of organism during assisted reproductive technology (ART) can affect epigenetic events of genome, e.g. genomic imprinting (19). Assessment of the relationships between epigenetics, genomic imprinting and ART offers new perspectives in the understanding of molecular bases of infertility and ART failure. This study focuses on understanding expression changes of the important developmental imprinted genes (*H19*, *Igf2* and *Cdkn1c*) and the epigenetic situation of their regulatory region in a set of tissues from 19-days-old fetuses of mice subjected to ovarian stimulation.

Material and Methods

Ovarian stimulation of naval medical research institute mice and obtaining embryos

In this experimental study, assessment was performed on two groups of 19-days-old fetuses of Naval Medical Research Institute (NMRI) mice (Pasteur Institute, Iran). In the first group, 16 fetuses were collected from uterus of four female mice, subjected to ovarian stimulation before gestation. The second group consisted of the 16 fetuses obtained from female mice with natural pregnancy, as control. Four fetuses were excluded and 12 fetuses were included for gene expression assessments in this study. Female mice were kept in the animal house of Royan Institute (Tehran, Iran) at temperature of 19-23°C and humidity of 40-50%, 12 hours light (6 am- 6 pm) and 12 hours darkness. For growth and maturation of ovarian follicles in 8-weeks-old female mice of the first group, 7.5 IU PMSG (pregnant mare serum gonadotropin) hormone (Folligon; Invert, Belgium) followed 48 hours later by 7.5 IU of hCG (Human chorionic gonadotropin) hormone (Organon, Netherlands) were administered. Female mice of the both groups were mated with NMRI male mice (20). After formation of vaginal plaque (mating indication) females were isolated and sacrificed on the 19th day of pregnancy. The fetuses were obtained, and seven different tissues of each fetus -including brain, lung, heart, liver, kidney, ovary and placenta- were collected. Few parts of tissues were preserved in RNA later (Ambion, USA) reagent at -70°C for future RNA isolation and the rest of tissues were preserved at -70°C for later epigenetic evaluations (20, 21). This study was approved by the Institutional Ethics Committee of Royan Institute (Tehran, Iran) on 2nd July 2014 (code: EC/93/1038).

RNA isolation and quantitative reverse-transcription PCR

RNA isolation and qRT-PCR quantitative reverse transcription PCR (qRT-PCR) were performed on tissues using the RNeasy micro kit (Qiagen, USA) according

manufacture's instruction. Quantification of mRNA levels of imprinted genes (*H19*, *Igf2* and *Cdkn1c*) was performed in duplicates by qRT-PCR on a StepOnePlus Real-Time PCR System (Applied Biosystems Instruments, USA) using SYBR Green master mix (Applied Biosystems). Designed primers are listed in Table 1. Condition of qRT-PCR amplification was 95°C for 10 minutes, followed by 40 cycles of 95°C for 15 seconds and 60°C for 60 seconds. Gene expression data were analyzed using $2^{-\Delta\Delta Ct}$ quantitative method to estimate relative fold change values in comparison with *Gapdh* gene, as an endogenous control [mean \pm SEM, (20)].

Chromatin immunoprecipitation real time polymerase Chain Reaction analysis

Chromatin immunoprecipitated (ChIP) PCR experiments were performed, using a histone ChIP kit according to manufacturer's instruction (Diagenode, Belgium). Briefly, all tissues were suspended in PBS. Then formaldehyde (1% final concentration) was added to the samples and then incubated gently on a shaking platform for 10 minutes at room temperature. In the next step, glycine was added into the samples to reach final concentration of 125 mM to quench the cross-linking reaction of formaldehyde. After washing the samples with PBS, lysis buffer was added and sonicated for 10 minutes (30 "on/30" off; Bioruptor sonication system, Diagenode) to get soluble sheared

chromatin. After 5 minutes centrifugation at 14000 g, the supernatant was divided into six parts (Each part 10 μ l). One part was used as input control, and the other 5 parts were incubated with 1 μ l of anti-H3K9ac, anti-H3K9me2, anti-H3K4me3, anti-H3K27me3 and anti-MeCP2 antibodies (1 μ g/ μ l; Abcam, UK) overnight at 4°C on rotator. Immune complexes were washed three times using 100 μ l ice-cold washing buffer and then incubated on a rotating wheel for 4 minutes at 4°C. Using a magnetic rack the beads were captured and immediately treated with 100 μ l DNA isolation buffer. The recovered DNA from immunoprecipitated fractions and total chromatin input, were quantified by real-time PCR. Data were expressed as fold enrichment of DNA associated with different immunoprecipitated histone modifications. DNA methylation was expressed as relative to a 1/100 dilution of input chromatin. Quantitative real-time PCR was carried out on a step one plus Real-Time PCR System (Applied Biosystems) using SYBR Green PCR master mix (Applied Biosystems) and designed primers (Table 1). The condition was 95°C for 10 minutes; and 40 cycles of 95°C for 15 seconds, 60°C for 45 seconds. Results were normalized to input DNA and expressed as (%) input, which means percentage of enriched DNA associated with immunoprecipitated chromatin [mean \pm SEM, (21)].

Table 1: Primers used in this study

Gene	Primer sequence (5'-3')	Product size (bp)	Location
Primers used in qRT-PCR			
<i>H19</i>	F: GCAGGAATGTTGAAGGAC R: CGGGATGAATGTCTGGCTC	132	NR-001592
<i>Igf2</i>	F: AGTTCTGCTGCTGCTTATTG R: CTACCTGGCTAGTCATTGG	168	NM-010514
<i>Cdkn1c</i>	F: TCCAGCGATACCTTCCCA R: GTCCACCTCCATCCACTG	148	NM-009876
<i>Gapdh</i>	F: GACTTCAACAGCAACTCCCAC R: TCCACCACCTGTTGCTGTA	125	NM-001289726
Primers used in ChIP real time PCR			
<i>H19</i>	F: AAGGGAACGGATGCTACC R: CTGGGATATTGCTGGGAATG	85	Promoter
<i>Igf2</i>	F: GTCACCACTGTATCATTCTGC R: TGCTAACACACGCCTATCC	152	DMR1
<i>Cdkn1c</i>	F: GTTCGCTTGCTCTCAGTC R: CATTATGCTAATCGTGAGGAGG	201	Promoter

Statistical analysis

Data analysis was carried out using IBM SPSS Statistics for Windows, Version 22.0 (IBM Corp., USA). In this study, continuous variables were expressed as mean ± SEM (standard error of mean). An independent t test was used to compare control and ovarian stimulation groups. All statistical tests were two-tailed and a P<0.05 was considered statistically significant.

Results

Alterations of gene expression in ovarian stimulation group

Relative mRNA expression levels of *H19* gene from all tissues except brain showed alteration in the ovarian stimulation group, compared to the control. This gene expression was decreased in lung (1.48 ± 0.41 , $0.23 \pm$

0.16 ; $P<0.01$), heart (0.91 ± 0.23 , 0.25 ± 0.09 ; $P<0.05$), liver (1.21 ± 0.3 , 0.29 ± 0.12 ; $P<0.05$), placenta (1.2 ± 0.21 , 0.31 ± 0.13 ; $P<0.01$) and ovary (1.11 ± 0.22 , 0.12 ± 0.06 ; $P<0.01$) in the 19-days-old fetuses of the ovarian stimulation group compared to the control fetuses, respectively. However, kidney (0.72 ± 0.23 , 2.22 ± 1.19) showed increased levels of *H19* in the experimental group, compared to control ($P<0.05$; Fig.1).

Igf2 gene showed significantly higher levels of expression in brain (1.01 ± 0.25 , 2.22 ± 0.42 ; $P<0.05$) and kidney (0.81 ± 0.29 , 3.21 ± 0.86 ; $P<0.05$). While, it was significantly lower expressed in lung (2.59 ± 0.61 , 0.91 ± 0.51) of ovarian stimulation group, than control fetuses ($P<0.05$; Fig.1).

Cdkn1c showed significant increase in lung (1.33 ± 0.22 , 3.17 ± 0.66 ; $P<0.05$) and significant decrease in placenta (1.24 ± 0.21 , 0.3 ± 0.07 ; $P<0.05$; Fig.1).

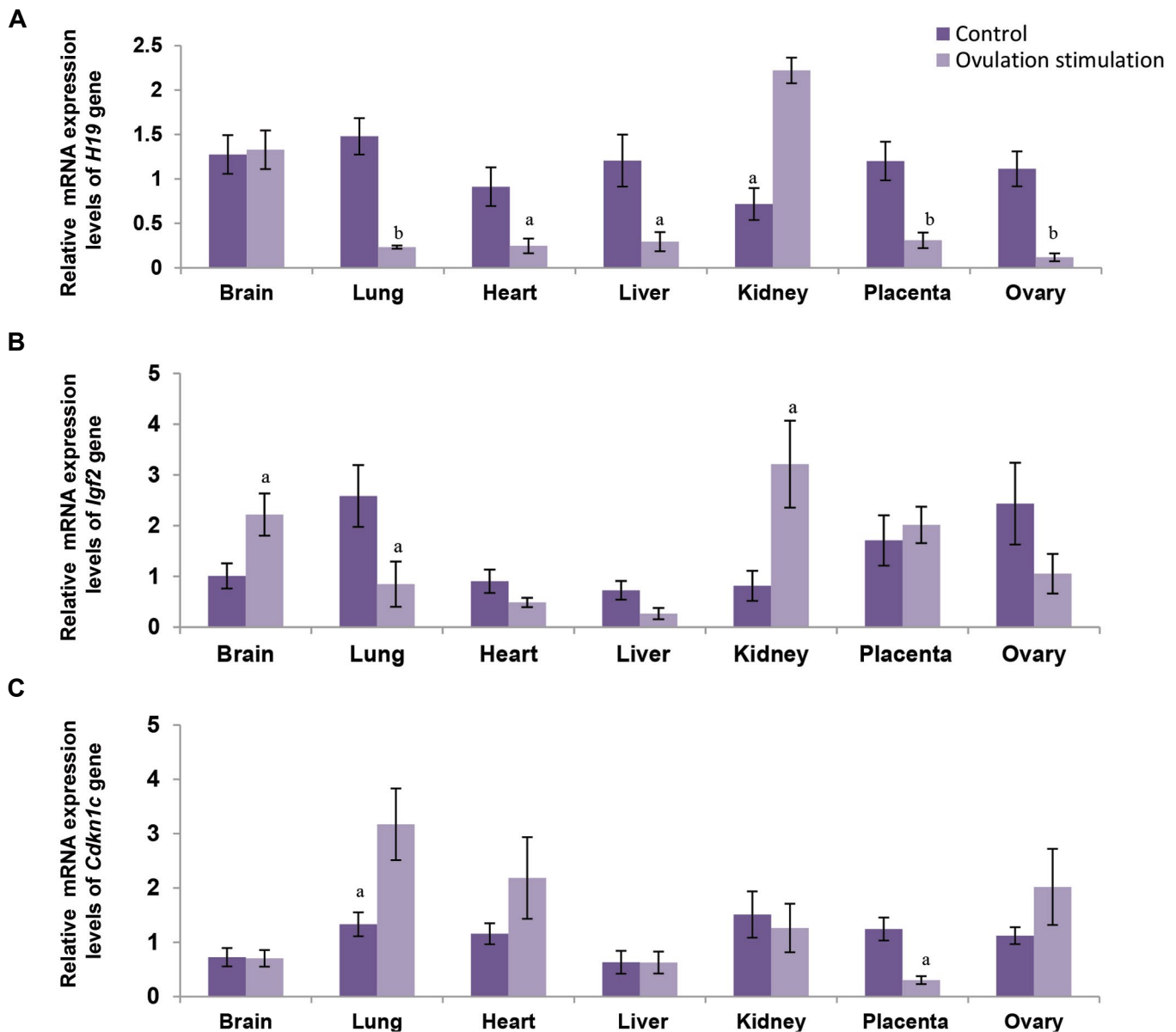


Fig.1: Relative mRNA expression of **A. *H19***, **B. *Igf2***, and **C. *Cdkn1c*** genes in brain, lung, heart, liver, kidney, placenta and ovary of fetuses from ovarian stimulation group (12 fetuses) in comparison with normal cycle fetuses (12 fetuses). Values are expressed as means ± SEM. The letters above the columns show significant difference between control and experimental groups. (a; P<0.05, b; P<0.01).

Histone modification profile of the studied genes in the experimental group embryos

Our histone modification analyses, based on the ChIP data, were in accordance with the gene expression profile. Thus, higher incorporation of H3K9me2 gene repressing mark was detected in the *H19* promoter region of lung ($P<0.05$), heart ($P<0.05$) and ovary ($P<0.05$), while lower incorporation of it was detected in brain ($P<0.05$) and kidney ($P<0.05$) of experimental group fetuses compared to the control fetuses. Higher incorporation of H3K27me3 gene repressing mark was detected in promoter region of *H19* in lung ($P<0.05$), heart ($P<0.05$), placenta ($P<0.05$) and ovary ($P<0.05$), whilst lower incorporation of it was determined in kidney ($P<0.05$) of ovarian stimulation group compared to control. H3K9ac gene activating histone mark was significantly higher in promoter region

of *H19* in brain ($P<0.05$), but it was significantly lower in lung ($P<0.05$), placenta ($P<0.05$) and ovary ($P<0.05$) of experimental group fetuses, rather than controls. H3K4me3 gene activating histone mark was significantly higher in promoter region of *H19* in brain ($P<0.05$) and kidney ($P<0.05$) but its expression was lower in heart ($P<0.05$), placenta ($P<0.05$) and ovary ($P<0.05$) of experimental group fetuses in comparison with control fetuses (Fig.2). CHIP analyses for DNA methylation showed higher incorporation of gene repressing mark of MeCP2, detecting in the promoter region of *H19* in lung ($P<0.05$), heart ($P<0.05$), placenta ($P<0.001$) and ovary ($P<0.05$). At the same time, lower incorporation in brain ($P<0.01$) and kidney ($P<0.05$) of experimental group fetuses was observed, in comparison with control fetuses (Fig.2).

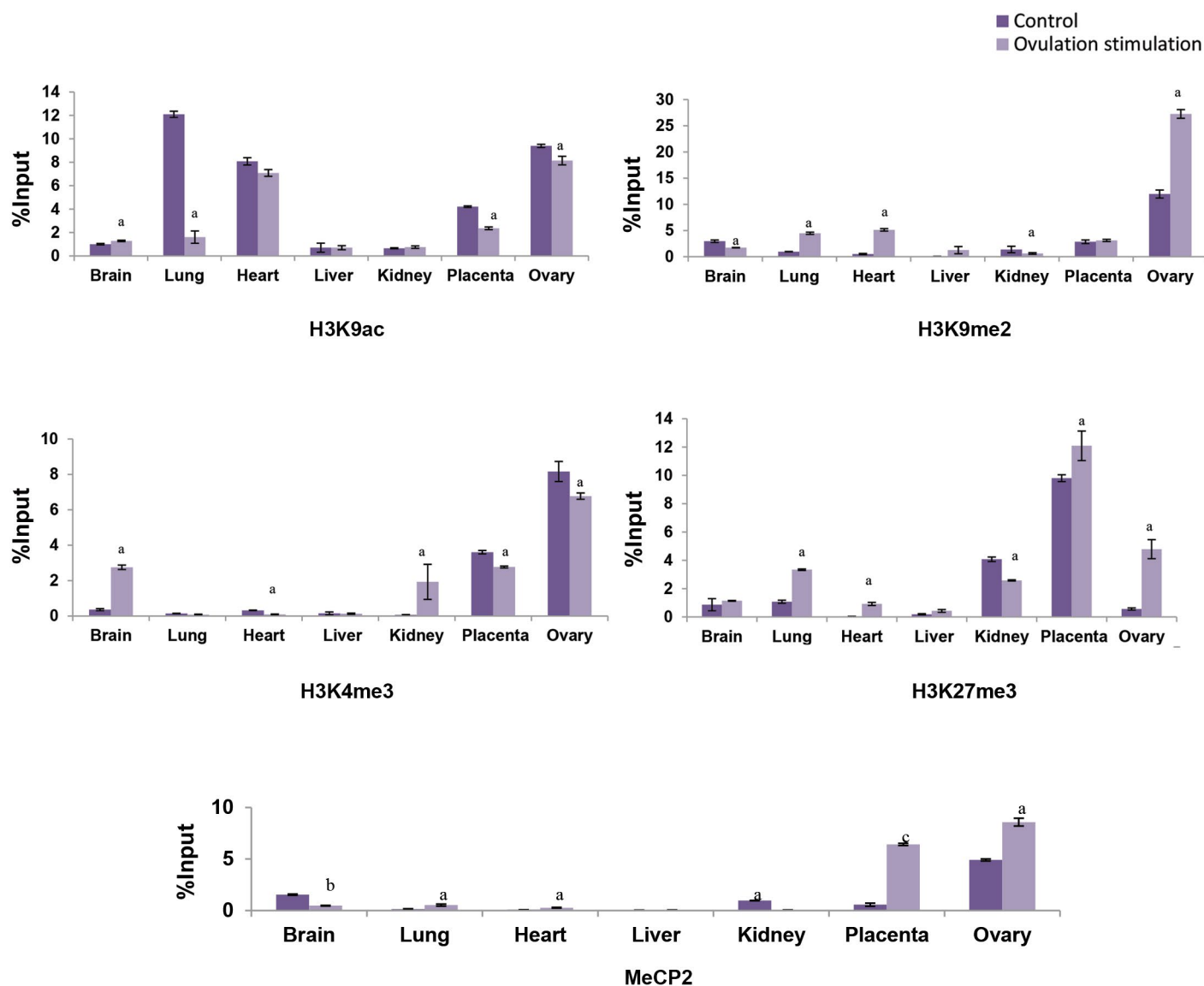


Fig.2: Incorporation of H3K9ac/me2 and H3K4/27me3 histone modifications and MeCP2 in regulatory region of *H19* gene in brain, lung, heart, liver, kidney, placenta and ovary tissues of ovarian stimulation fetuses (12 fetuses) versus control group (12 fetuses). Values are expressed as means \pm SEM. The letters above the columns show significant difference between control and experimental groups. (a; $P<0.05$, b; $P<0.01$, c; $P<0.001$).

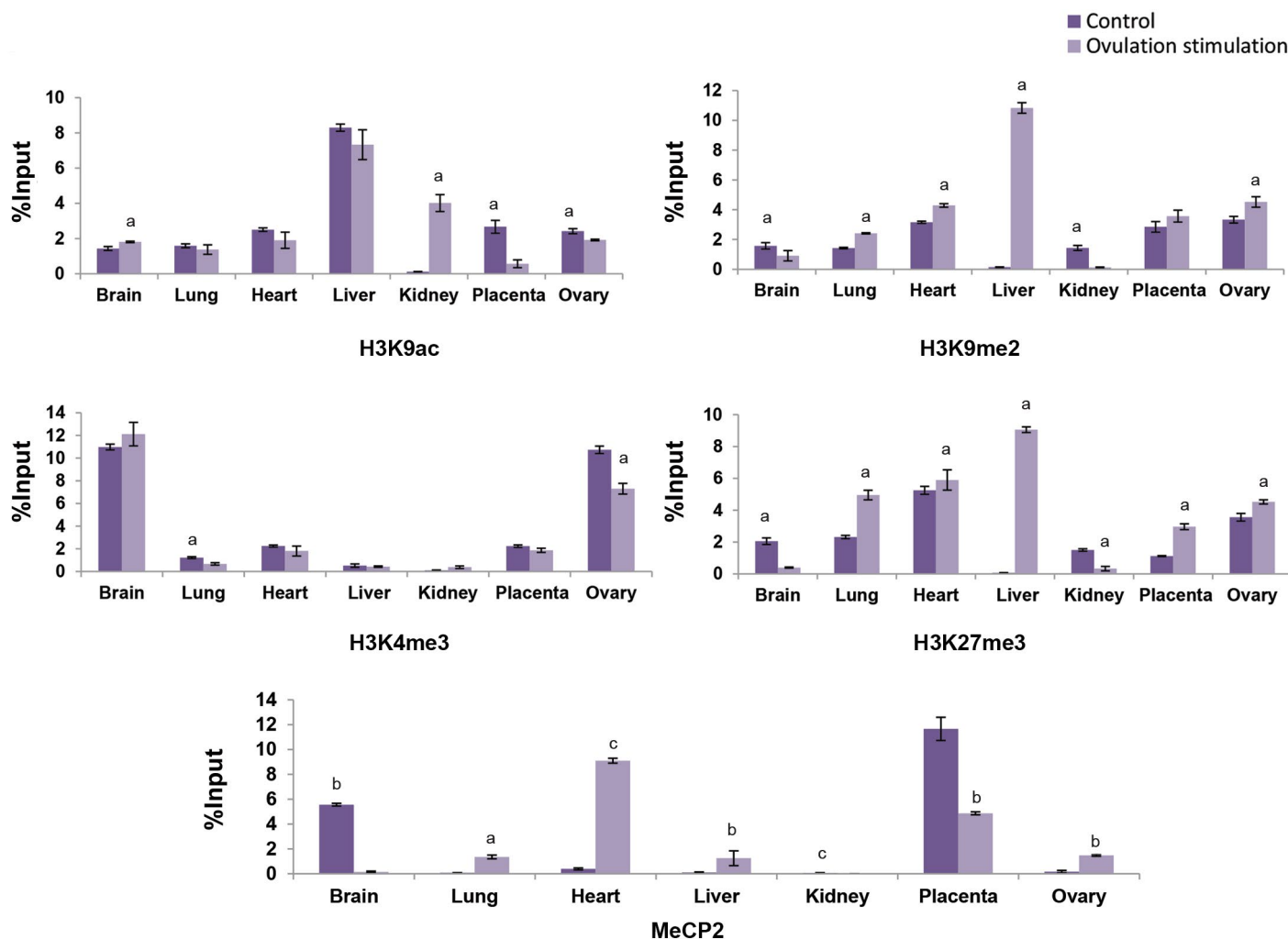


Fig.3: Incorporation of H3K9ac/me2 and H3K4/27me3 histone modifications and MeCP2 in regulatory region of *Igf2* gene in brain, lung, heart, liver, kidney, placenta and ovary tissues of ovarian stimulation fetuses (12 fetuses) versus control group (12 fetuses). Values are expressed as means \pm SEM. The letters above the columns show significant difference between control and experimental groups. (a; $P < 0.05$, b; $P < 0.01$, c; $P < 0.001$).

Higher incorporation of H3K9me2 gene repressing mark was detected in *Igf2* promoter region of lung ($P < 0.05$), heart ($P < 0.05$), liver ($P < 0.05$) and ovary ($P < 0.05$), while lower incorporation was detected in brain ($P < 0.05$) and kidney ($P < 0.05$) of ovarian stimulation group, compared to control. Higher incorporation of H3K27me3 gene repressing mark was detected in promoter region of *Igf2* in lung ($P < 0.05$), heart ($P < 0.05$), liver ($P < 0.05$), placenta ($P < 0.05$) and ovary ($P < 0.05$), but lower incorporation of it in brain ($P < 0.05$) and kidney ($P < 0.05$) of ovarian stimulation group was detected, in comparison with control. H3K9ac gene activating histone mark was significantly higher in the *Igf2* promoter region of brain ($P < 0.05$) and kidney ($P < 0.05$) tissues, but it was significantly lower in placenta ($P < 0.05$) and ovary ($P < 0.05$) of the experimental group fetuses compared to the control fetuses. H3K4me3 gene activating histone mark was significantly lower in the *Igf2* promoter region of lung ($P < 0.05$) and ovary ($P < 0.05$) of the experimental group fetuses than control fetuses. Using ChIP experiment, DNA methylation studies showed higher incorporation of gene repressing mark of MeCP2

in the *Igf2* promoter region of lung ($P < 0.05$), heart ($P < 0.001$), liver ($P < 0.01$) and ovary ($P < 0.01$), while it was lower incorporated in brain ($P < 0.01$), kidney ($P < 0.001$) and placenta ($P < 0.01$) experimental group fetuses, compared to control fetuses (Fig.3).

H3K9me2 gene repressing histone mark was expressed significantly lower in promoter region of *Cdkn1c* in ovary ($P < 0.05$) experimental group fetuses versus the control fetuses. Higher incorporation of H3K27me3 gene repressing mark was detected in promoter region of *Cdkn1c* in kidney ($P < 0.05$) and placenta ($P < 0.05$), but it was significantly lower in ovary ($P < 0.05$) of the experimental group fetuses than the control fetuses. Higher incorporation of H3K9ac gene activating histone mark was detected in the promoter region of *Cdkn1c* in ovary ($p < 0.05$), but it was significantly lower in kidney ($P < 0.05$) and placenta ($P < 0.05$) of the experimental group fetuses versus the control fetuses. H3K4me3 gene activating histone mark was significantly higher in the promoter region of *Cdkn1c* in the ovary ($P < 0.05$) of experimental group fetuses compared to the control fetuses. Analysis

of DNA methylation, using ChIP assay showed higher incorporation of gene repressing mark of MeCP2 in the *Cdkn1c* promoter region of kidney ($P<0.01$) and placenta ($P<0.001$). However, lower incorporation was detected in brain ($P<0.001$), lung ($P<0.001$), heart

($P<0.01$) and liver ($P<0.05$) of experimental group fetuses rather than control fetuses (Fig.4).

There was no significant difference between the fetus weight of ovarian stimulated and control groups, in our study (Table 2).

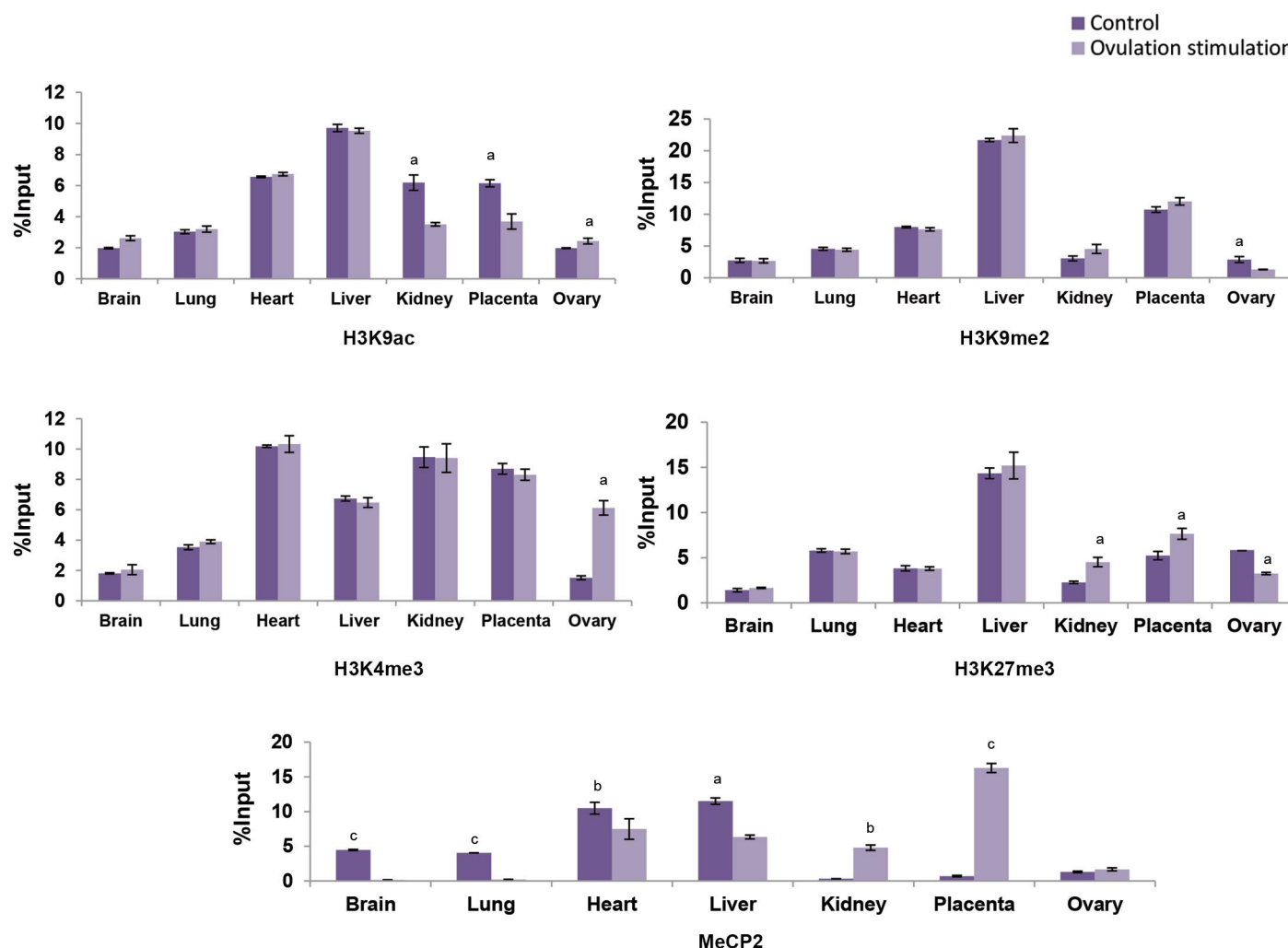


Fig.4: Incorporation of H3K9ac/me2 and H3K4/27me3 histone modifications and MeCP2 in regulatory region of *Cdkn1c* gene in brain, lung, heart, liver, kidney, placenta and ovary tissues of ovarian stimulation fetuses (12 fetuses) versus control group (12 fetuses). Values are expressed as means \pm SEM. The letters above the columns show significant difference between control and experimental groups. (a; $P<0.05$, b; $P<0.01$, c; $P<0.001$).

Table 2: Fetal birth weight in ovarian stimulated and natural cycle mice

Ovulation stimulation group fetuses		Control group fetuses	
Number of fetuses	Average weight of each fetus (g)	Number of fetuses	Average weight of each fetus (g)
79	1.53 \pm 0.1	69	1.66 \pm 0.07

Discussion

Exogenous gonadotropins, used in ART cycles, could have negative effect on gene expression and consequently embryo development and growth (14). Both of the animal and limited human studies showed high possibility of

ovarian stimulation responsibility for modifications in maternal-affected gene products that are later required for imprinting maintenance in developing embryos (18).

Although most ART children do not show any abnormality, some studies have suggested the correlation

between ART and increased incidences of low birth weight and also rare imprinting syndromes, such as Beckwith-Wiedemann syndrome (BWS), Angelman syndrome (AS) and etc. (22, 23).

H19 gene produces a regulatory non-coding micro-RNA that plays a critical role in regulation of imprinted genes network. Previous studies have shown that this gene contributes to growth regulation of fetus and placenta, which controls expression of *Igf2* gene (24). Further, *H19* plays an important role in the development of the pre- and post-natal mice (25, 26). In our study, expressions of *H19* gene in the lung, heart, liver, placenta and ovaries of the experimental fetuses were reduced. Le et al. showed some long lasting disturbances in *H19/Igf2* expression and consequently developmental disturbances of skeletal muscle and liver in mice conceived by IVF (25). So growth defect and weight loss may be a result of *H19* down-regulation. Mono-allelic expression of *H19* in placenta of mice was seen in Fortier et al. study. They demonstrated that may be susceptible to perturbation after ovarian stimulation (27). Reversal *H19* imprinting in human and mouse oocytes upon ovarian stimulation was reported by Sato et al. (18).

Our histone modification analyses based on the ChIP data was in accordance to the gene expression profile; in the way that higher incorporation of gene repressing marks of MeCP2, H3K9me2 and H3K27me3 were detected in promoter region of *H19* in lung, heart and ovary of ovarian stimulation group compared to the controls. In placenta, only MeCP2 and H3K27me3 were increased, but both of the activating marks were decreased. An increasing in the both of activating histone marks in the *H19* regulatory region of brain from the experimental fetuses compared to the control fetuses was seen, but H3K9me repressing mark was decreased. In kidney H3K4me was increased and all repressing marks of this study were decreased in accordance to the up-regulation of this gene.

It is important to note that tissues derived from trophoblast, unlike ICM (inner cell mass) derived tissues, have no control mechanisms through gene expression and they are more susceptible to imprinting disorders. There are two hypotheses. In the first, environment affects more on extra-embryonic cells and this causes loss of imprinting in mid-gestation placentas. In the second, loss of imprinting may also occur in cells destined to form the embryo. Biallelic expression was occasionally observed in the embryo, suggesting mechanisms that safeguard imprinting might be more robust in the embryo, than the placenta. Probably a de novo lineage-restricted wave of methylation occurs in ICM, but not in trophoblast lineages (28). This is consistent with the results of our study which showed extreme changes in gene expression of placenta.

Expression of *Igf2* was higher in brain and kidney of experimental group, compared to control fetuses. It is in accordance to higher levels of H3K9ac and lower levels of H3K9me2, H3K27me3 and MeCP2 in promoter of

this gene from the experimental group fetuses compared to the control fetuses. Decreased gene activating mark (H3K4me3), in accordance with significant increase of repressor marks (H3K9me2, H3K27me3 and MeCP2) in promoter of *Igf2* from the experimental group versus control, can be a reason for down-regulation of this gene in lung of the former group. It is expected that such expression pattern of *Igf2* gene results in developmental changes in brain, kidney and lung postpartum. In a study by Ye et al., expression of *Igf2* in different organs of adult mice was investigated (29). Their study showed that expression in brain and heart is much higher than kidney and liver. However in our study the expression of *Igf2* in brain, kidney, heart and liver was apparently similar in natural cycle fetuses, but higher expression level was seen in lung and ovary. It can be due to the examination of the mouse fetus instead of adult mice.

IGF1, IGF2 and their receptors are expressed in the fetal lung of humans, rodents and other species (30). There are increasing evidences suggesting that the IGF system plays a pivotal role in the development and differentiation of the fetal lung (31). Our study showed decrease in *Igf2* levels after ovarian stimulation in lung. Data were confirmed by histone modification results. Silva et al. showed that deficiency in *Igf2* expression in mice fetuses leads to delayed growth of lung (32). A study of Källén et al. (23) showed higher risk of respiratory problems in IVF-conceived babies (8.5% in IVF babies, compared to 2.99% among all infants born with other ART techniques like Intracytoplasmic sperm injection (ICSI), frozen embryos plus IVF babies) (23). So, expression of *Igf2* in IVF babies with respiratory problems may be disturbed. ICSI born babies had less respiratory problem than IVF born babies. This could be due to the male subfertility in ICSI cases and differences in the treated women of these groups. As it was shown in our study expression of *Igf2* is higher in experimental group kidneys, confirmed by MeCP2 decrease in its regulatory region and DNA methylation. *Igf2* is precisely regulated to ensure monoallelic expression in the most of tissues (33), emphasizing the importance of gene dosage. Normal development requires accurate expression and many disorders can be attributed to an abnormally high dose of *Igf2* caused by loss of imprinting (34).

Occurrence of *Igf2* overexpression as a result of ovarian stimulation could be a reason of why IVF born children suffer from urogenital dysfunction and they need urogenital operations more than natural born children (35).

Some observations have shown that methylation changes can be a highly consistent feature of carcinogenesis and methylation errors are perhaps common observations in cancer (36). Wilms' tumor, a childhood cancer of the kidney, is often associated with defects in the *WT1* gene, which encodes a transcriptional repressor of *Igf2* (37). Wilms' tumor is also associated with mutations in the 11p15.5 region that affect *Igf2* imprinting: altered *Igf2* expression accounts for nearly 50% of all cases of Wilms'

tumor, and *Igf2* loss of imprinting is found in the vast majority (90%) of pathological cases (38).

Low expression of *Cdkn1c* in placenta was confirmed by high levels of MeCP2 and H3K27me3, in addition to low level of H3K9ac in promoter of this gene in ovarian stimulation group versus control. The expression of *Cdkn1c* in the lung of experimental group fetuses was higher than control group. Presence of histone modifications in promoter of *Cdkn1c* gene in lung showed no significant difference between these two groups, however, level of MeCP2 in promoter region of *Cdkn1c* was significantly decreased in the experimental group in comparison with control group. Equal expression of *Cdkn1c* in brain and liver of these two groups was in line with equal level of histone modifications in promoter of this gene. However, MeCP2 showed low level in promoter of *Cdkn1c* from the experimental group in comparison with the control group.

Cdkn1c gene which is involved in development of embryo, encodes a protein that is an inhibitor of cyclic-dependent kinase, cell proliferation and growth. It seems that *Cdkn1c* is a suppressor gene, while disturbance and alteration in its expression in human causes Beckwith-Wiedemann syndrome (39). Previous studies showed that expression level of *Cdkn1c* gene is related to developments of lung and kidney in mouse and human (40). In our study increased expression of *Cdkn1c*, as a growth inhibitor, in lung and its coordination with low expression of *Igf2* (which is involved in lung development) may leads to the limited growth of lung in the experimental group versus the controls. Our findings showed that expression of *H19*, *Igf2* and *Cdkn1c* were changed in lung and kidney following the ovarian stimulation and these changes are related to epigenetic alteration. Our findings indicated that protective mechanisms of ICM may act poorly in the lung and kidney. Additionally, specific mechanisms of transcriptional regulation in each tissue are under influence of the various environmental factors (35). The findings of this study indicated that ovarian stimulation strongly affects these mechanisms in these two organs.

Conclusion

To summarize, the current study showed the impact of ovarian stimulation on the expression of genes and the epigenetic alterations- even at the end of gestation. Occurrence of these long lasting epigenetic changes may be a reason of growth and development disturbances, in future. Although many researchers believe that the fetus is able to eliminate and correct many of the problems created during its development, the present study showed that some of the problems could remain with fetus until birth and they can affect growth of the fetus.

Acknowledgement

This work was supported by the Royan institute for Reproductive Biomedicine (grant number 91000270). The authors would like to thank Royan institute for the financial support of this study. There is no conflict of

interest in the process of this study.

Authors' Contributions

B.M.; Was responsible for overall supervision and provided critical revision of the manuscript. A.O., A.V., M.S., R.F., S.M.; Participated in study design, data collection, evaluation and drafting. All authors read and approved the final manuscript.

References

1. Ferguson-Smith AC. Genomic imprinting: the emergence of an epigenetic paradigm. *Nat Rev Genet.* 2011; 12(8): 565-575.
2. Moore GE, Ishida M, Demetriou C, Al-Olabi L, Leon LJ, Thomas AC, et al. The role and interaction of imprinted genes in human fetal growth. *Philos Trans R Soc Lond B Biol Sci.* 2015; 370(1663): 20140074.
3. Gabory A, Jammes H, Dandolo L. The H19 locus: Role of an imprinted non-coding RNA in growth and development. *Bioessays.* 2010; 32(6): 473-480.
4. Chao W, D'Amore PA. IGF2: epigenetic regulation and role in development and disease. *Cytokine Growth Factor Rev.* 2008; 19(2): 111-120.
5. Algar EM, Deeb GJ, Smith PJ. CDKN1C expression in Beckwith-Wiedemann syndrome patients with allele imbalance. *J Med Genet.* 1999; 36(7): 524-531.
6. Tomizawa S, Sasaki H. Genomic imprinting and its relevance to congenital disease, infertility, molar pregnancy and induced pluripotent stem cell. *J Hum Genet.* 2012; 57(2): 84-91.
7. Wang J, Zhang P, Lu Y, Li Y, Zheng Y, Kan Y, et al. piRBase: a comprehensive database of piRNA sequences. *Nucleic Acids Res.* 2019; 47(D1): D175-D180.
8. Ogunwuyi O, Upadhyay A, Adesina SK, Puri R, Foreman TM, Hauser BR, et al. Genetic imprinting: comparative analysis between plants and mammals. *Plant Tissue Cult Biotechnol.* 2016; 26(2): 267-284.
9. Stirzaker C, Song JZ, Ng W, Du Q, Armstrong NJ, Locke WJ, et al. Methyl-CpG-binding protein MBD2 plays a key role in maintenance and spread of DNA methylation at CpG islands and shores in cancer. *Oncogene.* 2017; 36(10): 1328-1338.
10. Ausió J. MeCP2 and the enigmatic organization of brain chromatin. Implications for depression and cocaine addiction. *Clin Epigenetics.* 2016; 8: 58.
11. Bannister AJ, Kouzarides T. Regulation of chromatin by histone modifications. *Cell Res.* 2011; 21(3): 381-395.
12. Favaedi R, Shahhoseini M, Pakzad M, Mollamohammadi S, Baharvand H. Comparative epigenetic evaluation of human embryonic stem and induced pluripotent cells. *Int J Dev Biol.* 2016; 60(4-6): 103-110.
13. Reddington JP, Perricone SM, Nestor CE, Reichmann J, Youngson NA, Suzuki M, et al. Redistribution of H3K27me3 upon DNA hypomethylation results in de-repression of polycomb target genes. *Genome Biol.* 2013; 14(3): R25.
14. Santos MA, Kuijk EW, Macklon NS. The impact of ovarian stimulation for IVF on the developing embryo. *Reproduction.* 2010; 139(1): 23-34.
15. Velker BAM, Denomme MM, Kraffy RT, Mann MRW. Maintenance of Mest imprinted methylation in blastocyst-stage mouse embryos is less stable than other imprinted loci following superovulation or embryo culture. *Environ Epigenet.* 2017; 3(3): dxv015.
16. Van der Auwera I, D'Hooghe T. Superovulation of female mice delays embryonic and fetal development. *Hum Reprod.* 2001; 16(6): 1237-1243.
17. Teh WT, McBain J, Rogers P. What is the contribution of embryo-endometrial asynchrony to implantation failure? *J Assist Reprod Genet.* 2016; 33(11): 1419-1430.
18. Sato A, Otsu E, Negishi H, Utsunomiya T, Arima T. Aberrant DNA methylation of imprinted loci in superovulated oocytes. *Hum Reprod.* 2007; 22(1): 26-35.
19. Urrego R, Rodriguez-Osorio N, Niemann H. Epigenetic disorders and altered gene expression after use of assisted reproductive technologies in domestic cattle. *Epigenetics.* 2014; 9(6): 803-815.
20. Jahangiri M, Shahhoseini M, Movaghgar B. The effect of vitrification on expression and histone marks of *Igf2* and *Oct4* in blastocysts

- cultured from two-cell mouse embryos. *Cell J.* 2018; 19(4): 607-613.
21. Samadieh Y, Favaedi R, Ramezanali F, Afsharian P, Aflatoonian R, Shahhoseini M. Epigenetic dynamics of HOXA10 gene in infertile women with endometriosis. *Reprod Sci.* 2019; 26(1): 88-96.
 22. Hattori H, Hiura H, Kitamura A, Miyauchi N, Kobayashi N, Takahashi S, et al. Association of four imprinting disorders and ART. *Clin Epigenetics.* 2019; 11(1): 21.
 23. Källén B, Finnström O, Nygren K-G, Olausson PO. In vitro fertilization (IVF) in Sweden: infant outcome after different IVF fertilization methods. *Fertil Steril.* 2005; 84(3): 611-617.
 24. Royo H, Cavaillé J. Non-coding RNAs in imprinted gene clusters. *Biol Cell.* 2008; 100(3): 149-166.
 25. Le F, Wang LY, Wang N, Li L, Le Jun LI, Zheng YM, et al. In vitro fertilization alters growth and expression of Igf2/H19 and their epigenetic mechanisms in the liver and skeletal muscle of newborn and elder mice. *Biol Reprod.* 2013; 88(3): 75.
 26. Pope C, Mishra S, Russell J, Zhou Q, Zhong XB. Targeting H19, an imprinted long non-coding RNA, in hepatic functions and liver diseases. *Diseases.* 2017; 5(1). pii: E11.
 27. Fortier AL, Lopes FL, Trasler JM, Darricarrère N, Martel JM. Superovulation alters the expression of imprinted genes in the midgestation mouse placenta. *Hum Mol Genet.* 2008; 17(11): 1653-1665.
 28. Santos F, Hendrich B, Reik W, Dean W. Dynamic reprogramming of DNA methylation in the early mouse embryo. *Dev Biol.* 2002; 241(1): 172-182.
 29. Ye X, Kohtz A, Pollonini G, Riccio A, Alberini CM. Insulin like growth factor 2 expression in the rat brain both in basal condition and following learning predominantly derives from the maternal allele. *PLoS One.* 2015; 10(10): e0141078.
 30. Retsch-Bogart GZ, Moats-Staats BM, Howard K, D'Ercole AJ, Stiles AD. Cellular localization of messenger RNAs for insulin-like growth factors (IGFs), their receptors and binding proteins during fetal rat lung development. *Am J Respir Cell Mol Biol.* 1996; 14(1): 61-69.
 31. Liu H, Chang L, Rong Z, Zhu H, Zhang Q, Chen H, et al. Association of insulin-like growth factors with lung development in neonatal rats. *J Huazhong Univ Sci Technolog Med Sci.* 2004; 24(2): 162-165.
 32. Silva D, Venihaki M, Guo WH, Lopez MF. Igf2 Deficiency results in delayed lung development at the end of gestation. *Endocrinology.* 2006; 147(12): 5584-5591.
 33. Ohlsson R, Hedborg F, Holmgren L, Walsh C, Ekstrom TJ. Overlapping patterns of IGF2 and H19 expression during human development: biallelic IGF2 expression correlates with a lack of H19 expression. *Development.* 1994; 120(2): 361-368.
 34. Morison IM, Reeve AE. Insulin-like growth factor 2 and overgrowth: molecular biology and clinical implications. *Mol Med Today.* 1998; 4(3): 110-115.
 35. Bernstein BE, Meissner A, Lander ES. The mammalian epigenome. *Cell.* 2007; 128(4): 669-681.
 36. Ehrlich M. DNA hypomethylation in cancer cells. *Epigenomics.* 2009; 1(2): 239-259.
 37. Bae SK, Bae MH, Ahn MY, Son MJ, Lee YM, Bae MK, et al. Egr-1 mediates transcriptional activation of IGFII gene in response to hypoxia. *Cancer Res.* 1999; 59(23): 5989-5994.
 38. Ravenel JD, Broman KW, Perlman EJ, Niemitz EL, Jayawardena TM, Bell DW, et al. Loss of imprinting of insulin-like growth factor-II (IGF2) gene in distinguishing specific biologic subtypes of Wilms tumor. *J Natl Cancer Inst.* 2001; 93(22): 1698-1703.
 39. Diaz-Meyer N, Day CD, Khatod K, Maher ER, Cooper W, Reik W, et al. Silencing of CDKN1C (p57KIP2) is associated with hypomethylation at KvDMR1 in Beckwith-Wiedemann syndrome. *J Med Genet.* 2003; 40(11): 797-801.
 40. Milani D, Pezzani L, Tabano S, Miozzo M. Beckwith–Wiedemann and IMaGe syndromes: two very different diseases caused by mutations on the same gene. *Appl Clin Genet.* 2014; 7: 169-175.

Meiosis Resumption of Immature Human Oocytes following Treatment with Calcium Ionophore *In Vitro*

Elham Fazeli, Ph.D.^{1,2}, Ahmad Hosseini, Ph.D.², Mohammad-Hasan Heidari, Ph.D.^{1,3}, Fattaneh Farifteh-Nobijari, Ph.D.^{3,4}, Mohammad Salehi, Ph.D.^{3,5}, Hojjat-Allah Abbaszadeh, Ph.D.¹, Hamid Nazarian, Ph.D.¹, Zahra Shams Mofarahe, Ph.D.¹, Saman Ayoubi, M.Sc.⁶, Sara Hosseini, Ph.D.³, Mona Shayeghpour, M.Sc.⁴, Mojgan Bandehpour, Ph.D.^{3,5*}, Marefat Ghaffari Novin, Ph.D.^{1,3*}

1. Department of Biology and Anatomical Sciences, School of Medicine, Shahid Beheshti University of Medical Sciences, Tehran, Iran
2. Mehr Fertility Research Center, Guilan University of Medical Sciences, Rasht, Iran
3. Cellular and Molecular Biology Research Center, Shahid Beheshti University of Medical Sciences, Tehran, Iran
4. Genetics and In Vitro Assisted Reproductive (GIVAR) Center, Erfan Hospital, Tehran, Iran
5. Department of Medical Biotechnology, School of Advanced Technologies in Medicine, Shahid Beheshti University of Medical Sciences, Tehran Iran
6. Infertility and Reproductive Health Research Centre, Sara Hospital, Tehran, Iran

*Corresponding Addresses: P.O.Box: 1985717443, Cellular and Molecular Biology Research Centre, Shahid Beheshti University of Medical Sciences, Tehran, Iran

P.O.Box: 1985717443, Department of Biology and Anatomical Sciences, School of Medicine, Shahid Beheshti University of Medical Sciences, Tehran, Iran

Emails: bandehpour@gmail.com, mghaffarin@yahoo.com

Received: 31/August/2019 Accepted: 13/November/2019

Abstract

Objective: *In vitro* maturation (IVM) of human oocytes is used to induce meiosis progression in immature retrieved oocytes. Calcium (Ca²⁺) has a central role in oocyte physiology. Passage through meiosis phase to another phase is controlled by increasing intracellular Ca²⁺. Therefore, the current research was conducted to evaluate the role of calcium ionophore (CI) on human oocyte IVM.

Materials and Methods: In this clinical trial study, immature human oocytes were obtained from 216 intracytoplasmic sperm injection (ICSI) cycles. After ovarian stimulation, germinal vesicle (GV) stage oocytes were collected and categorized into two groups: with and without 10 µM CI treatment. Next, oocyte nuclear maturation was assessed after 24–28 hours of culture. Real-time reverse transcription polymerase chain reaction (RT-PCR) was used to assess the transcript profile of several oocyte maturation-related genes (*MAPK3*, *CCNB1*, *CDK1*, and *cyclin D1 [CCND1]*) and apoptotic-related genes (*BCL-2*, *BAX*, and *Caspase-3*). Oocyte glutathione (GSH) and reactive oxygen species (ROS) levels were assessed using Cell Tracker Blue and 2',7'-dichlorodihydrofluorescein diacetate (H2DCFDA) fluorescent dye staining. Oocyte spindle configuration and chromosome alignment were analysed by immunocytochemistry.

Results: The metaphase II (MII) oocyte rate was higher in CI-treated oocytes (73.53%) compared to the control (67.43%) group, but this difference was not statistically significant (P=0.13). The mRNA expression profile of oocyte maturation-related genes (*MAPK3*, *CCNB1*, *CDK1*, and *CCND1*) (P<0.05) and the anti-apoptotic *BCL-2* gene was remarkably up-regulated after treatment with CI (P=0.001). The pro-apoptotic *BAX* and *Caspase-3* relative expression levels did not change significantly. The CI-treated oocyte cytoplasm had significantly higher GSH and lower ROS (P<0.05). There was no statistically significant difference in meiotic spindle assembly and chromosome alignment between CI treatment and the control group oocytes.

Conclusions: The finding of the current study supports the role of CI in meiosis resumption of human oocytes. (Registration Number: IRCT20140707018381N4)

Keywords: Calcium Ionophores, *In Vitro* Oocyte Maturation Techniques, Maturation-Promoting Factor, Meiotic Spindle, Mitogen-Activated Protein Kinase

Cell Journal (Yakhteh), Vol 23, No 1, April-June (Spring) 2021, Pages: 109–118

Citation: Fazeli E, Hosseini A, Heidari MH, Farifteh-Nobijari F, Salehi M, Abbaszadeh HA, Nazarian H, Shams Mofarahe Z, Ayoubi S, Hosseini S, Shayeghpour M, Bandehpour M, Ghaffari Novin M. Meiosis resumption of immature human oocytes following treatment with calcium ionophore in vitro. Cell J. 2021; 23(1): 109-118. doi: 10.22074/cellj.2021.7130.

This open-access article has been published under the terms of the Creative Commons Attribution Non-Commercial 3.0 (CC BY-NC 3.0).

Introduction

In vitro maturation (IVM) of human oocytes is a valuable technique in assisted reproductive technology (ART). During the IVM procedure, immature oocytes are retrieved from small antral follicles and then meiosis progression occurs in the laboratory (1).

IVM could be an appropriate alternative in various conditions such as patients who have poor ovarian response to gonadotropin stimulation, high numbers of antral follicles, polycystic ovarian syndrome, egg factor

problems with only germinal vesicle (GV) oocytes in their stimulation cycles, and those who suffer from cancer who intend to cryopreserve their oocytes prior to the onset of cancer treatment (2). However, the developmental potential of oocytes reduces after IVM compared to *in vivo* matured oocytes (2, 3).

The IVM process differs from natural ovulation, in which an oocyte resumes meiosis after the luteinizing hormone (LH) surge. Therefore, IVM changes the usual timeline of cytoplasmic and nuclear maturation processes (2). Many

events occur during oocyte maturation, such as cytoplasmic reorganization, cytoskeletal dynamics, and meiotic resumption, which are essential for regular fertilization and embryonic development (1). The preovulatory LH surge by the activation of a signaling cascade leads to meiosis resumption in the oocyte *in vivo* (4).

Oocyte meiotic progression involves protein phosphorylation pathways that are regulated via cyclin-dependent kinases (CDKs) (5). Maturation-promoting factor (MPF) consists of two subunits, CDK1 and cyclin B, and is a key factor in meiotic resumption (6). MPF activity depends on the availability of cyclin B and phosphorylation status of CDK1 (7). Mitogen-activated protein kinase (MAPK) signalling is involved in the oocyte maturation process (5). In human oocytes, MAPK is inactive in the GV stage oocytes, reaches its highest activity in the metaphase II (MII) stage, and has reduced activity after pronucleus formation (8). MAPK signalling regulates MPF activation, and the MAPK inhibitors block germinal vesicle breakdown (GVBD) in oocytes (6). High cyclic adenosine monophosphate (cAMP) in oocytes promote meiotic arrest until ovulation (7). In the somatic follicular cells, cAMP synthesis is catalysed from ATP by the adenylyl cyclase enzyme and is transferred into the oocyte via gap junctions (5). During oocyte meiotic arrest, high levels of protein kinase A (PKA), a cAMP cell cycle mediator, inhibit the CDK1 subunit of MPF (5, 7). In the *in vivo* study, a preovulatory LH surge starts the meiosis resumption by destructing oocyte-somatic cell communication, preventing cAMP transfer, and it also activates the MAPK cascade in cumulus cells (5). The MAPK signalling cascade, which is known as extracellular signal-regulated kinases (ERK1/2) elevates phosphodiesterase, a cAMP degrading-enzyme activity in the oocyte, and thereby decreases cAMP in the oocyte. cAMP-degrading in the oocyte reduces PKA activity (7). A decrease in PKA activity leads to dephosphorylation of the inhibitory sites of CDK1 and results in MPF activation. Activated MPF phosphorylates histones, lamins, and other cellular components. Subsequently, meiosis is resumed (9).

Glutathione (γ -glutamyl-cysteinyl glycine, GSH) is an intracellular free thiol, which is an essential non-enzymatic antioxidant within cells. GSH levels in the oocyte are an excellent cytoplasmic maturation marker after IVM (10). A critical role of GSH, as an antioxidant, is defending the oocyte against oxidative injuries through decreasing reactive oxygen species (ROS) production in mitochondrial metabolism (11). The oxidative damage status in oocytes is one of the essential markers to assess the health of the oocyte. ROS damage in the oocyte can lead to unexpected apoptosis and subsequent arrest in embryonic development (12).

Reduction in anti-apoptotic factors, such as BCL-2, leads to an elevation in pro-apoptotic factors, including BAX. These apoptotic factors cause oocyte apoptosis (13). The BAX/BCL-2 ratio regulates a cascade of molecular events that determine the cell's fate (survival or apoptosis). Increased BAX/BCL-2 alters mitochondrial membrane polarization and results in cytochrome C influx from mitochondria into the cytosol, which involves

inactivation of the initiator (8 and 9) and effector (3, 6, and 7) caspases in oocytes (14). The BCL-2 protein kinase sites are phosphorylated during the G2 to M transition of the cell cycle. Phosphorylation of Thr-56, Thr-74, and Ser-87 BCL-2 residues inhibit proteasome function and prevent apoptosis. It has been suggested that MAPK and MPF have an essential role in this process (15).

Calcium ionophore (CI) is a fat-soluble molecule that increases cytosolic calcium (Ca^{2+}) by transferring Ca^{2+} from the plasma membrane to the cytoplasm (16). Ca^{2+} signaling is a key factor in the physiology of oocytes from oogenesis to maturation and fertilization. The passage through the meiosis phase to another phase is controlled by cell checkpoints, which act in many species by increasing intracellular Ca^{2+} levels (17). During fertilization, sperm-induced elevation in intracellular Ca^{2+} is necessary for oocyte activation, which is a trigger for transforming an oocyte into an embryo (1). Also, Ca^{2+} changes the activity of specific transcription factors in the nucleus, and these factors affect chromatin structure and, as a result, gene expression (18).

Previous studies have shown the relationship between Ca^{2+} and GVBD. Increasing Ca^{2+} during GVBD can indicate a correlation between intracellular Ca^{2+} and oocyte maturation in different species of mammals (17). Furthermore, it is reported that the duration of Ca^{2+} oscillation increases during oocyte maturation. Oocytes with increases levels of cytosolic Ca^{2+} have higher spontaneous parthenogenetic activation (19).

IVM conditions may influence the oocyte's developmental competence. In general, there is no accepted procedure in infertility clinics for the IVM of oocytes. On the other hand, IVM, as a clinical approach, should be optimized for the future (2). The current study was carried out to clarify the role of CI on IVM of human oocytes.

Materials and Methods

Ethics approval for the current randomized clinical trial study was given by the Ethics Committee at Shahid Beheshti Medical University, Tehran, Iran (IR.SBMU.MSP.REC.1396.416). Participants gave verbal and written consent for study participation. All procedures in this research were in accordance with the ethical guidelines of responsible institutional and national committees that involve human experimentation (IRCT20140707018381N4).

Patients

The oocytes were donated for the current study by the patients of the Genetics and In Vitro Assisted Reproductive (GIVAR) Center at Erfan and Taleghani Hospitals (Tehran, Iran) between October, 2017-November, 2018.

A total of 552 GV oocytes from 216 intracytoplasmic sperm injection (ICSI) procedures were included in the current study. These oocytes were not suitable for the ICSI procedure. All women participants were ≤ 40 years of age (mean: 32.13 ± 4.96 years). Cycles diagnosed as male

factor infertility (n=135), tubal factor infertility (n=70), uterine factor (n=4), and unexplained infertility (n=7) were included in the current study. Women who suffered from polycystic ovarian syndrome, endometriosis, and genetic disorders were excluded from this study.

Ovarian stimulation protocol and oocyte retrieval

Ovarian stimulation was carried out using the long protocol. Briefly, gonadotropin-releasing hormone (GnRH) agonist (Superfact, Aventis Pharma, Germany) was administered on day 21 of the menstrual cycle. rFSH (Gonal-F, Merck Serono, Germany) was injected subcutaneously each day (150–300 IU/day) after the third day of menstrual bleeding for a duration of five days.

For triggering ovulation, intramuscular administration of 10000 IU units of human chorionic gonadotropin (hCG) (Ovitrelle, Merck Serono Europe; Pregnyl, Organon) was performed when one of the follicles reached >18 mm in size as viewed by ultrasound. Transvaginal oocyte pick-up via ultrasound guidance was carried out 36–38 hours following the hCG injection.

After oocyte retrieval, the oocytes were denuded by brief exposure to hyaluronidase (LifeGlobal) and frequent pipetting. Then, oocytes were evaluated under an inverted microscope for nuclear maturation assessment: i. GV stage showed a germinal vesicle in the cytoplasm, ii. meiosis I (MI) stage did not show any germinal vesicle in the ooplasm and first polar body (PB) in the perivitelline space, and iii. MII stage showed the presence of the first PB in the perivitelline space.

In vitro maturation

A total of 552 GV stage oocytes were obtained from women who had an adequate number of MII oocytes after oocyte retrieval (>80%). Dimethyl sulphoxide (DMSO) was used to dissolve the CI A23187 (Sigma Aldrich; St. Louis, MO, USA) according to the manufacturer's protocol. Just before IVM, individual oocytes were transferred to 50 μ L droplets that contained 10 μ M CI of a stock solution diluted in culture medium (Global R, Life Global) for 15 minutes based on an artificial oocyte activation protocol (20). Then, the oocytes were washed in two, 50 μ L droplets of culture medium. In the control group, GV oocytes were not exposed to CI. Oocytes from the treated and control groups were transferred to 50 μ L droplets of culture medium (Global R, LifeGlobal) under mineral oil (LifeGlobal) and incubated in 6% CO₂ air atmosphere at 37°C. After 24–28 hours, oocyte maturation was assessed. Oocytes with the first PB (MII stage) were used for this study.

RNA isolation and cDNA synthesis

MAPK3, *CDK1*, *CCNBI*, *cyclin D1* (*CCND1*), *BCL-2*, *BAX*, *Caspase-3*, and β -*actin* gene expressions were assessed using real-time reverse transcription polymerase chain reaction (RT-PCR) in the IVM oocytes at the MII stage. Reverse transcriptions of samples were carried

out as explained previously (21). In summary, a total of 78 oocytes (39 oocytes in each group) were washed in phosphate-buffered saline (PBS, Invitrogen Corp.) + 1% polyvinyl alcohol (PVA), and pooled into six Eppendorf tubes (13 oocytes in each microtube) with 1.5 μ L of lysis buffer to isolate the RNA from the oocytes. The Eppendorf tubes were stored at -80°C. Next, we added 5 μ L nuclease-free water and 3 μ L random hexamer to the Eppendorf tubes and placed them in a Bio-Rad thermocycler.

Complementary DNA (cDNA) synthesis was performed with 10 mmol/L dNTP, 200 U RT enzyme, 10 U RNase inhibitor, and 5 \times RT buffer in a total reaction volume of 21 μ L for 10 minutes at 25°C, 15 minutes at 37°C, 45 minutes at 42°C, and 10 minutes at 72°C followed by overnight incubation at 4°C.

The investigated genes (*MAPK3*, *CDK1*, *CCNBI*, *CCND1*, *BAX*, *BCL-2*, and *Caspase-3*) and the internal control (β -*actin*) were amplified as follows. We added 1 μ g cDNA, 3 μ L nuclease-free water, 5 μ L Master Mix (Amplicon, Denmark), and 10 nmol specific forward and reverse primers (Table 1) to the PCR Eppendorf tubes and processed them for 5 minutes at 94°C, 30 seconds at 94°C, 30 seconds at 60°C, and 45 seconds at 72°C and 40 extension cycles. The amount of RNA was visualized after loading the samples. The amplification products were visualized on agarose gel electrophoresis under short UV.

Real-time RT-PCR analysis

In order to quantify *MAPK3*, *CDK1*, *CCNBI*, *CCND1*, *BAX*, *BCL-2*, and *Caspase-3* gene expressions, real-time RT-PCR was performed in 13 μ L of reaction buffer that contained synthesized cDNA, forward and reverse specific primers (1 mmol/L for each gene), and DNA Master SYBR Green I mix. The gene amplification program included 2 minutes at 95°C, 5 seconds at 95°C, 30 seconds at 60°C, 10 seconds at 72°C, and 40 extension cycles. The experiment for each sample was carried out in three replicates. Relative Expression Software Tool (REST, version 2009) was applied to calculate the expression of each of the investigated genes.

Glutathione and oxidative stress

The IVM-MII oocytes were collected from each group to determine their intracellular GSH (20 oocytes in each group) and ROS (23 oocytes in each group) levels by previously described methods (22). Briefly, the GSH and ROS content of the oocytes were detected using Cell Tracker Blue (CMF2HC; 4-chloromethyl-6, 8-difluoro-7-hydroxycoumarin; Invitrogen), and H2DCFDA (2',7'-dichlorodihydrofluorescein diacetate; Invitrogen) fluorescent dyes. Oocytes were transferred to a 30 μ L PBS droplet that consisted of 10 μ M Cell Tracker Blue, 10 μ M H2DCFDA, and 1 mg/mL PVA in the dark at 37°C for 45 minutes followed by three washes in PBS + 1% PVA. The samples' intracellular GSH and ROS concentrations were observed as blue and green fluorescence under a fluorescence microscope (Labomed Lx 400; Labo

America). The GSH and ROS contents were detected by 370 nm and 460 nm ultraviolet filters, respectively. Fluorescence images of oocytes were recorded as TIFF format graphics files and evaluated by ImageJ software (NIH, Bethesda, MD, USA), version 1.41.

Immunocytochemistry

Immunocytologic staining of the spindle structure and chromosome arrangement in the IVM-MII oocytes (10 oocytes in each group) was carried out using a previously described method (23). Briefly, MII stage oocytes were treated for about 30 seconds by Tyrode's acidic solution (pH=2.5) at room temperature to remove the zona pellucida. Next, 4% paraformaldehyde in PBS (pH=7.4) was applied for 30 minutes at 4°C to fix the oocytes. Following three washes in PBS + 0.02% Tween 20, oocyte membrane permeabilization was induced by 0.25% Triton X-100 for 60 minutes at room temperature. Then, the oocytes were exposed to 4N HCl for 30 minutes at room temperature, followed by 0.1 M Tris-HCl for neutralization. The oocytes were transferred to a blocking solution that contained 2% bovine serum albumin (BSA, Sigma Aldrich; St. Louis, MO, USA) + 0.02% Tween 20 in PBS for 60 minutes at room temperature. Subsequently, the oocytes were placed in mouse monoclonal anti- β -tubulin antibody (1/100 dilution, Sigma Aldrich; St. Louis, MO,

USA) in the blocking solution overnight in a humidified chamber at 4°C. After several washes, meiotic spindle staining was carried out following 30 minutes incubation at room temperature of the oocytes with conjugated goat anti-mouse (IgG) fluorescein isothiocyanate (FITC) at 1/100 dilution (Sigma Aldrich; St. Louis, MO, USA) in the dark. After several washes, the oocytes were placed in 10 mg of propidium iodide (PI; Sigma Aldrich; St. Louis, MO, USA) for chromatin staining for 20 minutes. The samples were individually mounted on microscope slides and a coverslip and etched rings were applied to prevent the samples from being ruptured by the coverslip. The slide was observed under a fluorescent microscope (Labomed Lx 400; Labo America) and the chromosomes, and spindle configurations were defined as normal (aligned chromosomes at the metaphase plate with barrel-shaped spindles) or abnormal (misaligned chromosomes in the metaphase plate with non-barrel-shaped spindles).

Statistical analysis

The t test and chi-square test using SPSS (SPSS, Chicago, IL, USA) software (version 16.0) was applied to analyse differences between the two groups. Mean \pm standard deviation (SD) and percentages were used to the express data. A p-value <0.05 was considered statistically significant.

Table 1: Primer sequences used in real-time RT-PCR

Gene	Sequence (5'-3')	Length	GC%	T _m (°C)
<i>MAPK3</i>	F: ATTGCCGATCCTGAGCATGACCAC	24	54.2	65
<i>MAPK3</i>	R: CAGATGTCGATGGACTTGGTATAG	24	45.8	58
<i>CDK1</i>	F: GGATGTGCTTATGCAGGATTCC	22	50.00	59.44
<i>CDK1</i>	R: CATGTACTGACCAGGAGGGATAG	23	52.17	59.42
<i>CCNB1</i>	F: GAAGATCAACATGGCAGGCG	20	55.00	59.62
<i>CCNB1</i>	R: GCATTTTGGCCTGCAGTTGT	20	50.00	60.25
<i>CCND1</i>	F: CATGCGGAAGATCGTCGCCACC	22	63.6	66
<i>CCND1</i>	R: CTCCTCCTCGCACTTCTGTTCC	22	59	61.5
<i>BAX</i>	F: GGAGGAAGTCCAATGTCCAG	20	55	59.505
<i>BAX</i>	R: GGGTTGTCGCCCTTTCTAC	20	55	60.856
<i>BCL-2</i>	F: GCTATAACTGGAGAGTGCTGAAG	23	47.8	57.7
<i>BCL-2</i>	R: CATCACTATCTCCCGGTTATCGT	23	47.8	58.5
<i>Caspase-3</i>	F: GACATCTCGGTCTGGTACAGATGTGC	26	53.9	63.5
<i>Caspase-3</i>	R: TTCACCATGGCTCAGAAGCACAC	23	52.2	62.5
<i>β-actin</i>	F: AGAGCTACGAGCTGCCTGAC	20	60	64
<i>β-actin</i>	R: AGCACTGTGTTGGCGTACAG	20	55	62

RT-PCR; Reverse transcription polymerase chain reaction, GC; Guanine-cytosine, and T_m; Melting temperature.

Results

Effects of pre-*in vitro* maturation CI treatment on percentage of *in vitro*-matured human oocytes after 24–28 hours

Overall, 216 couples participated in this study (Table 2). Out of 552 GV oocytes, 390 (70.65%) reached the MII stage and 96 (17.39%) arrested in the MI stage. There were 50 (9.05%) oocytes that arrested in the GV stage and 16 (2.89%) oocytes were degenerated. Although the MII oocyte rate was higher in CI-

treated oocytes (73.53%) compared to the control group (67.43%), this difference was not statistically significant ($P=0.13$). The GV arrested oocyte rate (CI-treated oocytes: 8.24% and control: 9.96%, $P=0.06$), oocyte degeneration rates (CI-treated oocytes: 2.40% and control: 3.44%, $P=0.46$), and arrested MI oocyte rates (CI-treated oocytes: 15.80% and control: 19.15%, $P=0.87$) after IVM was not statistically significant between CI-treated oocytes and the control group (Table 3). This finding suggested that CI treatment significantly affected the first PB extrusion in human oocytes.

Table 2: Baseline characteristics of the study population

Variables	Group	
	Control n(%) or mean \pm SD (range)	CI-treated n(%) or mean \pm SD (range)
Number of cycles	112	104
Female age (Y)	32.63 \pm 4.84 (20–40)	31.61 \pm 5.07 (21–40)
Cause of infertility		
Male factor	68 (60.71)	67 (64.42)
Tubal factor	38 (33.92)	32 (30.76)
Uterine factor	1 (0.89)	3 (2.88)
Unexplained	5 (4.46)	2 (1.92)
Number of total retrieved oocytes	12.17 \pm 6.85 (2–29)	13.06 \pm 7.10 (1–29)
GV retrieved oocytes	2.13 \pm 1.38 (1–7)	2.67 \pm 2.13 (1–12)
Degenerated retrieved oocytes	0.64 \pm 1.31 (0–6)	0.62 \pm 1.04 (0–6)
MI retrieved oocytes	0.90 \pm 1.36 (0–6)	1.29 \pm 1.66 (0–6)
MII retrieved oocytes	8.83 \pm 6.28 (0–28)	9.42 \pm 5.98 (0–27)

The t test was applied for statistical analysis. There was no statistically significant difference in any parameter between the CI-treated and control groups. CI; Calcium ionophore, Ns; Not significant, GV; Germinal vesicle, MI; Metaphase I, MII; Metaphase II, and SD; Standard deviation.

Table 3: Meiotic maturation of human oocytes after 24–28 hours of culture

Group	No. of GV cultured N (mean \pm SD)	GV arrest N (mean \pm SD)	Degenerated N (mean \pm SD)	MI N (mean \pm SD)	MII N (mean \pm SD)
CI-treated oocytes	291 (2.82 \pm 2.34)	24 (0.23 \pm 0.52)	7 (0.06 \pm 0.32)	46 (0.44 \pm 0.76)	214 (2.07 \pm 1.71)
Control	261 (2.33 \pm 1.52)	26 (0.23 \pm 0.46)	9 (0.08 \pm 0.35)	50 (0.44 \pm 0.88)	176 (1.57 \pm 1.27)

The t test was applied for statistical analysis. There was no significant difference in the meiotic maturation rate between the two groups. CI; Calcium ionophore, GV; Germinal vesicle, MI; Metaphase I, MII; Metaphase II, and SD; Standard deviation.

Effects of pre *in vitro* maturation calcium ionophore treatment on nuclear maturation and apoptosis-related gene expression levels of *in vitro*-matured human oocytes

In the present study, the transcript profiles of several oocyte maturation-related genes (*MAPK3*, *CCNB1*, *CDK1*, and *CCND1*) were evaluated by real-time RT-PCR. The results showed that *MAPK3*, *CCNB1*, *CDK1*, and *CCND1* mRNA expression levels compared with the housekeeping gene (β -*actin*) were up-regulated significantly in CI-treated oocytes ($P < 0.05$; Fig. 1). These findings led to the hypothesis that exposure of CI to human oocytes resulted in an apparent up-regulation in *MAPK3*, *CCNB1*, *CDK1*, and *CCND1* mRNA expressions.

A molecular mechanism that modulates human oocyte apoptosis might be induced by CI treatment. Therefore, we evaluated the *BCL-2*, *BAX*, and *Caspase-3* relative expression levels by real-time RT-PCR. The results of real-time RT-PCR demonstrated that the expression of anti-apoptotic *BCL-2* was remarkably up-regulated after treatment with CI ($P = 0.001$; Fig. 1), whereas the expression of pro-apoptotic *BAX* did not change significantly ($P = 0.76$). Thus, the *BAX/BCL-2* ratio decreased (13.60%). Also, real-time RT-PCR revealed that the expression level of *Caspase-3* mRNA did not change significantly in human oocytes after exposure to CI ($P = 0.81$; Fig. 1).

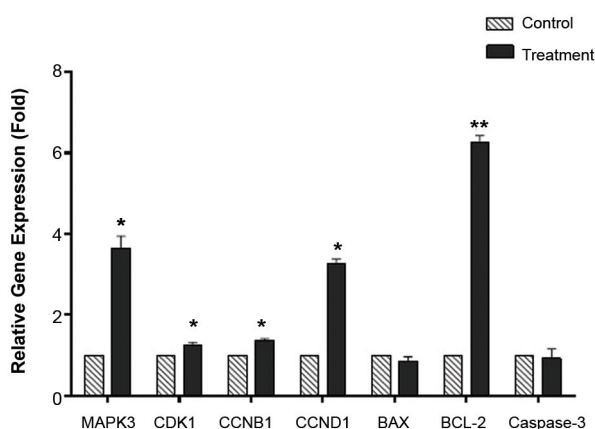


Fig. 1: Nuclear maturation and apoptosis-related gene mRNA expressions of human oocytes. The relative expression levels of mitogen-activated protein kinase 3 (*MAPK3*), *CCNB1*, *CDK1*, and *cyclin D1* (*CCND1*) were significantly higher and *BCL-2* was significantly lower in calcium ionophore (CI)-treated human *in vitro* maturation-meiosis II (IVM-MII) oocytes (* $P < 0.05$, ** $P < 0.001$).

Effects of pre-*in vitro* maturation calcium ionophore treatment on glutathione and oxidative stress of *in vitro*-matured human oocytes

The human oocyte GSH content was evaluated in the CI treatment and control groups. Analyses with ImageJ software indicated that CI treatment induced a statistically remarkable increase in oocyte intracellular GSH concentration ($P = 0.005$, Fig. 2A, B). A comparison of the intracellular ROS content

of human oocytes (23 oocytes in each group) revealed significantly diminished ROS content in CI-treated oocytes compared with the control group ($P = 0.04$; Fig. 2C, D).

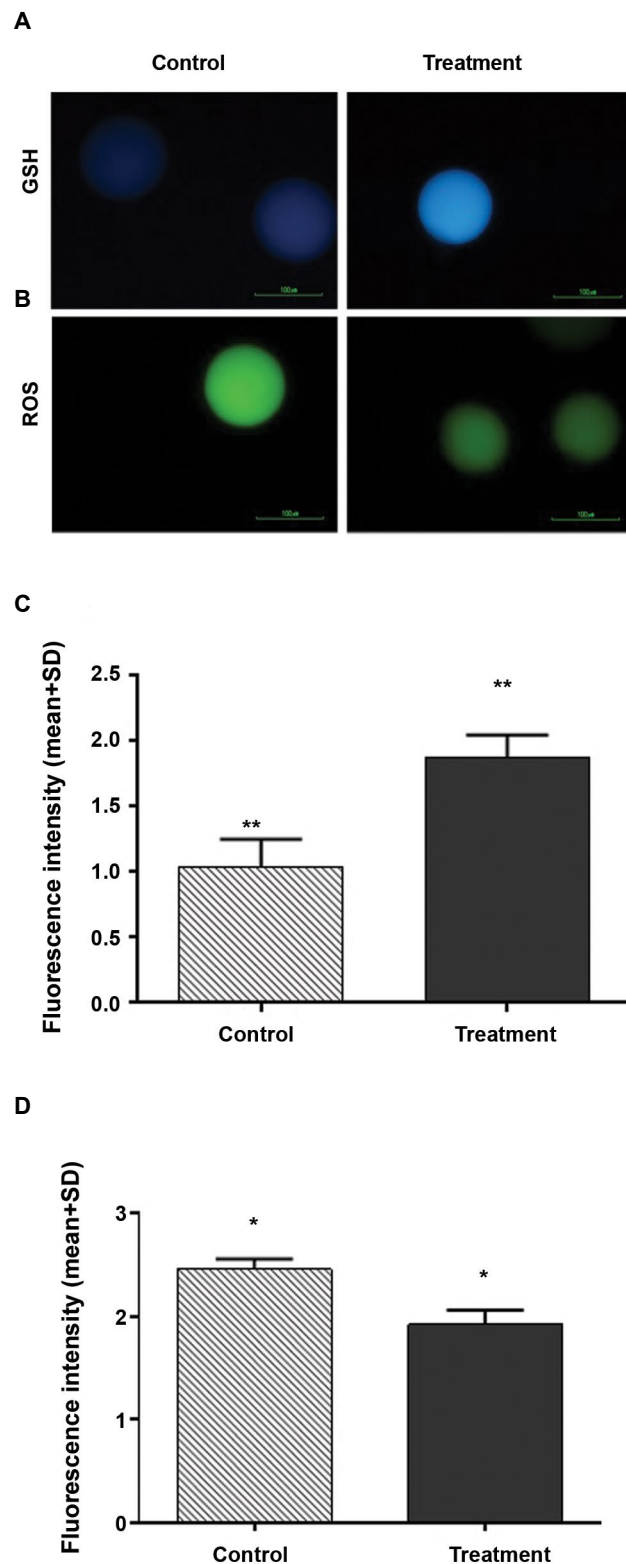


Fig. 2: Glutathione (GSH) and reactive oxygen species (ROS) content in human *in vitro* maturation-meiosis II (IVM-MII) oocytes evaluated by fluorescent staining. **A.** Oocytes were stained with Cell Tracker Blue to assess the level of intracellular GSH and **B.** 2-7-dichlorodihydrofluorescein diacetate (H2DCFDA) to determine ROS (bar: 100 μ m). **C.** GSH and **D.** ROS content in calcium ionophore (CI)-treated human oocyte and control groups. The data were analysed using the t test. As the graph depicts, CI-treated oocyte cytoplasm had significantly higher GSH and lower ROS content (** $P < 0.01$, * $P < 0.05$).

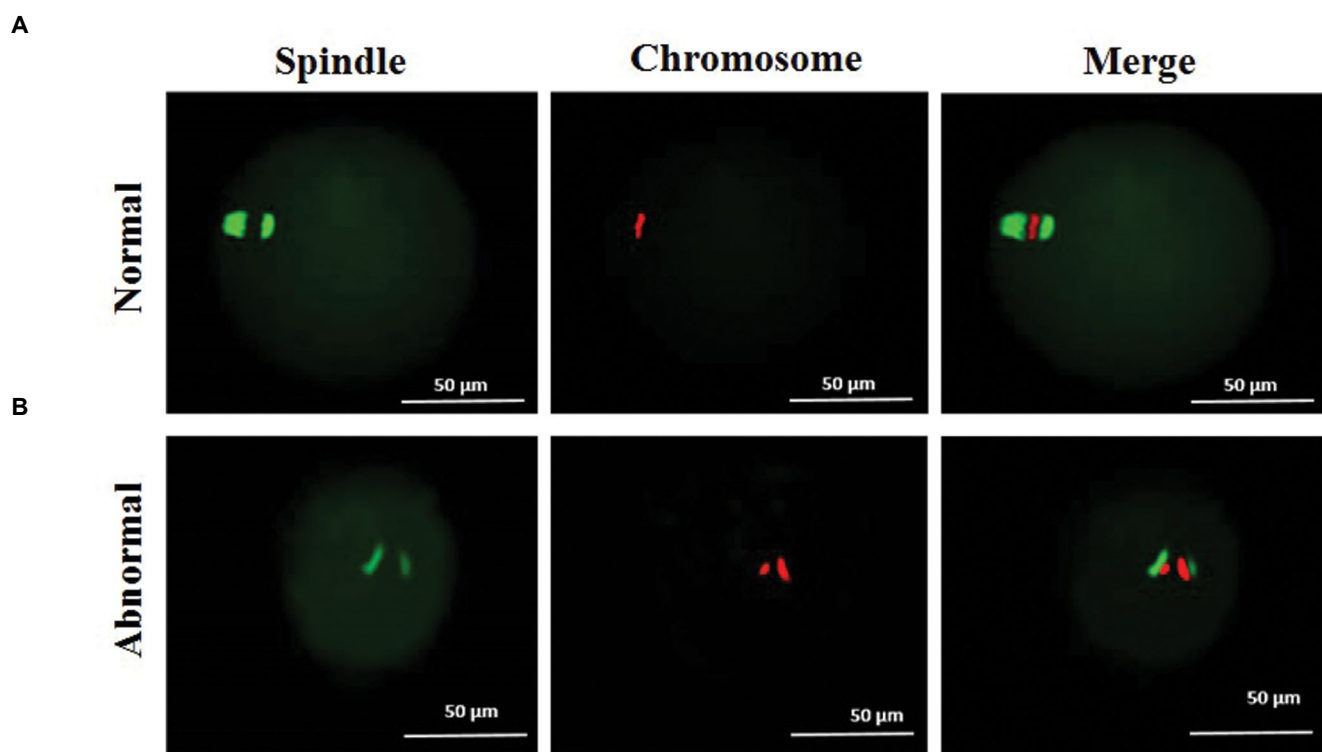


Fig.3: Meiotic spindle configuration and chromosome alignment in human *in vitro* maturation-meiosis II (IVM-MII) oocytes evaluated using immunocytochemistry. IVM-MII oocytes in calcium ionophore (CI)-treated human oocyte and control groups were fixed and stained for β -tubulin (green) and chromosomes (propidium iodide [PI], red), and analysed for meiotic spindle configuration and chromosome alignment. Meiotic spindles were classified as **A.** Normal with aligned chromosomes at the metaphase plate with barrel-shaped spindles and **B.** Abnormal with misaligned chromosomes in the metaphase plate with non-barrel-shaped spindles (bar: 50 μ m).

Effects of pre-*in vitro* maturation (pre-IVM) calcium ionophore (CI) treatment on chromosome alignment and meiotic spindle structure of *in vitro*-matured human oocytes

In order to find out whether the CI treatment could affect chromosome and spindle structure in human oocytes after IVM, we stained IVM-MII oocytes for β -tubulin to assess spindle configuration and PI to detect chromosomes. A total of 20 oocytes (10 oocytes in each group) were examined for meiotic spindle structure and chromosome alignment. Following the evaluation of β -tubulin positive spindles by fluorescent microscopy, one abnormal chromosome and spindle structure were observed in each group. There was no significant difference in normal spindle configuration and chromosome alignment rate (normal oocytes/examined oocytes) between the CI-treated group (90%) and control group (90%, Fig.3). This result showed that meiotic spindle bipolarity and chromosome alignment of human IVM-MII oocytes was not significantly affected by CI treatment.

Discussion

Due to the absence of ovarian niches, human oocyte maturation following IVM is suboptimal. Some studies have reported morphological and structural differences after IVM of human oocytes in comparison with *in vivo* oocytes (2, 3).

Although in previous animal and human studies the

influence of Ca^{2+} on oocyte maturation has been identified, its central role in human IVM as a mediator of MAPK, MPF, and apoptosis signalling cascade has not been proven.

In this study, in order to demonstrate the effect of CI in oocyte maturation, we used CI before oocyte meiosis resumption during 24-28 hours of IVM. The results showed beneficial effects of CI on increasing nuclear maturation and anti-apoptotic gene expressions and cytoplasmic maturation.

The effects of CI on human artificial oocyte activation have been shown before (20, 24). To our knowledge, this study is the first to identify the effects of CI on IVM of the human oocyte.

Promotive effects of CI on the IVM of human oocyte can be through several pathways.

The results of the present study demonstrated that CI up-regulates *MAPK*, *Cyclin B*, and *CDK1* gene expressions. These findings support the report of Liu et al., which stated that the cortical distribution of the calcium-sensing receptor regulated by gonadotropins in porcine oocytes improved oocyte IVM through the MAPK-dependent signalling cascade (25). The current study demonstrated that CI up-regulated *MAPK*, which then improved human oocyte maturation. This process might occur via the MAPK-related pathway. Protein kinase C (PKC) is the Ca^{2+} target downstream molecule

(26). Cell cycle regulation by PKC cascades is involved in the activation of MAPK and MPF. CDK1 and cyclin B1 are PKC substrates. PKC inhibitor decreases MPF activity in the oocyte and PKC regulates MAPK signalling (6). It has been shown that MAPK is activated in cumulus cells by PKC activators (4). The present study findings contradict a previous observation by Ito et al. in which porcine oocytes were parthenogenetically activated by CI. They reported that *MAPK* activity decreased after pronucleus formation (27). It should be considered while we evaluated the MAPK levels in MII stage oocytes; the latter study reported the MAPK levels decreased after fertilization. Zhang et al. reported that MAPK levels increased during oocyte maturation until the MII stage, but the levels decreased after fertilization (28).

The *CCNBI* expression level in the oocyte is a marker for cytoplasmic maturation (25). Liang et al. showed that stored mRNA of *CCNBI* in the cytoplasm of the oocyte could influence MAPK and the MPF pathway (29). These results indicated that CI could increase cytoplasmic maturation in IVM-MII oocytes by enhancement of MAPK activity. The finding of the present study supported their views.

The relative expression level of *CCND1*, a cell cycle regulator gene, is a proliferative marker. Increasing expression of *CCND1* has been reported during meiosis progression in mouse oocytes (31). In mammalian oocytes, *CCND1* was expressed both in the oocyte and granulosa cells during follicular growth (30) and has a crucial role in follicles and granulosa cell proliferation, survival, and early embryonic transition (30). Gatius et al. (32) showed that MAPK signalling promotes cell proliferation by activation of *CCND1*. Up-regulation of *MAPK* in the present study might be the result of the activation of *CCND1*.

In general, oxidative stress induced by overloading of Ca^{2+} is an apoptotic signal that can increase *BAX/BCL-2* and increase apoptosis in the oocyte (14). The findings of the present study show that CI could upregulate anti-apoptotic *BCL-2*. It does not up-regulate pro-apoptotic *BAX* and effector *Caspase-3* gene expression in IVM-MII human oocytes. In agreement with our findings, several studies have shown that decreased levels of MAPK and MPF in oocytes also lead to increased *BCL-2* protein degradation and activation of the apoptotic pathway in mice (15), rat (13), and canine (33) oocytes. Also, it has been reported that inhibition of CDK1 activity by reducing the MPF heterodimer prevents meiotic cell cycle progression and induces apoptosis (13, 15). Decreased CDK1 phosphorylation as well as increased degradation of cyclin B1 lead to MPF instability and result in fas ligand-induced apoptosis in oocytes (14). Thus, the increased expression levels of MAPK and MPF genes in our study might be responsible for an increased survival-promoting signalling in IVM-MII oocytes. Tripathi and Chaube added different concentrations of CI (0.5, 1, 2, 3, 4 μ M) to rat MII oocyte culture medium for 3 hours and

showed that high concentrations (3 and 4 μ M) of CI led to increased ROS production and apoptosis in oocytes (34). Moreover, Chaube et al. reported that the addition of CI (1.6 μ M) to the culture medium of rat MII stage oocytes for 3 hours induced hydrogen peroxide formation and apoptosis in these oocytes (35). In both of these studies, the oocyte developmental stage, CI concentrations, and exposure duration were not similar to our work.

In the current study, we observed higher GSH and lowered ROS content in CI-treated oocyte cytoplasm. Intracellular GSH concentration is an oocyte cytoplasmic maturation marker. Increasing GSH synthesis in oocytes starts from meiosis resumption in the GVBD stage and reaches its highest concentration at the MII stage (19). GSH regulates many processes in the oocyte, including modulating the intracellular redox balance, defending oocytes from ROS damage, influencing sperm nuclear decondensation, and male pronucleus formation, DNA synthesis, and amino acid and protein transport (11). *BCL-2* prevents the intrinsic apoptotic pathway in mitochondria. Besides its anti-apoptotic function, *BCL-2* has an antioxidant-like property that has been related to the regulation of the intracellular concentration of *GSH*. Previous studies have reported that increased *BCL-2* expression causes an increase in intracellular GSH content by enhanced GSH synthesis and reduced cellular GSH efflux (36). In our research, overexpression of *BCL-2* induced by CI treatment might be the reason for the increase in GSH content and, subsequently, reduced ROS status in oocytes after IVM.

In the present study, we showed that CI did not disturb the meiotic spindle structure and chromosome alignment. Abnormal spindle assembly and chromosome segregation cause aneuploidy in oocytes, which leads to the embryo development arrest and spontaneous abortion (37). Our finding might be due to the MAPK and MPF pathway that has a significant role in the remodeling of actin filaments and microtubule organization (4, 25). In agreement with our findings, Luo et al. (38) showed that inhibition of the activation of MAPK during porcine oocyte maturation resulted in prevention spindle microtubules assembly and first PB extrusion. Choi et al. (39) reported that increased oxidative stress and a decreased intracellular concentration of *GSH* led to the spindle structure defect in IVM mouse oocytes. Nevertheless, the normal spindle morphology was reported in IVM-MII macaque oocytes, which GSH ethyl ester was added to the IVM culture medium (10). Considering the protective effect of GSH on the meiotic spindle structure and cytoplasmic microtubules, CI might prevent the meiotic spindle disruption and chromosome misalignment in IVM-MII human oocytes through increased levels of the intracellular GSH level.

We did not find any effect of CI on the first PB extrusion in human oocytes. In contrast to our finding, Makki et al. (40) reported that addition of 15 μ g/ml selenium, 10 μ g/ml calcium, and 5 μ g/ml CI to the IVM medium for 24 hours improved IVM and fertilization of oocytes, and

the embryo cleavage rate. The differences between the findings of this study and our work might be due to the various times of exposure and compounds which were added to the culture medium.

In the current study, we showed that CI could improve oocyte cytoplasmic and nuclear maturation during IVM of human oocytes, but it could not alter the extrusion of the first PB of the oocytes. It should be mentioned that we evaluated the expression of genes related to maturation in oocytes at the RNA level, whereas the first PB extrusion was regulated when these RNAs were translated into protein. Hence, it seemed that the prolonged *in vitro* culture of the oocyte might lead to the conversion of maturation related RNA genes to proteins and improve the first PB extrusion of the oocytes. Therefore, further clarification of the impact of the CI on maturation related proteins is required.

Conclusion

The finding of the current study seems to support the beneficial effect of CI on the developmental competence of human oocytes, including nuclear and cytoplasmic maturation, and apoptosis of human oocytes. We suggest that the CI may optimize the human IVM procedure in the ART clinic.

Acknowledgments

This article was extracted from a Ph.D. thesis written by Elham Fazeli in the School of Medicine at Shahid Beheshti University of Medical Sciences (Registration No: 89). The authors thank the Cellular and Molecular Biology Research Center, Shahid Beheshti University of Medical Sciences for financial support of the present study. The authors declare no conflict of interest.

Authors' Contributions

E.F., A.H., F.F.-N., M.G.N., M.B., M.S., M-H.H., H-A.A.; Participated in study design, data collection and evaluation, drafting the manuscript, and statistical analysis. E.F., M.G.N., F.F.-N., H.N., Z.S.M., M.S., S.A.; Performed follicle collection and prepared oocytes for IVM pertaining to this component of the study. E.F., H-A.A., M.G.N., F.F.-N. H.A.; Contributed extensively to the interpretation of the data and the conclusion. M.S., M.B., S.H.; Conducted molecular experiments and real-time RT-PCR analysis. All authors performed the edition and approved the final version of this manuscript.

References

- Gardner DK, Weissman A, Howles CM, Shoham Z. Textbook of assisted reproductive techniques. 4th ed. Clinical perspectives: CRC press; London: CRC Press; 2012.
- Virant-Klun I, Bauer C, Ståhlberg A, Kubista M, Skutella T. Human oocyte maturation *in vitro* is improved by co-culture with cumulus cells from mature oocytes. *Reprod Biomed Online*. 2018; 36(5): 508-523.
- Walls ML, Hart R, Keelan JA, Ryan JP. Structural and morphologic differences in human oocytes after *in vitro* maturation compared with standard *in vitro* fertilization. *Fertil Steril*. 2016; 106(6): 1392-1398. e5.
- Prochazka R, Blaha M. Regulation of mitogen-activated protein kinase 3/1 activity during meiosis resumption in mammals. *J Reprod Dev*. 2015; 61(6): 495-502.
- Adhikari D, Liu K. The regulation of maturation promoting factor during prophase I arrest and meiotic entry in mammalian oocytes. *Mol Cell Endocrinol*. 2014; 382(1): 480-487.
- Zhao MH, Kwon JW, Liang S, Kim SH, Li YH, Oh JS, et al. Zinc regulates meiotic resumption in porcine oocytes via a protein kinase C-related pathway. *PLoS One*. 2014; 9(7): e102097.
- Bromfield JJ, Piersanti RL. Mammalian oogenesis: the fragile foundation of the next generation. 3rd ed. Cambridge: Academic Press; 2019: 157-164.
- Chian RC, Buckett WM, Tan SL. *In-vitro* maturation of human oocytes. *Reprod Biomed Online*. 2004; 8(2): 148-166.
- Strauss JF, Williams CJ. Ovarian life cycle. Yen and Jaffe's reproductive endocrinology. 8th ed. Elsevier; Philadelphia: 2019: 167-205. e9.
- Curnow EC, Ryan J, Saunders DM, Hayes ES. *In vitro* developmental potential of macaque oocytes, derived from unstimulated ovaries, following maturation in the presence of glutathione ethyl ester. *Hum Reprod*. 2010; 25(10): 2465-2474.
- Hidaka T, Fukumoto Y, Yamamoto S, Ogata Y, Horiuchi T. Variations in bovine embryo production between individual donors for OPU-IVF are closely related to glutathione concentrations in oocytes during *in vitro* maturation. *Theriogenology*. 2018; 113: 176-182.
- Jeon Y, Yoon JD, Cai L, Hwang SU, Kim E, Zheng Z, et al. Supplementation of zinc on oocyte *in vitro* maturation improves pre-implantation embryonic development in pigs. *Theriogenology*. 2014; 82(6): 866-874.
- Tripathi A, Chaube SK. Roscovitine inhibits extrusion of second polar body and induces apoptosis in rat eggs cultured *in vitro*. *Pharmacol Rep*. 2015; 67(5): 866-874.
- Tiwari M, Prasad S, Tripathi A, Pandey AN, Ali I, Singh AK, et al. Apoptosis in mammalian oocytes: a review. *Apoptosis*. 2015; 20(8):1019-1025.
- Tatone C, Carbone MC, Gallo R, Monache S, Di Cola M, Alesse E, et al. Age-associated changes in mouse oocytes during postovulatory *in vitro* culture: possible role for meiotic kinases and survival factor BCL2. *Biol Reprod*. 2006; 74(2): 395-402.
- Aytac PC, Kilicdag EB, Haydardeoglu B, Simsek E, Cok T, Parlakgumus HA. Can calcium ionophore "use" in patients with diminished ovarian reserve increase fertilization and pregnancy rates? A randomized, controlled study. *Fertil Steril*. 2015; 104(5): 1168-1174.
- Tosti E. Calcium ion currents mediating oocyte maturation events. *Reprod Biol Endocrinol*. 2006; 4(1): 26.
- Hagenston AM, Bading H. Calcium signaling in synapse-to-nucleus communication. *Cold Spring Harb perspect Biol*. 2011; 3(11): a004564.
- Abdoon ASS, Kandil OM, Zeng SM, Cui M. Mitochondrial distribution, ATP-GSH contents, calcium [Ca²⁺] oscillation during *in vitro* maturation of dromedary camel oocytes. *Theriogenology*. 2011; 76(7): 1207-1214.
- Nikiforaki D, Meerschaut VF, De Roo C, Lu Y, Ferrer-Buitrago M, De Sutter P, et al. Effect of two assisted oocyte activation protocols used to overcome fertilization failure on the activation potential and calcium releasing pattern. *Fertil Steril*. 2016; 105(3): 798-806. e2.
- Hosseini S, Dehghani-Mohammadabadi M, Ghafarri Novin M, Haji Molla Hoseini M, Arefian E, Mohammadi Yeganeh S, et al. Toll-like receptor4 as a modulator of fertilization and subsequent pre-implantation development following *in vitro* maturation in mice. *Am J Reprod Immunol*. 2017; 78(5): e12720.
- Wang F, Tian X, Zhang L, He C, Ji P, Li Y, et al. Beneficial effect of resveratrol on bovine oocyte maturation and subsequent embryonic development after *in vitro* fertilization. *Fertil Steril*. 2014; 101(2): 577-586. e1.
- Lee HH, Lee HJ, Kim HJ, Lee JH, Ko Y, Kim SM, et al. Effects of antifreeze proteins on the vitrification of mouse oocytes: comparison of three different antifreeze proteins. *Hum Reprod*. 2015; 30(9): 2110-2119.
- Kim JW, Yang SH, Yoon SH, Kim SD, Jung JH, Lim JH. Successful pregnancy and delivery after ICSI with artificial oocyte activation by calcium ionophore in *in-vitro* matured oocytes: a case report. *Reprod Biomed Online*. 2015; 30(4): 373-377.
- Liu C, Wu GQ, Fu XW, Mo XH, Zhao LH, Hu HM, et al. The Extracellular calcium-sensing receptor (CASR) regulates gonadotro-

- pins-induced meiotic maturation of porcine oocytes. *Biol Reprod.* 2015; 93(6): 131.
26. Morrison DK. MAP kinase pathways. *Cold Spring Harb Perspect Biol.* 2012; 4(11): a011254.
 27. Ito J, Shimada M. Timing of MAP kinase inactivation effects on emission of polar body in porcine oocytes activated by Ca²⁺ ionophore. *Mol Reprod Dev.* 2005; 70(1): 64-69.
 28. Zhang DX, Park WJ, Sun SC, Xu YN, Li YH, Cui XS, et al. Regulation of maternal gene expression by MEK/MAPK and MPF signaling in porcine oocytes during in vitro meiotic maturation. *J Reprod Dev.* 2011; 57(1): 49-56.
 29. Liang CG, Su YQ, Fan HY, Schatten H, Sun QY. Mechanisms regulating oocyte meiotic resumption: roles of mitogen-activated protein kinase. *Mol Endocrinol.* 2007; 21(9): 2037-2055.
 30. Chakravarthi VP, Kona S, Kumar AS, Bhaskara M, Rao V. Stage specific expression of cell cycle genes during in vivo or in vitro development of ovarian follicles in sheep. *Small Ruminant Research.* 2016; 143: 1-7.
 31. Moore GD, Ayabe T, Kopf GS, Schultz RM. Temporal patterns of gene expression of G1-S cyclins and cdk's during the first and second mitotic cell cycles in mouse embryos. *Mol Reprod Dev.* 1996; 45(3): 264-275.
 32. Gatus S, Velasco A, Azueta A, Santacana M, Pallares J, Valls J, et al. FGFR2 alterations in endometrial carcinoma. *Mod Pathol.* 2011; 24(11): 1500-1510.
 33. Suzukamo C, Hoshina M, Moriya H, Hishiyama N, Nakamura S, Kawai F, et al. Kinetics of nuclear status and kinase activities during in vitro maturation of canine oocytes. *J Reprod Dev.* 2009; 55(2): 116-120.
 34. Tripathi A, Chaube SK. High cytosolic free calcium level signals apoptosis through mitochondria-caspase mediated pathway in rat eggs cultured in vitro. *Apoptosis.* 2012; 17(5): 439-448.
 35. Chaube SK, Khatun S, Misra SK, Shrivastav TG. Calcium ionophore-induced egg activation and apoptosis are associated with the generation of intracellular hydrogen peroxide. *Free Radic Res.* 2008; 42(3): 212-220.
 36. Wilkins HM, Marquardt K, Lash LH, Linseman DA. Bcl-2 is a novel interacting partner for the 2-oxoglutarate carrier and a key regulator of mitochondrial glutathione. *Free Radic Biol Med.* 2012; 52(2): 410-419.
 37. Ou XH, Li S, Xu BZ, Chen LN, Jiang MX, Chen SQ, et al. Mitogen-activated protein kinase-activated protein kinase 2 is a critical regulator of pig oocyte meiotic maturation. *Reprod Fertil Dev.* 2017; 29(2): 223-233.
 38. Luo Y, Che MJ, Liu C, Liu HG, Fu XW, Hou YP. Toxicity and related mechanisms of dihydroartemisinin on porcine oocyte maturation in vitro. *Toxicol Appl Pharmacol.* 2018; 341: 8-15.
 39. Choi WJ, Banerjee J, Falcone T, Bena J, Agarwal A, Sharma RK. Oxidative stress and tumor necrosis factor- α -induced alterations in metaphase II mouse oocyte spindle structure. *Fertil Steril.* 2007; 88(4): 1220-1231.
 40. Makki M, Saboori E, Sabbaghi MA, Aram R, Fallahian MH, Peyghambari F, et al. Effects of selenium, calcium and calcium ionophore on human oocytes in vitro maturation in a chemically defined medium. *Iran J Reprod Med.* 2012; 10(4): 343.
-

Metformin Protects Myelin from Degeneration in A Mouse Model of lysophosphatidylcholine-Induced Demyelination in The Optic Chiasm

Saman Esmaeilnejad, M.Sc.¹, Saeed Semnanian, Ph.D.¹, Mohammad Javan, Ph.D.^{1,2*}

1. Department of Physiology, Faculty of Medical Sciences, Tarbiat Modares University, Tehran, Iran

2. Department of Brain and Cognitive Sciences, Cell Science Research Center, Royan Institute for Stem Cell Biology and Technology, ACECR, Tehran, Iran

*Corresponding Address: P.O.Box: 14115-331, Department of Physiology, Faculty of Medical Sciences, Tarbiat Modares University, Tehran, Iran
Email: mjavan@modares.ac.ir

Received: 21/September/2019, Accepted: 08/January/2020

Abstract

Objective: Multiple sclerosis (MS) is a demyelinating disease of the central nervous system. The autoimmune pathology and long-term inflammation lead to substantial demyelination. These events lead to a substantial loss of oligodendrocytes (OLs), which in a longer period, results in axonal loss and long-term disabilities. Neural cells protection approaches decelerate or inhibit the disease progress to avoid further disability. Previous studies showed that metformin has beneficial effects against neurodegenerative conditions. In this study, we examined possible protective effects of metformin on toxin-induced myelin destruction in adult mice brains.

Materials and Methods: In this experimental study, lysophosphatidylcholine (LPC) was used to induce demyelination in mice optic chiasm. We examined the extent of demyelination at different time points post LPC injection using myelin staining and evaluated the severity of inflammation. Functional state of optic pathway was evaluated by visual evoked potential (VEP) recording.

Results: Metformin attenuated LPC-induced demyelination ($P<0.05$) and inflammation ($P<0.05$) and protected against significant decrease ($P<0.05$) in functional conductivity of optic tract. These data indicated that metformin administration attenuates the myelin degeneration following LPC injection which led to functional enhancement.

Conclusion: Our findings suggest metformin for combination therapy for patients suffering from the myelin degenerative diseases, especially multiple sclerosis; however, additional mechanistic studies are required.

Keywords: Demyelination, Metformin, Multiple Sclerosis, Neuroprotection

Cell Journal(yakhteh), Vol 23, No 1, April-June (Spring) 2021, Pages: 119-128

Citation: Esmaeilnejad S, Semnanian S, Javan M. Metformin protects myelin from degeneration in a mouse model of lysophosphatidylcholine-induced demyelination in the optic chiasm. Cell J. 2021; 23(1): 119-128. doi: 10.22074/cellj.2021.7174.

This open-access article has been published under the terms of the Creative Commons Attribution Non-Commercial 3.0 (CC BY-NC 3.0).

Introduction

Multiple sclerosis (MS) is a chronic neuroinflammatory disorder affecting myelin sheaths and axons. This disease is described as a remarkable damage to oligodendrocytes (OLs) and myelin destruction (1). The autoimmune invasion and prolonged inflammation leads to a substantial elimination of myelin. These events cause a substantial loss of OLs and their precursors, which in a longer period, results in axonal loss. The long-term disability seen in MS is mainly because of damages to the axons, which are the consequence of the inflammatory attack and deterioration of the axon that remained demyelinated (2). Although the exact cause(s) of the disease is still unclear, both genetic and environmental factors appear to be involved (3). As yet, therapeutic approaches control the disease and limit the recurrence of autoimmune incursion but chronic inflammation remains; therefore, neuroprotection is being accepted as a therapy that may serve to decelerate or inhibit the disease progression to avoid higher levels of disability (4).

Metformin is a member of biguanide drugs and a widely prescribed medication in the treatment of diabetes mellitus (5). A long history of effectiveness and safety has made this small molecule the most frequently prescribed medication worldwide. In addition to its antidiabetic effects, metformin has been demonstrated to be a therapeutically efficient candidate in several central nervous system (CNS) disorders. A previous study demonstrated the neuroprotective effects of metformin in an Alzheimer's disease model (6). Moreover, the protective effects of metformin on neural cells against apoptosis was also reported (7). Beneficial effects of metformin in neuroinflammatory diseases (8), brain damage models including spinal cord injury (9) ischemia/reperfusion injury (10), Huntington's (11) and Parkinson's disease (12) were also reported. There are several studies demonstrating the ability of metformin to hinder the inflammation process in various diseases such as encephalomyelitis, peritonitis-induced sepsis, rheumatoid arthritis, endotoxin-induced uveitis, etc. (13-15). It was proposed

that this compound regulates the T helper 1 cells (Th1), Th17, regulatory T cells (Treg) lymphocytes function; such regulatory activity plays a substantial role in its protective effect (16, 17). Metformin's antioxidant (18) and anti-inflammatory (19) properties alongside the capacity to repair endothelial dysfunction (20) make this medication suitable for MS therapy. Although the mechanism of action of metformin has not yet been fully determined, but previous works showed that metformin-induced activation of AMP-activated protein kinase (AMPK) pathway is a crucial mechanism that triggers the downstream events (21). These pieces of evidence strengthen the idea that metformin may have protective effects on myelin degeneration in animal models of MS. The aim of this study was to examine the protective effect of metformin in a lysophosphatidylcholine (LPC) -induced mouse model of optic nerve demyelination.

Material and Methods

Animals

For this experimental study, 8 to 10-week-old (20-25 g) C57BL/6 male mice were provided by Pasteur Institute (Iran) and housed in plastic cages in groups of four with free access to water and pellet diet; animals were kept at constant temperature ($25 \pm 2^\circ\text{C}$) with 12 hour light/12 hour dark periods.

All animal experiments were conducted in accordance with international guidelines and approved by The Committee for Ethics in Research, Tarbiat Modares University (IR.TMU.REC.1394.189). All efforts were made to minimize the number of animals used and their suffering.

Induction of demyelination

For the surgery, the animals were deeply anesthetized by ketamine [70 mg/kg, intraperitoneal (i.p.); Alfasan, Holland] and xylazine (10 mg/kg, i.p., Alfasan, Holland). Optic chiasm demyelination was performed as mentioned in our previous reports (22) by injecting 1 μl of 1 % LPC (Sigma, St. Louis, USA) dissolved in 0.9% NaCl into the optic chiasm on a stereotaxic apparatus (Fig.1A). The skulls were situated in the stereotaxic apparatus (Stoelting, USA). The coordinates of the injection location were as follows: Anterior: -0.25 mm to the Bregma, lateral: 0, and ventral: 4.9 mm from the Dura (23). LPC was injected into the optic chiasm during 5 minutes. The needle was kept in site for another 5 minutes to avoid reflux through the needle track and was then removed.

Intervention

Metformin (Merck, Germany) was dissolved in distilled water and daily injected i.p. to the animals. The injection dose of metformin (200 mg/kg) was chosen based on a

previous report that showed its effect in a neurodegenerative condition (24). Mice were put into 3 separate groups: i. Control group: animals which received saline, ii. LPC: animals which received local LPC and saline as treatment, and iii. LPC + Met.: animals which received local LPC and metformin for up to 7 days post-lesion (dpi); these groups included subgroups which were sacrificed on days 3 or 7 dpi for immunohistofluorescent studies.

Histological analysis

Mice were anesthetized by ketamine and perfused transcardially using phosphate-buffered saline (PBS) and 4% formaldehyde. The brains were harvested and then, 4% buffered formaldehyde was used for post-fixation. The brains were placed in 15% sucrose for one day, and then, transferred to 30% sucrose solution. The brains were molded in optimum cutting temperature (OCT, Bio-Optica, Italy) compound, then, sectioned by a cryostat apparatus (Histo-Line Laboratories, Italy). Coronal sections of 7 μm thickness containing the optic chiasm, were prepared (23).

For Hematoxylin and Eosin (H&E) staining, the frozen sections were rehydrated in water, immersed in Harris' Hematoxylin (Bio-Optica, Italy) dye for 4 minutes. The tissues were washed for 3 minutes with tap water, then, placed in acid alcohol and washed again. Eosin staining was performed for 1-2 minutes. The sections were dehydrated by 70, 95 and 100% alcohol concentrations, immersed in xylene and cover-slipped by Entellan (Merck Chemicals, Germany). One slide containing 8 sections prepared along the chiasm was stained for each animal. Each group included 3 animals and was evaluated and scored for the severity of inflammation by a pathologist who was blind to the experimental groups. The scores were as follows: 0: no inflammation, 1: a few inflammatory cells, 2: perivascular infiltration, and 3: increased severity of perivascular cuffing extended into the adjacent tissues. The score of inflammation was calculated as the average of its section scores and then, and then groups averages were calculated (25).

For luxol fast blue (LFB) staining, sections were rehydrated in water, immersed in 0.1 % LFB (British Drug House, UK) at 60°C for 2 hours, placed in 95% alcohol and, then washed under running water each for 10 minutes. The contrast modification was performed by immersion of tissues in 0.05 % lithium carbonate; then, the slides were immersed in water for 10 minutes. The sections were counterstained with 0.1% cresyl violet (Merck, Germany) for 1 minute then, dehydrated in increasing alcohol concentrations. The tissues were cleared in xylene, mounted and then, cover-slipped. ImageJ software was used to measure total and damaged area of the optic chiasm. The extent of demyelination was calculated as the percentage of demyelinated area/total area. The average of the extent of demyelination for each

animal was calculated and statistical comparisons were made among the groups.

For FluoroMyelin (FM) staining, cryosections were incubated with the dye for 20 minutes and 4',6-diamidino-2-phenylindole (DAPI) for another 5 minutes, as stated in the manufacturer's protocol (Molecular Probes, UK). Olympus BX51 fluorescent microscope was used to observe the slides and photography was done using a DP-72 camera.

Quantitative real-time polymerase chain reaction

The optic chiasmata were collected from the mice brains for total RNA isolation using the RiboEx solution (Gene All, Korea) as stated in the manufacturer's protocol. Reverse transcription and cDNA production were performed by a cDNA reverse transcription Kit (Parstous Biotechnology, Iran) based on the manufacturer's instructions. The produced cDNA was used for analysis of gene expression. Real-time polymerase chain reaction (q-PCR) was performed by a Real q-PCR Master Mix (Ampliqon, Denmark,) on a Rotor-Gene device (Qiagen, Germany). All reactions were performed in duplicate. The relative amount of mRNA was calculated using the delta-delta cycle of threshold (Ct) method, and normalization was done using *Gapdh* as a housekeeping gene. Primer sequences are shown in Table 1.

Visual evoked potential recording

VEP recording is frequently used for measuring electrical activity of optic pathways in response to a light stimulus. This recording can reflect the extent of demyelination in the optic chiasm region (22). Mice were anesthetized, then, a screw as a recording electrode, was fixed on the surface of occipital cortex of the skull, posterior to Bregma: 3.8 mm, lateral: 3 mm to right. The reference electrode was located on the prefrontal cortex anterior to Bregma: +1, lateral: 1 mm to the left. To tightly fix the electrodes, dental cement was used in the place then, the incision was sutured.

Before VEP recording, the mice were maintained for 10 minutes in a dark recording chamber to adapt. For delivering flashing light, an LED light was placed 2 cm away from the left eye. The light was set to flash 150 times at a frequency of 0.5 Hz using a stimulator/recorder (sampling rate: 10000, bandpass filters: 10 to 100 Hz, gain: 1000X; Science Beam Co., Iran). Responses were averaged and analyzed. The latency of the recorded P1 wave was considered an index of myelination/demyelination of the optic chiasm.

Statistical analysis

Changes in the extent of demyelinated areas and P1 latency in VEP recordings and FluoroMyelin data were analyzed by Two-tailed unpaired t test. Inflammation scores were analyzed by non-parametric Mann-Whitney test. $P < 0.05$ were considered statistically significant.

Results

Metformin protects the optic chiasm from demyelination

In order to study the extent of demyelination at dpi 3 and 7, we used LFB and FM staining on frozen sections obtained from the LPC-demyelinated mouse optic chiasmata (26). The assessments done based on LFB staining showed that on dpi 7, in the treated animals, the extent of demyelination was lower than the non-treated animals. The difference between the two groups on dpi 7 was statistically significant ($P < 0.05$, Fig.1B, C). There was no difference between these two groups on dpi 3.

In order to verify the amount of demyelination, we analyzed the extent of demyelination in micrographs obtained from sections stained with FM. In line with LFB staining results, there was a lower amount of demyelination on dpi 7 in metformin-treated animals compared to non-treated group (Fig.2A, B). These data showed a marked protective effect for metformin against the demyelination process.

Table 1: Sequence of primers were used for real-time polymerase chain reaction amplification

Gene	Primers sequence (5'-3')	Annealing temperature	Product length (bp)
<i>Mbp</i>	F: CCCTCAGAGTCCGACGAGCT	62	218
	R: GCACCCCTGTCACCGCTA		
<i>Gapdh</i>	F: GGTCGGTGTGAACGGATTGG	61	198
	R: ATGACAAGCTTCCCATTCTCGG		

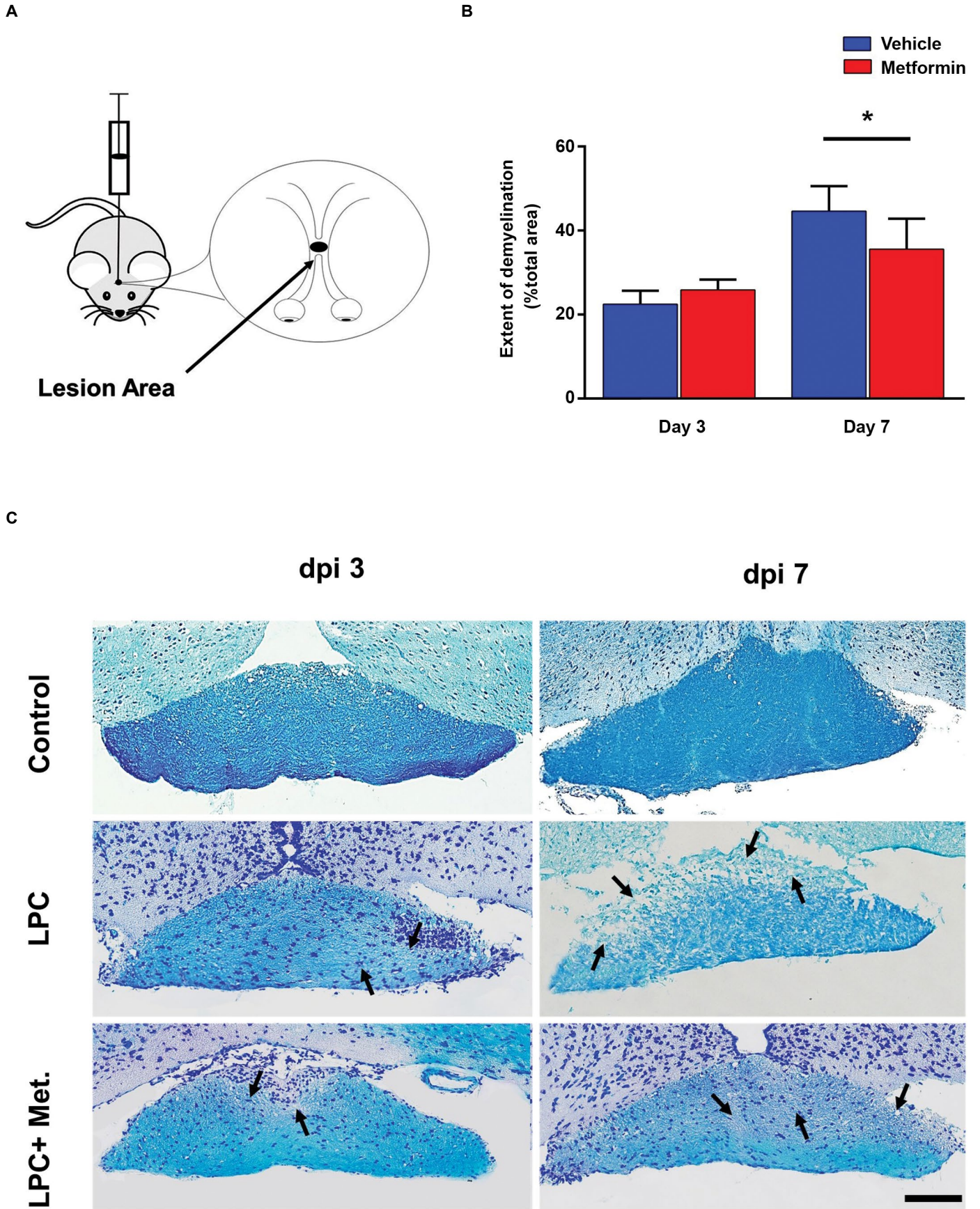
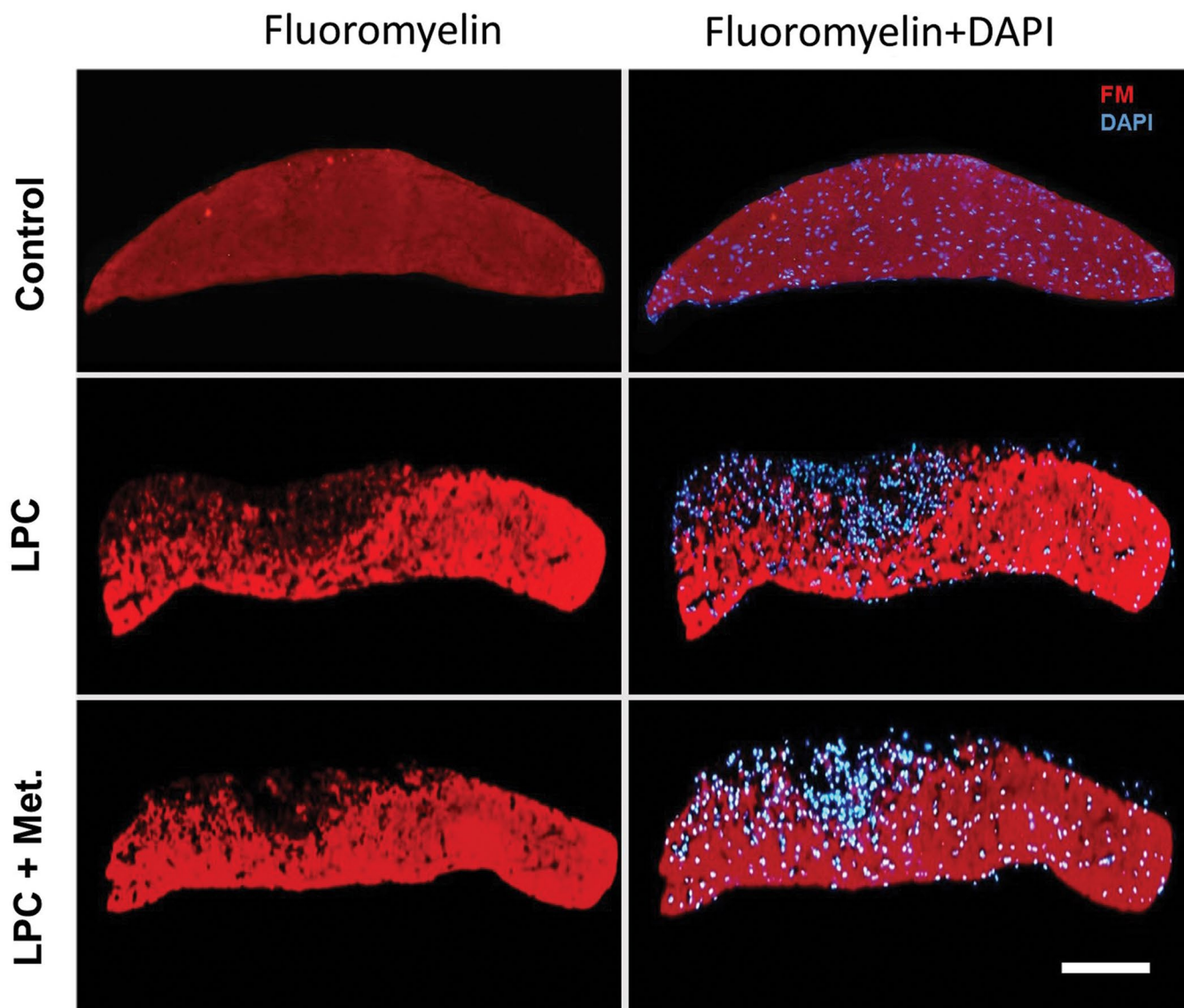


Fig.1: Metformin protects the optic chiasm from demyelination. **A.** Schematic representation of site of injection. **B.** Quantified data for part C. **C.** Representative of LFB-stained micrographs showing the effect of metformin on demyelination in mouse optic chiasm on dpi (days post injection) 3 and 7. The arrows show the demyelinated area (scale bar: 50 μ m). Data are shown as mean \pm SD (n=3 mice per group). *, P<0.05 shows significant differences compared vehicle, LFB; luxol fast blue, LPC; Lysophosphatidylcholine, and Met; Metformin.

A



B

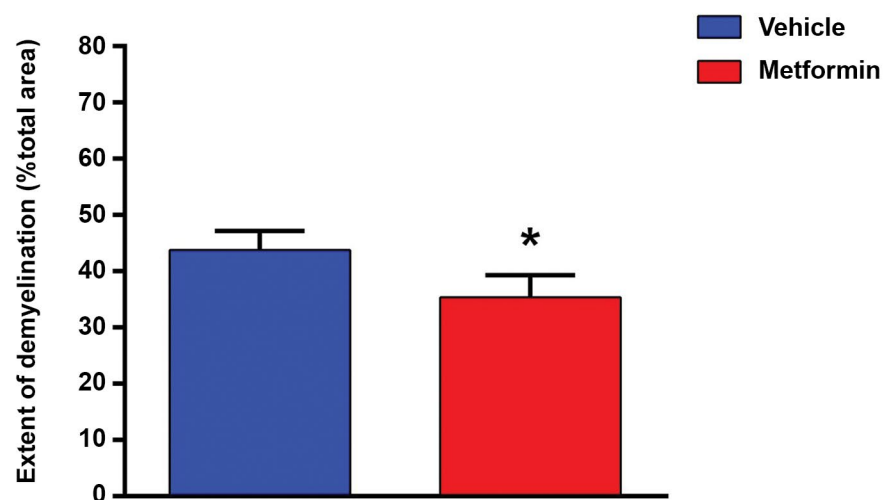
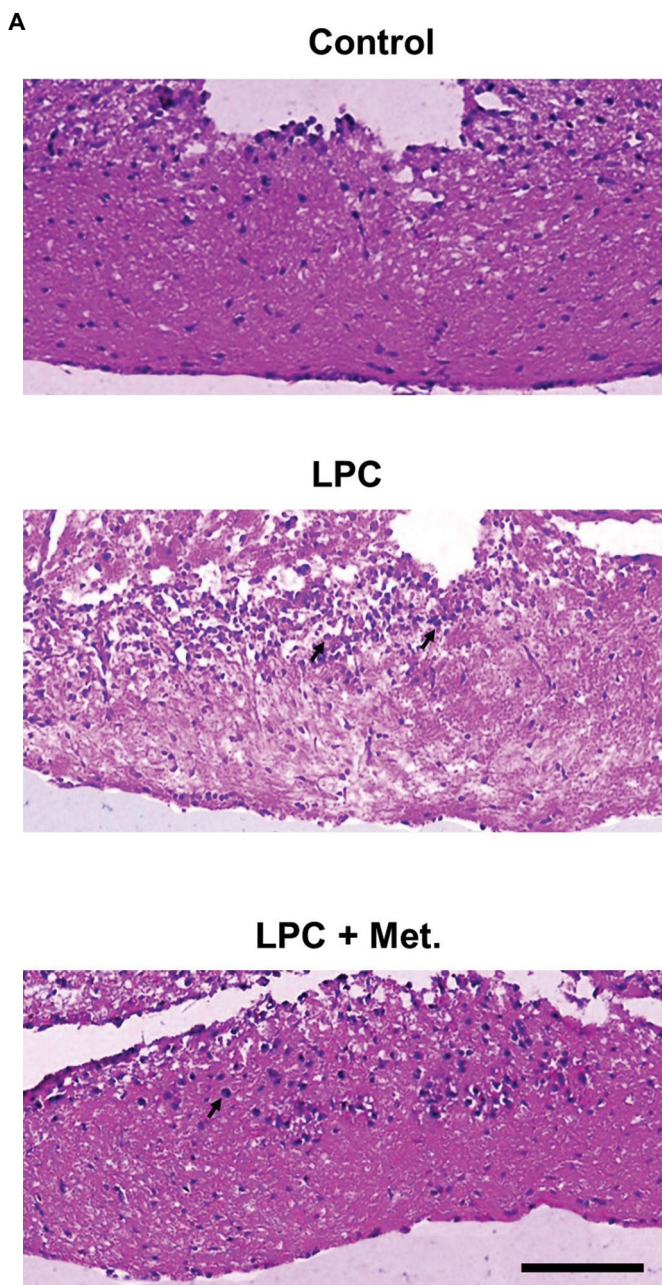


Fig.2: Metformin protects the optic chiasm from demyelination. **A.** Representative micrographs from FM-stained slides showing the effect of metformin on myelin repair in mouse optic chiasm on dpi 7. **B.** Quantified data for the extent of demyelination from FM-stained optic chiasmata (Scale bar: 50 μ m). Data are shown as mean \pm SD (n=3 mice per group).

*; P<0.05 shows significant differences compared to LPC, LPC; Lysophosphatidylcholine, and Met; Metformin.

The effects of metformin on inflammation severity following Lysophosphatidylcholine-induced demyelination

LPC administration causes a significant leakage in the blood-brain barrier (BBB) at the injection site (27) which enables robust infiltration of immune cells to the lesion site. To measure the extent of inflammation induced by LPC, the brain samples were collected on dpi 3 for H&E staining. In line with our previous studies (27, 28), our results showed that LPC caused a substantial inflammatory reaction in the injection site (Fig.3A). Quantitative analysis of micrographs obtained from stained sections by a blind pathologist, showed a significant reduction in inflammation score of optic chiasmata in metformin-treated animals (Fig.3B, $P < 0.05$). These results showed that the anti-inflammatory effect of metformin probably plays a positive role in its effect on the extent of demyelination.



B

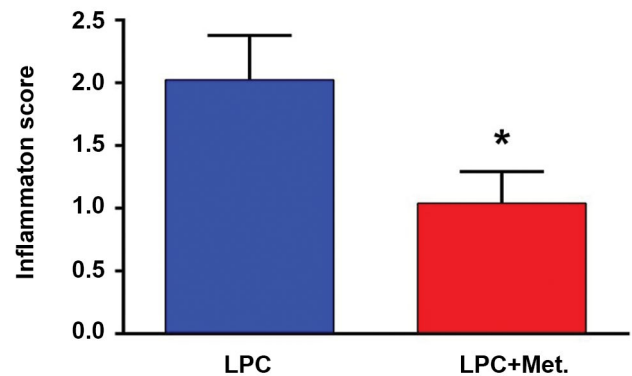


Fig.3: Metformin reduced inflammation in the optic chiasm following LPC-induced demyelination. **A.** Representative micrographs from H&E-stained slides showing the effect of metformin on inflammation in mouse optic chiasm on 3 dpi. **B.** Quantitative analysis of H&E-stained sections comparing the inflammation scores for LPC+Met and LPC groups on dpi 3. The arrows show the inflammatory cells (Scale bar: 50 μ m). Data are shown as mean \pm SD ($n=3$ mice per group). *; $P < 0.05$ shows significant differences compared to LPC group, LPC; Lysophosphatidylcholine, and Met; Metformin.

The effect of metformin on level of gene expression

For further investigation of the molecular basis of these results, we studied the expression of myelinating cell marker, *Mbp*, in treated and non-treated animals on dpi 7 as well as in the control animals. The analysis of gene expression using real-time PCR, showed that the expression of *Mbp* was increased in metformin-treated animals in comparison with non-treated animals. These results may indicate that metformin has exerted protective effects on myelinating cells (Fig .4, $P < 0.01$).

The effects of metformin on the integrity of visual pathway

Visual evoked potential (VEP) recording is a noninvasive approach to assess the functional integrity of optic pathway. While demyelination delays signal conduction, protection restores it to near the normal values. VEPs recorded from the mice visual cortices were used to examine effect of metformin on demyelination of the optic chiasm (22-29). The most stable component of VEP, P1-wave, which was sensitive to LPC-induced optic chiasm demyelination, was selected for further analysis. The recording site and time points of recordings are presented in Figure 5A. The sample VEP recording and P1-latency obtained from a control animal are presented in Figure 5A. Quantitative analysis of P1-wave latency is presented in Figure 5B. Our results shows that, P1 latency was increased on dpi 7 in LPC-injected mice but metformin treatment during days 0-7, reduced the P1 latency time recorded on dpi 7. In fact, metformin administration protected the functional integrity of visual pathway.

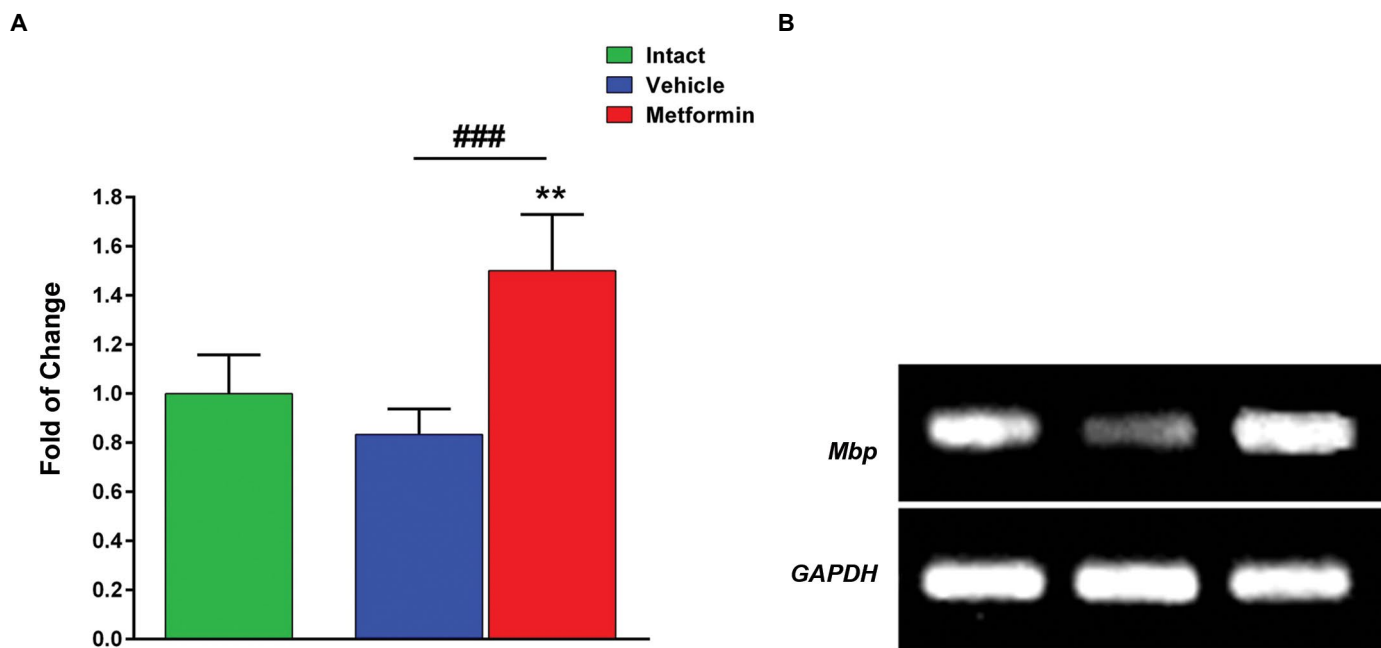


Fig.4: Metformin enhanced level of gene expression. **A.** Changes in the expression of *Mbp* genes within the optic chiasmata following LPC injection on dpi 7 for metformin and non-treated groups. **B.** Representative of *Mbp* and *Gapdh* bands on gel electrophoresis. Data are shown as mean \pm SD (n=6 mice per group).

**; P<0.01 shows significant differences compared to intact, ###; P<0.01 shows significant differences compared to vehicle, and LPC; Lysophosphatidylcholine.

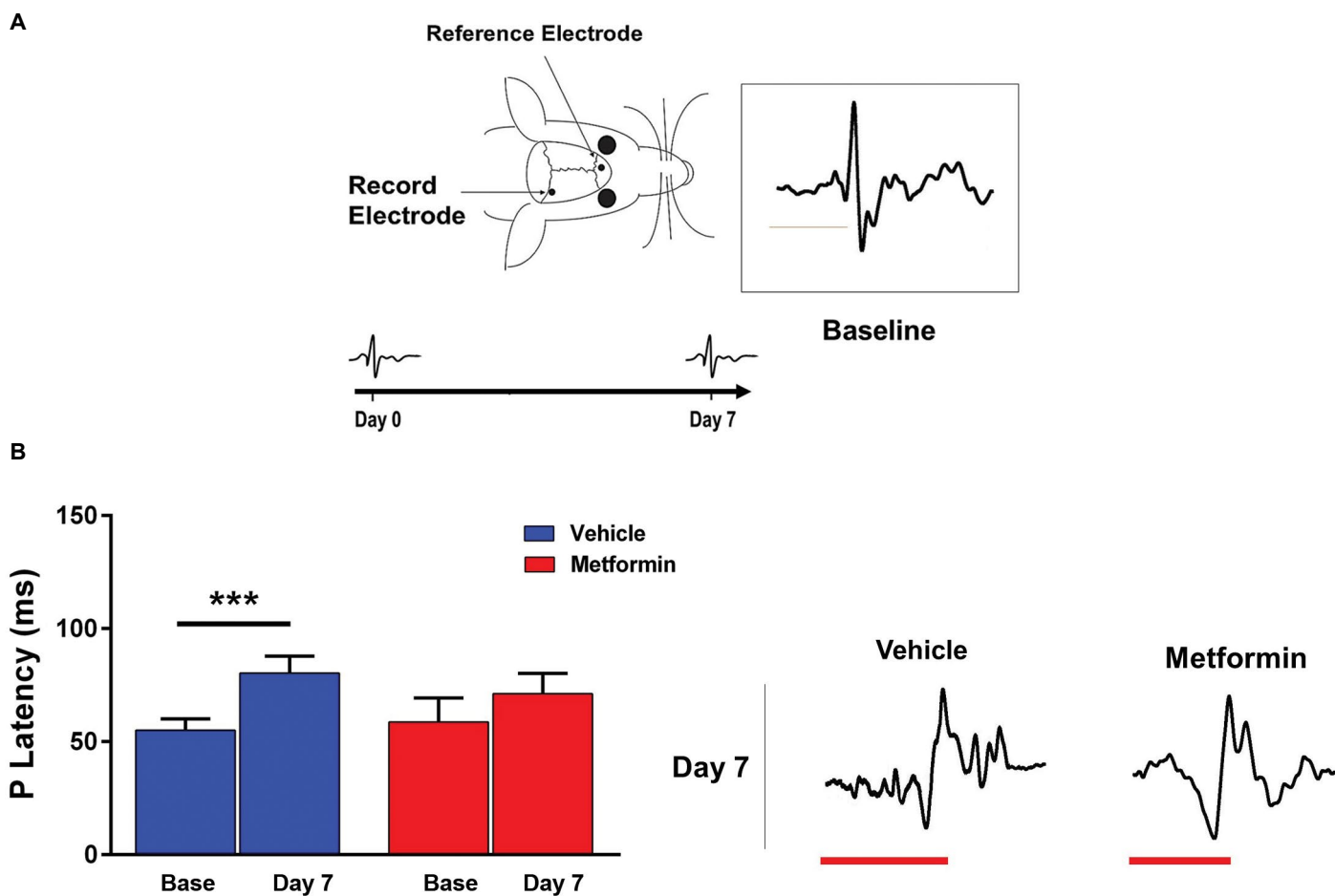


Fig.5: Metformin enhanced recovery of optic tract function after LPC-induced demyelination. **A.** Schematic representation of sites of electrode positioning and experimental procedure for VEP recordings. Box: A sample recording representing the baseline P1-latency. **B.** Results of quantitative analysis of P1 wave latency at baseline and on 7 dpi. Representative traces for day 7 are mentioned below the graph. Data are shown as mean \pm SD (n=5 mice per group). ***; P<0.001 shows significant differences compared to base, LPC; Lysophosphatidylcholine, and VEP; Visual evoked potential.

Discussion

Searching for neuroprotective compounds is a major part of developing new treatments for inflammatory and degenerative neurological disorders including MS. One of these medications that have been shown to have beneficial effects in several studies, is metformin. Metformin as the first-line medication for diabetes mellitus, is famous for its few side effects (30, 31). It was shown that metformin exerts many beneficial effects in various pathophysiological conditions. It has anti-oxidative (32), anti-apoptotic (33) and anti-inflammatory (13) effects in nervous system diseases. Prolonged metformin therapy decreases the risk of stroke and cardiovascular mortality by 26% (34). After oral administration, this compound crosses the BBB and activates AMPK pathway in the brain cells (11) which plays a fundamental role in cellular processes. There are several studies demonstrating the protective effects of metformin on neuronal cells in a variety of CNS diseases including Parkinson's and Alzheimer's diseases (21)(Chiang, 2016 #27; Wang, 2016 #28; Bayliss, 2016 #29; Inzucchi, 2014 #63). Taken the results of all the above-mentioned studies together, it was hypothesized that metformin may have positive effects on the pathology of MS.

In this study, we examined the protective effects of metformin on optic chiasm myelination. Our findings showed that metformin had a protective effect against optic chiasm demyelination induced by LPC. One of the major cellular components triggered by metformin is AMPK. AMPK plays a key role as a master regulator of cellular energy homeostasis. Therefore, this protection may be resulted from its effect on mitochondrial functions as it is widely reported as one of the metformin's mechanism of action in cell protection. It was also reported that metformin has protective effect on neural and oligodendroglial cells in animal models of cerebral ischemic injury through action on mitochondrial dysfunction which usually occur under neurodegenerative conditions (11, 12).

Neuroinflammation is an essential immune response which includes cellular and vascular events which play a crucial role in escaping the damaging circumstance and controlling the disrupted homeostasis (35). Acute inflammation is a short-term occurrence which is associated with local blood flow increase, elevated permeability in vascular system, immune cell influx, fluid leakage, increased release of cytokines and free radicals (36, 37). In view of MS as an autoimmune disorder mediated by the Th1 and Th17 immune cells, inhibition of the activity of these immune cells can down-modulate the pro-inflammatory immune response and avoid inflammatory response-mediated CNS impairments (38). In this study, we showed that metformin could decrease the inflammatory response after induction of demyelination by LPC

administration to the optic chiasm. Our findings are in line with previous studies which showed that metformin can modulate the immune response via decreasing the activity of invading cells and at the same time, increasing the activity of regulatory cells which limits the extent of damage (16, 17).

The results of the molecular investigations showed a significant change in the *Mbp* expression in the injured chiasmata on dpi 7. In an intact tissue, myelinating cells are constantly producing mRNA for Mbp protein maintenance and if there is a reduction in the number of these cells, lower levels of *Mbp* mRNAs will be observed. Our findings show that there was a reduction in *Mbp* expression in non-treated group while an increase in metformin-treated group could be seen. Increased *Mbp* expression in metformin group could be partly due to the greater number of protected myelinating cells and in part, it may be related to the fact that newly formed OLs in the area express higher levels of *Mbp* gene for new myelin sheath production.

We next focused on the functional aspects of the effect of metformin on demyelinated optic chiasm. Our findings showed that metformin prevented functional impairments in the optic pathway after LPC injection to the optic chiasm as the P1 wave latency was preserved from increasing to the higher levels. Our results showed that metformin could attenuate the impairment in the mice visual pathway which was in accordance with the results of our histological analysis. Functional effects of metformin in the context of neural degeneration were studied previously, where this compound improved the memory function in the hypoxic/ischemic brain injured mice, which is in line with our results (24, 39).

In this study, several limitations must be taken into account. First of all, although we found the beneficial effects of metformin on decreasing the extent of demyelination, the precise mechanism(s) remains to be investigated. Second, it is also remained unclear whether the observed effects are just due to the protective effect of metformin on myelin sheets or it is partially the result of accelerating the remyelination process. Therefore, according to the limitations of our study, we propose conducting further research on the actual mechanism of the observed effect. Despite the promising results of our study, it would be very important to conduct further studies in MS patients by carrying out clinical trials focused on protective capabilities of metformin as an FDA-approved drug.

Conclusion

In this study, the neuroprotective effects of metformin on mice optic chiasmata damaged by LPC were examined. Our findings showed that metformin inhibited inflammation and protected myelin sheets and significantly

preserved the functionality of optic tract as demonstrated by histological, molecular and functional assessments. These results may contribute to finding new therapeutic approaches for multiple sclerosis.

Acknowledgements

This work was financially supported by a grant from Tarbiat Modares University, Tehran, Iran (grant No. Med-46093) and Iran National Science Foundation (INSF, grant No. 95844516) and Royan Institute. There is no conflict of interest in this study.

Authors' Contributions

S.E.; Contributed to experiment design, performing the experiment, data analysis and drafting the manuscript. S.S.; Contributed to data analysis and project supervision. M.J.; Contributed to conception and experiment design, data analysis, finalizing the manuscript and project supervision. All authors read and approved the final manuscript.

References

- Patrikios P, Stadelmann C, Kutzelnigg A, Rauschka H, Schmidbauer M, Laursen H, et al. Remyelination is extensive in a subset of multiple sclerosis patients. *Brain*. 2006; 129(Pt 12): 3165-3172.
- Correale J, Marrodan M, Ysraelit MC. Mechanisms of neurodegeneration and axonal dysfunction in progressive multiple sclerosis. *Biomedicines*. 2019; 7(1): pii: E14.
- Franklin RJ, Ffrench-Constant C. Remyelination in the CNS: from biology to therapy. *Nat Rev Neurosci*. 2008; 9(11): 839-855.
- Harlow DE, Honce JM, Miravalle AA. Remyelination Therapy in multiple sclerosis. *Front Neurol*. 2015; 6: 257.
- Chakraborty A, Chowdhury S, Bhattacharyya M. Effect of metformin on oxidative stress, nitrosative stress and inflammatory biomarkers in type 2 diabetes patients. *Diabetes Res Clin Pract*. 2011; 93(1): 56-62.
- Asadbegi M, Yaghmaei P, Salehi I, Ebrahim-Habibi A, Komaki A. Neuroprotective effects of metformin against A β -mediated inhibition of long-term potentiation in rats fed a high-fat diet. *Brain Res Bull*. 2016; 121: 178-185.
- El-Mir MY, Demaille D, R-Villanueva G, Delgado-Esteban M, Guigas B, Attia S, et al. Neuroprotective role of antidiabetic drug metformin against apoptotic cell death in primary cortical neurons. *J Mol Neurosci*. 2008; 34(1): 77-87.
- Labuzek K, Liber S, Gabryel B, Okopien B. Metformin has adenosine-monophosphate activated protein kinase (AMPK)-independent effects on LPS-stimulated rat primary microglial cultures. *Pharmacol Rep*. 2010; 62(5): 827-848.
- Wang C, Liu C, Gao K, Zhao H, Zhou Z, Shen Z, et al. Metformin preconditioning provide neuroprotection through enhancement of autophagy and suppression of inflammation and apoptosis after spinal cord injury. *Biochem Biophys Res Commun*. 2016; 477(4): 534-540.
- Ge XH, Zhu GJ, Geng DQ, Zhang HZ, He JM, Guo AZ, et al. Metformin protects the brain against ischemia/reperfusion injury through PI3K/Akt1/JNK3 signaling pathways in rats. *Physiol Behav*. 2017; 170: 115-123.
- Jin J, Gu H, Anders NM, Ren T, Jiang M, Tao M, et al. Metformin protects cells from mutant huntingtin toxicity through activation of AMPK and modulation of mitochondrial dynamics. *Neuromolecular Med*. 2016; 18(4): 581-592.
- Bayliss JA, Lemus MB, Santos VV, Deo M, Davies JS, Kemp BE, et al. Metformin prevents nigrostriatal dopamine degeneration independent of AMPK activation in dopamine neurons. *PLoS One*. 2016; 11(7): e0159381.
- Nath N, Khan M, Paintlia MK, Singh I, Hoda MN, Giri S. Metformin attenuated the autoimmune disease of the central nervous system in animal models of multiple sclerosis. *J Immunol*. 2009; 182(12): 8005-8014.
- Kang KY, Kim YK, Yi H, Kim J, Jung HR, Kim IJ, et al. Metformin downregulates Th17 cells differentiation and attenuates murine autoimmune arthritis. *Int Immunopharmacol*. 2013; 16(1): 85-92.
- Park DW, Jiang S, Tadie JM, Stigler WS, Gao Y, Deshane J, et al. Activation of AMPK enhances neutrophil chemotaxis and bacterial killing. *Mol Med*. 2013; 19: 387-398.
- Sun Y, Tian T, Gao J, Liu X, Hou H, Cao R, et al. Metformin ameliorates the development of experimental autoimmune encephalomyelitis by regulating T helper 17 and regulatory T cells in mice. *J Neuroimmunol*. 2016; 292: 58-67.
- Paintlia AS, Mohan S, Singh I. Combinatorial effect of metformin and lovastatin impedes T-cell autoimmunity and neurodegeneration in experimental autoimmune encephalomyelitis. *J Clin Cell Immunol*. 2013; 4.
- Kukidome D, Nishikawa T, Sonoda K, Imoto K, Fujisawa K, Yano M, et al. Activation of AMP-activated protein kinase reduces hyperglycemia-induced mitochondrial reactive oxygen species production and promotes mitochondrial biogenesis in human umbilical vein endothelial cells. *Diabetes*. 2006; 55(1): 120-127.
- Isoda K, Young JL, Zirlik A, MacFarlane LA, Tsuboi N, Gerdes N, et al. Metformin inhibits proinflammatory responses and nuclear factor-kappaB in human vascular wall cells. *Arterioscler Thromb Vasc Biol*. 2006; 26(3): 611-617.
- Majithiya JB, Balaraman R. Metformin reduces blood pressure and restores endothelial function in aorta of streptozotocin-induced diabetic rats. *Life Sci*. 2006; 78(22): 2615-2624.
- Markowicz-Piasecka M, Sikora J, Szydłowska A, Skupien A, Mikiciuk-Olasik E, Huttunen KM. Metformin - a future therapy for neurodegenerative diseases : theme: drug discovery, development and delivery in alzheimer's disease guest editor: Davide Brambilla. *Pharm Res*. 2017; 34(12): 2614-2627.
- Pourabdolhossein F, Mozafari S, Morvan-Dubois G, Mirnajafi-Zadeh J, Lopez-Juarez A, Pierre-Simons J, et al. Nogo receptor inhibition enhances functional recovery following lysolecithin-induced demyelination in mouse optic chiasm. *PLoS One*. 2014; 9(9): e106378.
- Franklin K, Paxinos G. Paxinos and Franklin's the mouse brain in stereotaxic coordinates. 4th ed. Boston: Academic Press; 2012.
- Wang J, Gallagher D, DeVito LM, Cancino GI, Tsui D, He L, et al. Metformin activates an atypical PKC-CBP pathway to promote neurogenesis and enhance spatial memory formation. *Cell Stem Cell*. 2012; 11(1): 23-35.
- Yang J, Yan Y, Xia Y, Kang T, Li X, Ciric B, et al. Neurotrophin 3 transduction augments remyelinating and immunomodulatory capacity of neural stem cells. *Mol Ther*. 2014; 22(2): 440-450.
- Dehghan S, Hesaraki M, Soleimani M, Mirnajafi-Zadeh J, Fathollahi Y, Javan M. Oct4 transcription factor in conjunction with valproic acid accelerates myelin repair in demyelinated optic chiasm in mice. *Neuroscience*. 2016; 318: 178-189.
- Seyedsadr MS, Weinmann O, Amorim A, Ineichen BV, Egger M, Mirnajafi-Zadeh J, et al. Inactivation of sphingosine-1-phosphate receptor 2 (S1PR2) decreases demyelination and enhances remyelination in animal models of multiple sclerosis. *Neurobiol Dis*. 2019; 124: 189-201.
- Yazdi A, Baharvand H, Javan M. Enhanced remyelination following lysolecithin-induced demyelination in mice under treatment with fingolimod (FTY720). *Neuroscience*. 2015; 311: 34-44.
- Satarian L, Javan M, Kiani S, Hajikaram M, Mirnajafi-Zadeh J, Baharvand H. Engrafted human induced pluripotent stem cell-derived anterior specified neural progenitors protect the rat crushed optic nerve. *PLoS One*. 2013; 8(8): e71855.
- Inzucchi SE, Lipska KJ, Mayo H, Bailey CJ, McGuire DK. Metformin in patients with type 2 diabetes and kidney disease: a systematic review. *JAMA*. 2014; 312(24): 2668-2675.
- Werner EA, Bell J. CCXIV.—The preparation of methylguanidine, and of $\beta\beta$ -dimethylguanidine by the interaction of dicyanodiamide, and methylammonium and dimethylammonium chlorides respectively. *J Chem Soc, Trans*. 1922; 121: 1790-1794.
- Ullah I, Ullah N, Naseer MI, Lee HY, Kim MO. Neuroprotection with metformin and thymoquinone against ethanol-induced apoptotic neurodegeneration in prenatal rat cortical neurons. *BMC*

- Neurosci. 2012; 13: 11.
33. Alzoubi KH, Khabour OF, Al-Azzam SI, Tashtoush MH, Mhaidat NM. Metformin eased cognitive impairment induced by chronic l-methionine administration: potential role of oxidative stress. *Curr Neuropharmacol.* 2014; 12(2): 186-192.
 34. Selvin E, Hirsch AT. Contemporary risk factor control and walking dysfunction in individuals with peripheral arterial disease: NHANES 1999-2004. *Atherosclerosis.* 2008; 201(2): 425-433.
 35. Pandey A, Kumar VL. Protective effect of metformin against acute inflammation and oxidative stress in rat. *Drug Dev Res.* 2016; 77(6): 278-284.
 36. Medzhitov R. Origin and physiological roles of inflammation. *Nature.* 2008; 454(7203): 428-435.
 37. Begum R, Sharma M, Pillai KK, Aeri V, Sheliya MA. Inhibitory effect of *Careya arborea* on inflammatory biomarkers in carrageenan-induced inflammation. *Pharm Biol.* 2015; 53(3): 437-445.
 38. Heikamp EB, Patel CH, Collins S, Waickman A, Oh MH, Sun IH, et al. The AGC kinase SGK1 regulates TH1 and TH2 differentiation downstream of the mTORC2 complex. *Nat Immunol.* 2014; 15(5): 457-464.
 39. Dadwal P, Mahmud N, Sinai L, Azimi A, Fatt M, Wondisford FE, et al. Activating endogenous neural precursor cells using metformin leads to neural repair and functional recovery in a model of childhood brain injury. *Stem Cell Reports.* 2015; 5(2): 166-173.
-

Bioinspired Device Improves The Cardiogenic Potential of Cardiac Progenitor Cells

Zahra Shams, M.Sc.¹, Babak Akbari, Ph.D.^{1*}, Sarah Rajabi, Ph.D.^{2*}, Nasser Aghdami, M.D., Ph.D.³

1. Department of Life Science Engineering, Faculty of New Sciences and Technologies, University of Tehran, Tehran, Iran

2. Department of Cell Engineering, Cell Science Research Centre, Royan Institute for Stem Cell Biology and Technology, ACECR, Tehran, Iran

3. Department of Regenerative Medicine, Cell Science Research Centre, Royan Institute for Stem Cell Biology and Technology, ACECR, Tehran, Iran

*Corresponding Addresses: P.O.Box: 14395-1561, Department of Life Science Engineering, Faculty of New Sciences and Technologies, University of Tehran, North Kargar St., Tehran, Iran.

P.O.Box: 16635-148, Department of Cell Engineering, Royan Institute, Banihashem Sq., Banihashem St., Resalat Highway, Tehran, Iran

Emails: babakbari@ut.ac.ir, srajabi@royaninstitute.org

Received: 21/October/2019, Accepted: 09/December/2019

Abstract

Objective: Functional cardiac tissue engineering holds promise as a candidate approach for myocardial infarction. Tissue engineering has emerged to generate functional tissue constructs and provide an alternative means to repair and regenerate damaged heart tissues.

Materials and Methods: In this experimental study, we fabricated a composite polycaprolactone (PCL)/gelatine electrospun scaffold with aligned nanofibres. The electrospinning parameters and optimum proportion of the PCL/gelatine were tested to design a scaffold with aligned and homogenized nanofibres. Using scanning electron microscopy (SEM) and mechanophysical testes, the PCL/gelatine composite scaffold with a ratio of 70:30 was selected. In order to simulate cardiac contraction, a developed mechanical loading device (MLD) was used to apply a mechanical stress with specific frequency and tensile rate to cardiac progenitor cells (CPCs) in the direction of the aligned nanofibres. Cell metabolic determination of CPCs was performed using real-time polymerase chain reaction(RT-PCR).

Results: Physicochemical and mechanical characterization showed that the PCL/gelatine composite scaffold with a ratio of 70:30 was the best sample. *In vitro* analysis showed that the scaffold supported active metabolism and proliferation of CPCs, and the generation of uniform cellular constructs after five days. Real-time PCR analysis revealed elevated expressions of the specific genes for synchronizing beating cells (*MYH-6*, *TTN* and *CX-43*) on the dynamic scaffolds compared to the control sample with a static culture system.

Conclusion: Our study provides a robust platform for generation of synchronized beating cells on a nanofibre patch that can be used in cardiac tissue engineering applications in the near future.

Keywords: Aligned Scaffold, Cardiac Progenitor Cells, Cardiac Tissue Engineering, Mechanical Simulation

Cell Journal(yakhteh), Vol 23, No 1, April-June (Spring) 2021, Pages: 129-136

Citation: Shams Z, Akbari B, Rajabi S, Aghdami N. Bioinspired device improves the cardiogenic potential of cardiac progenitor cells. Cell J. 2021; 23(1): 129-136. doi: 10.22074/cellj.2021.7232.

This open-access article has been published under the terms of the Creative Commons Attribution Non-Commercial 3.0 (CC BY-NC 3.0).

Introduction

Cardiovascular diseases are one of the leading causes of death worldwide, with almost 40% of morbidity and mortality in both developed and developing countries (1). In 2013, more than 17.3 million deaths were attributed to cardiovascular diseases and this number is expected to exceed 23.6 million by 2030 (2). Various types of treatments used in patients diagnosed with heart failure include non-invasive methods (medications) and invasive methods such as angioplasty, ventricular assist devices, pacemakers, and eventually heart transplantation (3, 4). In these methods, the main goal is to help the heart to partially restore cardiac function and prevent disease progression, despite the loss of some cardiac cells. None of these procedures repair lost tissue. The heart transplant, which is considered an end-stage treatment, has many limitations due to the lack of donors and complications associated with immune suppressive treatments (5).

Therefore, scientists have focused on modern

approaches such as cell therapy and tissue engineering (4). In cell therapy, viable cells can be directly injected into the infarcted area or arterially infused (6). These procedures were not very successful because only 15% of the cells could reach the intended site following the arterial injection. In the case of direct injections also, only a small number of injected cells could function properly due to the lack of an appropriate scaffold for feeding and growth (7, 8).

In this regard, scaffolds that contain cardiac progenitor cells (CPCs) can function with high productivity in therapeutic procedures (9-11). The suitable scaffold for cardiac tissue engineering should mimic the natural extracellular matrix (ECM) of cardiomyocytes (12, 13). In addition to its appropriate adhesion and strength, as heart tissue is imposed under tension loadings of continuous and cyclic contraction and expansion, a suitably fabricated scaffold should withstand this level of tension to provide mechanical support for cardiac cells during the repair

period (14-16). Heart muscle has a Young's elastic modulus range from 10-20 kPa in diastole with a tension rate of <10%. At the end of diastole, Young's modulus will increase to 50 in normal cardiac muscle and 200–300 kPa in the damaged heart. Therefore, an elastomer scaffold such as polycaprolactone (PCL) has a very appropriate application in contractive cycles of cardiac tissue (17). PCL has good mechanical properties and a controllable degradability rate (17, 18). However, intrinsically it is hydrophobic and cannot provide the appropriate conditions for cell adhesion. Therefore, it is better to integrate a natural scaffold such as gelatine with PCL to produce a composite with better adhesion and mechanical strength. The composite ratio of these polymers is very important (17, 18).

An important issue with the transplantation of cell-seeded scaffolds to the infarcted area is that the seeded cells lack the ability to regulate themselves with other natural cardiomyocytes during beating. Therefore, they will cause heart arrhythmia (19). Exposing CPCs to mechanical loadings at a frequency and tension similar to natural tissues will increase expressions of the genes related to cell contraction and synchronization (20-22).

Mechanical loading transmission in a specific, direct way has a greater impact on the speed and quality of the conduction (23, 24). Thus, in this study, we designed a two-dimensional (2D) aligned nanofibre composite scaffold that was fabricated with the appropriate rate of two PCL and gelatine polymers using electrospinning techniques with a rotating mandrel. We exposed the scaffold to mechanical loading in the direction of the parallel nanofibres at specific frequency and tension rates created by a mechanical loading device (MLD). Therefore, we simulated the conditions of natural cardiac cells as much as possible *in vitro*. Although numerous researches have been conducted that imposed mechanical and electrical loadings to the scaffolds with cells (25-27), mechanical loadings have not been directly imposed on 2D anisotropic electrospun scaffolds in the direction of parallel nanofibres that contain CPCs.

In the present study, mechanical loading was transferred in the direction of the aligned nanofibres; therefore, the interactive effects of anisotropy and scaffold tension induced the human cardiac progenitor cells (hCPCs) to differentiate into cardiac cells.

Materials and Methods

Scaffold fabrication

In this experimental study, a mixture of formic acid and acetic acid (7:3) (Sigma Aldrich Corporation) was used as solvent to obtain a 14% (wt %) polymer solution (28). The proportion of formic acid was Greater in the solvent because of its high dielectric constant (29). To achieve optimum electrospinning parameters for an aligned and homogenized nanofibre scaffold, PCL (mw: 80 000 g/mol, Sigma Aldrich) and porcine skin gelatine type A (Sigma Aldrich) polymers were mixed at a PCL/gelatine ratio of 70:30 and added to the solvent. The solvent was shaken on a stirrer at 500 rpm for one hour without heat. Electrospinning techniques were applied to fabricate the scaffold from the prepared solution. The Mandrel rotation technique was used to have aligned nanofibres. To obtain optimum electrospinning parameters, we used varied feeding ratios, needle distance to collector, voltage, and the Mandrel rotation speed [(30), Table 1]. The samples were prepared for scanning electron microscopy (SEM) imaging to assess the morphological features, level of homogeneity, and direction of the nanofibres. To obtain the image from a polymer surface using electron radiation, a gold coating should be applied in order to make a conductive surface. The samples were imaged at 2000 V.

After specifying the appropriate electrospinning parameters, we assessed the different ratios in terms of hydrophilicity and mechanical strength. To achieve this purpose, three scaffold samples were fabricated with PCL/gelatine composite ratios of 80:20, 70:30 and 60:40 according to optimum electrospinning parameters.

Table 1: Different electrospinning parameters of the polycaprolactone (PCL)/gelatine (70:30) at a 14% (wt%) concentration at room temperature

Sample	Rate (ml/hour)	Distance: Needle to collector (cm)	Voltage (kV)	Collector speed (RPM)	Electrospinning Time (minutes)
A1	0.1	15	17	2000	10
A2	0.2	12	15	2000	15
A3	0.1	12	12	1800	10
B1	0.3	10	17	1500	20
B2	0.3	10	17	2000	20
B3	0.3	10	17	2500	20

According to SEM studies, the scaffold diameter distribution and discrepancy levels were compared using SPSS software in order to detect those composites with the highest homogeneity. Hydrophilicity was studied using contact angle tests in the three scaffold composites with different ratios. The static contact angle was measured with the sessile drop technique by placing a 3 μ l droplet on a polymer surface to obtain images with a camera when the droplet stabilized. Mechanical strength was compared among the three composite ratios using an Instron TM-SM (Instron®, UK). First, the length and diameter values were measured in the samples, then a tension force was imposed on samples in the direction of the nanofibres with a strain rate of 5 mm/minute (31). After five repetitions for each sample, tension-strain curves were plotted and compared, and the best electrospinning parameters and polymer ratio to fabricate the main scaffold were chosen.

Cell viability assessment

Human cardiac progenitor cells (hCPCs) were purchased from Royan Institute (code no. RSCB0180, Tehran, Iran). The cells were cultured in a culture medium that included Iscove's modified Dulbecco's medium (IMDM, Sigma), 1% L-glutamine (Invitrogen), non-essential amino acids (Invitrogen), penicillin/streptomycin (Invitrogen) and 10% fetal bovine serum (FBS, Gibco). The medium was changed every two days. Cells were passaged with 0.025% trypsin/EDTA (Gibco) for 3 minutes at 37°C. Gelatine is a hydrophilic polymer, and the nanofibre morphology could be destroyed in aqueous fluids. Therefore, the nanofibre was cross-linked by treatment with 25% glutaraldehyde (Merck, Germany) in a desiccator for six days. Approximately 3000 cells were cultured on scaffolds for two, four, and six days. The MTS (Promega, G5421) assay was performed to determine cytotoxicity at the specified time and according to the manufacturer's instructions. Absorbance was measured at 490 nm using an enzyme-linked immunosorbent assay (ELISA) plate reader (Thermo Scientific Multiscan Spectrum). The PCL scaffold was used as the control group.

Mechanical loading device fabrication

To mimic the morphological and functional properties of native cardiomyocytes in the body, the cells that were seeded on the scaffold should be exposed to mechanical loading according to a normal heart beat (32-34). Therefore, a device was designed where its applied force could be controlled with specific tension rate and frequency (Fig.1). This device was designed with a stainless steel body and an armature that could be run according to the frequency and force values determined, and confirmed by a frequency generator board. The armature included a coil and core placed inside. The core was connected to a metal shaft. The shaft passed through a hole in the bottle lid and connected to two steel bases inside the bottle. The scaffold was placed on these bases. The coil could generate a strong magnetic field with an imposed voltage of 5 V (35), where

the core would move in the direction of the magnetic field and create a distance between two bases. After the imposed voltage is disconnected, the bases return to the initial locations. The distance between two bases and the time switch were considered to be capable of generating a tension force with a 10% strain and frequency of 1 Hz (25, 33, 35, 36) in the scaffold, which was adhered to two bases with antibacterial silicone glue. All parts that were in direct and indirect contact with the scaffold were made of Teflon and steel so they could be autoclaved.

The voltage input of the armature was turned on and off by a frequency generator board (Fig. 1, See supplementary online information at www.celljournal.org). The scaffold could be exposed to a 10% strain per second. In order to set a temperature of 37°C for cells without an incubator, we designed a system to control the temperature, which included a heating element, thermostat board, relay to turn the currents on and off, a non-contact thermal sensor for temperature control and a display device to represent temperature values during each moment (Fig.2, See supplementary online information at www.celljournal.org). The non-contact sensor mounted on the bottle sends infrared light into the cell culture medium, measures the returned light and determines the internal temperature of the culture container. If the recorded temperature is less or more than 37°C, the sensor would send an on/off command to the thermostat board and relay. By using the mentioned system and continuous monitoring temperature on the display, we were assured that the temperature was appropriate for the cultured cells.

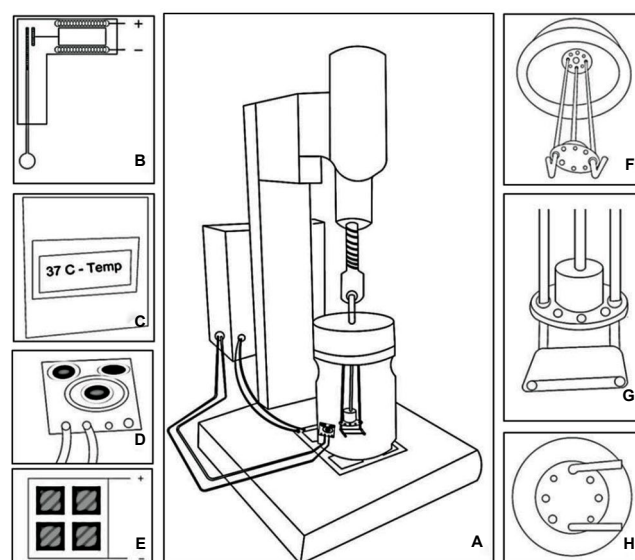


Fig.1: Assembly simulation of the mechanical loading device (MLD). **A.** MLD schematics. **B.** Armature for applying the mechanical load. **C.** Frequency board and heat controller in a box. The LCD embedded in the box displays the off/on mode of the heater and the temperature of the culture media in the bottle. **D.** Non-contact infrared temperature sensor measures the media temperature. **E.** Steel holder, which includes a 10x10 cm heater at the bottom of the steel plate. **F.** Steel bases attached to the door. The steel shaft attached to the armature core causes two bases to open and close at a specific frequency. **G.** Electrospun scaffold located on the steel bases. **H.** Teflon piece with eight holes (four optional axes of force). R=2 cm.

Mechanical loading device experiment

CPCs were seeded on the nanofibre composite scaffold at 2×10^6 per 2×2 cm² and placed in the cell culture medium. One of the scaffolds was placed on the stainless-steel bases in the mechanical loading device (MLD). After three days in a fixed culture, the MLD was turned on and the cell-seeded scaffold was exposed to a mechanical loading in the direction of aligned parallel nanofibres at 10% elongation and frequency of 1 Hz for five days (33, 35). The temperature, humidity, oxygen, and pH were controlled in the culture environment to provide an appropriate environmental condition for cell growth and differentiation. To achieve this aim, the culture medium was changed daily to keep pH and oxygen levels at constant values (25). Also, the inner container temperature was monitored on an LCD display. During this period, the control scaffold was placed in an incubator with static culture medium. After applying the mechanical loading for five days, we prepared both scaffolds for imaging via SEM and gene expression analysis by real-time polymerase chain reaction (RT-PCR).

Scanning electron microscopy images in the main and control scaffolds

Samples were fixed in 2% glutaraldehyde in 0.1 M PBS and left for 24 hours at 4°C. The samples were washed with 0.1 M PBS and fixed in 1% OsO₄ in 0.1 M PBS (pH=7.3) for 2 hours at 25°C. The samples were subsequently dehydrated in a graded ethanol-water series to 100% ethanol, then allowed to completely dry. Finally, the samples were mounted on aluminium stubs and coated with a thin layer of gold. Cell morphology on the scaffolds was analysed with a scanning electron

microscope (VEGA\TESCAN, Czech Republic) at an operating voltage of 15 kV.

Determination of gene expression

In the present study, the expression levels of three genes (*TTN*, *MYH-6* and *GJA1*) were analysed and compared by real-time PCR (RT-PCR) in the dynamic and static culture conditions. RNA was extracted manually with TRIzol reagent (Ambion) and chloroform according to the manufacturer's instructions. First strand cDNA synthesis was performed with a TaKaRa kit. Real-time PCR was performed using three cell samples: CSCs without any scaffolds, and cells seeded on scaffolds under static and dynamic conditions. Each condition was repeated four times (primer sequences in Table 1, Supplementary Information).

Statistical analysis

All data were expressed as mean \pm standard error mean. Statistical analysis was performed using one-way analysis of variance (ANOVA) followed by the appropriate post hoc test in Excel software (Microsoft Excel 2010). P values were considered significant at: *P <0.05, **P <0.01, and ***P <0.001.

Results

Scaffold characterization

Figure 2 shows the SEM results of the composite scaffolds of the PCL/gelatine with a PCL to gelatine ratio of 70:30 that were created according to the mentioned electrospinning parameters in Table 1. According to the SEM images of all the samples, sample B2 was selected as the optimum sample.

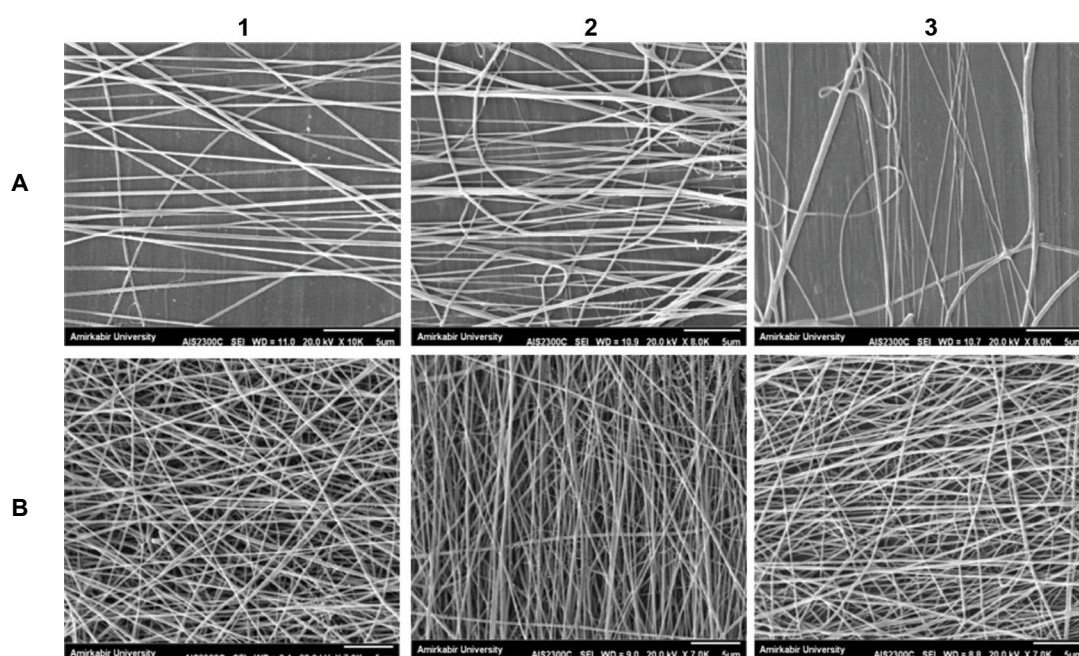


Fig. 2: Scaffold homogeneity analysis by scanning electron microscopy (SEM) micrographs of the aligned polycaprolactone (PCL)/gelatine (70:30) with different electrospinning parameters (Table 1) for the A1, A2, A3, B1, B2 and B3 samples.

To obtain the optimum ratio of the composite scaffold, physicochemical and mechanical properties of different ratios of the PCL/gelatine (80:20, 70:30, 60:40) were evaluated. SPSS results and SEM images showed that as the gelatine ratio increased, the nanofibres showed higher heterogeneity [Fig.3, (18)].

The mechanical strength evaluation results demonstrated that the studied scaffolds tolerated a tension of 5 mm/minute in the direction of the parallel nanofibres. The results were plotted in stress-strain figures for all samples

(Fig.4E). Table 2 shows the results of the contact angle test and mechanical strength. Based on our results from SEM images and the contact angle and mechanical strength experiments, we selected the PCL/gelatine scaffold that had a composite ratio of 70:30 for further studies. The chosen scaffold had a contact angle of 46.96° and ultimate tensile strength of 22 MPa, which occurred at 17% elongation (Fig.4C). Since in this study, the scaffold was going to be exposed to 10% elongation, we concluded that our chosen scaffold could be used for the relevant tests.

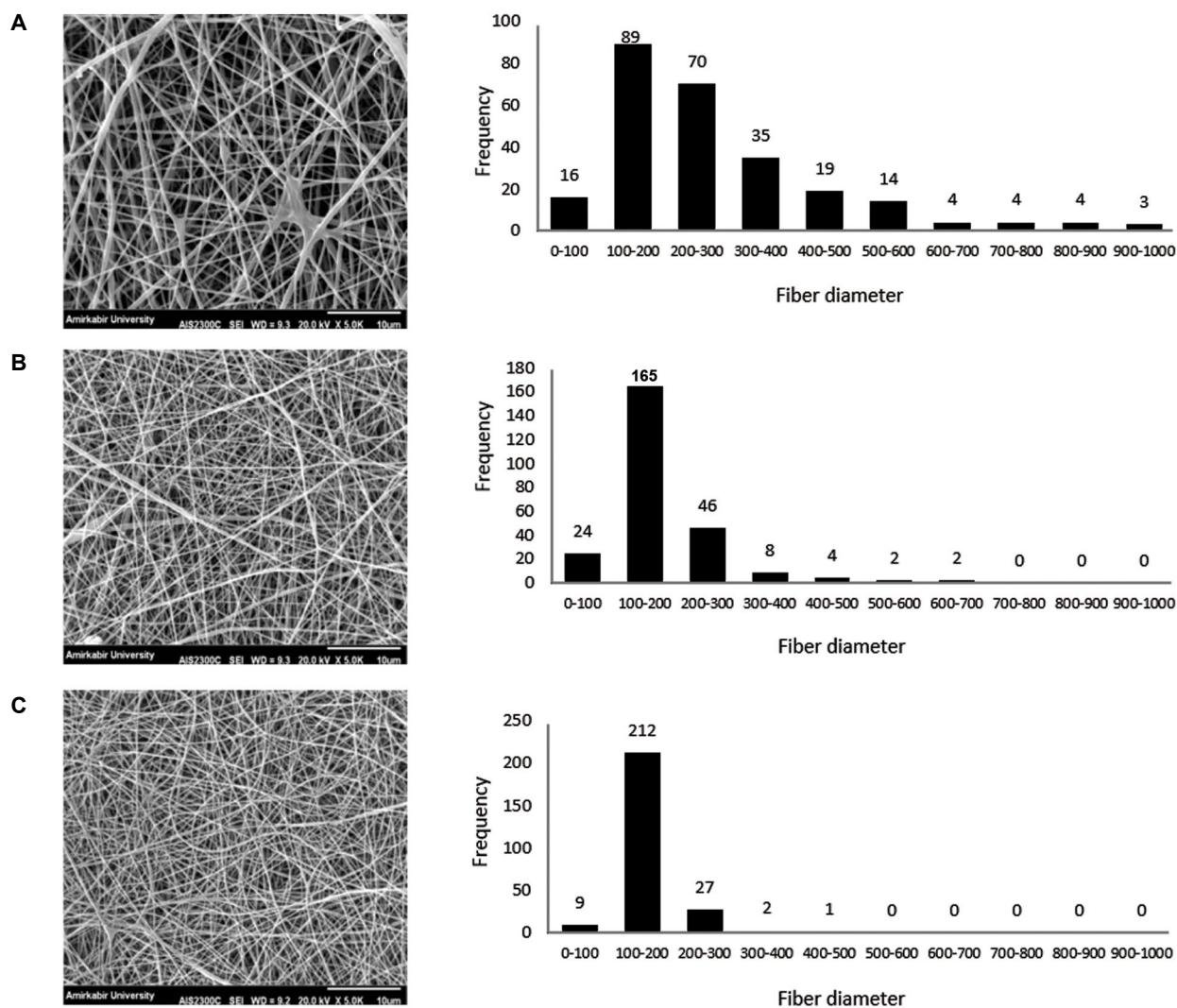


Fig.3: Scanning electron microscopy (SEM) micrographs and fibre diameter frequency of the random: **A.** polycaprolactone (PCL)/gelatine (60:40), **B.** PCL/gelatine (70:30), and **C.** PCL/gelatine (80:20).

Table 2: Young's modulus and contact angle of the scaffolds with different ratios of Polycaprolactone and gelatine.

Composite ratio (PCL/gelatine)	Young's modulus (MPa)	Contact angle	Ultimate tensile strength (MPa)	Elongation at break point (%)
60:40	200	38.97°	11	12
70:30	460	46.96°	22	17
80:20	504	68.71°	28	22

Cell viability

We performed the MTS assay to evaluate the cytotoxicity of the PCL/gelatine composite scaffold compared to the control PCL scaffold. As shown in Figure 4F, the number of cells on the scaffolds increased over time. At the fourth day, SEM images of the scaffolds indicated that the CPCs adhered to the aligned scaffold in the direction of the nanofibres (Fig.4B).

Cell proliferation in the static and dynamic samples

We cultured CPCs on the selected composite scaffolds

for three days. Then, we carried out mechanical loading on one of the scaffolds for five days using the MLD (Fig.1). Figures 5A, B show SEM images of these two samples.

Gene expression results in the static and dynamic samples

Quantitative real-time PCR analysis was performed to evaluate expressions of the *TTN*, *MYH-6* and *GJAI* genes (Fig.5C).

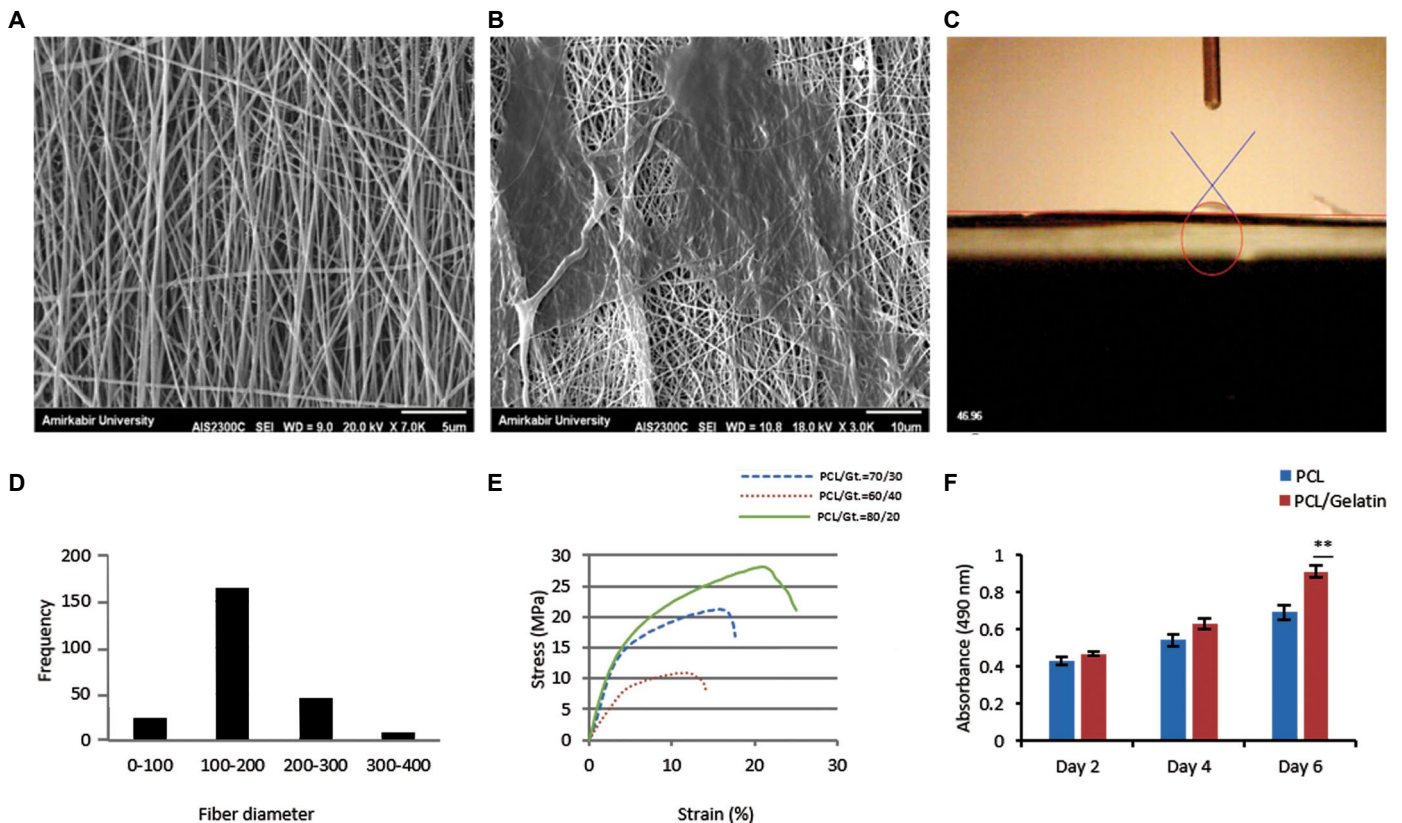


Fig.4: Mechanical, chemical and physical characteristics of the main scaffold. **A.** Scanning electron microscopy (SEM) image of the aligned polycaprolactone (PCL)/gelatine (70:30). **B.** SEM micrograph of cardiac progenitor cells (CPCs) on the scaffold at the fourth day of the static culture. **C.** Contact angle measurement. **D.** Fibre diameter frequency of the nanofibres (SPSS). **E.** Typical stress–strain curve of the PCL/gelatine 70:30 in comparison with the PCL/gelatine 60:40 and 80:20 nanofibres. **F.** Cell proliferation and viability assays of the PCL/gelatine 70:30 nanofibres on days two, four, and six. *Significant differences and **P<0.01 versus control. PCL was used as the control (n=12).

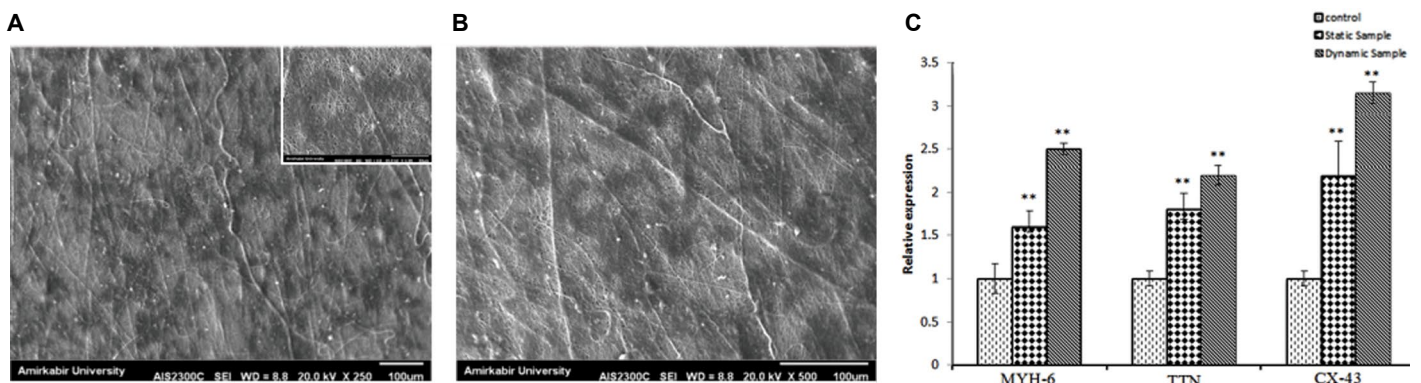


Fig.5: Cell morphology and gene expression on the scaffolds in the static and dynamic conditions. Scanning electron microscopy (SEM) micrographs of the cardiac progenitor cells (CPCs) on: **A.** dynamic sample after three days of static culture and five days of dynamic culture by the mechanical loading device (MLD) and **B.** static sample after eight days of static culture. **C.** Real-time PCR graph of the cardiac genes, *MYH-6*, *TTN* and *CX-43*, expressions in the control, static, and dynamic samples. *; Significant differences, and **P<0.01 versus control. Cardiac stem cells (CSCs) were used as the control (n=4).

Discussion

We compared different scaffolds by varying the electrospinning parameters to investigate the optimum parameters for a suitable cardiac scaffold. According to the SEM results of six scaffolds obtained from different electrospinning parameters listed in Table 1, the following observations were made: i) a decrease in the polymer feeding rate along with an increase in the distance between the needle and collector resulted in dramatic reduction in the nanofibre diameters in addition to a partial loss in homogenization of the fibres (Samples A1 and A2) (30). ii) When the voltage was decreased, the nanofibres with high discrepancy and a non-homogenized distribution were produced. This observation indicated that the imposed voltage was not suitable to generate a Taylor cone in the mentioned electrospinning process (Samples A1 and A2) (30). iii) When SEM images were studied based on Mandrel rotation speed, it was concluded that increasing the Mandrel rotation speed to a value over its threshold did not result in more aligned nanofibres. The high speed of the mandrel caused the polymer to spread around the collector, which resulted in non-homogenous distribution of the nanofibres (sample B3). iv) Conversely, when the Mandrel rotation speed was less than the threshold, we obtained a scaffold with a weak alignment (sample B1). Therefore, sample B2 was selected as the optimum sample based on the SEM images from all of the samples.

In order to achieve the best composite proportion, the prepared scaffolds were studied based on their mechanical strength and cellular adhesion properties. As expected, evaluation of the contact angle indicated that increasing the rate of the hydrophilic polymer (gelatine) resulted in a decreased contact angle and increased cellular adhesion (18). As indicated in Stress-Strain graph, when the PCL rate increased, the slope of the stress-strain plots and elasticity modulus were also elevated (18, 37). The fracture point in the scaffold composited with a higher PCL ratio occurred when a higher tension percentage was applied (37). Therefore, the results appear to be promising for future advances with the mechanical loading imposed with a 10% strain on the scaffold. Due to the results of MTS assay, the number of cells on the scaffolds increased over time. It was found that integration of gelatine led to an increase in cellular adhesion on the PCL/gelatine composite scaffold compared to the control scaffold.

Eventually, according to all the tests performed on the scaffold, it was clear that we achieved a proper cardiac scaffold; therefore, the scaffold could be subjected to mechanical loading. The dynamic scaffold after five days of simulation was compared with the static scaffold. As shown in SEM micrographs of CPCs, the number of cells grown on the scaffold with the dynamic culture conditions was increased. Quantitative real-time PCR analysis indicated that the cardiac genes were expressed more in the dynamic scaffold compared with the static scaffold. *TTN* and *MYH-6* are transcribed to the Titin protein and α -MHC, respectively, which are responsible for cardiac muscle contraction. *GJAI* is transcribed to

Connexin-43, which is a Gap junction protein responsible for regulating intercellular relations and synchronized cardiac contraction (25, 35). Our results elucidated that the expressions of the *TTN*, *MYH-6* and *GJAI* genes increased in the scaffold with the mechanical loading profile compared to the static culture condition. This finding indicated the appropriate transfer of tension force to the cardiomyocytes in the scaffold that had a mechanical loading profile. The dynamic condition induced higher gene expressions that were related to the transfer of a contractile force through natural cardiac tissue.

Conclusion

The goal of our study was to appropriately simulate and mimic cardiac ECM and the mechanical conditions in the heart tissue *in vitro*. We used an electrospun scaffold with aligned nanofibres combined with two PCL and gelatine polymers and produced a scaffold with suitable cellular adhesion and mechanical strength. The resultant scaffold showed a homogenous and consistent diameter distribution with a chemical-physical profile similar to cardiac ECM. Next, an MLD was used to produce a 10% strain with 1 Hz frequency to CPCs seeded on the scaffold for five days in the direction of the parallel nanofibres. This established a similar condition to the heart muscle with simultaneous contraction among cells with mechanical loading transferred through Gap junctions. Based on physics theories, applying a mechanical force in a special direct way would allow it to transmit more efficiently, such that the applied stress to the 2D aligned nanofibre scaffold would stimulate the CPCs to express more cardiac genes. Therefore, the relevant genes that are responsible for synchronized cardiac contraction and regular intercellular relationship (*MYH-6*, *TTN* and *CX-43*) could be expressed at higher levels in these cells. Finally, these cells would be suitable candidates for transplantation to the damaged heart tissue without the possibility of developing arrhythmias. A relevant future topic could focus on the effect of infrared radiation from a non-contact sensor applied in the thermal control system in this project. According to a study by a research team at Utah University in 2011, infrared radiation was used to stimulate neonatal rat ventricular cardiomyocytes and toadfish middle ear cells to send neural signals to the brain.

Acknowledgments

This study was financially supported by Royan Institute and the University of Tehran, Faculty of New Sciences and Technologies. We would like to thank Seyyedeh Sahar Hosseini Salekdeh for her assistance with the cell culture process. There are no conflicts of interest to declare.

Authors' Contributions

Z.Sh.; Contributed to all experimental work, data and statistical analysis, and interpretation of data. B.A., S.R.; Contributed to study conception, design, and overall supervision. N.A.; Contributed to conception, design and

manuscript revision. All authors read and approved the final manuscript.

References

- Sidney S, Rosamond WD, Howard VJ, Luepker RV. The "heart disease and stroke statistics-2013 update" and the need for a national cardiovascular surveillance system. *Am Heart Assoc.* 2013; 127: 21-23.
- Henderson K, Sligar AD, Le VP, Lee J, Baker AB. Biomechanical regulation of mesenchymal stem cells for cardiovascular tissue engineering. *Adv Healthc Mater.* 2017; 6(22): 201700556.
- Remme WJ, Swedberg K, Task Force for the Diagnosis and Treatment of Chronic Heart Failure, European Society of Cardiology. Guidelines for the diagnosis and treatment of chronic heart failure. *Eur Heart J.* 2001; 22(17): 1527-1560.
- Chen Q, Harding SE, Ali NN, Lyon AR, Boccaccini AR. Biomaterials in cardiac tissue engineering: ten years of research survey. *Materials Science and Engineering: R: Reports.* 2008; 59(1-6): 1-37.
- Rowin EJ, Maron BJ, Abt P, Kiernan MS, Vest A, Costantino F, et al. Impact of advanced therapies for improving survival to heart transplant in patients with hypertrophic cardiomyopathy. *Am J Cardiol.* 2018; 121(8): 986-996.
- Jawad H, Ali NN, Lyon A, Chen QZ, Harding SE, Boccaccini AR. Myocardial tissue engineering: a review. *J Tissue Eng Regen Med.* 2007; 1(5): 327-342.
- Donato BB. Addressing the heart failure epidemic: from mechanical circulatory support to stem cell therapy. Doctoral dissertation. 2014.
- Goradel NH, Hour FG, Negahdari B, Malekshahi ZV, Hashemzahi M, Masoudifar A, et al. Stem cell therapy: a new therapeutic option for cardiovascular diseases. *J Cell Biochem.* 2018; 119(1): 95-104.
- Gaetani R, Doevendans PA, Metz CH, Alblas J, Messina E, Giacomello A, et al. Cardiac tissue engineering using tissue printing technology and human cardiac progenitor cells. *Biomaterials.* 2012; 33(6): 1782-1790.
- Rajabi S, Pahlavan S, Ashtiani MK, Ansari H, Abbasalizadeh S, Sayahpour FA, et al. Human embryonic stem cell-derived cardiovascular progenitor cells efficiently colonize in bFGF-tethered natural matrix to construct contracting humanized rat hearts. *Biomaterials.* 2018; 154: 99-112.
- Jalili-Firoozinezhad S, Rajabi-Zeleti S, Marsano A, Aghdami N, Baharvand H. Influence of decellularized pericardium matrix on the behavior of cardiac progenitors. *J App Polym Sci.* 2016; 133(14).
- Shimizu T, Yamato M, Akutsu T, Shibata T, Isoi Y, Kikuchi A, et al. Electrically communicating three-dimensional cardiac tissue mimic fabricated by layered cultured cardiomyocyte sheets. *J Biomed Mater Res.* 2002; 60(1): 110-117.
- Rajabi-Zeleti S, Jalili-Firoozinezhad S, Azarnia M, Khayyatan F, Vahdat S, Nikeghbalian S, et al. The behavior of cardiac progenitor cells on macroporous pericardium-derived scaffolds. *Biomaterials.* 2014; 35(3): 970-982.
- Khait L, Hecker L, Blan NR, Cohan G, Migneco F, Huang Y-C, et al. Getting to the heart of tissue engineering. *J Cardiovasc Trans Res.* 2008; 1(1): 71-84.
- Sharma D, Ferguson M, Kamp TJ, Zhao F. Constructing biomimetic cardiac tissues: a review of scaffold materials for engineering cardiac patches. *Emergent Materials.* 2019; 3(1): 1-11.
- Dattola E, Parrotta EI, Scalise S, Perozziello G, Limongi T, Candeloro P, et al. Development of 3D PVA scaffolds for cardiac tissue engineering and cell screening applications. *RSC Adv.* 2019; 9(8): 4246-4457.
- Boffito M, Sartori S, Ciardelli G. Polymeric scaffolds for cardiac tissue engineering: requirements and fabrication technologies. *Polym Int.* 2014; 63(1): 2-11.
- Ghasemi-Mobarakeh L, Prabhakaran MP, Morshed M, Nasr-Esfahani MH, Ramakrishna S. Electrospun poly (ϵ -caprolactone)/gelatin nanofibrous scaffolds for nerve tissue engineering. *Biomaterials.* 2008; 29(34): 4532-4539.
- Paez-Mayorga J, Hernández-Vargas G, Ruiz-Esparza GU, Iqbal HM, Wang X, Zhang YS, et al. Bioreactors for cardiac tissue engineering. *Adv Healthc Mater.* 2019; 8(7): e1701504.
- Vunjak-Novakovic G, Tandon N, Godier A, Maidhof R, Marsano A, Martens TP, et al. Challenges in cardiac tissue engineering. *Tissue Eng Part Rev.* 2009; 16(2): 169-187.
- Tandon N, Cannizzaro C, Chao PH, Maidhof R, Marsano A, Au HT, et al. Electrical stimulation systems for cardiac tissue engineering. *Nat Protoc.* 2009; 4(2): 155-173.
- Radisic M, Park H, Shing H, Consi T, Schoen FJ, Langer R, et al. Functional assembly of engineered myocardium by electrical stimulation of cardiac myocytes cultured on scaffolds. *Proc Natl Acad Sci USA.* 2004; 101(52): 18129-18134.
- Riehl BD, Park JH, Kwon IK, Lim JY. Mechanical stretching for tissue engineering: two-dimensional and three-dimensional constructs. *Tissue Eng Part B Rev.* 2012; 18(4): 288-300.
- Peroglio M, Gaspar D, Zeugolis DI, Alini M. Relevance of bioreactors and whole tissue cultures for the translation of new therapies to humans. *J Orthop Res.* 2018; 36(1): 10-21.
- Shimko VF, Claycomb WC. Effect of mechanical loading on three-dimensional cultures of embryonic stem cell-derived cardiomyocytes. *Tissue Eng Part A.* 2008; 14(1): 49-58.
- Mihic A, Li J, Miyagi Y, Gagliardi M, Li SH, Zu J, et al. The effect of cyclic stretch on maturation and 3D tissue formation of human embryonic stem cell-derived cardiomyocytes. *Biomaterials.* 2014; 35(9): 2798-2808.
- Friedrich O, Schneidereit D, Nikolaev YA, Nikolova-Krstevski V, Schürmann S, Wirth-Hücking A, et al. Adding dimension to cellular mechanotransduction: Advances in biomedical engineering of multi-axial cell-stretch systems and their application to cardiovascular biomechanics and mechano-signaling. *Prog Biophys Mol Biol.* 2017; 130(pt B): 170-191.
- Van der Schueren L, Steyaert I, De Schoenmaker B, De Clerck K. Polycaprolactone/chitosan blend nanofibres electrospun from an acetic acid/formic acid solvent system. *Carbohydr Polym.* 2012; 88(4): 1221-1226.
- Mengistie DA, Ibrahim MA, Wang P-C, Chu C-W. Highly conductive PEDOT: PSS treated with formic acid for ITO-free polymer solar cells. *ACS Appl Mater Inter.* 2014; 6(4): 2292-2299.
- Pham QP, Sharma U, Mikos AG. Electrospinning of polymeric nanofibers for tissue engineering applications: a review. *Tissue Eng.* 2006; 12(5): 1197-1211.
- Kai D, Prabhakaran MP, Jin G, Ramakrishna S. Guided orientation of cardiomyocytes on electrospun aligned nanofibers for cardiac tissue engineering. *J Biomed Mater Res B Appl Biomater.* 2011; 98(2): 379-386.
- Zimmermann W-H, Schneiderbanger K, Schubert P, Didie M, Munzel F, Heubach J, et al. Tissue engineering of a differentiated cardiac muscle construct. *Circ Res.* 2002; 90(2): 223-230.
- Zhang T, Wan LQ, Xiong Z, Marsano A, Maidhof R, Park M, et al. Channelled scaffolds for engineering myocardium with mechanical stimulation. *J Tissue Eng Regen Med.* 2012; 6(9): 748-756.
- Yang H, Schmidt LP, Wang Z, Yang X, Shao Y, Borg TK, et al. Dynamic myofibrillar remodeling in live cardiomyocytes under static stretch. *Sci Rep.* 2016; 6: 20674.
- Radisic M, Park H, Gerecht S, Cannizzaro C, Langer R, Vunjak-Novakovic G. Biomimetic approach to cardiac tissue engineering. *Philos Trans R Soc Lond B Biol Sci.* 2007; 362(1484): 1357-1368.
- Zimmermann WH, Fink C, Kralisch D, Remmers U, Weil J, Eschenhagen T. Three-dimensional engineered heart tissue from neonatal rat cardiomyocytes. *Biotechnol Bioeng.* 2000; 68(1): 106-114.
- Zheng R, Duan H, Xue J, Liu Y, Feng B, Zhao S, et al. The influence of Gelatin/PCL ratio and 3-D construct shape of electrospun membranes on cartilage regeneration. *Biomaterials.* 2014; 35(1): 152-164.
- Dittami GM, Rajguru SM, Lasher RA, Hitchcock RW, Rabbitt RD. Intracellular calcium transients evoked by pulsed infrared radiation in neonatal cardiomyocytes. *J Physiol.* 2011; 589(pt 6): 1295-1306.

Hydrocortisone Promotes Differentiation of Mouse Embryonic Stem Cell-Derived Definitive Endoderm toward Lung Alveolar Epithelial Cells

Mohammad Reza Mokhber Dezfouli, D.V.M., D.V.Sc.^{1,2*}, Sirous Sadeghian Chaleshtori, D.V.M., D.V.Sc.^{1,2}, Azadeh Moradmand, M.Sc.³, Mohsen Basiri, Ph.D.³, Hossein Baharvand, Ph.D.^{3,4}, Yaser Tahamtani, Ph.D.^{3*}

1. Department of Internal Medicine, Faculty of Veterinary Medicine, University of Tehran, Tehran, Iran

2. Institute of Biomedical Research, Faculty of Veterinary Medicine, University of Tehran, Tehran, Iran

3. Department of Stem Cells and Developmental Biology, Cell Science Research Center, Royan Institute for Stem Cell Biology and Technology, ACECR, Tehran, Iran

4. Department of Developmental Biology, University of Science and Culture, ACECR, Tehran, Iran

**Corresponding Addresses: P.O.Box: 14155-6453, Department of Internal Medicine, Faculty of Veterinary Medicine, University of Tehran, Tehran, Iran*

P.O.Box: 16635-148, Department of Stem Cells and Developmental Biology, Cell Science Research Center, Royan Institute for Stem Cell Biology and Technology, ACECR, Tehran, Iran

Emails: mokhberd@ut.ac.ir, yasertahamtani@royaninstitute.org

In this article which was published in Cell J, Vol 20, No 4, winter 2019, on pages 469-479, the authors regret to acknowledge that we failed to mention in our article that a patent based on this study had been filed by Royan Institute and Tehran University with S.S.C., M.R.M.D., H.B., and Y.T. as inventors.

The authors would like to apologies for any inconvenience caused.

Citation: Mokhber Dezfouli MH, Sadeghian Chaleshtori S, Moradmand A, Basiri M, Baharvand H, Tahamtani Y. Hydrocortisone promotes differentiation of mouse embryonic stem cell-derived definitive endoderm toward lung alveolar epithelial cells. Cell J. 2021; 23(1): 137. doi: 10.22074/cellj.2021.7929.
This open-access article has been published under the terms of the Creative Commons Attribution Non-Commercial 3.0 (CC BY-NC 3.0).

***In Vitro* Differentiation of Human Umbilical Cord Blood CD133+ Cells into Insulin Producing Cells in Co-Culture with Rat Pancreatic Mesenchymal Stem Cells**

Fazel Sahraneshin Samani, M.Sc.^{1,2}, Marzieh Ebrahimi, Ph.D.^{1,3*}, Tahereh Zandieh, Ph.D.¹,
Reyhaneh Khoshchehreh, M.Sc.^{1,2}, Mohamadreza Baghaban Eslaminejad, Ph.D.¹,
Nasser Aghdami, Ph.D.³, Hossein Baharvand, Ph.D.¹

1. Department of Stem Cells and Developmental Biology at Cell Science Research Center, Royan Institute for Stem Cell Biology and Technology, ACECR, Tehran, Iran
2. Department of Developmental Biology, University of Science and Culture, ACECR, Tehran, Iran
3. Department of Regenerative Biomedicine at Cell Science Research Center, Royan Institute for Stem Cell Biology and Technology, ACECR, Tehran, Iran

*Corresponding Address: P.O.Box: 16635-148, Department of Stem Cells and Developmental Biology at Cell Science Research Center, Royan Institute for Stem Cell Biology and Technology, ACECR, Tehran, Iran
Email: mebrahimi@royaninstitute.org

In this article which was published in Cell J, Vol 17, No 2, Summer 2015, on pages 211-220, the authors found that Figures 3 and 4 had some errors that accidentally happened during organizing figures as well as because of mislabeling of some images and saving them in an incorrect folder. The following figures are corrected.

The authors would like to apologies for any inconvenience caused.

Citation: Sahraneshin Samani F, Ebrahimi M, Zandieh T, Khoshchehreh R, Baghaban Eslaminejad M, Aghdami N, Baharvand H. In vitro differentiation of human umbilical cord blood CD133+ cells into insulin producing cells in co-culture with rat pancreatic mesenchymal stem cells. Cell J. 2021; 23(1): 138-139. doi: 10.22074/cellj.2021.7935.

This open-access article has been published under the terms of the Creative Commons Attribution Non-Commercial 3.0 (CC BY-NC 3.0).

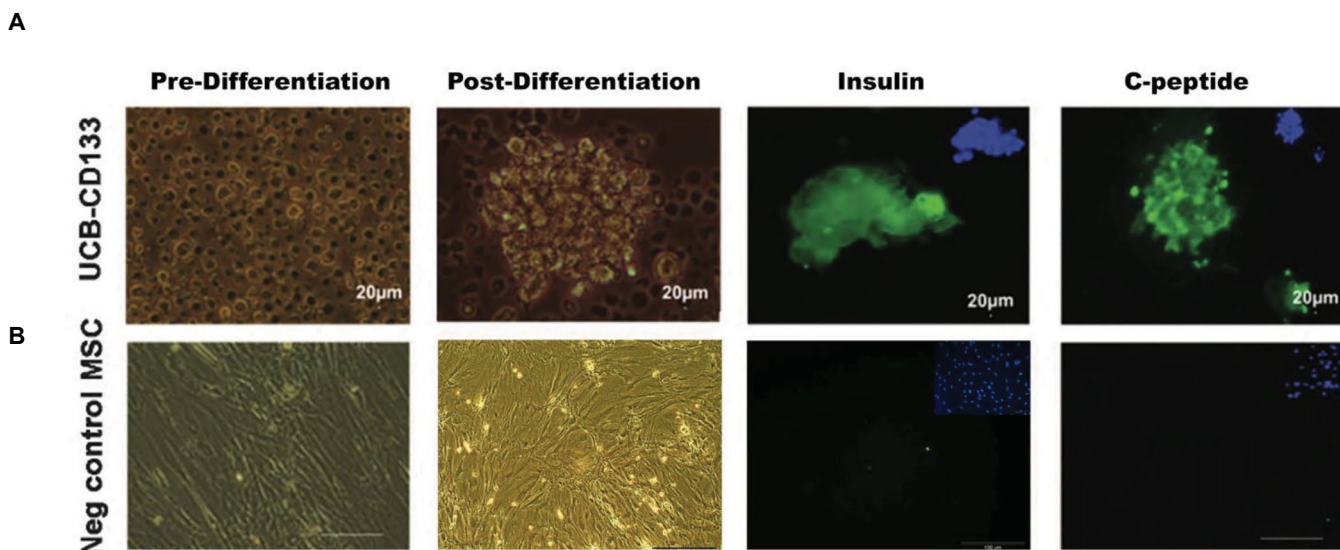


Fig.3: Immunofluorescence staining for insulin (FITC) and C-peptide (FITC) in differentiation umbilical cord blood cluster of differentiation 133+ (UCB-CD133+) cells. **A.** The bright field images of pre- and post-differentiation UCB-CD133+ cells. Expressions of insulin and C-peptide conjugate with FITC (green) and nucleus stained with DAPI and **B.** Bright field images of mesenchymal stem cells (MSCs) pre- and postdifferentiation and lack of expressions of insulin and C-peptide in the cells ($\times 100$).

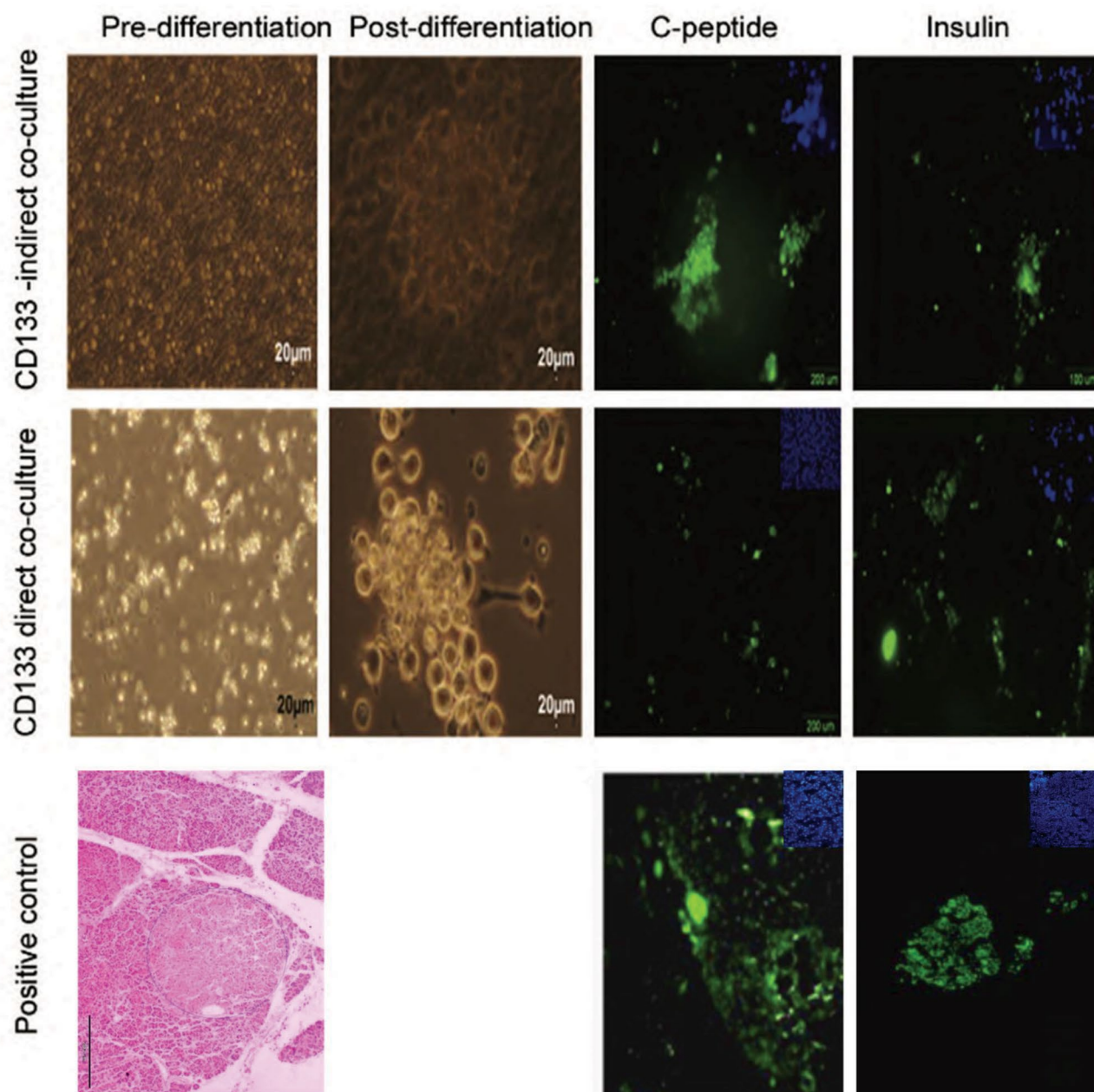


Fig.4: Effect of rat pancreatic mesenchymal cells on differentiation of umbilical cord blood cluster of differentiation (UCB-CD133+) into pancreatic β cells. Morphology and immunophenotyping of cells pre- and post-differentiation ($\times 100$). Immunofluorescence staining of cells for insulin (FITC) and C-peptide (FITC) in the groups co-cultured with rat pancreatic stromal cells. As observed with fluorescent microscope, insulin and C-peptide expressed after pancreatic differentiation in islet-like clusters. Human cadaver pancreas was the positive control. Nuclei were counterstained with 4',6-diamidino-2-phenylindole (DAPI).

Stem Cells from Human Exfoliated Deciduous Tooth Exhibit Stromal-Derived Inducing Activity and Lead to Generation of Neural Crest Cells from Human Embryonic Stem Cells

Khadijeh Karbalaie, M.Sc.¹, Somayyeh Tanhaei, M.Sc.², Farzaneh Rabiei, M.Sc.², Abbas Kiani-Esfahani, M.Sc.², Najmeh Sadat Masoudi, M.Sc.³, Mohammad Hossein Nasr-Esfahani, Ph.D.^{1*}, Hossein Baharvand, Ph.D.^{4, 5*}

1. Department of Cellular Biotechnology at Cell Science Research Center, Royan Institute for Biotechnology, ACECR, Isfahan, Iran
2. Department of Molecular Biotechnology at Cell Science Research Center, Royan Institute for Biotechnology, ACECR, Isfahan, Iran
3. Department of Genetics at Reproductive Biomedicine Research Center, Royan Institute for Reproductive Biomedicine, ACECR, Tehran, Iran
4. Department of Stem Cells and Developmental Biology at Cell Science Research Center, Royan Institute for Stem Cell Biology and Technology, ACECR, Tehran, Iran
5. Department of Developmental Biology, University of Science and Culture, ACECR, Tehran, Iran

**Corresponding Addresses: P.O. Box: 8165131378, Department of Cellular Biotechnology at Cell Science Research Center, Royan Institute for Biotechnology, ACECR, Isfahan, Iran
Email: mh.nasr-esfahani@RoyanInstitute.org
P.O. Box: 16635-148, Department of Stem Cells and Developmental Biology at Cell Science Research Center, Royan Institute for Stem Cell Biology and Technology, ACECR, Tehran, Iran
Email: Baharvand@RoyanInstitute.org*

In this article which was published in Cell J, Vol 17, No 1, Spring 2015, on pages 37-48, we found that Figure 1H, Figure 2 (OTX2, row 3), and Figure 3 (row 4) had been published incorrectly. The following figures are corrected.

The authors would like to apologies for any inconvenience caused.

Citation: Karbalaie KH, Tanhaei S, Rabiei F, Kiani-Esfahani A, Masoudi NS, Nasr-Esfahani MH, Baharvand H. Stem cells from human exfoliated deciduous tooth exhibit stromal-derived inducing activity and lead to generation of neural crest cells from human embryonic stem cells. Cell J. 2021; 23(1): 140-142. doi: 10.22074/cellj.2021.7931.

This open-access article has been published under the terms of the Creative Commons Attribution Non-Commercial 3.0 (CC BY-NC 3.0).

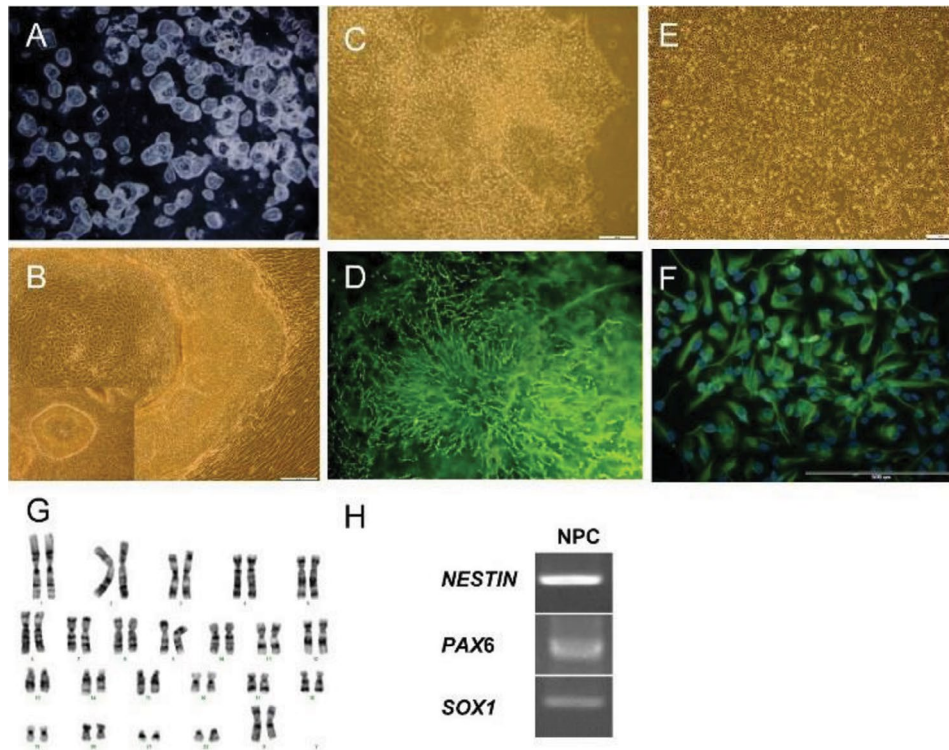


Fig.1: Induction of human embryonic stem cells (hESCs) into neural cells by co-culture with stromal stem cells from human exfoliated deciduous teeth (SHED). **A.** Stereo photomicrographs of hESC colonies with central crater-like structures, **B.** Numerous neural tube-like structures located in the margin of the colonies on day 14, **C.** Neural progenitor cells (NPCs) with rosette-like structures before passaging, **D.** were ZO1 (epithelial marker) positive, **E.** Adherent culture of NPCs, **F.** was NESTIN positive, **G.** NPCs showed normal karyotype and **H.** expressed *NESTIN*, *SOX1* and *PAX6*.

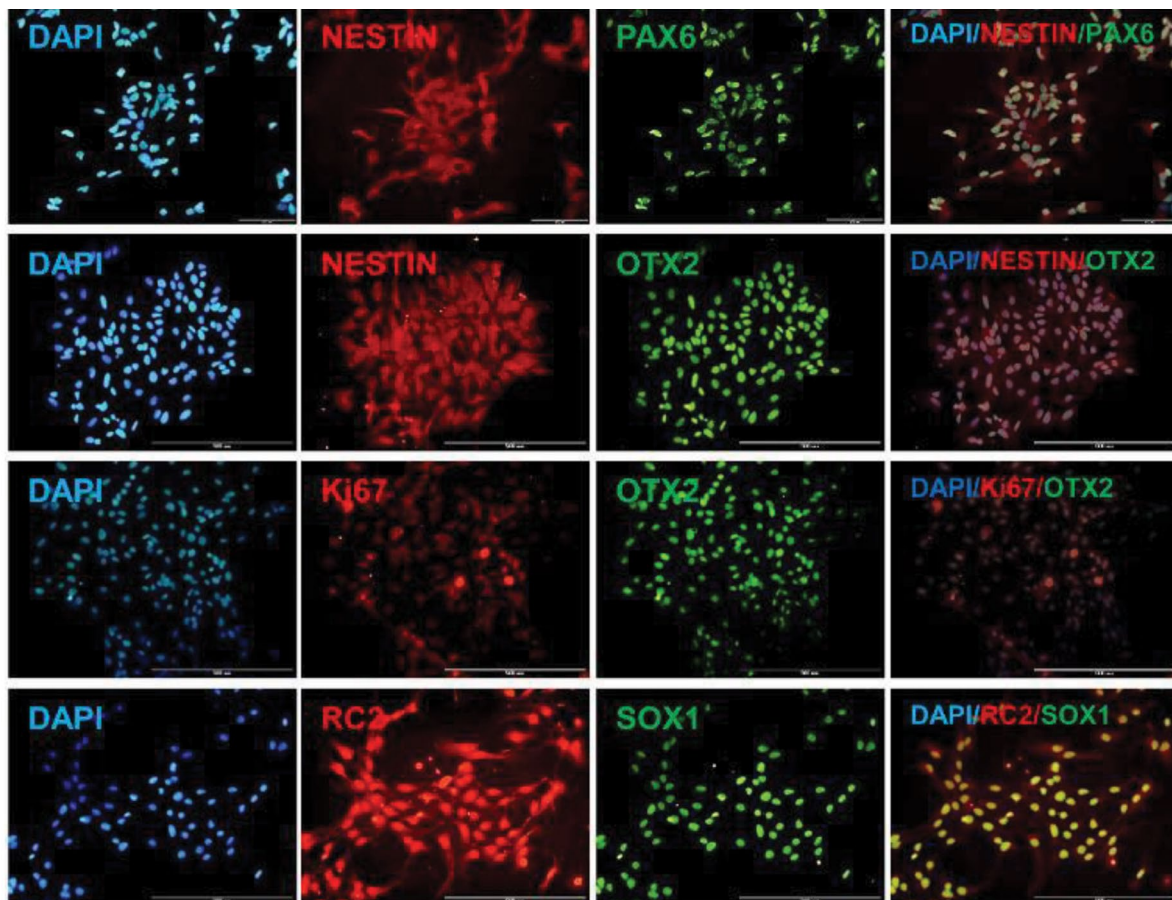


Fig.2: Immunofluorescence staining of human embryonic stem cell derived neural precursor cells (hESC-NPCs). Rostral identity and proliferation potency showed by immuno co-staining for NESTIN/OTX2, NESTIN/PAX6 and OTX2/Ki67. Neuroepithelial and radial glia characteristic demonstrated by RC2/SOX1 immuno co-staining.

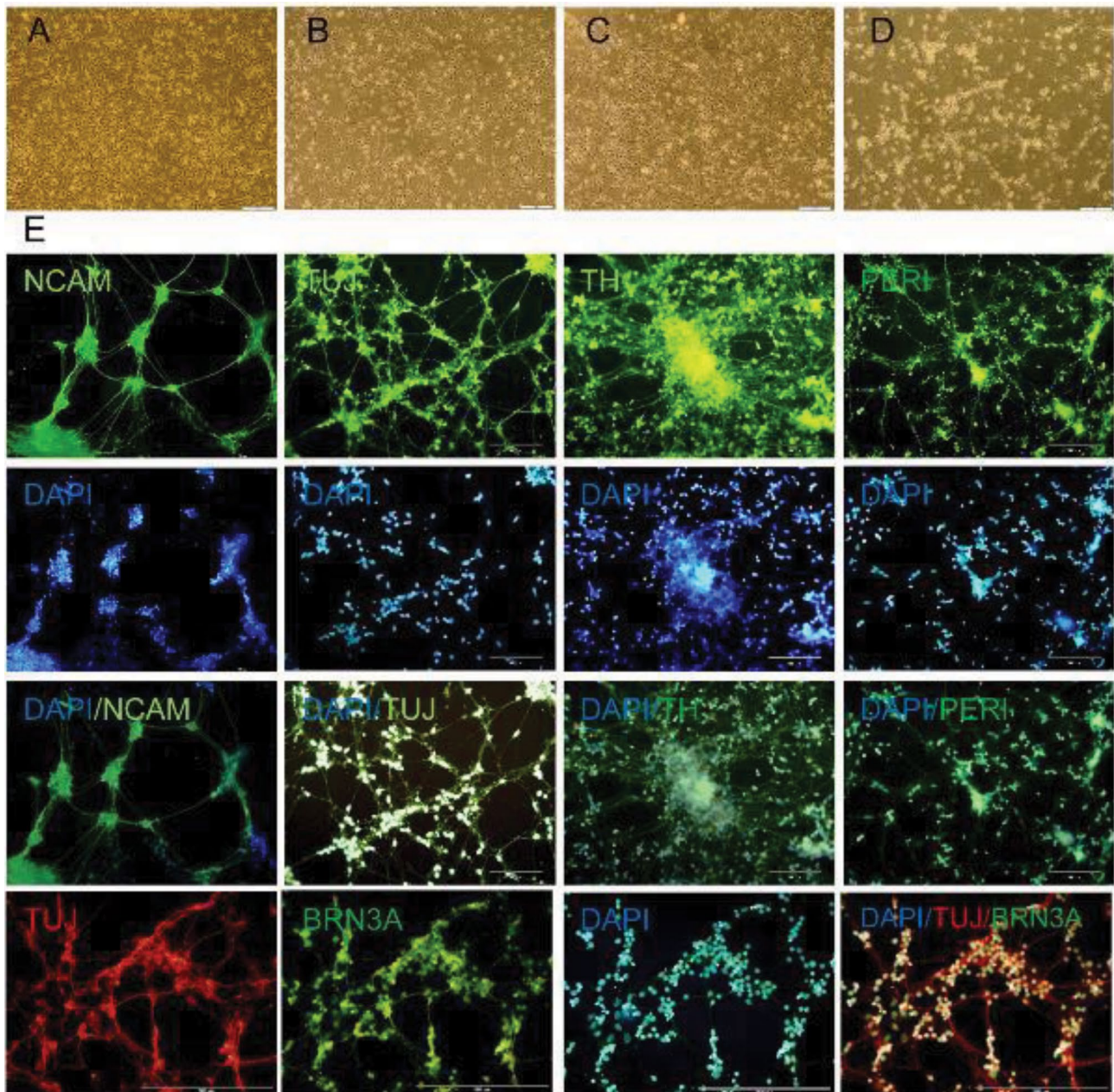


Fig.3: Phase contrast (A-D) and immunofluorescence staining (E) of differentiated human embryonic stem cell derived neural progenitor cells (hESC-NPCs). Visible network structures appeared following a long culture period of neural cells that had bipolar morphology and distinct soma. The differentiated cells were positive for TUJ, NCAM mature neural markers and TH, PERIPHERIN and BRN3A as markers of peripheral neurons.

Conditioned Media Derived from Human Adipose Tissue Mesenchymal Stromal Cells Improves Primary Hepatocyte Maintenance

Zahra Azhdari Tafti, M.Sc.^{1,2}, Mehdi Mahmoodi, Ph.D.^{2,3}, Mohamad Reza Hajizadeh, Ph.D.^{2,3}, Vahid Ezzatizadeh, Ph.D.^{1,4}, Hossein Baharvand, Ph.D.^{1,5}, Massoud Vosough, M.D., Ph.D.^{1,6*}, Abbas Piryaee, Ph.D.^{7,8*}

1. Department of Stem Cells and Developmental Biology, Cell Science Research Center, Royan Institute for Stem Cell Biology and Technology, ACECR, Tehran, Iran
2. Department of Clinical Biochemistry, School of Medicine, Rafsanjan University of Medical Sciences, Rafsanjan, Iran
3. Molecular Medicine Research Center, Rafsanjan University of Medical Sciences, Rafsanjan, Iran
4. Department of Medical Genetics, Medical Laboratory Center, Royesh Medical Group, Tehran, Iran
5. Department of Developmental Biology, University of Science and Culture, Tehran, Iran
6. Department of Regenerative Biomedicine, Cell Science Research Center, Royan Institute for Stem Cell Biology and Technology, ACECR, Tehran, Iran
7. Department of Biology and Anatomical Sciences, School of Medicine, Shahid Beheshti University of Medical Sciences, Tehran, Iran
8. Department of Tissue Engineering and Applied Cell Sciences, School of Advanced Technologies in Medicine, Shahid Beheshti University of Medical Sciences, Tehran, Iran

**Corresponding Addresses: P.O. Box: 16635-148, Department of Stem Cells and Developmental Biology, Cell Science Research Center, Royan Institute for Stem Cell Biology and Technology, ACECR, Tehran, Iran
P.O.Box: 19395/4719, Department of Biology and Anatomical Sciences, School of Medicine, Shahid Beheshti University of Medical Sciences, Tehran, Iran
Emails: masvos@royaninstitute.org, piryae@sbmu.ac.ir*

In this article which was published in Cell J, Vol 20, No 3, Autumn 2018, on pages 377-387, the scale bars in Figures 5-A missed unintentionally during production. The following figure is corrected.

The authors would like to apologies for any inconvenience caused.

Citation: Azhdari Tafti Z, Mahmoodi M, Hajizadeh MR, Ezzatizadeh V, Baharvand H, Vosough M, Piryaee A. Conditioned media derived from human adipose tissue mesenchymal stromal cells improves primary hepatocyte maintenance. Cell J. 2021; 23(1): 143-144. doi: 10.22074/cellj.2021.7936.
This open-access article has been published under the terms of the Creative Commons Attribution Non-Commercial 3.0 (CC BY-NC 3.0).

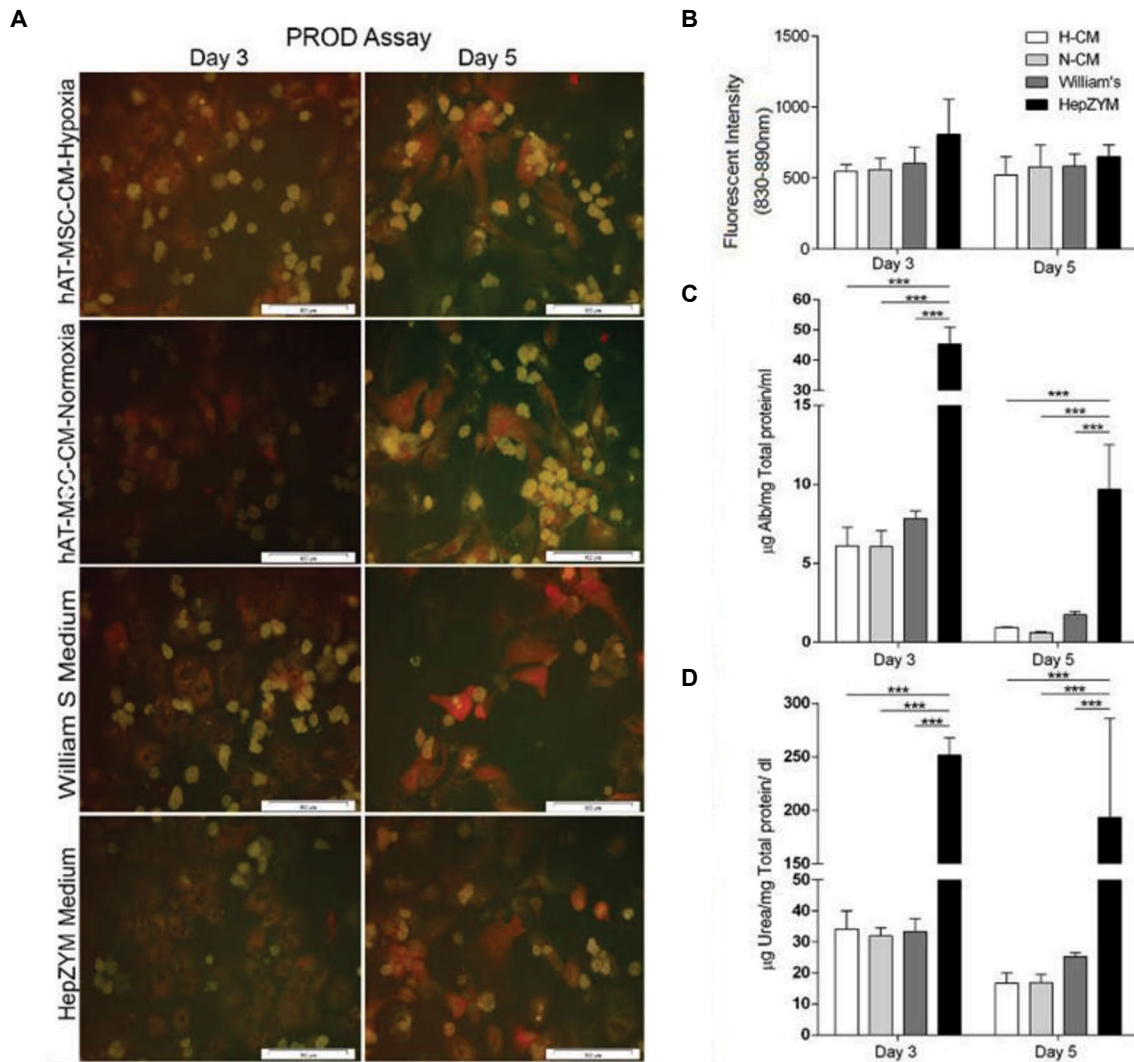


Fig.5: Hepatocyte function analysis in different media. **A, B.** PROD assay in hepatocytes cultured in different media on days 3 and day 5. Representative image and quantitative analysis of PROD activity in primary hepatocytes. Red areas demonstrated PROD activity in the respective cells. There were no significant differences in the CYP activity between all groups, **C.** Albumin secretion, and **D.** Urea synthesis in the different groups. The Alb secretion and urea production from hepatocytes cultured in HepZYM were significantly higher ($P=0.0001$) on days 3 and 5, compared to the other three groups. The data were presented as mean \pm SD ($n=5$, ***, $P<0.0001$) (scale bar: 100 μ m). hAT-MSC-CM; Human adipose tissue-mesenchymal stromal cells-conditioned media, H-CM; hypoxic-CM, and N-CM; Normoxic-CM.